RAPID PROTOTYPING OF MICRO-OPTICS FOR BRIGHTNESS RESTORATION OF DIODE LASERS

By

Krzysztof Michał Nowak MSc (Hons)

Thesis Submitted for the Degree of Doctor of Philosophy

Heriot-Watt University

School of Engineering and Physical Sciences

Optoelectronics and Laser Engineering

July 2003

This copy of the thesis has been supplied on condition that anyone who consults it is understood to recognize that the copyright rests with its author and that no quotation from the thesis and no information derived from it may be published without the prior written consent of the author or of the University (as may be appropriate).

Abstract

The work presented in the thesis addresses rapid-prototyping of micro-optical structures by CO_2 laser ablation of silica glass for production of brightness restoring custom micro-optics for high power, diode laser arrays (HPLDA). These devices are very attractive for industrial material processing applications, like cutting and welding, which are currently carried out using well established CO_2 and solid-state laser technology. They are also excellent pump sources for solid state and fibre lasers. HPLDAs offer substantial reduction of usage and maintenance costs due to their high wall plug efficiency, high average optical powers and exceptional reliability.

However, the beam quality and brightness of these devices is reduced mainly by beam pointing errors and aberrations of beams from the individual emitters forming the laser array, reducing the quality of collimation and limiting the performance of beam shaping optics. These random pointing errors and aberrations are introduced during assembly of the array of individual diode laser bars and cannot be corrected by by the beam collection and shaping optics. Consequently, the intrinsic diode facet radiance is degraded, for example during launch into the fibre optics used for power delivery or as fibre lasers. The effective radiance is reduced by one or two orders of magnitude. A novel solution to these problems is presented in this thesis, using CO_2 laser ablation of silica glass for the rapid manufacture of custom corrective plates for HPLDAs, whose beam errors have been previously characterised by wavefront measurement and analysis.

CO_2 laser ablation of silica has been successfully applied by other researchers to fabricate fibre lenses and refractive micro-optics and has been shown to be capable of unrivalled productivity and optical surface quality compared to other available laser ablation tools like VUV and ultra-fast pulsed lasers. In this thesis, the CO_2 ablation of silica glass has been studied in detail and the optimal machining conditions for precision machining of micro-optical components have been identified. A flexible machining facility has been developed to study rapid fabrication and laser polishing of custom refractive micro-optics. Laser polishing of the micro-optical structures has been investigated and shown to produce the desired optical finish in a well controlled manner. The fabrication of test optical structures has been demonstrated and the profile fidelity has been shown to be better than $\lambda/4$ for a typical HPLDA wavelength.

The design and fabrication of corrective plate for a number of diode laser bars in the HPLDA is presented together with a performance analysis of the fabrication scheme. An improvement of beam quality (M^2 $\sim$12 down to $\sim$2.4) and substantial reduction of beam pointing errors (an order of magnitude) has been demonstrated.

Acknowledgments

I'd like to thank all the people I've met during last three years, those well-wishing and helpful, those planting confusion and those not disturbing, they all enriched my experience. I pay special tributes to prof. Krzysztof Abramski for lending me a key to a door of Heriot-Watt University. I bow to my supervisor prof. Howard Baker for numerous hours of discussion and constructive critics, help offered and for flattering recognition. I'm very grateful for the credit of trust I was given by prof. Denis Hall. Special thanks to Steve Hughey for well-wishing and support during my stay in Edinburgh. I thank my Parents for their never-ending emotional support and inexhaustible faith in me. I'm more than happy to have received the friendship and the lessons of patience from Józef Wendland. I'm deeply and unspeakably grateful to Yuki for standing by me in the times of great peril, for her love and affection.

Contents

List of Figures

List of Tables

Presentations

1. H. J. Baker, G. A. Markillie, F. Villarreal, K. M. Nowak, C. Janke and D. R. Hall, "Rapid prototyping of refractive micro-optics using slab waveguide CO_2 lasers", CLEO/Europe , Nice, 2000

2. K. M. Nowak, G. A. Markillie, A. Holdsworth, H. J. Baker and D. R. Hall, "Rapid prototyping of refractive micro-optics using CO_2 laser machining of silica", Micro Optics and Lens Arrays, IOP, London, 14 September 2001

3. H. J. Baker, K. M. Nowak and G. A. Markillie, "Glass machining using infrared lasers", Application of Laser Micro-engineering, AILU, Edinburgh, 27 February 2002

4. K. M. Nowak, H. J. Baker and D. R. Hall, "Pulsed-laser machining and polishing of silica micro-optical components using a CO_2 laser and an acousto-optic modulator", Photonics Fabrication Europe 2002, Brugge, Belgium, 28 October - 1 November

5. J. Monjardin, K. M. Nowak, A. Holdsworth, H. J. Baker and D. R. Hall, "Brightness improvement for micro-lensed, laser diode bar stacks", Advanced Solid-State Photonics, San Antonio, Texas USA, 2-5 February 2003

6. H. J. Baker, K. M. Nowak, J. Monjardin and D. R. Hall, "Laser machining of silica micro-optics for diode laser arrays applications", Laser Precision Microfabrication 2003, Munich, Germany, 21-28 June 2003

Publications

1. K. M. Nowak, H. J. Baker, and D. R. Hall, "Pulsed-laser machining and polishing of silica micro-optical components using a CO_2 laser and an acousto-optic modulator," *Proc. SPIE*, vol. 4941, pp. 107–112, October 2002.

2. J. F. Monjardin, K. M. Nowak, A. R. Holdsworth, H. J. Baker, and D. R. Hall, "Brightness improvement for micro-lensed, laser diode bar stacks," *ASSP TOPS Proc.*, pp. 76–78, Technical Digest 2003.

Chapter 1

INTRODUCTION

1.1 Background

First working optical laser was demonstrated by Maiman in 1960 [1]. It was more a novelty and a triumph of quantum physics than anything of practical importance at the time. However, the unique features of laser light quickly became appreciated. An explosion of discoveries and inventions, which followed the demonstration of the laser, has presented the world with numerous types of lasers utilizing various lasing media (gases, liquid dyes, solid-state) that practically covered the optical spectrum of radiation. Many new applications exploited exceptional properties of laser sources such as excellent coherence and unnaturally high brightness, which allowed for processing of materials (cutting, welding, heat treatment), medical applications (dentistry, surgery, therapeutics), scientific research, telecommunication, optical computing, optical data storage, image recording, entertainment and more [2, 3]. Optical power levels from μW to tens of kW have been achieved.

The lasers are indispensable nowadays and it is difficult to imagine any area of modern life without them. They have found numerous applications in industry and also appeared in significant numbers in a consumer sector [2]. Semiconductor lasers are an example of successful technology capable of cheap mass production and high optical powers (up to tens of W) from very compact packages. Growing demand for the consumer products utilizing the technology (optical storage, printing, image recording) drives the research towards cheaper solutions and better performance.

The lasers alone are not of much use if their output cannot be customized for a particular application. The delivery and focusing of laser beam, to achieve

very high power densities in a very small area, is the most common laser beam transformation, for example in the material processing applications. In case of conventional high power sources, such as CO_2 and solid-state lasers, this task can be easily accomplished with conventional optics, such as bulk lenses and mirrors. However, the applicability of conventional solutions to the output transformation of miniature semiconductor lasers is limited due to available range of miniature conventional optics.

The development of cheap, miniature semiconductor lasers has thus prompted a search for technologies capable of producing cheap custom micro-optics to perform beam shaping for efficient launch into optical fibres, aperture filling of diode laser arrays, optical interconnects and more. Many techniques have been reported so far (for literature review see Section 5.2, p. 105), such as direct writing in photo-resists with electron beam and UV lasers, UV ablation of polymers, ink jet printing of polymer structures and ablation of glasses using UV, ultrafast and infrared lasers. The choice of photo-resists as a substrate material of early fabrication techniques was dictated by availability of precision (< 1 μm resolution) stepper writers, used in semiconductor industry for a preparation of photolithographic masks. After the photonics industry set-off in the last decade, more interest has been directed towards a direct fabrication of micro-optical structures in glasses, which are valued for excellent optical, thermal and mechanical properties. Although the deep UV ablation (F_2 lasers, 157 nm wavelength) seems to be the best suited tool for precision shaping of glasses (minimal heat affected zones, sub-micron resolution and smooth ablated surfaces), its current productivity is too low to be of practical importance when material removal depth of few microns is considered (see Sections 2.5, p. 54 and 5.2, p. 105). However, a development of practical deep UV lasers operating at wavelengths shorter than 133 nm, which corresponds to energy band-gap of silica, is only a matter of time. Such lasers can be expected to be the leading glass shaping tools of future. Ultrafast laser ablation with visible and near-infrared lasers has also been observed by many researchers, in spite of weak normal (single-photon) absorption of these wavelengths by most of inorganic glasses (see Sections 2.5, p. 54 and 5.2, p. 105). Material removal rates were found to be comparable to that of UV lasers, but resultant surface quality was much worse (microcracks, flaking, texturing). Additionally, strong incubation effects add to already complicated, nonlinear mechanism (double-photon, many-photon) of material decomposition. However,

the amount of recent interest and investment into ultrafast processing of materials may result in improvement of surface quality, leading to the development of powerfull and cheap techology for rapid manufacture of micro-optics in near future. In contrast, long 10.6 μm wavelength CO_2 lasers have been reported to cleanly and smoothly ablate silica glass without thermal micro-cracking (see Section 2.5, p. 54). Large volume of removed material per laser pulse, an order of magnitude larger than that of deep UV and ultrafast lasers, has been reported [4]. The advantage of clean ablation of large volumes with CO_2 lasers comes at a price - the lateral resolution is limited by the minimal achievable spot size to 30−50 μm. Although CO_2 laser ablation is not suitable for fabrication of diffractive optical elements (DOE), where the feature sizes are smaller than operating wavelength, it can be successfully applied to manufacture of sub-millimeter refractive optical elements (ROE). A pilot study on a machining of cylindrical lens with slab waveguide CO_2 laser has been carried out in our group [5] and demonstrated such possibility. The additional advantage of using the CO_2 laser lies in a possibility of polishing of the as-machined surfaces by surface tension driven viscous mass re-flow. The process preserves the machined shape but removes machining debris and strongly suppresses the characteristic machining pattern, which give rise to efficient scattering and diffraction of light on the as-machined surfaces. Chapter 6 has been dedicated to the issues of laser polishing of silica micro-optics.

This thesis demonstrates a novel, maskless rapid-prototyping scheme for fabrication of arbitrary ROEs by CO_2 laser ablation of silica glass, developed primarily for beam quality correction of high power, laser diode arrays (HPLDA). The method can be used to fabricate the custom micro-optics for any other semiconductor laser and is capable of competing with an alternative method, ink jet printing with UV-curable organic monomers, renowned for high flexibility and high productivity (see Section 5.2, p. 105).

High power diode laser arrays, which first emerged in 1989 (see Section 1.2, p. 4), have gained enough potential to enter the field of material processing, dominated by CO_2 and solid state lasers. In spite of many advantages over other industrially relevant lasers (see Table 1.1, p.7), the HPLDAs currently occupy an area of low-beam-quality applications, shown in Figure 1.2 on page 8. A technological revolution in a field of material processing is expected if only the intrinsic brightness (see Section 1.2, p. 4) of these devices is restored. Brightness restoration would

allow for direct use of HPLDAs for cutting and welding of metals and replacement of inefficient, conventional laser sources. The corrected HPLDAs can also boost the pumping of solid-state lasers and emerging high power fibre lasers, which require high-brightness optical pumps. The following part of this Chapter is dedicated to a review of history, characteristics and applications of HPLDA devices.

1.2 LDA devices - history, characteristics and applications

A drive for high power, diffraction limited diode laser sources for telecommunications, optical storage, blue light generation via frequency doubling, optical signal processing, pumping of solid state lasers, medical applications and material processing, has resulted in significant scientific and technological breakthroughs in the semiconductor industry in the last two decades [6, 7]. The amount of research material accumulated over the years is beyond a scope of this chapter, which concentrates on the analysis and restoration of beam quality of commercially available HPLDAs. Brightness improvement of practical HPLDA-based systems is necessary if these very promising devices are to compete and finally replace well established CO_2 and solid-state laser technology in various areas of laser applications requiring high radiance or brightness (power per unit area per unit solid angle), such as material processing or pumping of solid-state and fibre lasers.

A lot of attention has been directed towards the development of capable solutions and reliable HPLDA manufacture technologies. Power limits, imposed by the catastrophic optical mirror damage (COMD) irradiance ($\sim 17 \cdot 10^6$ W/cm^2), have been overcome with an advent of monolithic laser diode arrays (LDA) in late seventies. Instead of fabricating a single, large aperture diode laser with highly degraded output characteristics, the optical power was spread over a large area of the chip in a number of stripe waveguide emitters with array fill factor usually around 50% (see Figure 1.1). In great simplification, heat management issues could be then relaxed and optical stability of the device improved significantly. However, the problems associated with insufficient lateral mode confinement and reliability of operation (beam filamentation and catastrophic hot spots, self-focusing and beam profile instability, spatial hole burning) have resulted in a number of solutions, such as broad-area devices (BA), Anti-Resonant Ridge Optical Waveguide (ARROW)

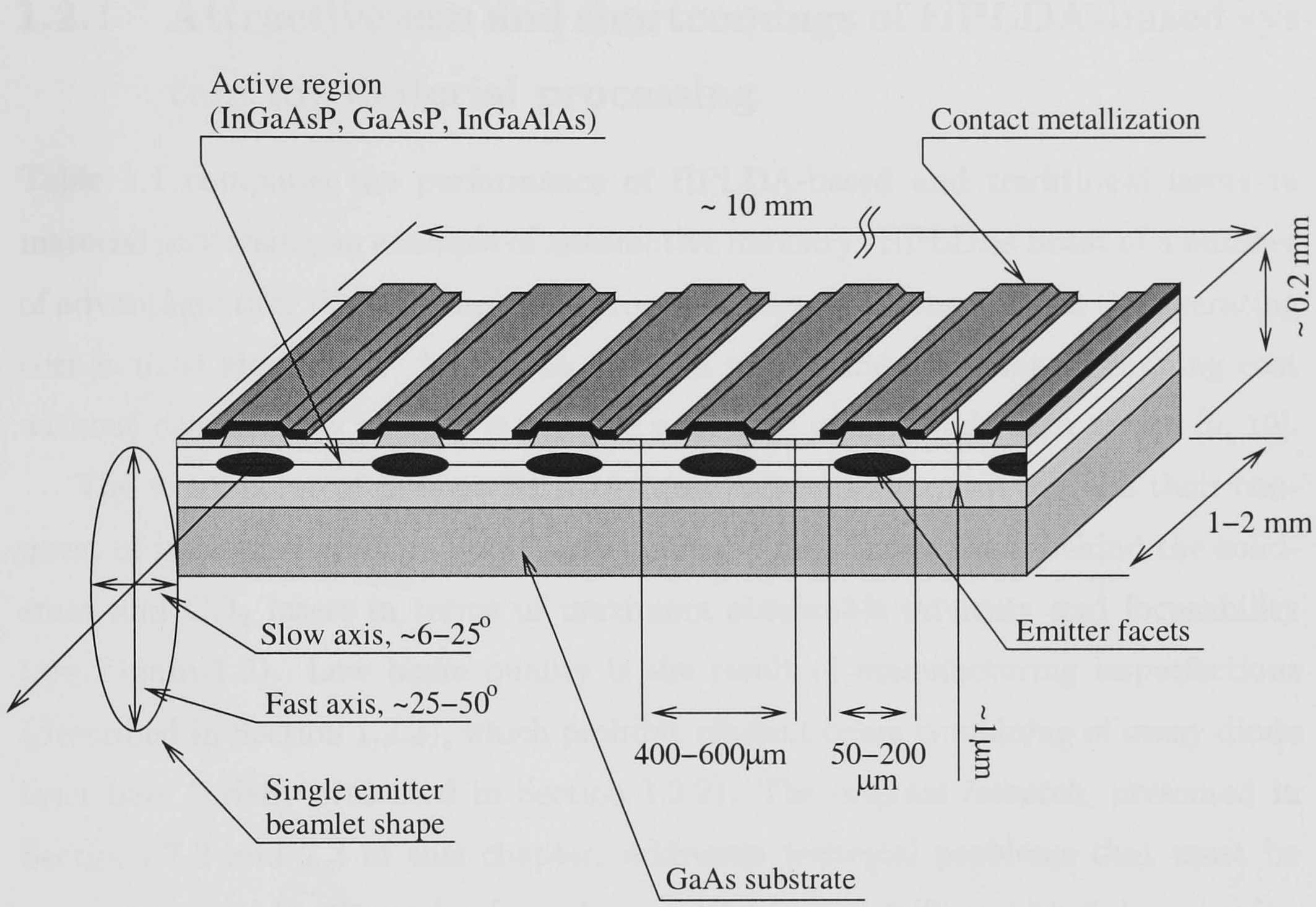

Figure 1.1: Schematic view of a monolithic diode laser bar, consisting of optically and electrically separated single emitters. The fill factor of the array, the ratio between emitter aperture and the emitter section of the bar, is usually between 30 and 50%. Aspect ratio of features not preserved. Single emitter can supply 1−2 W of power. In a typical 1-cm bar there are 25−50 emitters, yielding 30−60 W per bar. Further power scaling can be done by bar stacking.

lasers, high-brightness tapered devices and more described elsewhere [6, 7].

Modern HPLDAs can deliver stable and reliable output up to 80 °C and withstand a temperature surge up to 100 °C. They also boast of low costs of ownership, ~50% power conversion, ~25% wall plug efficiency and the lifetime in excess of 10000 hours.

1.2.1 Attractiveness and shortcomings of HPLDA-based system for material processing

Table 1.1 compares the performance of HPLDA-based and traditional lasers in material processing on example of automotive industry. HPLDAs boast of a number of advantages over the other material processing lasers, amongst which the operating cost is most significant. Almost an order of magnitude reduction of running cost without productivity penalty is possible with high power diode laser arrays [9, 10].

The weak point of present HPLDA-based systems that still inhibits their conquest of industrial arena is poor beam quality, which leaves them behind the solid-state and CO_2 lasers in terms of maximum obtainable intensity and focusability (see Figure 1.2). Low beam quality is the result of manufacturing imperfections (described in Section 1.2.3), which prohibit efficient beam combining of many diode laser bars (briefly presented in Section 1.2.2). The original research, presented in Sections 7.2 and 7.3 of this chapter, addresses technical problems that must be overcome to ignite the technological revolution in a £-million material processing market [3, 2] dominated so far by CO_2 lasers, flash-pumped and diode-pumped solid-state lasers.

1.2.2 Power and brightness scaling of diode laser arrays

The applications, such as key-hole welding of metals or pumping of solid-state lasers, require high power lasers of high brightness (optical power per unit area per unit solid angle). Traditionally, these areas have been dominated by the CO_2 and solid-state laser technology, which meet radiance requirements of these applications. Semiconductor diode laser arrays have a potential to compete with the well-established technology if only the power and brightness criteria can be satisfied (see Figure 1.2). To achieve that, a number of individual diode laser bars has to be incorporated in the HPLDA-based system. Power can be scaled by stacking

	HPLDA-based	CO_2	Nd:YAG flash pumped	Nd:YAG diode pumped
Hourly operation cost (Continuous operation at 100% power and a 4000 hours work year)	£0.75	£5	£15	£3
Net system efficiency (Continuous operation at 100%, including chiller)	25%	6%	1%	6%
Footprint for laser, power supply and chiller [sq. ft.]	8	50	100	60
Wavelength [μm]	0.7–2.3	10.6	1.06	1.06
Absorption - steel	40%	12%	35%	35%
Absorption - aluminum	13%	2%	7%	7%
Average intensity [W/cm^2]	10^{4-5}	10^{6-7}	10^{6-7}	10^{6-7}
Beam quality, M^2	20-2000	~1.1–2	~1.1–2	~1.1–2
Maximum power commercially available [kW]†	4	50	4	4
Part replacement	Laser arrays 10000-20000 hours	Optics 2000 hours, Blower, Turbine 20000-30000 hours	Lamps 1000 hours	Pumping arrays 10000 hours
Laser mobility	High	Low	Low	Low
Beam mobility	High	Medium	High	High

†2001

Table 1.1: Performance comparison of leading material processing lasers, after [8]. Advantages of HPLDAs are underlined, weak sides (targeted by this thesis) are boxed.

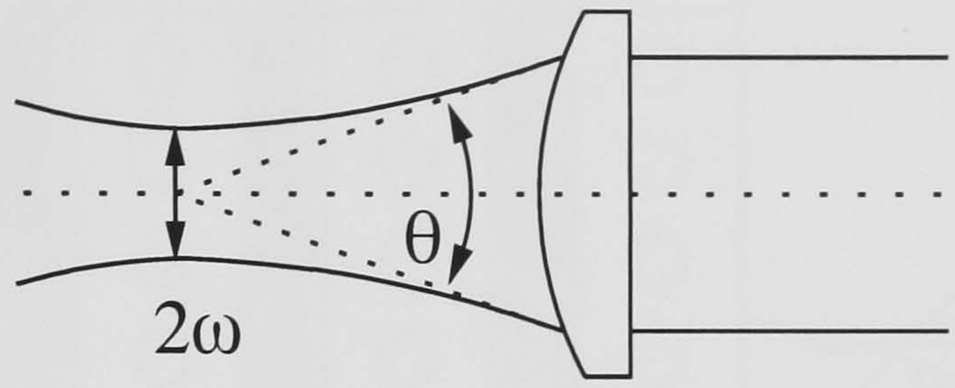

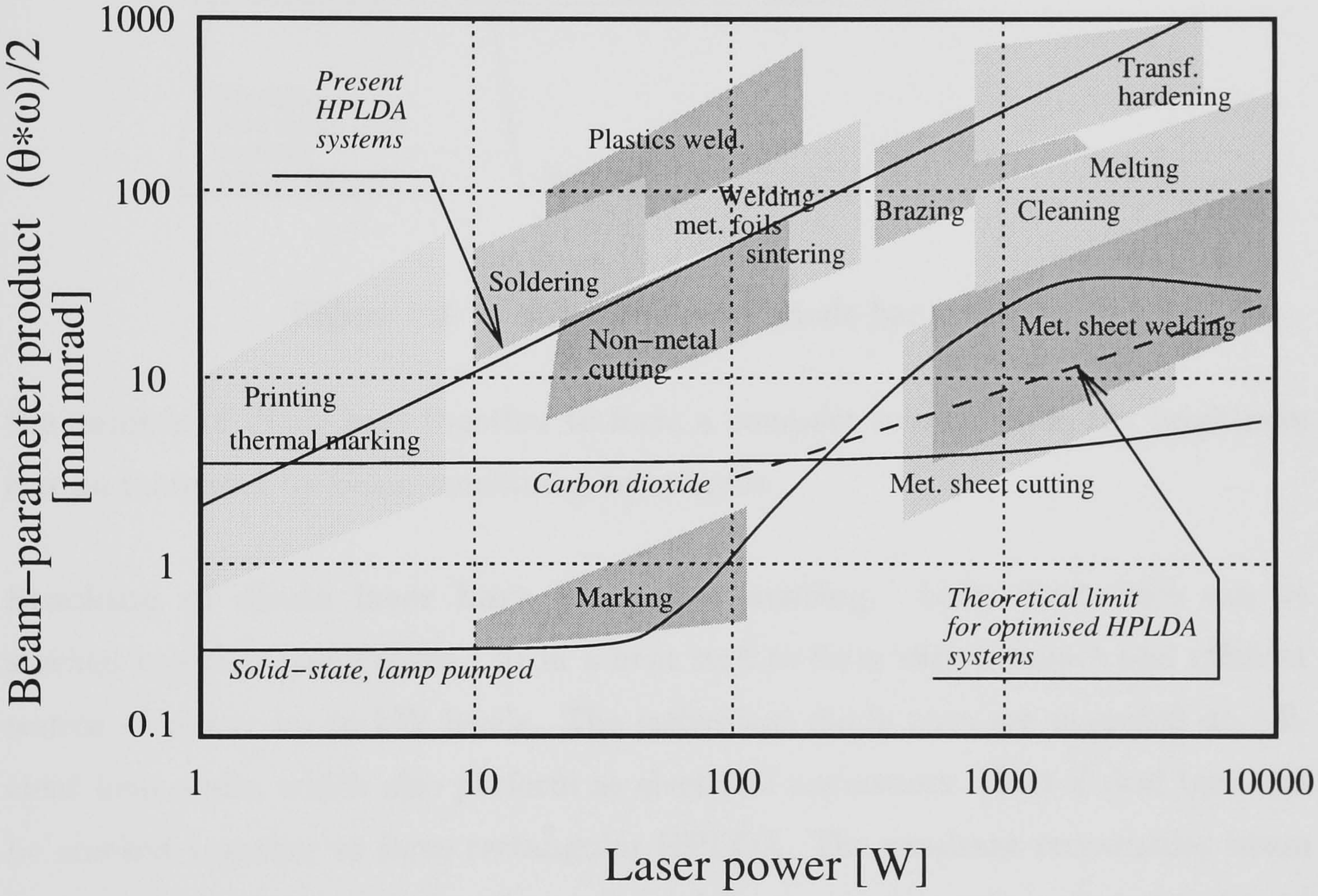

Figure 1.2: Typical beam-parameter requirements of the common laser applications in material processing, after [7]. Beam quality is represented here as a product of beam waist and beam divergence. The performance of HPLDA laser systems is compared with well established laser technology. HPLDA arrangements currently suit the low-beam-quality applications, but with restored beam quality they can effectively compete with other lasers.

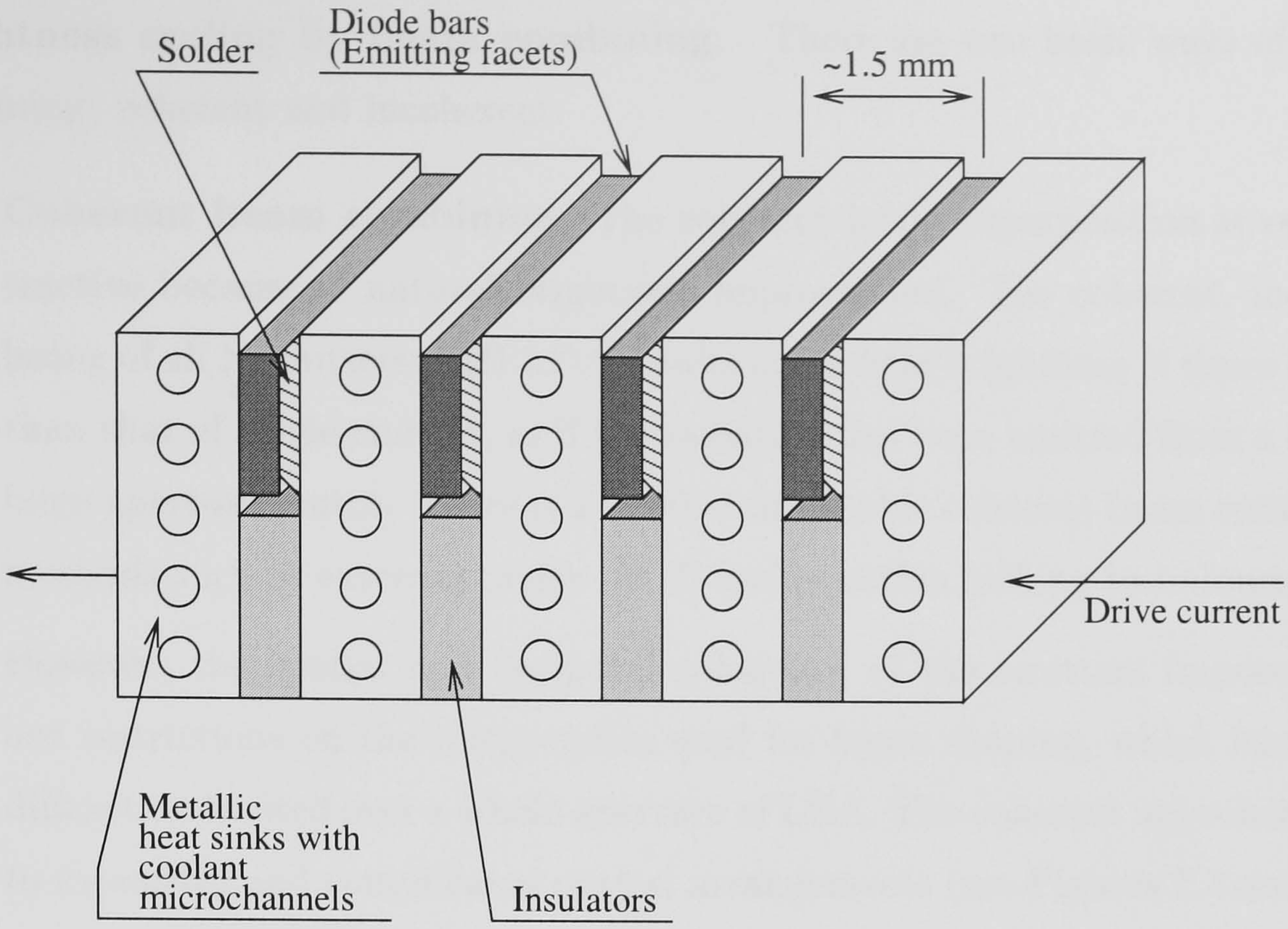

Figure 1.3: Schematic view of diode bar stack.

the number of diode bars together to form a compact source, while the brightness can be increased by beam combining techniques.

Stacking of diode laser bars for power scaling. Laser diode bars can be stacked together (see Figure 1.3) in a heat sink to form very compact and efficient source of power up to kW levels. The individual diode bars are mounted on efficient heat sinks, which also perform as electrical connectors. Heat-sinked bars can be stacked together to form rectangular HPLDA. The resultant rectangular beam becomes quasi-homogeneous after a short free-space propagation distance due to high fast axis divergence ($\pm 50^o$) of emitters in the array. It thus became quite common among manufacturers to equip the diode stacks with microlenses for fast axis collimation of each bar in the stack. High fast-axis divergence demands microlenses of high NA (>0.8) thus effective focal lengths of these devices fall in a range of hundreds of microns. These collimating lenses comprise the first stage of beam shaping and relax the design of further beam collection optics.

The precision of assembly is of paramount importance for the quality of the output beam. The important issues of assembly imperfections, the type of collimation optics and their impact on beam quality are described in Section 1.2.3.

Brightness scaling by beam combining. There are two basic ways of beam combining: coherent and incoherent.

- **Coherent beam combining.** The coherent beam superposition is very attractive because of natural brightness improvement. The coherent, in-phase lasing of all N emitters of HPLDA results in far-field brightness N times higher than that of single emitter, as if the radiation has been emitted from a single, large aperture source. There is a number of capable coherent beam combining methods such as external cavity [6, 7] and injection locking techniques [11].

  However, the spatial and temporal coherence of the emitters imposes serious restrictions on the micro-optics used for beam shaping, which has to be diffraction limited over a whole aperture of LDA. The coherent approach leads to expensive and complicated optical arrangements (see Figures 1.4 and 1.5), which may counter the low-cost advantage of HPLDAs.

- **Beam combining of incoherent LDAs.** Another approach, which offers high optical power levels at low cost of the optical system, combines the beams of incoherent or partially coherent diode laser arrays. Incoherent LDAs are cheaper to manufacture and do not require expensive and sophisticated optical arrangements for beam shaping, since the diffraction limit applies only to the individual emitters in the laser bar. As an outcome of incoherence however, maximum obtainable radiance usually does not scale with a number of emitters in the array and cannot be greater than that of single emitter. For many material processing applications however, the facet radiance of diode laser bar is satisfactory for successful competition with other industrially relevant lasers [10]. The key aspect of incoherent beam combining techniques is thus the preservation of brightness.

  Intrinsic facet brightness can be preserved by beam shaping methods using dual mirror methods [14], microprisms [15]. Incoherent beam combining techniques, involving polarising beam splitters, can increase the brightness by a factor of two. Wavelength multiplexing [10] is capable of brightness scaling proportional to the number of multiplexed HPLDAs. Diffraction gratings arrangements [6] and spectral beam combining [16] are the effective ways of brightness improvement of single diode laser bars.

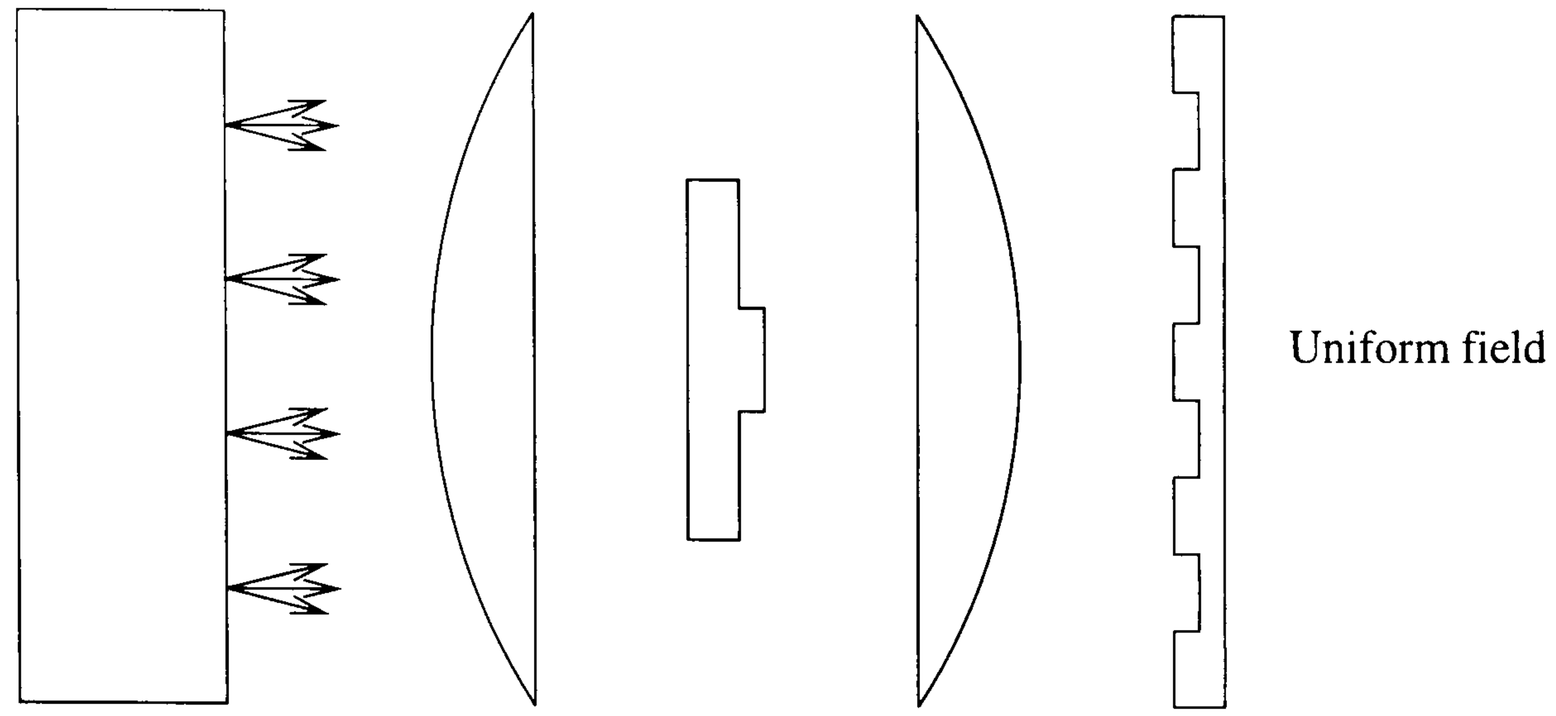

Figure 1.4: Optical setup for aperture filling of a coherent array by phase spatial filtering, after [12].

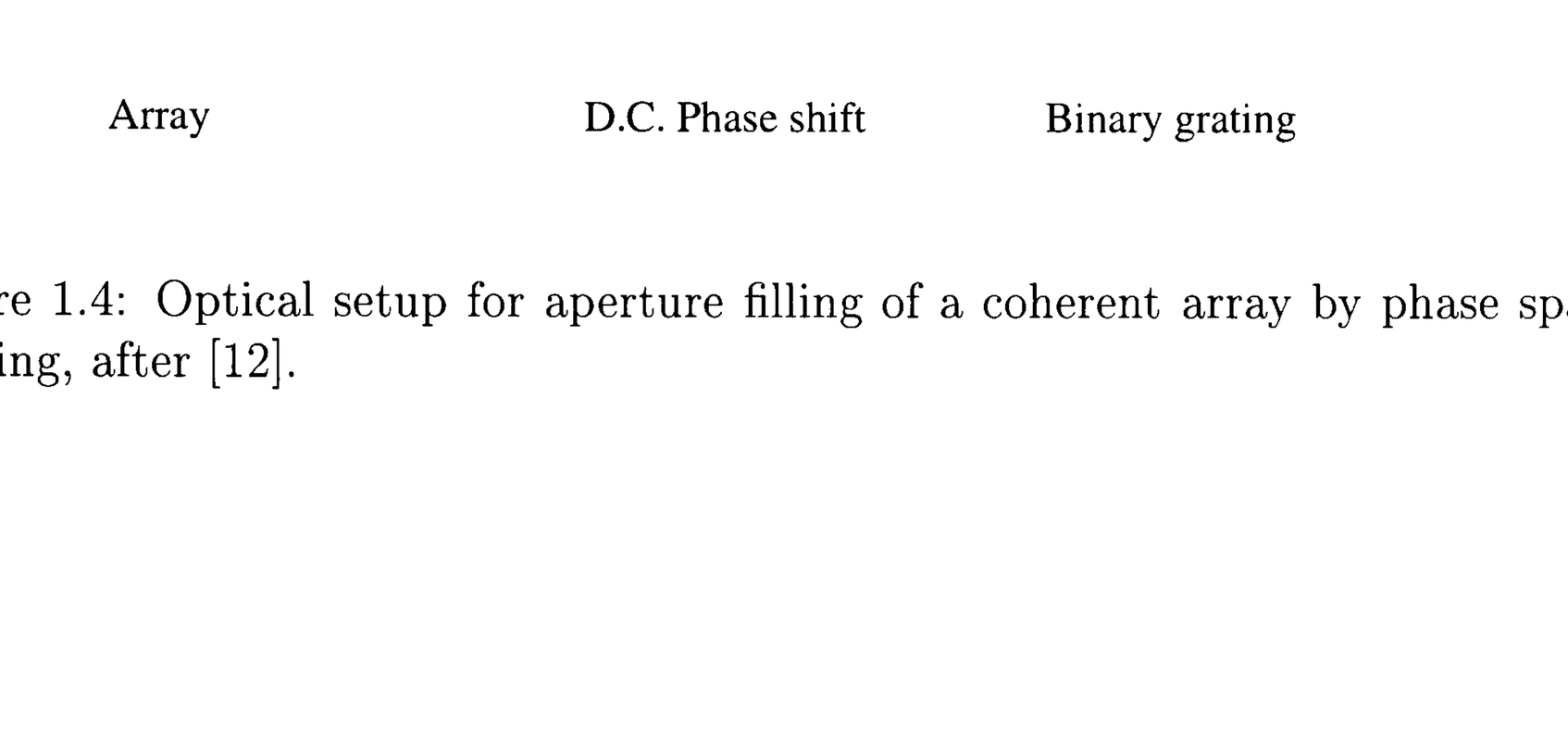

Figure 1.5: Laser beam superposition using binary phase grating in external cavity configuration, after [13].

Incoherent beam combining of HPLDAs is presently widely used in laser systems for material processing as a straight-forward way of achieving high power densities at low cost.

1.2.3 Mechanisms of beam quality deterioration of practical HPLDA arrangements

The beams from many collimated diode bars can be combined together for brightness improvement, as mentioned in Section 1.2.2. In practice however, there is a number of mechanisms, such as assembly inaccuracies and collimation aberrations, which dramatically reduce the quality of collimation and affect the resultant brightness of practical HPLDA arrangements. These aberrations pose a technical challenge, since they are random in nature and cannot be corrected by typical beam shaping optics. The work presented in this thesis delivers a solution to this problem in a form of rapid-prototyped, custom correction micro-optics.

Assembly errors and related beam collimation issues. Random positioning errors (in order of microns) are inevitably introduced during the assembly of the HPLDA. The soldering stage, at which the diode bars are attached to the heat sinks, introduces a number of aberrations, such as shifts, tilts and finally bowing, often referred to in the literature as a "smile".

The misalignments of similar nature may be introduced during the attachment of collimating micro-optics. The microlenses can be misplaced relative to the diode bars (already misplaced relative to the whole stack during soldering) further worsening the output quality. Figures 1.6 and 1.7 illustrate the impact of lens misalignment on the collimation precision and resultant beam pointing errors. The inaccuracies as small as single microns hugely compromise the quality of collimation with regard to the collimation angle and the pointing of resultant beam. In case of a single bar, the correct alignment of collimating micro-optics for all the emitters in the bar cannot be assured, resulting in random beam pointing errors of individual emitters in order of few mrad, too much for efficient beam shaping and combining. With a number of individual bars stacked together, the situation becomes even more critical, leading to one to two orders of magnitude loss of brightness.

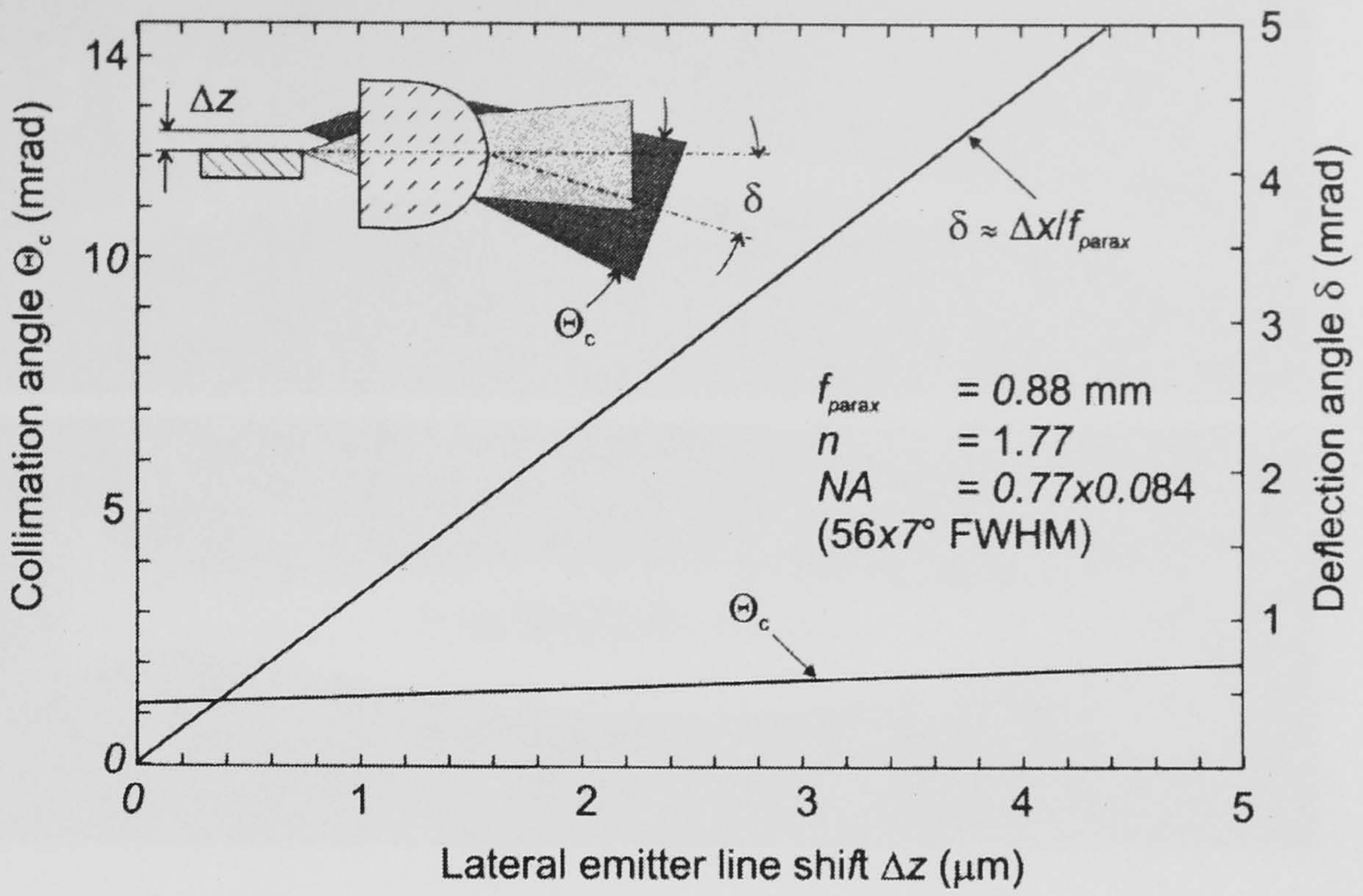

Figure 1.6: Dependence of the collimation angle and the beam pointing on the shift of the lens along the fast axis of diode laser bar. Reproduced from [7], copyright Springer Verlag.

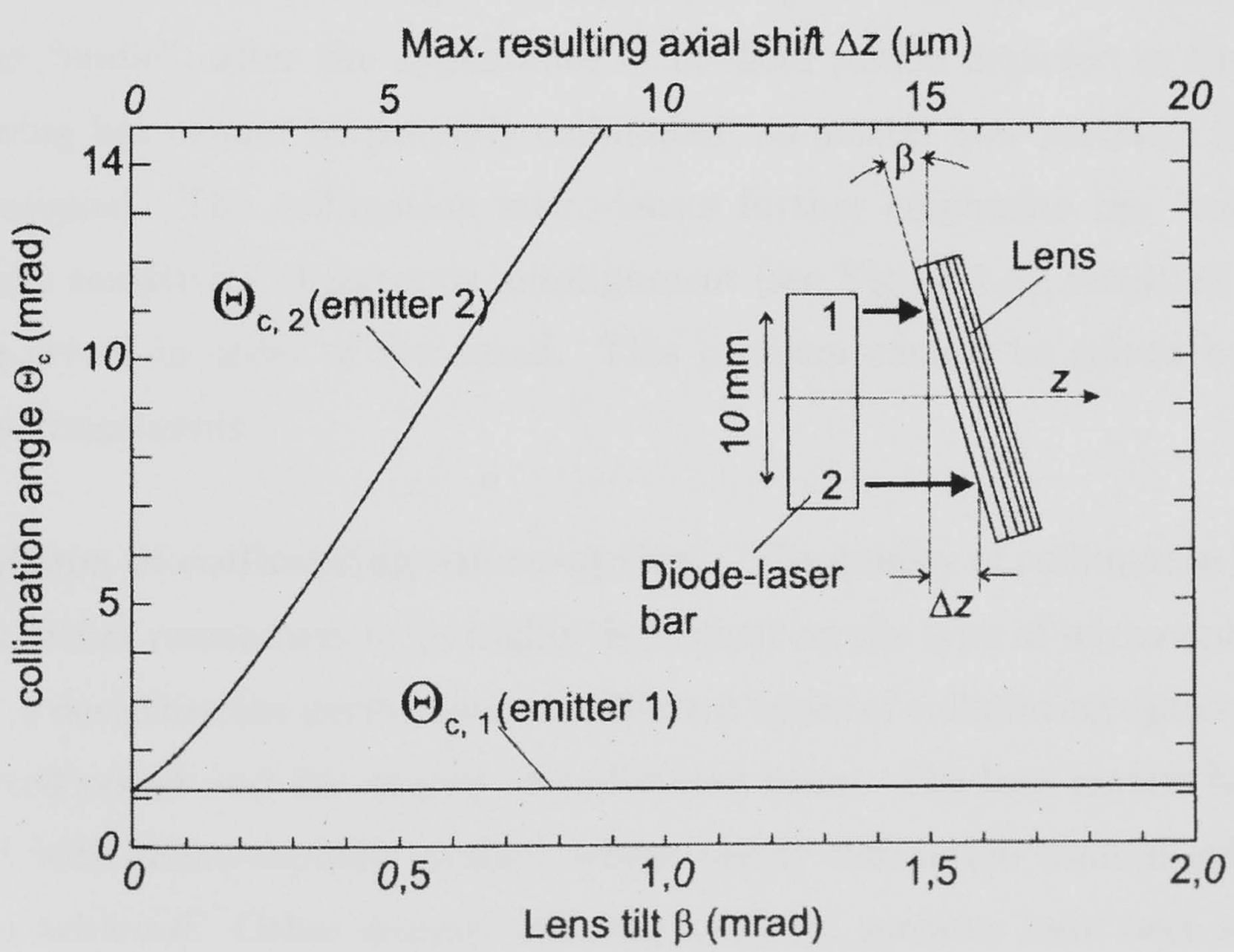

Figure 1.7: Increase of the collimation angle due to the misalignment angle β between the microlens and the emitting facet of the diode laser bar (NA_{fast}=0.77, NA_{slow}=0.084, paraxial focal length of the lens f = 0.88 mm). Reproduced from [7], copyright Springer Verlag.

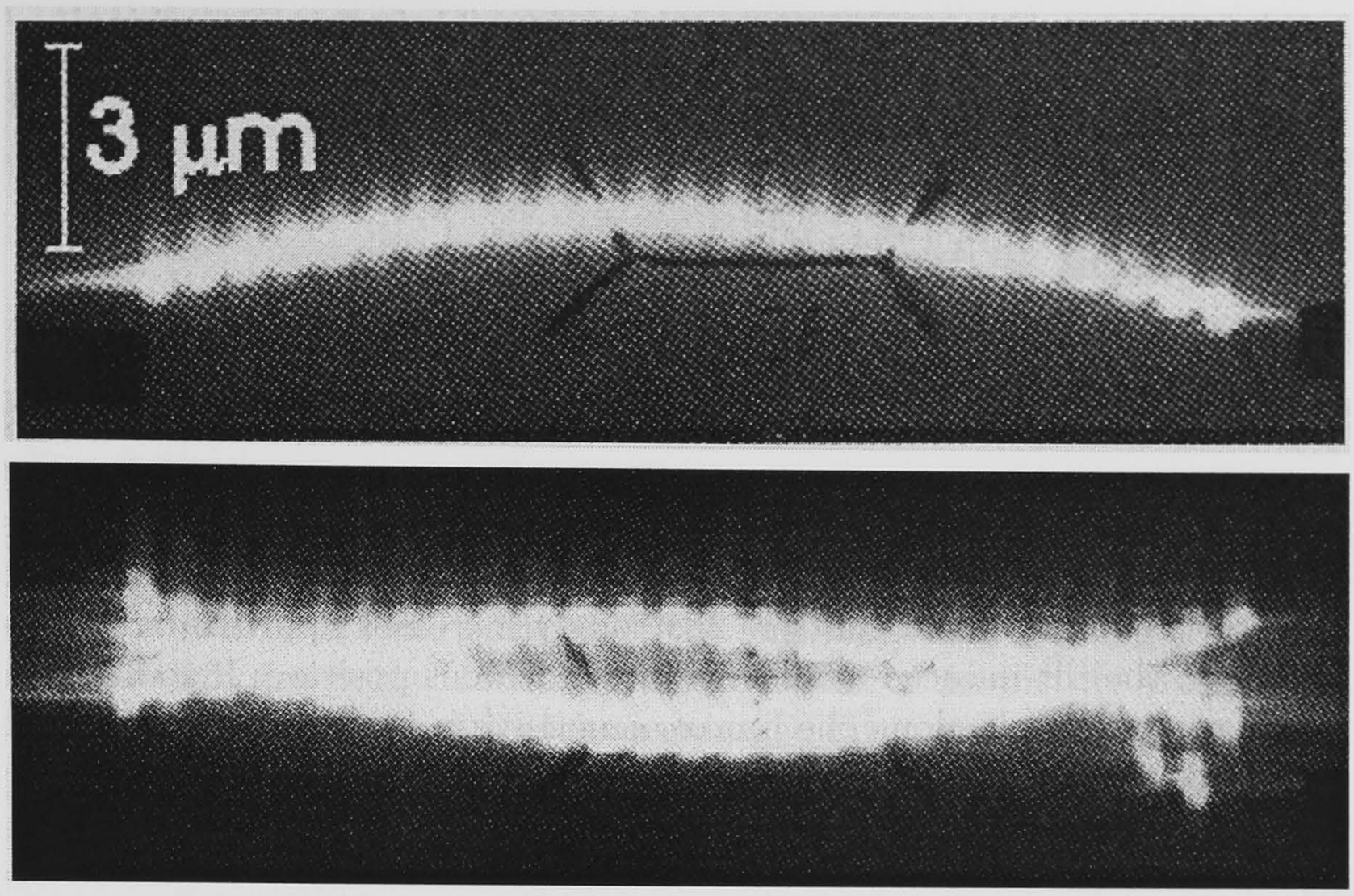

Figure 1.8: Enlarged near-field beam profile of the laser bar with a "smile" of approx. 2 μm a). The superposition of a number of such bars with randomly varying smiles leads to an enlarged beam profile b). Reproduced from [7], copyright Springer Verlag.

The bars often bow during the soldering stage. This effect is often referred to as the "smile", after the appearance of far-field profile depicted in Figure 1.8. The bowing bar cannot be properly collimated, no matter how precisely the lenses can be aligned. The collimation micro-lenses further emphasize the "smile" due to extreme sensitivity of fast-axis misalignment (see Figure 1.6), resulting in beam pointing errors in order of few mrad. This problem cannot be solved by typical optical arrangements.

Aberrations of collimating micro-optics. The quality of collimation has been shown by other researchers to be highly dependent on the type of micro-optics used. Figure 1.9 describes the performance of different types of collimating optics in terms of collected power and the quality of collimated beam. The best results have been recorded with plano-aspheric design, where nearly diffraction limited collimation has been achieved. Other designs utilizing spherical surfaces have been shown to greatly deteriorate beam quality and brightness.

However, the compromise has to be found between good beam quality and practical aspects of beam collimation. Holdsworth *et al.* [17] have assessed the performance of commercially available collimating microlenses (fibre, graded index,

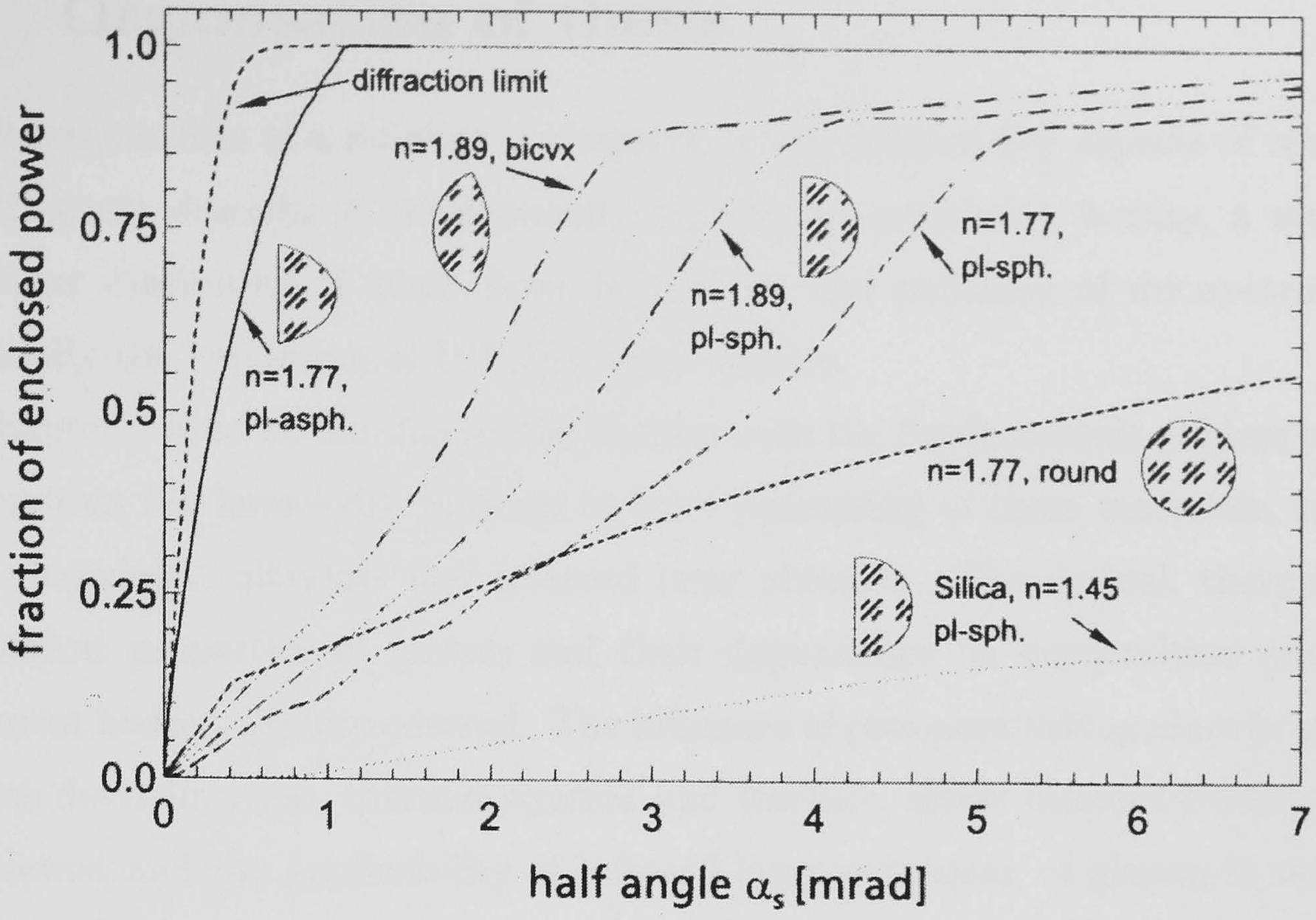

Figure 1.9: Comparison of the quality of diode laser beams after collimation by different types of cylindrical lenses (diode laser NA_{fast}= 0.77, NA_{slow}= 0.084). Reproduced from [7], copyright Springer Verlag.

hyperbolic and high index meniscus lenses) and the influence of positioning accuracy on the resultant beam quality. The results confirmed the high sensitivity of beam profile and quality to a lens type and misalignment errors. Cheap lenses (fiber, spherical) have been shown to be more tolerant to misalignment errors than aspheric design but at a price of intrinsically high aberrations, which limit the achievable brightness. More expensive aspheric lenses have been demonstrated to offer best collimation, but the extreme positioning sensitivity prohibited full exploitation of their potential due to assembly inaccuracies, mentioned earlier.

Summarizing, the type of lens used is critical for high quality beam collimation. The aspheric design seems to be the most suitable for that task, but the micron-size, random misalignment errors disable efficient collimation and further beam shaping. The novel technique, presented later in this chapter, corrects beam pointing errors and beam profile of collimated diode bars.

1.3 Organisation of thesis

The thesis consists of a number of chapters, which address key aspects of research. The chapters describe a development of precision machining facility, a study of CO_2 laser machining of silica, laser fabrication and polishing of micro-structures and finally the correction of HPLDA beam quality.

Chapter 2 aims to familiarize the Reader with the fundamentals of glass science and reviews the knowledge relevant to laser processing of these materials, such as deep ultraviolet, ultrafast and infrared laser ablation. The optical, thermal and mechanical properties of glasses and their dependence on composition and heat treatment history are also covered. The influence of processes taking place in glasses, such as devitrification, thermal stresses and fracture, stress induced birefringence, is reviewed and the applicability of infrared laser processing of glasses is assessed. The attention has been directed towards pure silica glass, which has been chosen as a substrate material due to its excellent resistance to thermal shock and related thermal fracture when irradiated with the CO_2 laser, as opposed to other silicate glasses used for fabrication of photonic devices.

Chapter 3 describes the development of key equipment required for successful research, the precision laser machining facility. The performance requirements and realisation of the novel machining station are described in detail. The issues of spectral and temporal power stability of RF excited slab waveguide CO_2 laser, used in the station, have been investigated and quantified. The technical solution to the problem of laser instability, in a form of high precision temperature stabiliser, has been developed. This chapter also describes the custom software created to achieve a goal of rapid and flexible prototyping scheme.

Chapter 4 presents the results of experimental study on CO_2 laser ablation of silica glass. The parameters, such as machining threshold and material removal rate, have been characterised as a function of irradiance, laser spot size and pulse repetition frequency. An influence of wavelength on these parameters has also been investigated. Optimal laser pulse properties, which assure low machining threshold, repeatable material removal and optimal ablation crater topography, have been found in a course of detailed experiments.

Chapter 5 reviews fabrication methods used by other researchers to manufacture micro-optical elements in a range of photonic materials and relates them to the work

presented here. The attractiveness of machining scheme presented in this thesis is pointed out. The experimental work contained here has used the findings from the previous chapter and investigated the fabrication regimes of arbitrary shapes in silica glass by means of overlapped, Gaussian-like ablation craters. Various types of overlapped crater regimes have been experimentally verified and their advantages and disadvantages pointed out. In the end of the chapter, the fidelity of surface fabrication has been quantified together with an assessment of as-machined surface quality.

Chapter 6 reviews the techniques used so far to provide bulk optics with the optical quality finish, such as conventional abrasive polishing, fire and laser polishing. These methods cannot be applied to polishing of micro-optical components. A novel approach presented here, a laser micro-polishing, allows for a well controlled removal of characteristic surface features, left after laser machining, without a modification of designed surface shape. A successful, experimental verification of that laser treatment, aiming at an improvement of surface quality of machined elements, is provided.

A novel way of unleashing the potential of HPLDAs by the means of brightness and beam quality improvement, based on wavefront analysis and fabrication of corrective plate, is presented in Chapter 7. An experimental evaluation of performance of corrective plates has been carried out and the fabricated optics have been shown to significantly improve the beam quality.

In the end of thesis, the concluding remarks are contained in Chapter 8. Future work needed to improve performance of the correction scheme (which is still in experimental stage of development) to a level of practical application, is outlined in this chapter.

Chapter 2

PHYSICS OF GLASS PROCESSING

2.1 Introduction

The beginning of active research on thermal, mechanical, chemical and optical properties of glasses dates three centuries ago [18]. Remarkable progress in these areas has been made in late 19-th and in 20-th century, enabled by the extended knowledge of chemical and physical sciences and new experimental techniques.

Vast amounts of information on glasses have been collected so far, but a scope of this chapter is limited to the aspects of glass science relevant to fabrication of micro-optical components by laser processing. This chapter aims at reviewing some of fundamental knowledge concerning structure, formation and properties of widely used inorganic glasses, such as soda-lime-silicates, boro-silicates, lead-silicates and alumino-silicates, with a focus on vitreous silica. The important, from optical application standpoint, physical properties of glasses, such as refractive index, absorption of light and photo-elasticity, are discussed here. The origin and dependence of these parameters on chemical composition, temperature, phase transitions and stresses are briefly reviewed in this chapter. Thermal and mechanical properties, relevant to CO_2 laser machining and polishing (covered in Chapters 4 and 6 respectively), such as characteristic transition temperatures, fictive temperature, thermal expansion and related stresses, thermal conductivity, elastic constants and viscosity, are reviewed. Finally, a review of current state-of-the-art laser processing of glasses is presented.

2.2 Formation and structure of glass

The term *glass* is used commonly to describe the products of fusion of inorganic materials, which have been cooled to form a rigid body without crystallizing. The most common notion of glass is an ordinary silicate glass, used for making window panes and glassware, such as bottles, jars, etc. Glasses are not, however, limited to inorganic compounds. Organic substances, such as glucose, can also form glasses.

The common feature of hundreds of diverse glass types, developed to date, is a lack of long range periodic order of constituent molecules, as electron and X-ray diffraction studies indicate [19]. Their atomic distribution also resembles the atomic arrangement of liquids and not that of crystals. The glassy state became widely considered as another state of aggregation, beside gaseous, liquid and crystalline forms of the same composition. The phenomenological description of a glassy state would be "... it is a state of matter which maintains the energy, volume and atomic arrangement of liquid, but for which the changes in energy and volume with temperature and pressure are similar to those of crystalline solid ..." (after [19], p. 4).

The glassy state is generally obtained by *undercooling* a liquid below it's freezing temperature T_f, but it can also be obtained by compressing the liquid. During solidification, the liquid releases stored thermal energy in a form of latent heat of fusion, which must be extracted from the liquid to maintain the condition of undercooling. For a liquid to form a glass the rate of heat removal must be high enough to prevent the crystallisation (see Section 2.4.1).

2.2.1 The glass - distinctive state of aggregation

Figure 2.1 illustrates the difference between liquid, glassy and crystalline states of matter. Upon cooling, the liquid from initial state A, the specific volume will decrease steadily along AB. If the cooling rate is low, the crystal growth may commence, provided the crystallisation nuclei are present (see Section 2.4.1). The volume will undergo a sharp decrease along BC at a fusion temperature T_f of growing crystals. Once all liquid has crystallized, the solid will contract steadily with decreasing temperature along CD.

If the rate of cooling is rapid enough, there will be no time for crystallisation to start, since the rate of nucleation and crystal growth are finite. Theoretically, it is

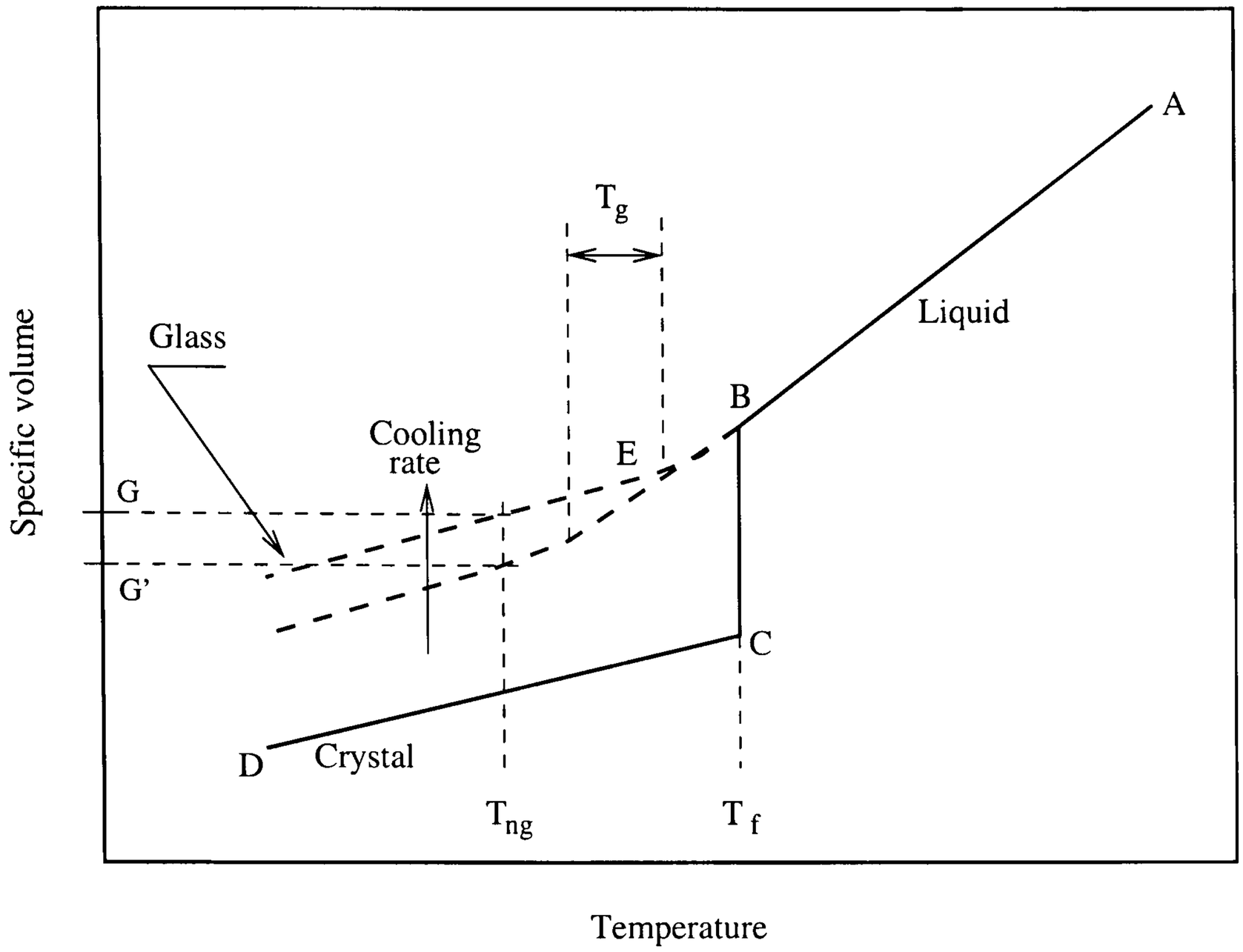

Figure 2.1: Relationship between the glassy, liquid and solid states.

then possible to obtain glass with any material if only the proper cooling rates can be induced. It has been experimentally confirmed by snap-melting of fine powders of various oxides, which do not produce glasses normally such as La_2O_3, using xenon flash and laser pulse heating techniques [20].

The volume of undercooled liquid will decrease along BE without discontinuity at the temperature T_f. After reaching E, the transition from liquid to glass takes place at *glass transition temperature* T_g. Dependingly on the cooling rate, the temperature T_g may vary, it is more appropriate to speak of a range of glass transition temperatures. Very high viscosity, approximately 10^{12} Pa·s, is a characteristic feature of glass held at temperature T_g. The viscosity of glasses and it's temperature dependence is covered in greater detail in Section 2.3.3. Below T_g, the glass will contract with decreasing temperature along EG, with a coefficient similar to that of a crystalline state CD.

Volume G will continue to decrease slowly if the glass is held at constant temperature T_{ng} just a bit below T_g. After some time, from minutes to hours, the volume level G′ will be reached, which lies on the line being a smooth continuation of BE. This process is referred to as a stabilisation, since the glass structure undergoes a

rearrangement to settle in a more stable condition at a given temperature. Many glass parameters, including refractive index, change with time in vicinity of T_g as a direct consequence of structural change on molecular level. An entity called a *fictive temperature*, covered later in Section 2.3.2, has been introduced to describe the state of the molecular arrangement corresponding to that temperature but frozen upon cooling. This feature of glasses must be taken into consideration by glass-forming technologies, including laser fabrication of micro-optics, since it determines the optical homogeneity and accuracy of the final product.

2.2.2 Composition of common glasses

Some substances form glasses more readily than others in typical experimental and manufacturing conditions and they are called *glass-formers*. Oxides, such as SiO_2, B_2O_3, GeO_2 and P_2O_5, easily form glasses on their own and provide a skeleton for other mixed-oxide glasses, properties of which can be engineered to some extent. Table 2.1 shows the constituents of commercial glasses and their impact on the properties of a target material.

Table 2.2 shows the composition of typical glasses used for fabrication of every-day life glassware and for other applications. Pure silica is renowned for the highest melting point, smallest thermal expansion and high chemical resistance and that is a reason the silica is used particularly for high temperature applications, such as furnace windows, halogen bulbs, etc. On the other hand, processing of silica is expensive and poses technical difficulties due to high temperatures required (>1800 °C) for a level of working viscosity (see Section 2.3.3). For many applications such excellent thermal resistance is not required, window panes for example.

An addition of Na_2O and CaO to pure silica produces a soda-lime glass, most commonly used for window panes and bottle-ware. This type of glass melts at considerably lower temperature, which makes it better suited for that kind of application.

Borosilicate glasses, consisting mainly of SiO_2 and B_2O_3, exhibit high chemical durability and thermal expansion just slightly higher that of silica (see Table 2.3, p. 27). These features make borosilicate glasses most suitable for the labware and domestic ovenware, Pyrex^{TM} for example.

Oxide	Function	Properties
SiO_2	Basic glass-former (network former)	Crystalline silica has very high melting point and liquid silica very high viscosity. High concentration of silica in a glass confers high softening temperature, low thermal expansion, good chemical durability.
B_2O_3	Network former	Will join network structure of silica glasses reducing viscosity without producing adverse changes in thermal expansion and durability. Is a component of all heat-resisting and 'chemical' glasses.
PbO	Not a network former but can link SiO_2 tetrahedra	Widely used for high dielectric constant, refractive index, and resistivity. Expensive. Needs oxidising furnace atmosphere.
Na_2O	Network modifier	Markedly lowers softening point. **Raises thermal expansion** and ionic conductivity. **Reduces durability**.
K_2O	Network modifier	Similar to Na_2O, but larger K^+ ion less mobile.
LiO_2	Network modifier	Similar to Na_2O, but smaller Li^+ ion more mobile. **Promotes devitrification**.
CaO	Network modifier	Inhibits mobility of alkali ions, hence increases resistivity and durability of alkali glasses. Shortens the working range.
MgO	Network modifier	as CaO
ZnO	Network modifier	as CaO
BaO	Network modifier	Cheaper substitute for PbO
Al_2O_3	Intermediate	Can join network in AlO_4 tetrahedra which are a different size from SiO_4. Strongly suppresses devitrification; increases viscosity and therefore makes melting and refining more difficult.

Table 2.1: Common constituents of glasses and their influence on properties, after [21]. The undesired properties, from laser processing viewpoint, are underlined.

Glass	Composition (weight per cent) SiO_2	Na_2O	K_2O	CaO	MgO	B_2O_3	Al_2O_3	Fe_2O_3	PbO
Soda-lime-silica (plate glass)	72.5	13.0	0.3	9.3	3.0		1.5	0.1	
Soda-lime-silica (bottles, jars)	73.0	15.0		10.0			1.0	0.05	
Soda-lime-silica (lamp bulbs)	73.0	16.0	0.6	5.2	3.6		1.0		
Borosilicate (Pyrex™)	80.6	4.2		0.1	0.05	12.6	2.2	0.05	
Lead-silicate (tableware)	55.5		11.0						33.0
Lead-silicate (seal to lead-in wires, lamp bulbs and valve bases)	63.0	7.6	6.0	0.3	0.2	0.2	0.6		21.0
Lead-silicate (radiation shields)	30.0		3.0						65.0
Aluminosilicate (electrical, high durability glass fibers)	54.6	0.6	0.6	17.4	4.5	8.0	14.8		

Table 2.2: Typical compositions of commercial glasses, after [21].

2.2.3 Methods of fabrication of silica glass

This section reviews the fabrication methods of silica glass, which result in a number of glass types with different physical properties. The impact of production method on optical properties of resultant material is highlighted here.

Earth's crust is abundant in natural crystalline form of SiO_2, quartz. However, very high melting temperature of quartz (1710 °C) and high viscosity of resultant melt ($\sim 10^6$ Pa·s) make it impossible to produce silica glass by conventional glass making techniques. Secondly, the impurities can be brought into the glass structure from the raw quartz sand, modifying optical properties.

High purity silica has been produced for the first time after the invention of oxy-hydrogen flame (1821) and was available commercially only since 1900 [21]. The quartz has been considered infusible before that significant technological break-through. To date, there are several methods known to produce fairly pure and very pure silica glasses, such as electric, flame and arc-fusion and chemical deposition of volatile silicon compounds. This section aims to outline the differences in optical performance between various types silica glasses, obtained with different methods.

Fusion of quartz. Electrical fusion technique utilized a carbon rod to heat up the surrounding quartz sand by passing huge currents through it. The glass obtained this way, called *fused quartz*, suffered from large bubble content and only partial amorphisation, since the quartz did not fully melt. The content of impurities was also significant, but that could be reduced by selection of pure sands. Different variations of the method involved flame and arc fusion, which produced bubble free glasses but introduced impurities as well. Electrical fusion was advantageous to flame fusion with respect to a concentration of impurity HO^- groups, which give rise to strong absorption in 2-3 μm wavelength region of near-infrared spectrum (see Figure 2.6 p. 38). The content of hydroxyl groups can be greatly reduced by electrical fusion, allowing for production of IR-grade fused silica.

Chemical vapour deposition. A modern method, called chemical vapour deposition (CVD), capable of synthesis of exceptionally pure SiO_2, involves oxidisation of volatile silicon compounds, such as tetra-chloro-silane, $SiCl_4$, and other silanes and metalorganic compounds (MOCVD). These highly poisonous gases can be obtained and purified chemically to achieve outstandingly low level of impurities. The

silanes can be oxidized in high temperatures to produce SiO_2 in a form of fine powder, which could subsequently be flame or electrically fused. Unfortunately, large volume production of fused silica by CVD is not economically beneficial.

CVD has been extensively used for fabrication of optical fibre preforms, which require materials of highest purity to assure low transmission losses and also to provide a possibility of doping for refractive index manipulation. A fabrication stage of fibre preform consists of a deposition of SiO_2 soot produced from oxygen and silane flowing inside a lower-grade, silica tube. The production of soot is possible thanks to high temperatures created by a traveling flame, which heats up the tube. The mixture of gases flowing through the tube could be enriched with $GeCl_4$ for doping and control over the distribution of the refractive index in the core of the preform.

Purification of borosilicates. Fused silica, independently of the fabrication method, is very difficult to work with due to high viscosity and high temperatures required. An original method of overcoming this obstacle was devised and patented by Corning Glass Works (US). The trick was to work on the borosilicate glass, containing high proportion of boric oxide B_2O_3 and a few percent of alkali oxides, which has much lower softening point than pure silica. After shaping, newly formed articles are kept for a number of hours in temperatures 500-600 °C to allow for phase separation into nearly pure silica phase and the patches of remaining constituents. After this treatment, the B_2O_3 and alkali oxides can be washed away by acid, leaving the porous glass consisting in 96 percent of silica. Another heat treatment at ~1200 °C closes the pores and causes ~30% shrinkage of the final article. This method is cheaper than CVD and most of silica products are made this way nowadays.

All forms of silica glass discussed so far are generally referred to as *vitreous silica*. Names, such as *fused quartz*, *fused silica*, *synthetic silica* and *96% silica* refer to a product of particular fabrication method. The experiments, described in Chapters 4–7, have been carried out on synthetic silica glass samples, manufactured by Heraeus GmbH in Germany.

2.3 Selected physical properties of common optical glasses

A number of important physical properties, from laser-processing point of view, is revised here. This section summarizes thermal, mechanical and optical properties of glasses relevant to laser ablation and laser polishing, covered further in the thesis.

2.3.1 Thermal properties

Thermal properties of solids can be generally divided into two categories of structure sensitive and structure insensitive ones. Structural sensitivity means that the parameter is significantly affected by occasional irregularities in the arrangement of atoms - structural defects. Structure insensitive parameters, such as specific heat capacity, melting point and latent heat of evaporation, are related to macroscopically observable results of local, short-range atomic interactions. For glasses, these parameters are quite similar in values to those of crystalline form of the same composition. The properties like thermal conductivity and thermal expansion depend on the molecular arrangement thus they are structure sensitive. In glasses, atomic arrangement depends also on the temperature and thermal history (fictive temperature, see Section 2.3.2) and so do the structurally sensitive entities.

Thermal expansion is generally an outcome of nonlinear character of atomic oscillation, due to an asymmetry of attractive-repulsive forces bonding atoms together in the structural network. An increased temperature causes an increase in an equilibrium separation between atoms oscillating with increased amplitude - macroscopically speaking the material has expanded. However, an anomalous thermal behaviour of silica has been recorded, it's expansion coefficient becomes negative below ~ -80 °C, as shown in Figure 2.2.

The strength of atomic bonding has a big impact on a value of thermal expansion as well as on a value of melting point temperature T_f. In general, the stronger the interactions on the atomic level the smaller the coefficient of thermal expansion and higher elasticity modulus E and T_f. Table 2.3 compares the thermal expansion and softening/melting temperatures of glasses and crystalline solids correspondingly.

From technological point of view the thermal expansion of glasses is of highest importance from all thermal properties, since it determines a capability of fusion with other materials in engineering applications. The glasses, available in a broad

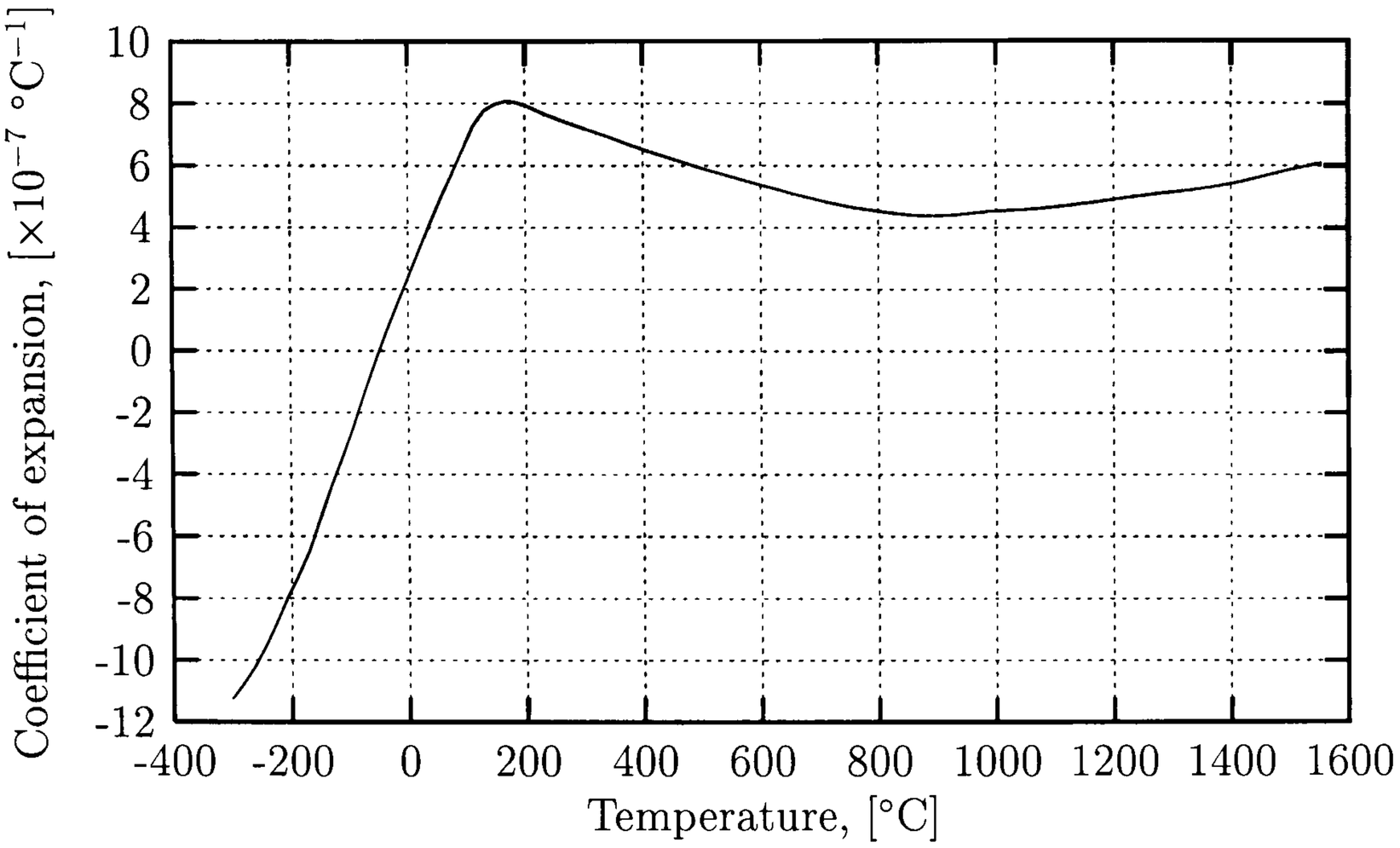

Figure 2.2: Representative thermal expansion of fused silica vs temperature, based on data published by GE Quartz Inc.

Glasses	Softening point [°C]	Lin. exp. $\times 10^{-7}$ [K^{-1}]	
Silica	1667	5.5	
96% silica	1500	8	
Aluminosilicate	940	33	
Borosilicate (Pyrex)	820	32	
Soda-lime-silica	700	92	
Lead silicate	580	91	
High lead	380	100	
Crystallines	**Melting point [°C]**	**Lin. exp. $\times 10^{-7}$ [K^{-1}]**	
Diamond	>3500	12	
Magnesium oxide	2900	100	
Al_2O_3	2050	87	
Quartz	1710	80	$\parallel$ axis
		134	$\perp$ axis

Table 2.3: Thermal expansivity and melting points of glasses and crystalline solids - a comparison.

range of thermal expansivities, allow for matching with various metals for realisation of lead-in wires in bulbs and vacuum valves and other seals.

Thermal conductivity is a structure sensitive property and, as may be expected, glasses conduct heat poorly in comparison to metals and crystalline states of aggregation of the same composition. Thermal conduction coefficient k describes the magnitude of 1-D heat flux Q, passing through the sample of unit thickness, to generate unit temperature gradient across that sample:

$$Q = k \frac{dT}{dx} \tag{2.1}$$

In glasses, which are partly transparent in infrared, the conduction of heat is realised by thermal lattice vibrations (phonons) and by emission and reabsorption of thermal radiation. The irregular atomic structure of glasses promotes scattering of phonons, thus glasses usually conduct heat worse than crystals of the same composition.

Specific heat, as well as thermal expansion and specific volume, is a structure insensitive, additive property of glasses consisting of more than one ingredient. These properties do, however, depend on temperature. In general, the additive property A can be expressed as [21]:

$$A = C + \sum B_i W_i \tag{2.2}$$

where C is a refinement constant, B_i is the property value for an ingredient i and W_i is it's weight fraction in the glass. Table 2.4 displays the values of mentioned additive properties of oxides used for production of most types of glasses.

An entity frequently appearing in heat flow formulas is the diffusivity K, describing the rate of thermal front propagation in a material. K is defined as:

$$K = \frac{k\ V_{sp}}{C_{sp}} \tag{2.3}$$

where C_{sp} is the specific heat and V_{sp} is the specific volume. Figure 2.3 shows the value of K for fused silica as a function of temperature.

2.3.2 Fictive temperature

The term has been proposed in 1946 by Tool [22], who suggested that after cooling through the transition range the glass has got a frozen-in structure corresponding to some equilibrium temperature. In a glass transformation region, the material undergoes structural changes to reach an equilibrium arrangement that corresponds

Component	Linear exp. coeff. [$\times 10^{-6}$ K^{-1}]	Specific heat [$\times 10^{2}$ J kg^{-1} K^{-1}]	Specific volume [$\times 10^{-4}$ m^{3} kg^{-1}]
SiO_2	2.7	8.02	4.35
B_2O_3	0.3	5.33	5.26
Na_2O	33.3	11.2	3.85
K_2O	28.3	7.81	3.57
MgO	0.3	10.2	2.63
CaO	16.7	7.98	3.03
BaO	10.0	2.81	1.43
PbO	10.0	2.14	1.04
Al_2O_3	16.7	8.69	2.44

Table 2.4: Additive factors for the properties of compound glasses, after [21].

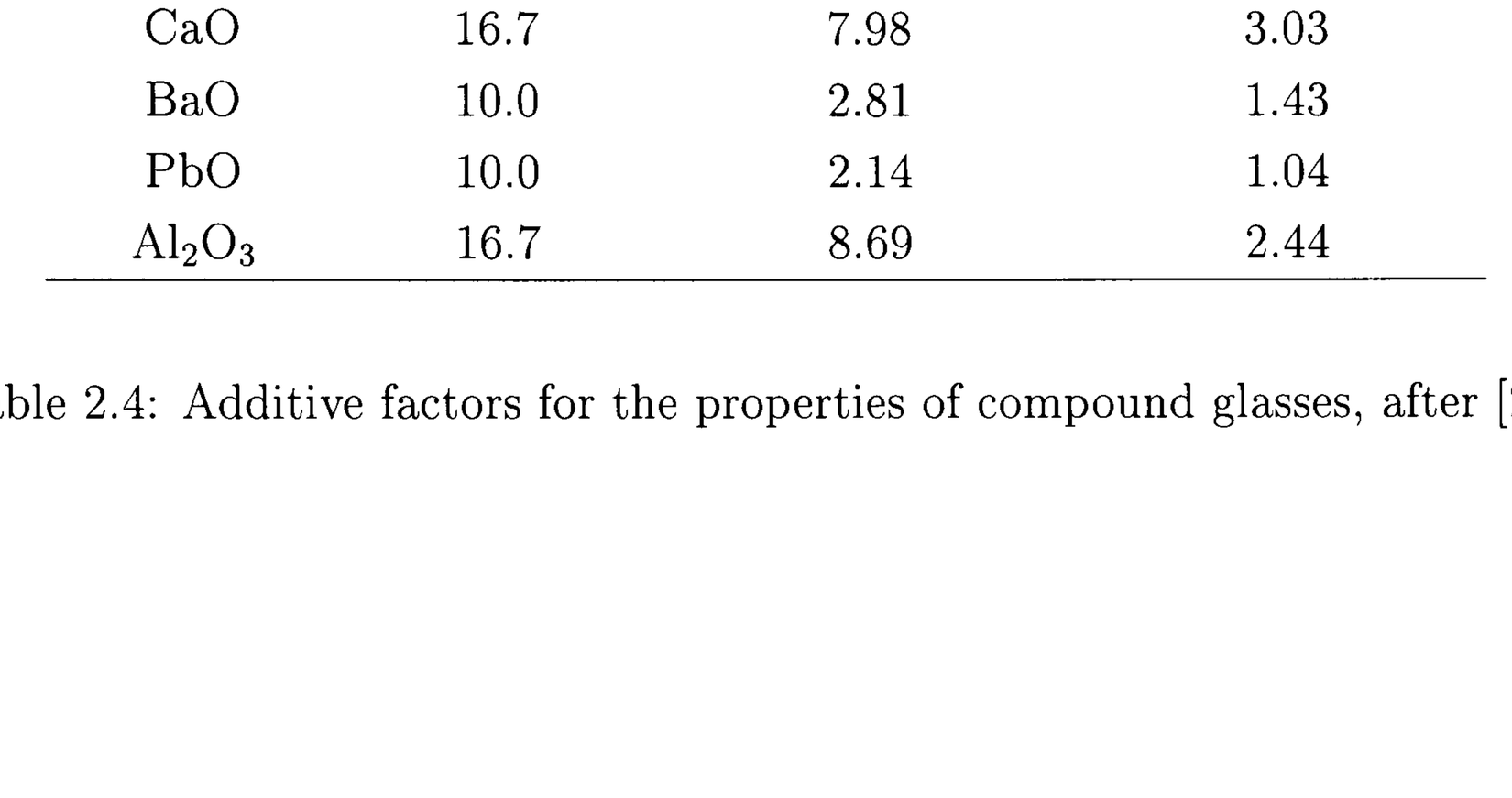

Figure 2.3: Representative thermal diffusivity of silica as a function of temperature, based on data published by GE Quartz Inc.

to a particular temperature the glass is held at. The material properties, such as specific volume, viscosity or refractive index, which are covered in greater detail in Sections 2.3.3 and 2.3.4, also change. It has been observed that the rate of change of these parameters can be much lower than the rate of temperature drop in the transformation region. As an effect, the atomic configuration, for example corresponding to equilibrium temperature in the upper region of glass transformation range, can be maintained by the glass provided the cooling rate is sufficiently high, by water quenching for instance. Such glass is called to have a high *fictive temperature*. The value of fictive temperature may vary from evaporation to strain point temperature for a particular glass. In case of fused silica, fictive temperature may take any value from ~1000 to ~1700 °C, dependingly on the rate of cooling in the transformation region. As a result of that behaviour, the parameters of the glass do not only depend on the temperature but also on a history of heat treatment.

In case of laser ablation of silica there is a high probability of increasing the fictive temperature of a thin molten layer and therefore increasing its refractive index (see Section 2.3.4) by $\Delta n_{max} \simeq 10^{-4}$. However, some annealing effect may be anticipated in a timescale of a total lifetime of the melt zone during laser micropolishing, described in Chapter 6, and the possible change of refractive index may be an order of magnitude smaller than the Δn_{max}.

2.3.3 Viscosity

As opposed to crystalline states, glasses do not undergo abrupt phase transitions and related sharp change of physical parameters. The phase transition between solid and liquid is smoothly spread over a range of temperature, which is related to a range of certain values of viscosity. The viscosity is extremely strongly temperature dependent and varies from non-measurable levels $\gg 10^{14}$ Pa·s at room temperature to $10^{6.6}$ Pa·s at *softening point* temperature in less than 10^3 °C for compound glasses and $2 \cdot 10^3$ °C for pure silica. The softening point is regarded as an onset of plasticity, since the material can substantially deform under its own weight. The viscosity can change at least seven orders of magnitude, as seen in Figure 2.4, which shows the viscosity of common glasses as a function of temperature.

Four characteristic viscosity values are used to formally quantify the smooth transition and technologically important temperatures, the *strain*, *annealing* and *softening* points. Table 2.5 shows these values for commercial glasses. The char-

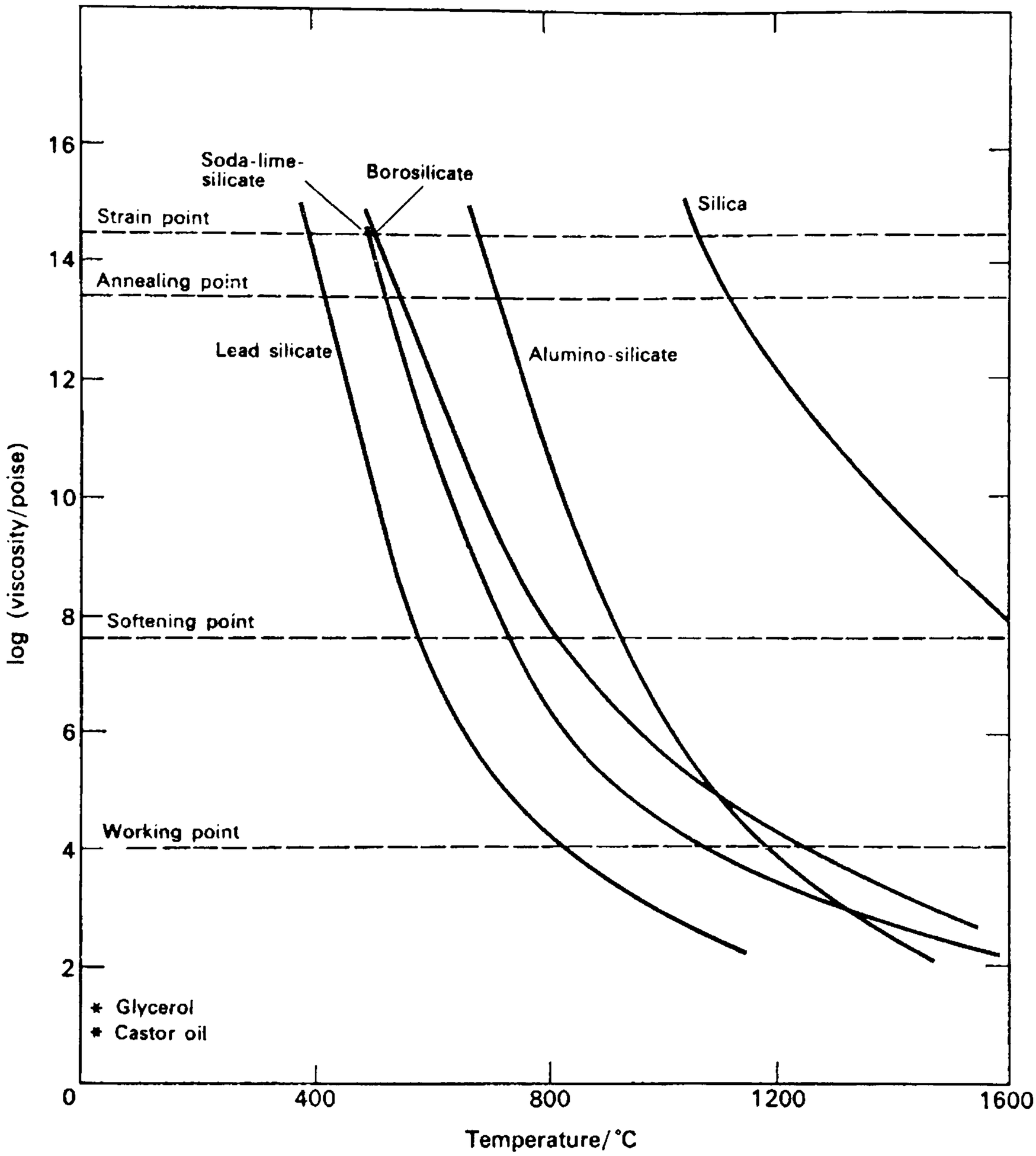

Figure 2.4: Viscosity of common glasses as a function of temperature, reproduced from [21], copyright Wykeham Publications.

Ref. point	Viscosity [Pa·s]	Temperatures [°C]						
		Silica	96% silica	Alumino-silicate	Pyrex	Soda-lime-silica	High lead glass	Lead glass
Strain	$10^{13.5}$	1070	820	670	520	470	300	390
Annealing	$10^{13.4}$	1140	910	720	565	510	320	430
Softening	$10^{6.6}$	1667	1500	940	820	700	380	620
Working	10^{3}	–	–	1220	1220	1000	500	970

Table 2.5: Characteristic reference temperatures for commercial glasses, from [21].

acteristic temperature not mentioned so far is a *working point*, viscosity 10^3 Pa·s, allowing for easy shaping of glasses to form the final products. Fused silica is exceptionally difficult to shape because the viscosity cannot be reduced to less than 10^4 Pa·s due to a significant volatilisation above 2800 °C at an atmospheric pressure (see the vapour pressure data in Figure 2.16 on page 60).

Viscosity describes the magnitude of shearing force needed to cause a laminar flow of liquid with a certain rate. Two parallel plates of area A each, spaced by a fluid of thickness d, travel with speed v relative to each other after a shearing force F is applied to the plates. The viscosity η is defined as a ratio of shearing force F to the rate v of displacement:

$$\eta = \frac{F\ d}{A\ v} \tag{2.4}$$

In spite of the fact that "Pa·s" is the SI unit of viscosity, an old CGS unit "poise" (10 poise = 1 Pa·s) still appears in literature.

The liquids, viscosity of which does not depend on force F, are called Newtonian fluids. Glasses, however, especially in a region of high viscosity, undergo elastic deformation as well as flowing. At viscosity $\sim 10^9$ Pa·s a glass rod can be fractured in a brittle way if the appropriate uniaxial load is applied to it sufficiently quickly. Application of a smaller load leads to instantaneous elastic elongation and a creep due to a viscous flow. If the elongating load is kept sufficiently long, the rod may be eventually drawn into a fibre.

This elongation technique is used for the measurement of viscosity above 10^8 Pa·s, since a concentric cylinder method is no longer applicable in that range. The

shear viscosity η can be derived by a measurement of a creep rate $\frac{dl}{dt}$:

$$\eta = \frac{F\ l}{\pi r^2\ 3\ \frac{dl}{dt}} \tag{2.5}$$

where l and r are the rod length and radius and F is the applied force.

The viscosity of glasses has been found to be also dependent on time, especially in the higher viscosity region of transformation temperature range, which is attributed to a fictive temperature described in Section 2.3.2. Some relaxation time, from minutes to many hours, is required for the viscosity to stabilise after warming up the glass or cooling it down a few degrees, suggesting the occurrence of structural changes, which may not keep up with a rate of temperature change. In general, the lower is the temperature the longer the relaxation time becomes, which can be practically infinite below a strain point temperature. It is not, however, very important from the laser ablation or laser polishing point of view, since the change of the viscosity due to rapid variation of temperature alone is many orders of magnitude bigger than the effect described.

2.3.4 Refraction

The refraction of light in media, in brief, originates from the light and matter interactions, which lead to a reduction of propagation speed of light in the medium. The refractive index or refractive power, a ratio of propagation speeds in material and vacuum, is the most important parameter in a design of optical components. A lot of attention has been thus directed by numerous researchers in the last two centuries towards understanding the dependence of that property on composition and structure of glasses. It is now known that a close relationship exists between refractive index and chemical composition of these materials [19]. It has been found that refractive index is an additive property, similarly to thermal expansivity, specific volume and specific heat capacity, and is equal to a sum of *molar refraction* $\mathrm{R_m}$ of constituent oxides:

$$\mathrm{R_m} = M \cdot \frac{n^2 - 1}{n^2 - 2}\ V_{sp} \tag{2.6}$$

where V_{sp} is a specific volume, n is the refractive index and M is a molar mass. Molar refraction is proportional to the atomic numbers of constituents, thus it is proportional to the number of electrons in the atom. A temperature change does not alter a value of molar refraction as long as there is no chemical transformation.

Material	R $[\times 10^{-6}$ MPa$^{-1}]$
Soda-lime glass	2.5
Silica glass	3.4
Perspex	5
Epoxy resin	7
Bakelite	53
Gelatin	2000-14000

Table 2.6: Stress-optical coefficients for some materials, after [21].

In reality, a deviation from additive character of molar refraction takes place, which indicates chemical interaction between the ingredients of glass.

This additiveness enables refractive index engineering by a choice of proportion of raw constituents and has been extensively used in the optical industry over a number of centuries. Glass manufacturers are able to produce glasses with refractive index accuracy of 10^{-4}–10^{-3}.

Stress induced birefringence. Vitreous or glassy state, unlike crystalline, is an amorphous state of aggregation with a constant atomic density in every direction. The ensuing optical isotropy is of paramount importance in optical applications. However, glasses and many other normally isotropic materials, can exhibit crystal-like behaviour under an influence of externally applied or internal stresses (see Section 2.4.3 on thermal stresses). In crystals, birefringence is a result of optical anisotropy associated with that state of aggregation. In glasses, the anisotropy and birefringence can be generated by stresses. Such phenomenon is called a *photo-elastic effect*. It has been found that the following relationship exists between the refractive indices n_z and n_y for the directions as illustrated in Figure 2.5:

$$n_z - n_y = R\,\sigma_y\,n \tag{2.7}$$

where n is the refractive index of relaxed medium, R is a stress-optical coefficient and σ_y is an external stress applied to the medium. Table 2.6 shows the values of R for some materials. In case of silica, which has a higher stress-optical sensitivity than soda lime glasses, optical anneal stresses (see Section 2.4.4) amount to $\sim 10^{-6}$-10^{-4} in differential term $n_z - n_y$. It is only one or two orders of magnitude lower than the accuracy of precision optics. Badly annealed optics will not suffer from

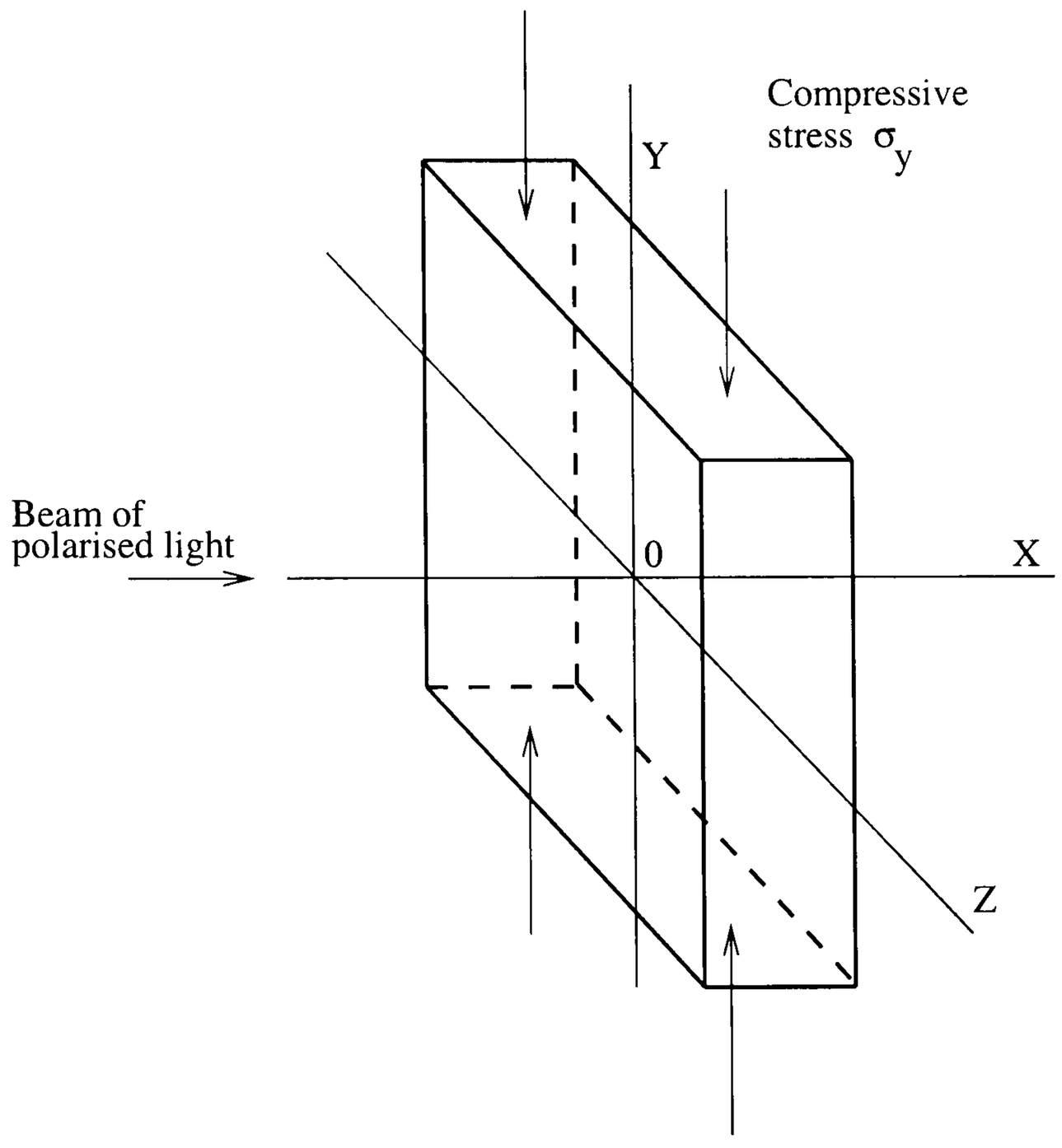

Figure 2.5: Geometry of photo-elastic effect, after [21].

cracking and serious deformation at ~30 MPa (~80 MPa is a practical strength of glasses), but the optical performance will be impaired.

Fictive temperature versus refractive index. The work carried out by Haken *et al.* [23] has supplied quantitative answers regarding the impact of fictive temperature on the refractive index. Commercially available samples of synthetic and natural fused silica have been studied. The refractive index of fused silica shows an anomalous dependence on the value of fictive temperature T_{fv}, it almost linearly increases with increasing T_{fv} with a rate $\sim 8.4 \cdot 10^{-7}$ °C^{-1} in a temperature range ~1000−1600 °C. The relaxation times, over which stabilisation of refractive index occurs, have been found to vary from 2−20 minutes at 1100 °C dependingly on the type of glass. The influence of fictive temperature is very strong in comparison to the impact of typical optical anneal stresses. It affects third decimal place of refractive index value. It is even clearer now how carefully the annealing must be carried out to not only relieve the internal stresses but also make sure that maximum fictive temperature difference in a bulk of optical element does not exceed ~100 °C (see section 2.4.4 p.52). The situation is more relaxed when dealing with laser ablation of glasses, since only a very thin layer of material is affected.

2.3.5 Absorption and scattering of light

As light propagates through the real medium, it's intensity decays along the optical path. There are basically two mechanisms giving rise to the intensity decay, true absorption and scattering of light. For both processes, the intensity of radiation along the optical path follows the exponential Lambert-Beer law:

$$\begin{aligned} \mathrm{I}(x) &= \mathrm{I}_o \exp(-\alpha\, x) \\ \alpha &= \alpha_{abs} + \alpha_{scatter} \end{aligned} \tag{2.8}$$

where α_{abs} and $\alpha_{scatter}$ are true absorption and scattering coefficients respectively. In visible and infrared region the scattering of light in glasses is many times weaker that true absorption, thus is often neglected for practical reasons.

A dimensionless entity k called *extinction* coefficient is very often used in optics to describe the strength of material absorption. It links complex refractive index $n' = n + ik$ with absorption coefficient α for a particular wavelength λ:

$$\alpha = \frac{4\pi k}{\lambda} \tag{2.9}$$

Another frequently used absorption related parameter is the *absorption length* $\beta = 1/\alpha$, the length over which the intensity drops by a factor $1/e$.

Scattering. Scattering of light occurs on sub-wavelength sized local variations of density, such as atoms and clusters of atoms. This kind of scattering has been studied by Lord Rayleigh, who has shown that the intensity of scattered light is proportional to a square of scattering particle volume and to λ^{-4} of the incident light. This effect accounts for the visibility and the colour of a sky. As the inhomogeneity size increases to $\sim \lambda$ and above, absorption, reflection and diffraction effects become significant in a process of scattering, leading to complex spectra observed in many natural minerals, fauna and flora.

The scattering can be expected to be stronger in glasses that in crystals of the same composition, since they lack the regular atomic arrangement and local variations of density are more frequent. The number and size of scattering sites determine the appearance of glass, transparent when small and translucent when large enough. The number of such scattering sites can be easily increased in glasses by a heat treatment that favours nucleation and crystal growth, leading to the devitrification of glass. Similar effect can be achieved in compound glasses kept long enough at the liquidus temperature, where the separation of liquid phase may lead to an increase of scattering efficiency. In general, the contribution of scattering to a loss of irradiance is negligible in comparison to absorption in UV and infrared bands of interest.

Absorption bands in inorganic glasses. Most oxide glasses are transparent in visible region and absorb strongly in ultraviolet and infrared parts of the optical spectrum (Figure 2.6). These strong absorption bands in UV and IR allow for efficient coupling of light into material and open the possibility of material processing with lasers operating at these wavelengths. Figure 2.7 shows a more detailed picture of absorption (extinction coefficient k) and real refractive index n' of fused silica as a function of wavelength.

VUV absorption. Strong interactions in ultraviolet are the consequence of electronic excitation of constituent ions. The energy of absorbed ultraviolet photons may modify the chemical relationship between the neighbouring ions (bond breaking) or trigger the electronic transitions that account for photofluorescence and

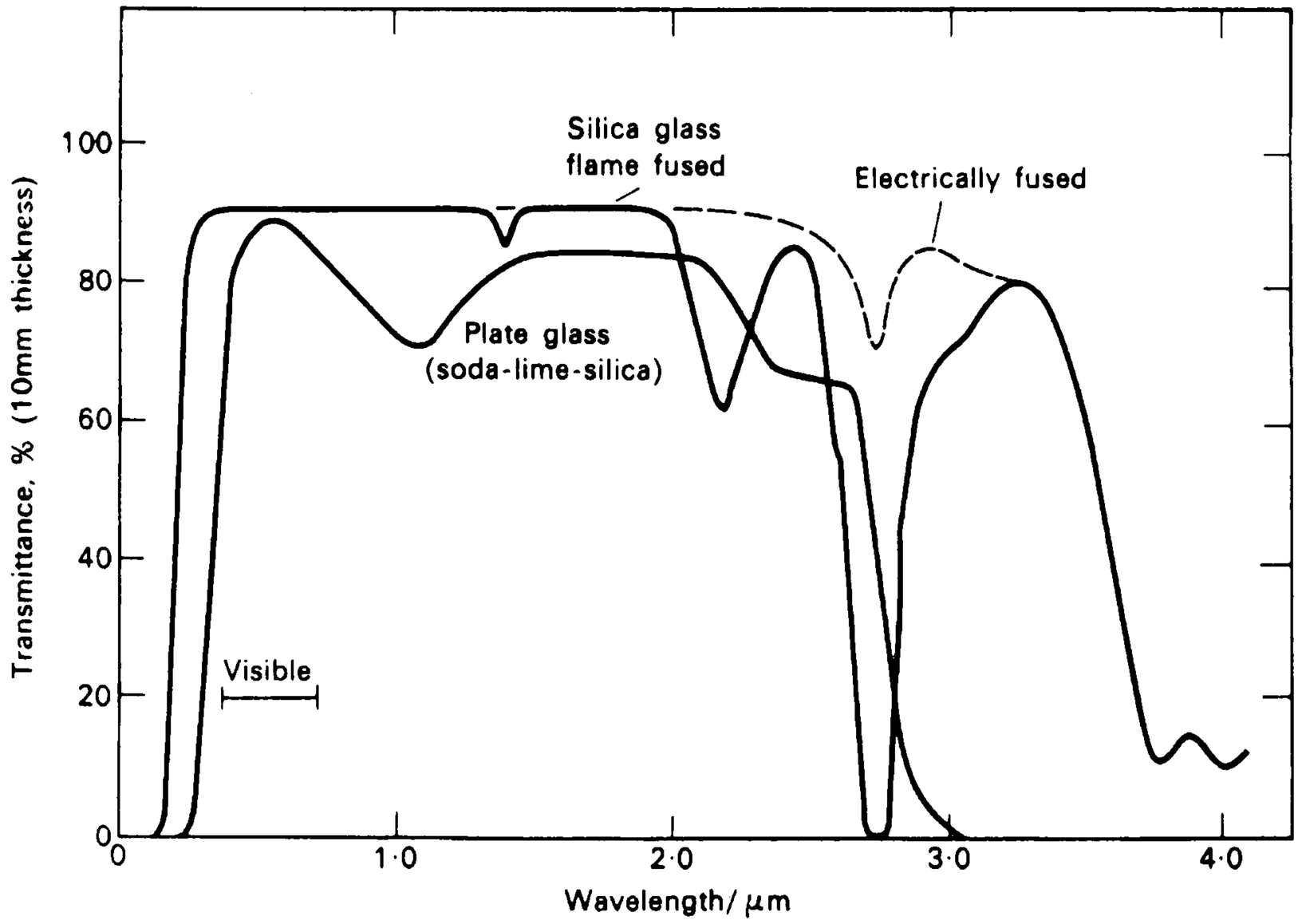

Figure 2.6: Transmission of common glasses as a function of wavelength, reproduced from [21], copyright Wykeham Publications.

absorption of remaining energy as heat in the lattice. X-ray, γ and high-intensity ultraviolet radiation may also create transient local lattice defects called colour centres, which may substantially increase the ultraviolet absorption.

Strong VUV absorption occurring in glasses promises a possibility of precision laser machining of these materials. High spatial resolution of machined features, comparable with VUV wavelengths, is achievable together with a possibility of virtually instant photo-decomposing with extremely thin heat affected zones, due to suppression of thermal coupling with the lattice. These important issues, from a viewpoint of laser material processing, are discussed in greater detail in Section 2.5.

The impurity ions, especially metallic elements present in silica sands, modify the absorption spectrum of glasses in UV, visible and infrared. For example, the typical greenish tint of soda-lime window panes, when viewed from a side, is caused by a tail of infrared absorption band of Fe^{+2} ions [21]. Glasses can also be doped with "impurities" to modify the absorption spectra to suit a particular laser wavelength for production of grey scale masks, for example.

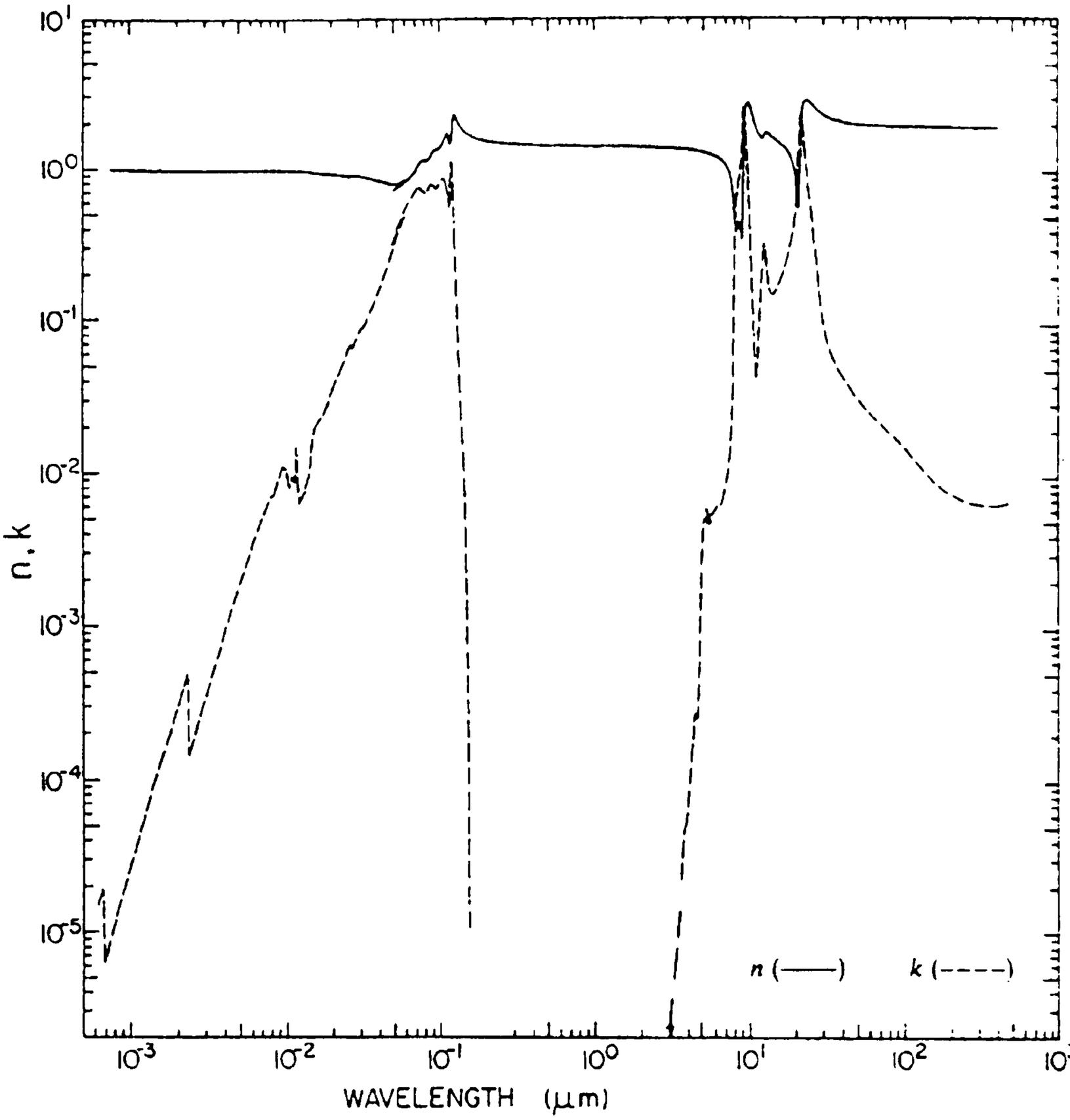

Figure 2.7: Complex refractive index of fused silica as a function of wavelength, reproduced from [24], copyright Academic Press.

Infrared absorption. The absorption in the infrared part of optical spectrum is caused by lattice resonances, thus the absorption characteristics depends more on the lattice structure, bond strength and masses of coupled ions than on their electronic structure. In case of silica, the IR cutoff begins near 4 μm (see Figures 2.7 and 2.6) due to Si-O network vibrations. The absorption band near 2.7 μm is associated with Si-OH bonds, created during a fusion of silica in an oxy-hydrogen flame. The content of hydroxyl groups can be greatly reduced by electrical fusion, which produces IR grade material. Electrical fusion also excludes the presence of "impurity" water, which contributes to weak absorption bands at 1.4 and 2.2 μm.

As a consequence of nature of absorption in infrared, the laser ablation in this band is inherently associated with thermal processes, which are undesired in pre-

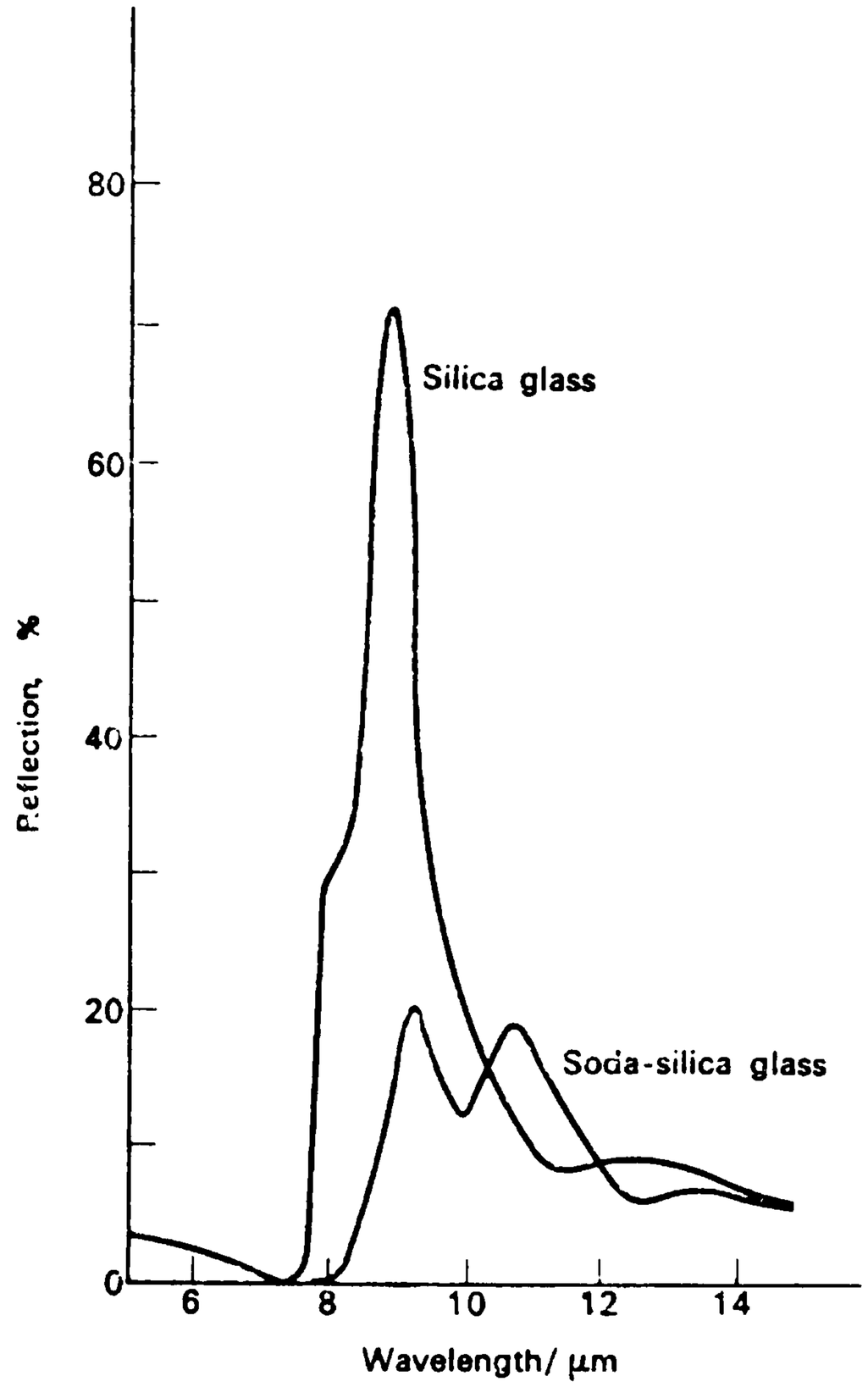

Figure 2.8: Infrared reflectivity of common glasses as a function of wavelength, reproduced from [21], copyright Wykeham Publications.

cision shaping of photonic material due to thermal stresses and modification of material properties. The lateral resolution of direct-write IR laser machining is two orders of magnitude lower than that of VUV. However, as it will be shown in Section 2.5, in some cases it can be advantageous to use CO_2 lasers operating at 10.6 μm wavelengths, which seem to perfectly suit a role of an IR ablation tool. Very strong absorption (absorption length $\beta < 35$ μm [25]) and reasonably small reflection (~20%, see Fig. 2.8) guarantee good control of ablation and energy coupling into the lattice.

The reflectance measurements confirm the expected increase of reflectivity at lattice absorption peaks. Figures 2.8 and 2.9 show the reflectivity spectra of common silicate glasses measured at a normal incidence. The peak at 8.5-9.5 μm is attributed to a bond stretching vibration of the Si and O ions in the Si-O-Si linkage. Another

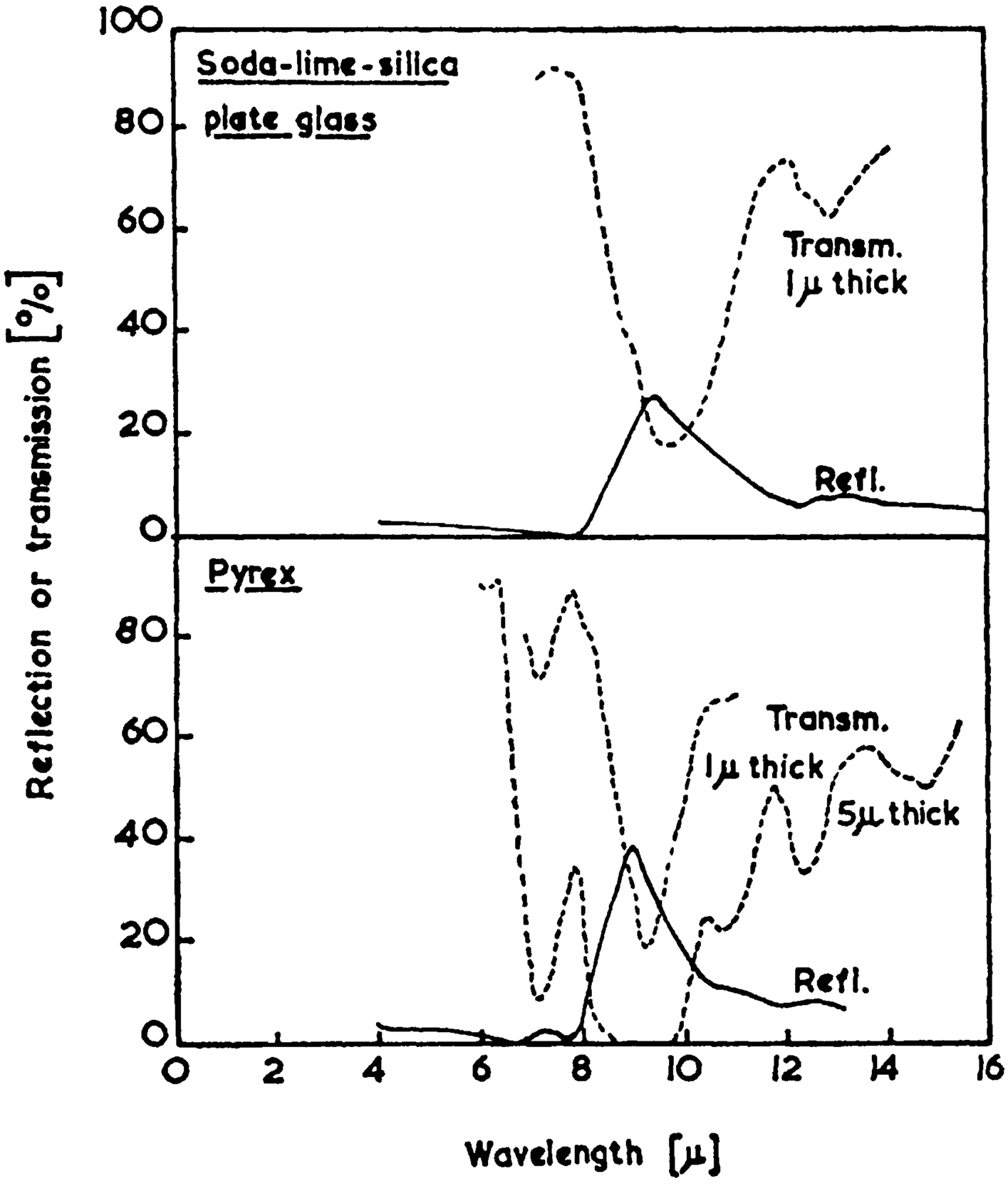

Figure 2.9: Infrared reflectivity of common glasses as a function of wavelength, reproduced from [18], copyright Chapman and Hall.

peak at 10-11 μm, coinciding with the CO_2 laser wavelengths, is a result of bond stretching vibration in a Si-non-bridging oxygen linkage. Although the reflectance peak suggests low-efficiency coupling of the laser radiation into the glass, these wavelengths are promising for the precision machining due to absorption depths as little as a fraction of micron (see Section 4.8).

Temperature dependence of extinction coefficient of silica. McLachlan *et al.* [25] have studied the temperature dependence of extinction coefficient for CO_2 wavelengths in a wide range of temperatures. The measurements were carried out using thin samples (25-30 μm) of different types of silica (fused and 96% silica) made by a number of manufacturers. Significant variation of extinction coefficient k with temperature, CO_2 wavelength and also with silica type has been observed. The results of their work are shown in Figure 2.10 and Table 2.7. They have found that k varies approximately linearly in a wide temperature range, so absorption depths of 34 μm at room temperature drops down to $\sim$4 μm at 1800 °C. Further reduction of absorption length may be anticipated by extrapolation of the curves from Figure 2.10. This fact supports the choice of CO_2 laser for an ablation tool, since additional confinement of ablation depth contributes to better process control.

Nonlinear absorption. After invention of lasers capable of tremendous levels of irradiance ($>10^{11}$ W/cm^2), it was possible to study a nonlinear behaviour of absorption. At such extremely high irradiances, even visible and near infrared wavelengths can be strongly absorbed in glasses [26, 27, 28]. There is a number of recognized mechanisms behind the nonlinear absorption, such as harmonic absorption, network defect formation, two photon and many photon absorption processes. These effects may lead to the avalanche ionisation and breakdown of the material if certain threshold values of irradiance are exceeded. The nonlinear absorption of glasses and its application for laser machining is reviewed in Section 2.5.2.

2.4 Technological aspects of phase transformation

This section outlines some of most important phase transitions occurring in glasses that determine the properties of glass products when kept in vicinity and above characteristic glass transition temperatures. It is shown here that the devitrification, detrimental to the performance of optical components, does not occur in fused silica

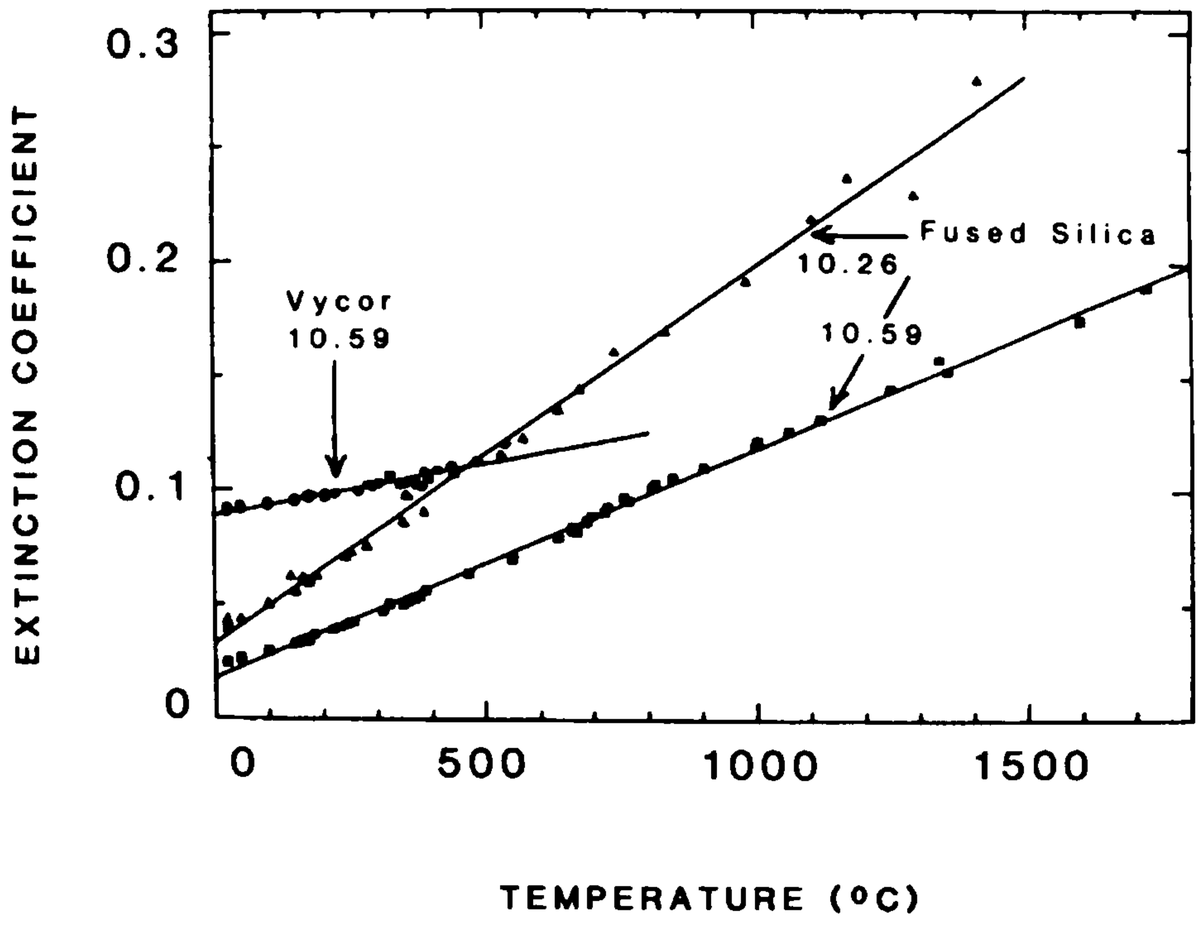

Figure 2.10: Temperature dependence of extinction coefficient of silica at some CO_2 laser wavelengths, reproduced from [25], copyright Appl. Optics.

Material	Wavelength [μm]	a [$\times 10^{-2}$]	b [$\times 10^{-5}$]	Temperature range [°C]
Fused silica	10.61 (P-22)	2.25	7.71	25-400
	10.59 (P-20)	1.82	10.10	25-1800
	10.57 (P-18)	2.15	8.53	25-400
	10.55 (P-16)	1.82	11.04	25-1600
	10.26 (R-18)	3.41	16.67	25-1200
	10.21 (R-26)	4.70	14.36	25-300
	9.6	3.71	8.27	25-300
Vycor (96% silica)	10.61 (P-22)	9.74	2.79	25-400
	10.59 (P-20)	8.87	4.59	25-600
	10.57 (P-18)	8.50	3.71	25-400
	10.55 (P-16)	7.89	4.61	25-400
	10.26 (R-18)	4.04	16.63	25-600

Least-squares fit: $k = a + bT$ (T in °C)

Table 2.7: Fitting parameters of extinction coefficient for different CO_2 wavelengths, from [25].

in short timescales of laser treatment, such as machining or polishing. The risk of thermal shock is unavoidably associated with any kind of thermal treatment. The methods of reducing the built-up thermal stresses and related modification of other physical properties, are also discussed.

2.4.1 Phase transitions

In general, the glasses undergo a phase change between solid, liquid and gaseous states of aggregation in suitable conditions, defined by the pressure and temperature. In case of silica, sub-classes of solid phase can exist in normal conditions, as shown in Figure 2.13 and summarized in Table 2.8. The following phase transitions have been observed in glasses:

1. Melting - a smooth transition between solid and liquid state, in contrast to the crystalline materials, see section 2.3.3

2. Crystallisation, surface or volume - occurs when molten glass is undercooled below the fusion temperature of constituent species, described later in this Section,

   - homogeneous - crystal growth initiated within a single phase of molten glass, e.g. pure SiO_2
   - heterogeneous - initiated by impurities in a single phase molten glasses (e.g. Li^+ cations in SiO_2), or on interface between different phases

3. Liquid-liquid phase separation - separation of a homogeneous mixture of liquids into separate phases, e.g. SiO_2 and B_2O_3 exploited for production of 96% silica

4. Evaporation - at high enough temperatures the pressure of vapours exceeds ambient pressure and the mass is lost from liquid phase. The issues concerning the evaporative mode of IR laser ablation of silica are covered in Section 2.5.3.

The crystallisation is generally considered undesired from a point of view of fabrication of optical components, since it leads to increased scattering and loss of transparency (devitrification, see Section 2.4.2). Point 3. relates to systems containing more than one constituent, e.g. borosilicate glasses, thus this transition does not occur in single-component fused silica glass.

Homogeneous crystallisation The bulk or volume crystallisation begins with temperatures below the freezing point when the crystal growth takes place with a finite rate in a finite number of nucleation centres. Silicate glasses can be formed because the rate of nucleation or rate of crystal growth are low in comparison to other systems, which do not form glasses readily.

The stability of nuclei in the liquid depends on a difference in free energy between two phases and on interfacial energy [19]. The free energy change for nucleation ΔG, following this classical reasoning, can be formulated :

$$\Delta G = -\frac{4}{3}\pi r^3 \ \overline{\Delta G} + 4\pi r^2 \ \sigma \tag{2.10}$$

where r is a radius of the atom cluster, $\overline{\Delta G}$ is the increase in free energy per volume for the crystal-liquid transformation and σ is a surface tension. The critical size of radius r_{cr}, above which the energy balance favours the particle growth is:

$$r_{cr} = \frac{2\ \sigma}{\overline{\Delta G}} \tag{2.11}$$

The particles with radii smaller than r_{cr}, called embryos, are unstable and may be dissolved back into the liquid. The particles with radii larger than r_{cr} are stable and can grow with expense of free energy.

The *thermodynamic energy barrier to nucleation* ΔE_{cr} must be overcome to form a stable nucleus that can carry on growing:

$$\Delta E_{cr} = \frac{16\pi\sigma^3}{3(\overline{\Delta G})^2} \tag{2.12}$$

Following the classical reasoning on the probability of embryo formation and probability of attachment of atoms to the embryo ([19] p.19-20), one arrives with a formula describing the rate of nucleation I:

$$I = N_s \frac{kT}{h} \exp\left(-\frac{\Delta E_a}{kT}\right) \cdot N \exp\left(-\frac{16\pi\sigma^3\ T_f}{3\ \Delta T^2\ \Delta H_f^2\ kT}\right) \tag{2.13}$$

where N_s is a number of atoms adjacent to the embryo in position to attach themselves, N is a number of atoms per unit volume, ΔE_a is the *kinetic energy barrier to nucleation*, T_f is a fusion temperature, ΔT is an undercooling and ΔH_f is the heat of fusion per unit volume. Figure 2.11 shows the rate of nucleation versus undercooling temperature. The nucleation rate is zero at fusion temperature T_f, but increases with decreasing temperature to reach the peak and then decay to zero at a

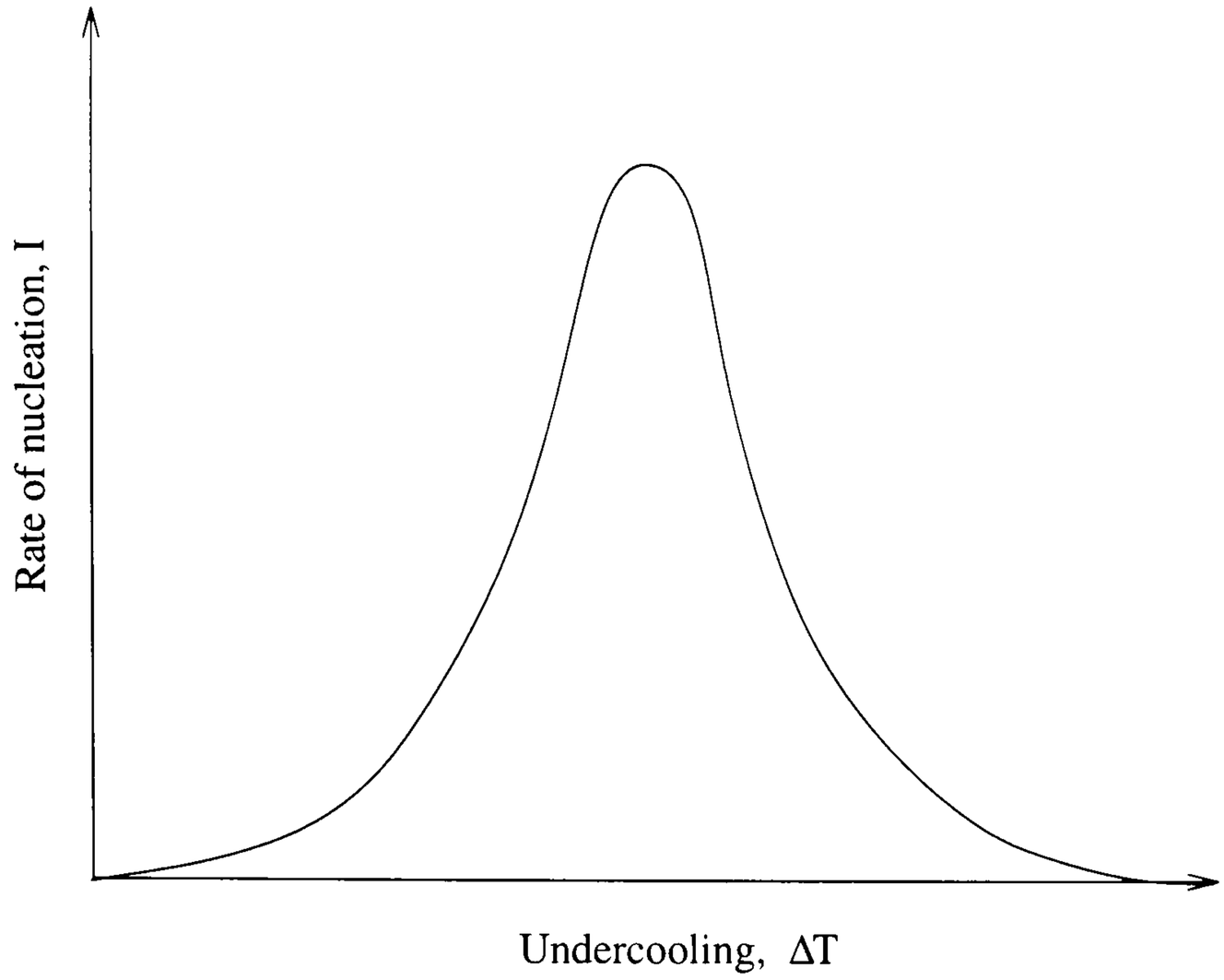

Figure 2.11: Exemplary nucleation rate as a function of undercooling for a glass system.

certain value below T_f. An amount of time the liquid spends in temperature range of nonzero I determines the number of nuclei formed, thus from a technological point of view on glass forming, the shorter that time the better.

The nucleation and following crystallisation may not develop provided the cooling rate is high enough. Substances such as SiO_2 do not crystallize as long as the cooling rate is higher than 1 °C/hour. This natural ability of silicate melts to solidify without crystallisation in normal conditions is responsible for their widespread use in glass-making industry. This fact has got important implications for laser processing of materials, since the heating and cooling rates can be extremely high. Laser melting of metallic compounds allows to form thin-film metallic glasses since the necessary cooling rates in order of $10^6 - 10^{12}$ °C/s can be easily achieved [29].

The considerations on probability of atoms attaching themselves to nuclei ([19] p.24) yield a formula describing a rate of crystal growth u:

$$u = \lambda \, \nu_0 \exp\left(- \frac{\Delta E_a}{kT} \right) \left[1 - \exp\left(- \frac{\Delta G}{RT} \right) \right] \tag{2.14}$$

where λ is a distance between crystalline interface and the atom to be attached, ν_0 is the frequency of thermal oscillations of the atom attempting to cross the energy barrier and R is a gas constant. Figure 2.12 shows the comparison of rates of homogeneous nucleation and crystal growth. The important conclusion from

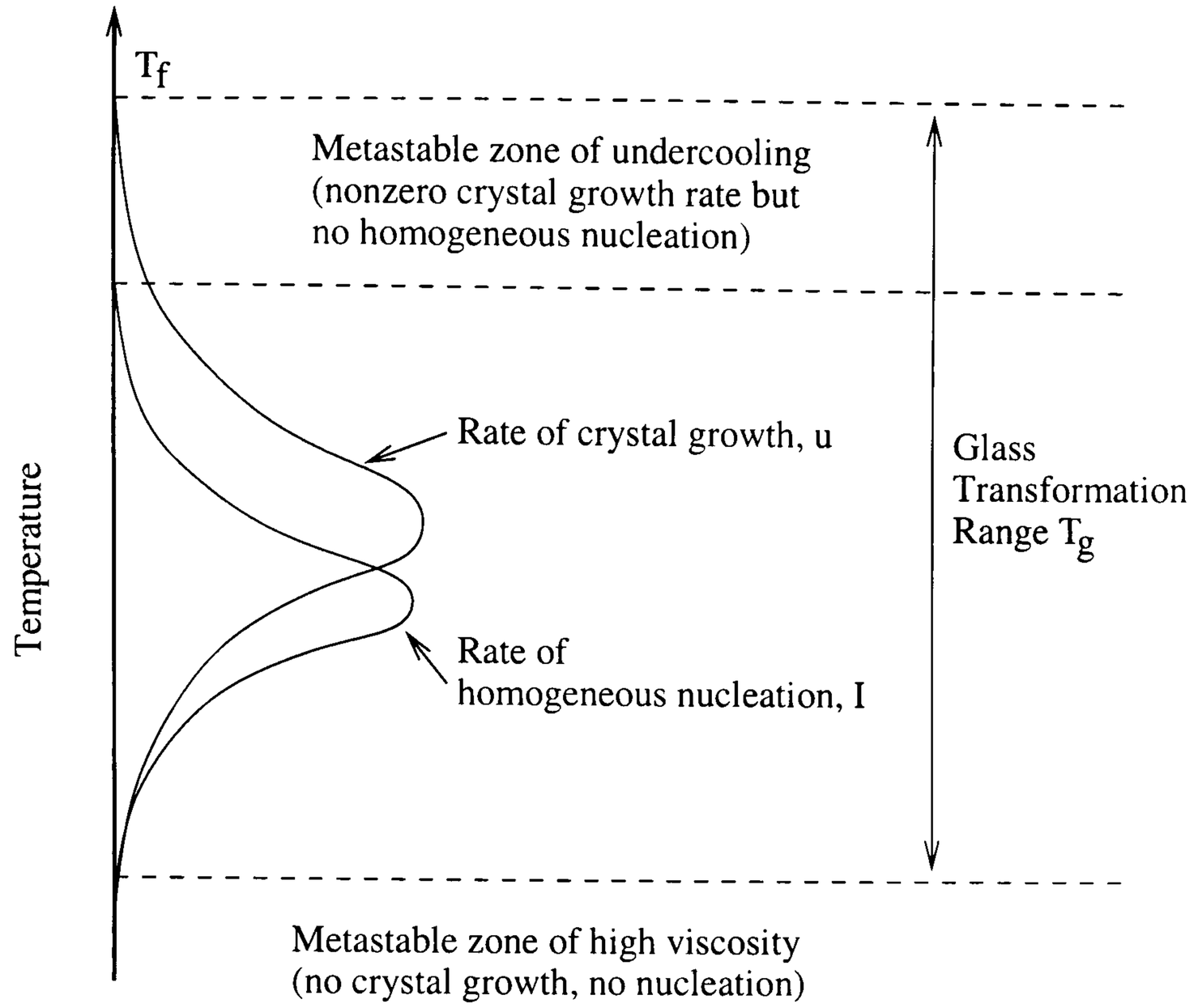

Figure 2.12: Comparison of exemplary nucleation and crystal growth rates for a glass system, after [19].

the presented calculation is that the crystal growth rate can be significant even if the homogeneous nucleation does not occur (metastable zone of undercooling in Figure 2.12) for the small undercooling ΔT. The impurities, adhering to the surface, play an important role in this temperature range as foreign nucleation and crystal growth centres.

Heterogeneous crystallisation A presence of alien nucleation centres (metal ions, interface boundaries) in the melt may initiate the crystallisation, called now heterogeneous, in a region of temperatures where natural homogeneneous nucleation does not occur (see Figure 2.12). That property has been utilized in early stages of microelectronics manufacturing as a method of growing semiconductor crystals on foreign substrates of very similar parameters, known as liquid phase epitaxy (LPE). In case of glasses however, the heterogeneous crystallisation poses a problem for applications that require a prolonged exposure of transparent glasses to high temperatures near the glass transition region. The contaminants, especially metals, deposited on a surface of glass, may create a much higher number of effective nucleation centres than that expected from a rate of homogeneous nucleation.

As an outcome, surface crystallisation and related loss of transparence is greatly accelerated.

2.4.2 Devitrification

The effect described, called *devitrification*, affects glasses exposed to temperatures below the fusion temperature of crystalline phases. Clean silica glass devitrifies in temperatures above 1200 °C, but devitrification may also take place in temperatures below 1000°C if contaminants are present. The rate of devitrification is practically zero at room temperature.

Another effect, which is often confused with devitrification, is called a *weathering*. It is linked to chemical reactions that modify the properties of glass surface when exposed to reactive environment, such as slurries used for polishing (see Chapter 6) or corrosive atmospheres. High temperatures are not required to activate the process. Although the weathering can also lead to a loss of transparence of glass surface, it is a process different to devitrification.

Silica can exist in various structural forms, as shown in phase diagram in Figure 2.13. In normal conditions glassy state and the crystalline states have been recorded, as shown in Table 2.8. During devitrification process, which is usually heterogeneously initiated, the amorphous surface undergoes a phase change into polycrystalline structure called cristoballite. The devitrification front propagates into the material with a rate of <1 μm/s at 1300 °C [31]. Table 2.9 shows the relation between the devitrification rate of clean fused silica and atmospheres the glass was exposed to at high temperature [31]. The accelerating influence of impurities on a rate of devitrification is apparent, however even in a worst case the rate of crystallisation is nearly zero in a timescale of a CO_2 laser pulse ablation (see Section 2.5.3) or even milliseconds of laser polishing treatment. Anyway, devitrification cannot take place during laser ablation in air because the ablation front velocity is few orders of magnitude larger than rate of devitrification (see Section 4.5 p. 87). It does not either take place above melting point of quartz (1750 °C), since the undercooling criterion of the crystal growth is not satisfied.

Handling of fused silica. Direct hand contact should be avoided since skin's natural salts contain alkali metal elements, such as sodium, potassium and other impurities, that greatly accelerate the devitrification. Silica-ware should be washed

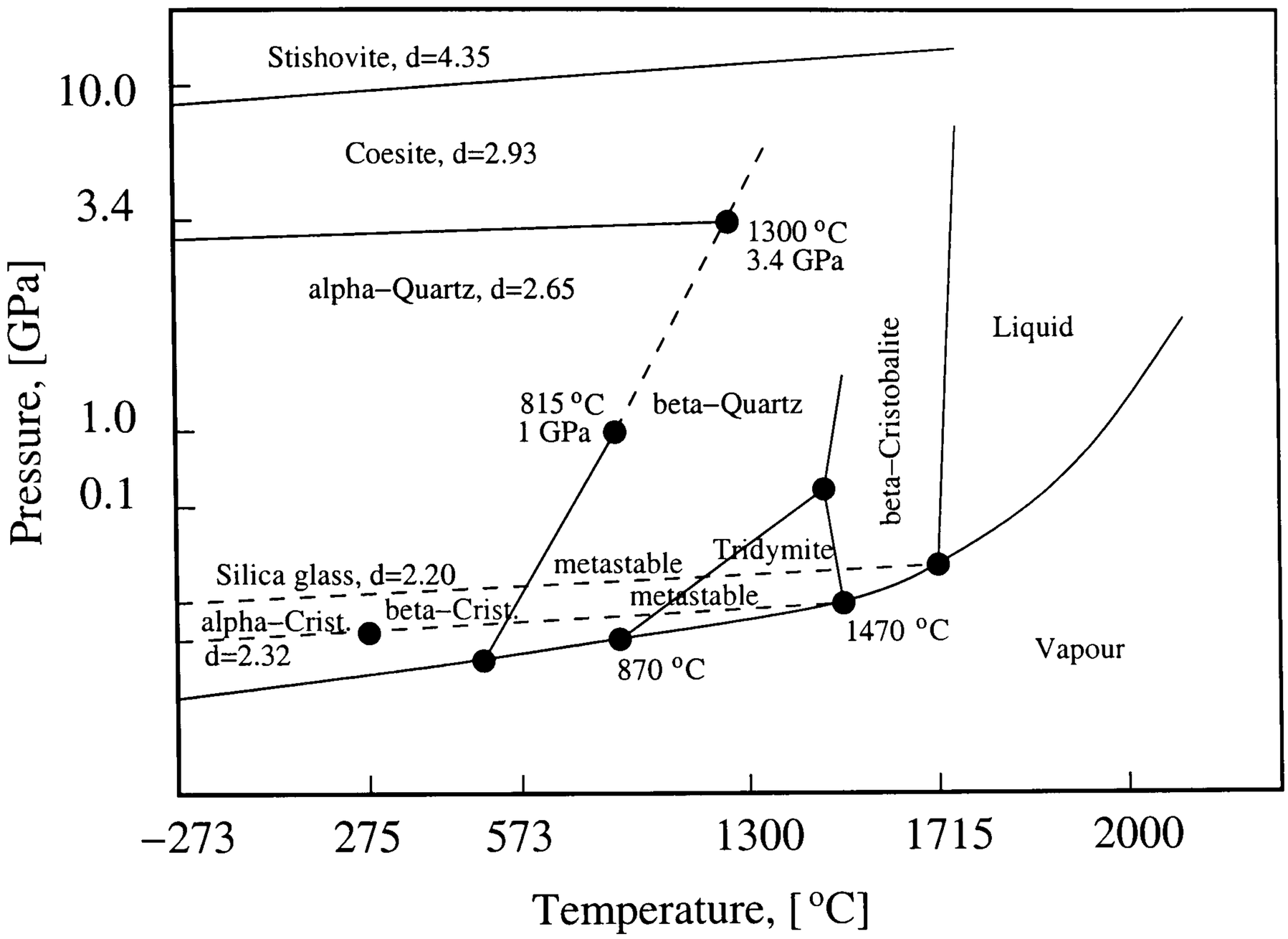

Figure 2.13: Phase diagram of pure SiO_2, redrawn from [30].

Form	Density [g/cm^3]	Refractive index (at 589 nm)
Quartz	2.65	1.55
Cristoballite	2.32	1.49
Tridymite	2.28	1.47
Silica glass	2.20	1.46

Table 2.8: Forms of SiO_2 in normal conditions.

Gas composition	Temperature [°C]	Time [h]	Degree of devitrification	Thickness devitrificated
Air	1300	72	Surface perfectly devitrificated	250 mm
Dried O_2	1300	72	Devitrification - 50% of all surface	100-150 mm
Industrial N_2	1300	72	Surface devitrificated	-
Nitrogen removing O_2 and H_2O	1300	72	No devitrification	-
Hydrogen removing O_2 and H_2O	1300	4	No devitrification	-

Table 2.9: Dynamics of silica devitrification in different atmospheres, from [31].

in pure deionised or distilled water, then air-dried in clean environment or wiped dry with a clean alcohol-wetted cloth. In some cases 5-10% HF acid solution may be used to remove thin contaminated layer prior to washing.

2.4.3 Thermal stresses and related issues

The glasses are in general poor conductors of heat, thus big temperature gradients may be easily created inside these brittle materials. They may suffer a fracture if the thermal stresses exceed their strength. The temperature gradients inevitably arise in the material due to the fabrication techniques, involving melting of glass constituents together and subsequently cooling them down, at appropriate rates, to freeze the liquid structure. In case of laser processing of glasses, the thermal stresses determine the failure or success of the process [32].

The poor conduction of heat is responsible for build-up of residual stresses in a surface and bulk of glass, since the surface will always be cooled down first. Appropriately low rate of heat removal must be then induced to guarantee temperature uniformity and low thermal stresses throughout the bulk of cooled material. At a same time, the cooling rate must be as high as possible to avoid the crystallisation and devitrification, thus manufacturers have to find a compromise always resulting in a presence of residual stresses.

Upon cooling, the layers of material close to the surface can be cooled down

much faster than the deeper layers and are very likely to develop tensile stresses. The glasses are much less resistant to tensile stresses than to the compressive ones mainly due to surface flaws that promote the development of micro-cracks. That is the reason why most glasses are sensitive to the cooling rate and not so much to the heating rate. The situation reverses after the bulk of material is cooled down. The surface is now compressively stressed. This effect, called *tempering* of glasses, is used to increase the strength of glass products, since the compressively stressed surfaces are more resistant to crack development and following fracture.

The situation is different when the glass is treated with a laser, since only the thin layer of glass is affected by the heat. In such case, the development of tensile surface stresses after the cool down is certain if the softening or ablation of glass has taken place in the laser irradiated zone. The effect has been observed with CO_2 lasers [32], used for laser fire polishing of bulk optics (see Chapter 6) and deep UV fluorine laser ablation of silica glass [33]. The development of tensile surface stresses in the ablation zone after cool down is responsible for instantaneous or delayed cracking along the boundary of heat affected zone. The delay time can range from nearly zero to many days, thus it is important to make sure that the surface is relieved from stresses by annealing (see Section 2.4.4).

Thermal expansion coefficient α can be used as a parameter determining the resistance of glasses to thermally induced fracture, since Young moduli E and Poisson's ratios ν are almost identical for many glasses [32]. The magnitude of thermal stresses may be estimated by a simple formula:

$$\sigma = \frac{E}{1-\nu}\,\alpha\,\Delta T \tag{2.15}$$

The practical strength of glasses has been found to be $\sim 10^{-4}-10^{-3}\,E$ [32], 1000−100 times smaller than the results of calculations based on bonding structure of glass. This significant reduction in strength is mainly caused by surface flaws that develop into cracks and lead to premature fracture. The temperature difference between melting and room temperatures can be as much as $\sim 10^3$ °C, typical value of expansion coefficient α 10^{-5} °C^{-1}, thus producing stresses $\sim 10^{-2}E$, which get very close to the value of practical strength of glasses.

Stressed glasses, in general, are undesired in optical applications, since their optical performance suffers from photo-elastic effect (see Section 2.3.4 p. 33), a stress induced birefringence that can amount up to ~ 700 λ optical path difference

per meter of material near breaking stress 10^{-3}E for visible wavelengths.

2.4.4 Annealing

Frozen internal stresses in glasses can be substantially removed in a process called *annealing*. The annealing consists of a scheduled heat treatment in a region of temperatures between *annealing point* temperature, corresponding to viscosity of $10^{12.4}$ Pa·s, and a *strain point* temperature, at which the viscosity reaches $10^{13.5}$ Pa·s. A glass kept at annealing point can have all its internal stresses relieved in about 15 minutes. The strain point is a characteristic temperature from which the glass can be rapidly cooled down to room temperature without developing serious internal stresses.

The manufacturers of glass recognize three levels of annealing based on a product purpose. **Optical annealing** provides the highest level of performance since the optical glasses require lowest possible stresses to minimize the photo-elastic effects and the impact of fictive temperature. **Commercial annealing** corresponds to the acceptable level of stresses in commercial applications. The least effective, **mechanical anneal**, reduces the stresses only to satisfy the quartz-ware application requirements in semiconductor industry.

The annealing process consists of a heat treatment schedule depicted schematically in Figure 2.14 [34]. The temperature is raised up to a range between annealing and strain points to allow stress relieve and also to avoid deformation of delicate products. The heat up rate should be low enough to prevent thermal fracture of the product, but is not critical to the overall annealing performance.

In case of silica, the typical hold temperature lies within a range 1165-1185 °C dependingly on a product thickness and a kind of silica used. The hold times typically range from 20-120 minutes and depend on the hold temperature.

The initial cooling down stage is a most critical part of the annealing process, since it is responsible for the introduction of internal stresses. The engineering formula 2.16 [34] relates the acceptable midplane stresses σ_{ac}, created in a slab of thickness d, and the initial cooling rate R_c:

$$R_c = \frac{24\ K\ \sigma_{ac}\ (1-\nu)}{E\ \alpha\ d^2} \tag{2.16}$$

where K is thermal diffusivity, ν Poisson's ratio, α thermal expansion coefficient and E Young's modulus. The magnitude of final stresses is proportional to the cooling

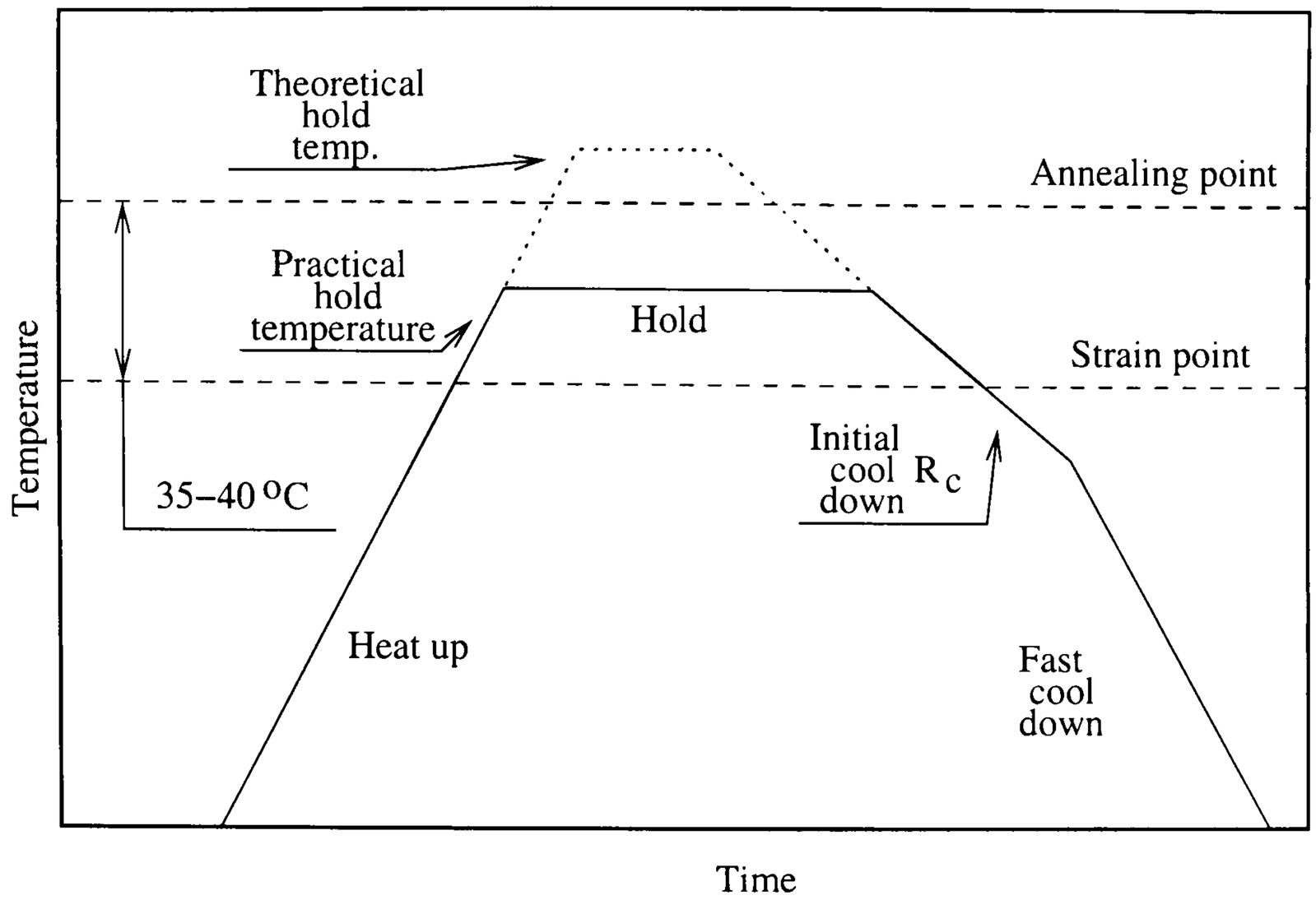

Figure 2.14: Schematic diagram of an annealing schedule, after [34].

rate and inversely proportional to the thermal expansion coefficient and square of material thickness. The typical cooling rates, aiming at residual stresses less than 15 MPa, range from 10 to 100 °C/hour for quartz-ware used in semiconductor industry.

Extent of annealing effect during CO_2 ablation of silica. Formula 2.16 can be used to compare the magnitude of threshold cooling rate and experimentally observed one (see Section 4.11) for a thin, 35 μm (absorption depth of CO_2 radiation at room temperature [25]) silica slab, irradiated with CO_2 laser. A selection of such thickness allows for calculation of worst case cooling rates, because in practice the absorption depth increases with temperature and can fall below 4 μm at temperatures exceeding 1800 °C [25]. Equation 2.16 yields 2.5–25 °C/μs of the threshold cooling rate that would introduce stresses nearing a practical strength of silica $10^{-3}E$–$10^{-2}E$, input data were quoted at 1400 °C. It has been experimentally found in Section 4.11 that cooling rate was ~6 °C/μs. It can explain silica's resistance to cracking after CO_2 laser ablation.

After repeating the calculations of cooling rate for soda-lime glass, thermal expansivity of which is more than an order of magnitude higher than that of silica, one gets 0.15-1.5 °C/μs. Practical cooling rate of the crater in a soda-lime glass is close to that of silica, since the thermal parameters are similar and crater geometry

the same. It becomes clear why these glasses do not tolerate CO_2 ablation and crack during the process or shortly after.

Thermal expansion coefficient of glass and the thickness of heat affected zone determine the possibility of post-process cracking. In case of CO_2 laser ablation, thermal expansion can be used as a measure of material's resistance to cracking during or after the process. It is shown in Chapter 6 that the low value of that parameter is also needed for a success of CO_2 laser polishing of glasses.

2.5 Glass shaping with lasers

Last two decades were abundant in new findings on application of lasers to processing of various photonic materials. UV lasers have proven capable of precision machining of high resolution diffractive micro-optics in a range of photosensitive polymers [35, 35, 36, 37, 38]. More and more attention is directed towards fabrication of photonic structures in a range of transparent glasses, which offer excellent mechanical, thermal and optical properties. Photonic devices, which one day shall substitute conventional microelectronics in telecommunication for instance, require high precision of manufacture in order of 1/10 of the operating wavelength. The technical difficulty associated with laser machining of these materials is a lack of practical laser sources that address ~9.3 eV energy bandgap of fused silica, which corresponds to 133 nm wavelength [28]. For most practical lasers it means weak absorption, poor process control and large heat affected zones.

2.5.1 VUV laser ablation

F_2 lasers. F_2 lasers are currently at the forefront of practical UV lasers in terms of wavelength (157 nm). In spite of weak normal absorption $\alpha = 10\ \mathrm{cm}^{-1}$ F_2 lasers have been reported to cleanly ablate fused silica surfaces, leaving them smooth and free of micro-cracks [28]. The AFM study revealed short-range periodic (~5 μm) surface roughness of 6 nm rms, which could be a manifest of laser induced periodic surface structures (LIPSS). Long-range roughness (~15 μm) has been attributed to beam inhomogeneity. The increase of absorption coefficient up to $\alpha = 170000\ \mathrm{cm}^{-1}$ has been associated with nonlinear absorption effects that take place in a timescale of typical F_2 nanosecond laser pulse, such as wrong Si-Si bonds that accumulate with exposure and give rise to large density of transient single-photon absorption

states.

Volume compaction and following refractive index change has also been observed in glasses exposed to 157 nm F_2 radiation [28] below the ablation threshold level. Dependingly on dopant type and concentration, refractive index change $10^{-5}-10^{-3}$ has been induced in silicate glasses, giving a possibility of writing volume gratings, such as Bragg reflectors in Ge-doped optical fibre core. The weak incubation effect, an exposure to a finite number of pulses prior to onset of ablation, has been observed below ablation threshold too.

Excimer lasers. In case of longer wavelengths, supplied by excimer lasers (193 nm ArF, 247 nm KrF), the two-photon absorption becomes the mechanism behind compaction and ablation of glasses. It manifests in a prompt ablation threshold fluence, below which no ablation takes place even after hundreds of laser pulses. The strong incubation effect for 193 nm wavelength is a feature that limits the depth resolution to 100−300 nm per pulse. Surface morphology is generally worse than in case of F_2 laser ablation. A formation of micro-cracks also takes place occasionally. The condition of the glass surface ablated by excimer lasers is far from excellent optical quality [26, 27].

2.5.2 Ultrafast laser ablation

Another approach uses visible and near infrared ultrafast lasers, Ti:sapphire, dye lasers, Nd:YAG to name a few. Although material absorption of most glasses is very small in that spectral range (<1 cm^{-1}, unless specially doped to increase absorption), the ultra-high intensities (TW/cm^2) produced by pico- and femtosecond laser pulses get absorbed in depths <200 nm by means of nonlinear effects. Very shallow absorption depths and extremely short interaction time, which practically inhibits heat diffusion and assures very thin heat affected zones, lay a promise of high machining precision. Additionally, lack of plume formation and subsequent plasma screening on femtosecond timescale allows for good energy coupling into material [27]. However, the work carried out by a number of researchers [39, 40, 41, 42] has highlighted the imminent difficulties of ultrafast processing of glasses, such as incubation that affects machining rates, poor surface morphology, shock-induced flaking and micro-cracking and laser induced periodic surface structures (LIPSS) [43, 36]. From optical application viewpoint, these morphological

Parameter	F_2 (157 nm, 15 ns)	ArF laser (193 nm, 15 ns)	Ultrafast Nd:glass (1.054 μm, 1.2 ps)
$1/\alpha_{eff}$ [nm]	59	96	250
prompt F_{th} [J/cm^2]	1.1	5.5	5.5
$\alpha_{eff} \cdot F_{th}$ [kJ/cm^3]	187	–	231
min. etch. depth [nm]	20	125	20
lateral resolution [nm]	120	180	500
surface roughness[1]	0.1–1%	–	10%
micro-cracks	no	occasional	yes
incubation	~no	yes	yes
processing approach	mask projection	mask projection	scanning

[1]Relative to ablation depth

Table 2.10: Comparison of ultrafast and UV laser ablation of silica, after [28].

factors determine the success of laser fabrication of photonic components.

An improvement in ablated surface morphology has been observed [41, 44] following the transition from pico- to femto-second laser pulses. Together with better quality of resulting surfaces, the repeatability and machining accuracy have been significantly enhanced. However, the surface quality still needs some improvement to reach optical grade. Table 2.10 compares the performance of UV and ultrafast ablation of fused silica.

2.5.3 Infrared laser ablation

In the infrared part of spectrum the presence of strong lattice absorption bands allows for efficient energy coupling into a glass. As shown in Figures 2.7 p. 39 and 2.8 p. 40, the first peak occurs near 9.2 μm for fused silica, with extremely short absorption depth in order of hundreds of nanometers. The energy coupling directly into vibrational modes of the glass lattice provides an effective mechanism of material decomposition for micro-structuring purposes.

Tunable FEL laser ablation of silica. The influence of laser radiation near that strong absorption peak on the dynamics of material removal in fused silica has been studied by Haglund *et al.* [45], who have used tunable free electron laser (FEL). FEL produced 4 μs long train of 1 ps pulses with 350 ps interval, giving peak irradiance of 10^{11} W/cm^2, thus some nonlinear effect could be present. The

thermal nature of coupling and μm scale wavelength place limitations on maximum resolution of such machining regime, and also infer larger heat affected zones than in case of UV and ultrafast ablation.

In a range 3-5 μm, far from the 9.2 μm peak, the dominant mechanism of absorption is an excitation of harmonic lattice vibrations, in other words heat. The absorption length is large (>500 μm) in that wavelength region and one decidedly deals with a volume heating regime. The ablation is thus poorly defined and irreproducible material removal has been observed. Additionally, subsurface boiling and thermal fracture further degrades the morphology of ablated surfaces.

In a range 6-8 μm, where the thermal diffusion is comparable with absorption depth (<50 μm), the ablation has been more controllable. However, melt splashes and redeposited material around the rim of smooth ablation craters were observed.

Tuning into peak of Si-O stretch vibration 9.2–9.4 μm brings changes into the morphology of ablated craters. The material from the high intensity center has been cleanly ablated without splashes and debris around the crater. The bed of the crater was uneven in figure and that could be the result of explosive vaporisation as a consequence of extremely short energy deposition time. The residual stresses, left in a close vicinity of crater walls, were strong enough on some occasions to cause full cleave-off of these walls to expose smooth sidewalls.

CO_2 laser ablation of silica. The absorption coefficient of silica near 8 μm is similar to that of CO_2 wavelengths, thus the CO_2 laser ablation may be similar to that of FEL. The main difference between FEL and typical CO_2 pulses lies in a timescale and peak intensity. Tens to hundreds μs pulses with peak irradiance $0-10^6$ W/cm^2 can be easily produced, allowing for an ablation study in less extreme conditions without an onset of nonlinear effects. Smooth evaporative mode of material removal, in contrast to explosive vaporisation observed by Haglund *et al.*, has been reported to produce ablated silica surfaces of exceptional smoothness and free of micro-cracks [46, 47, 5, 4].

A study on high-temperature vaporisation of silica, carried out by Schick in the sixties [48], has shown that silicon monoxide SiO and oxygen are main constituents of silica vapours, produced by thermal decomposition of liquid phase of SiO_2 according to reaction 1:

1. $SiO_2(l) \rightarrow SiO(g) + \frac{1}{2}O_2$

Temperature 3000 °K	
Species	Pressure, [atm]
SiO	0.43
SiO_2	0.04
Si_2O_2	$5{\cdot}10^{-5}$
$(SiO)_x$	Unknown†
O_2	0.18
O	0.05
Si	$1.3{\cdot}10^{-6}$
Total pressure	0.70

†but likely to be less than that of the dimer

Table 2.11: Partial pressures of main constituents of silica vapours near boiling point in neutral conditions, after [48].

2. $\frac{1}{2}O_2(g) \rightarrow O(g)$

3. $SiO_2(l) \rightarrow SiO_2(g)$, T>2000 °K

4. $2SiO(g) \rightarrow Si_2O_2(g)$

Other decomposition species (reactions 2-4), shown in Table 2.11, play, according to Schick, minor role in a contribution to total vapour pressure of silica. Schick has analyzed and calculated partial pressures of dominant volatile products of thermal decomposition (see Figure 2.15) and was able to obtain the value of boiling point of silica in normal, neutral conditions. The calculated value of 3070±75 °K (2797±75 °C) has been compared with those obtained experimentally by other researchers and found to be most probable. Schick has also shown that even if one takes only reaction 1 for calculation of vapour pressure curve, the boiling point increases by mere 15 °C, thus reaction 1 is predominant in thermal decomposition of silica.

The presence of reducing atmosphere has been found to influence the vaporisation thermodynamics. The oxidising conditions of the air at normal pressure suppress the formation of SiO(g) at temperatures lower than boiling point, however this effect decreases near boiling and practically does not influence the value of the boiling point temperature (see Figure 2.16).

Bearing in mind the above, Markillie *et al.* [4] have identified possible CO_2 laser processing windows for fused silica. Figure 2.17 shows the viscosity and vapour

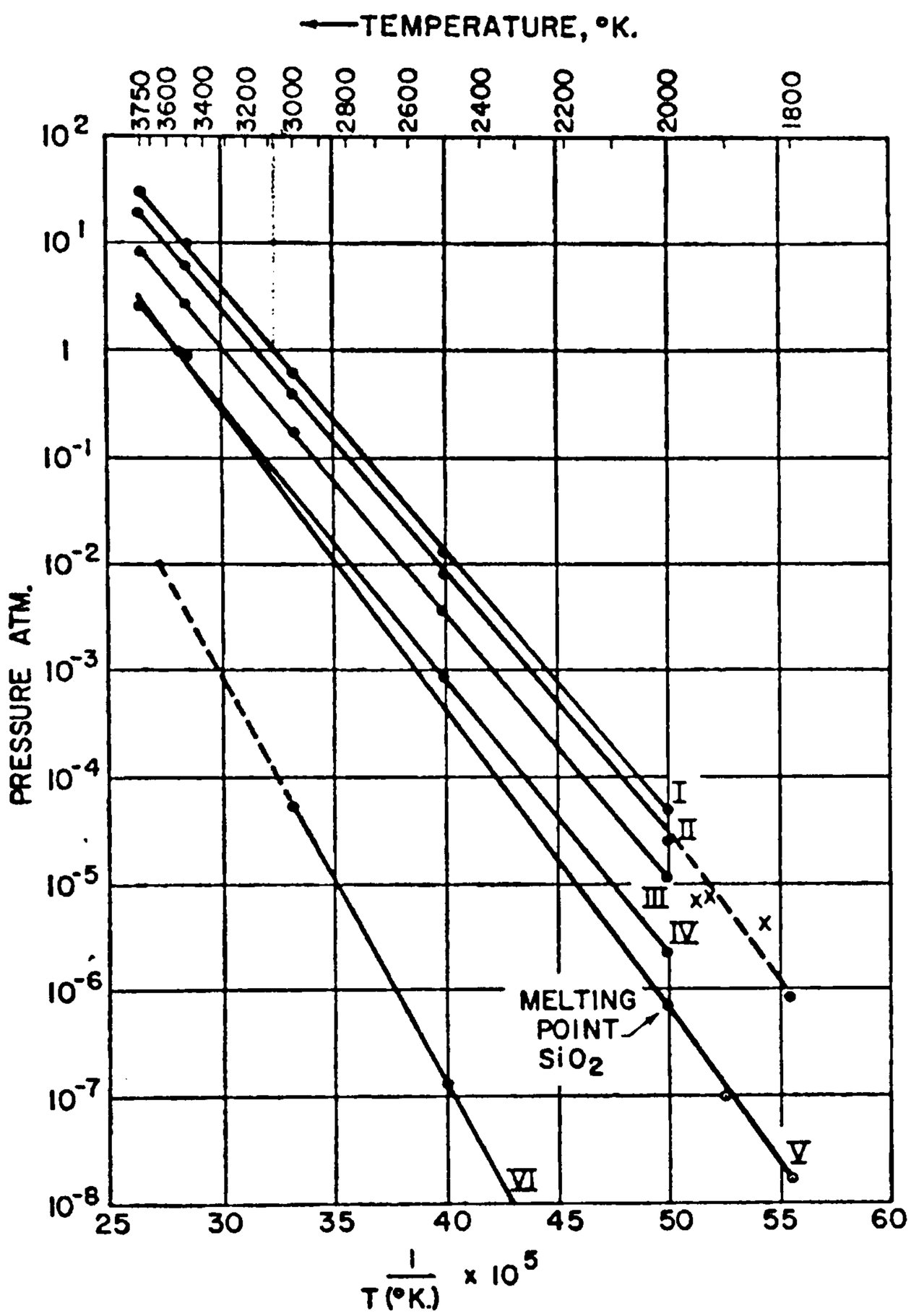

Figure 2.15: Partial pressure of decomposition products of silica in neutral, normal conditions, I) total pressure, II) p_{SiO}, III) p_{O2}, IV) p_{O}, V) p_{SiO2}, VI) p_{Si2O2}, reproduced from [48], copyright Chem. Rev.

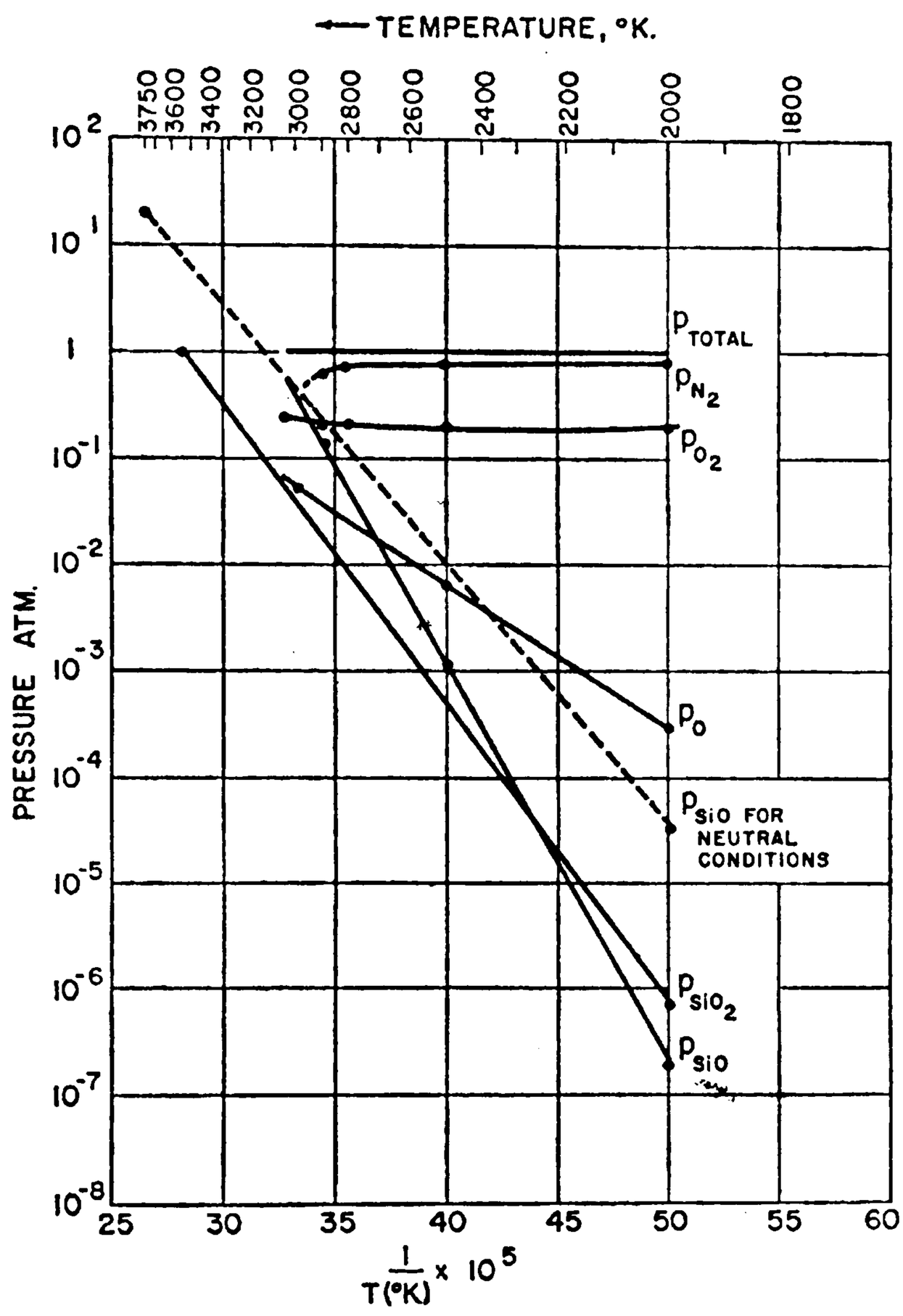

Figure 2.16: Partial pressure of decomposition products of silica in air at 1 atm, nitrogen assumed to be inert, reproduced from [48], copyright Chem. Rev.

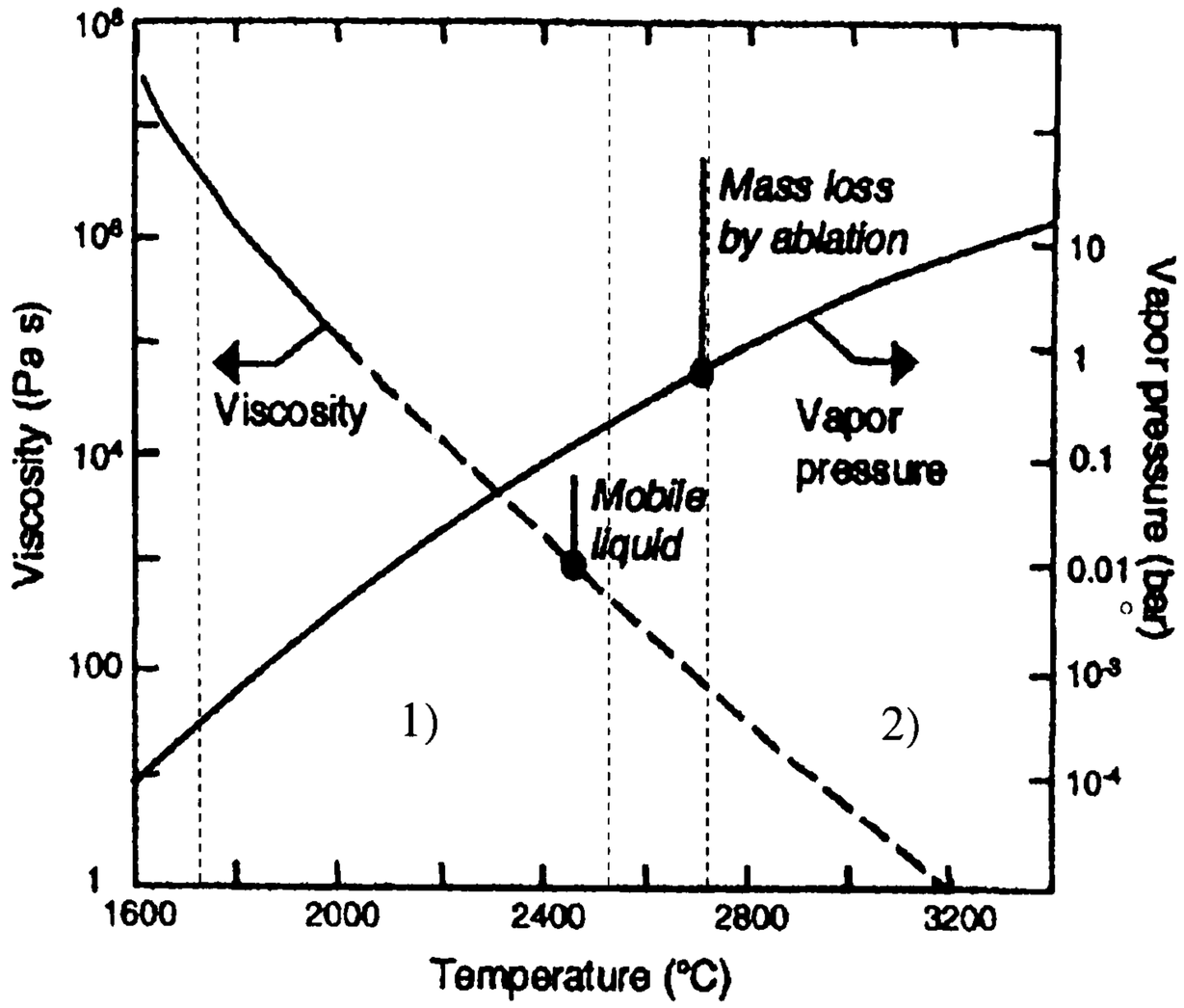

Figure 2.17: Laser polishing 1) and laser machining 2) regions for fused silica, reproduced from [4], copyright Appl. Optics.

pressure of silica as a function of temperature. The drop in a value of viscosity (extrapolated data) in a temperature range 1800-2400 °C allows for a significant viscous mass flow under the surface tension, providing a mechanism for laser polishing and re-flow of silica surfaces [49, 50, 51, 52], such as the micro-optics demonstrated in Chapters 5 and 7. The vapour pressure in that temperature range is much smaller than atmospheric pressure, thus no significant mass loss takes place and unwanted machining does not occur. Conversely, in temperatures above boiling point >2700 °C, vapour pressure exceeds the atmospheric pressure and the mass is lost from the solid. This region is of interest to laser machining and shaping of fused silica with CO_2 lasers.

The study on dynamics of CO_2 ablation, summarized in [4], has enabled the researchers to find the optimal machining window for laser machining of fused silica with respect to irradiance and laser pulse duration. The rates of depth removal per shot have been found to be at least one order of magnitude higher than corresponding performance of UV and ultrafast ablation. It has been also found that melt ejection in a form of fibres takes place after exceeding 1.6-1.7 MW/cm^2 threshold of pulse irradiance (see Figure 2.18). This effect, caused by vapour pressure piston action, is undesired from a precision machining point of view. However, the

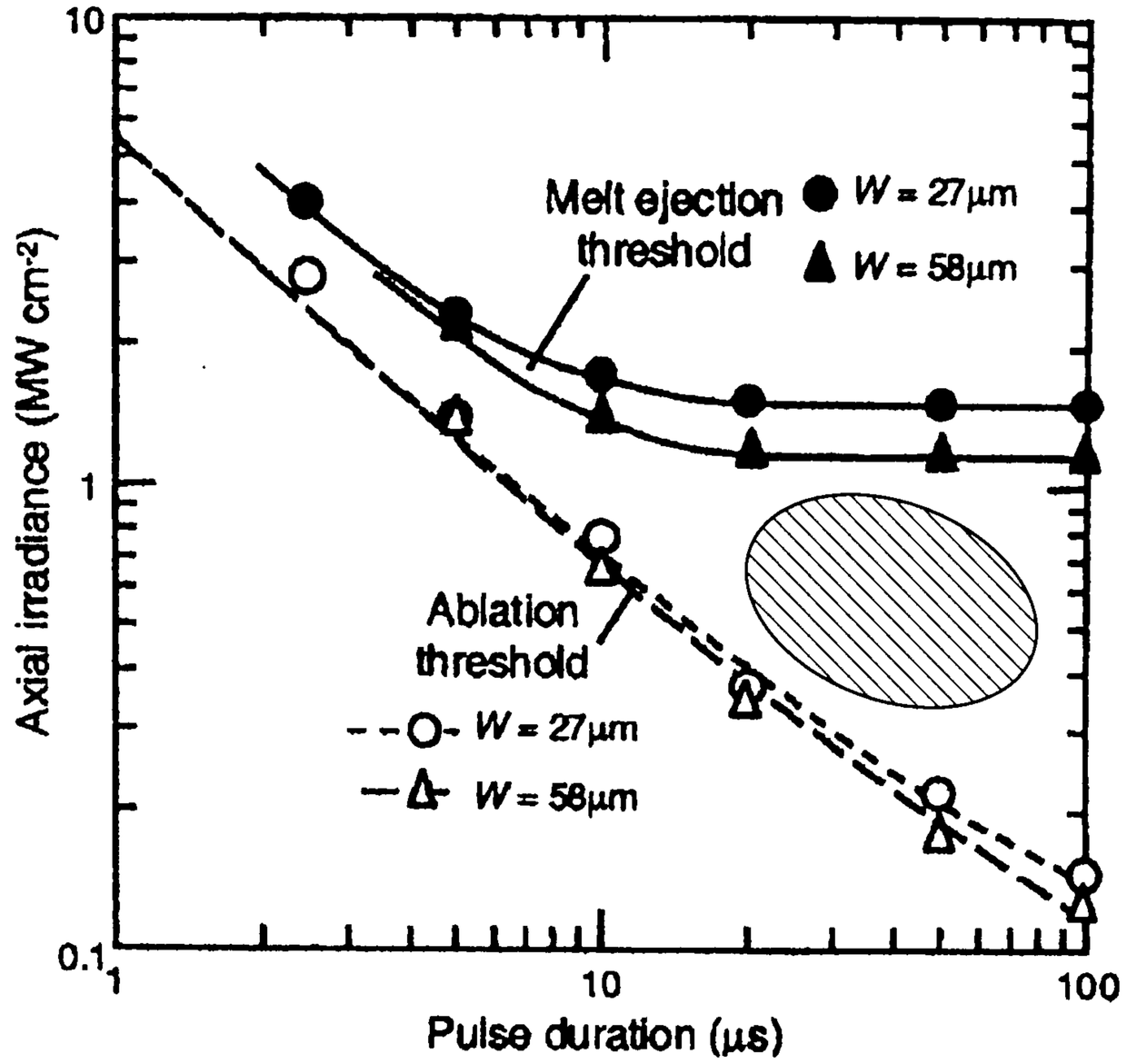

Figure 2.18: CO_2 laser machining window of fused silica (shown here as hatched area), reproduced from [4], copyright Appl. Optics. W denotes the spot diameter.

ablation threshold determines the lower value of possible pulse irradiance, thus a compromise must be sought between low machining threshold (high irradiance) and smooth evaporation of significant mass of the material without melt displacement. Such compromise has been found for pulse duration range 30-80 μs at irradiance level 0.5-1.0 MW/cm^2, which offer low machining threshold (<20 J/cm^2) and assure large mass removal per shot (picolitres) in a smooth manner.

The discussed issues, combined with productivity and flexibility of high pulse repetition frequency (PRF), give CO_2 lasers a competitive edge over available UV and ultrafast technology in a niche of refractive micro-optics fabrication. The extra possibility of laser surface polishing by CO_2 lasers is another argument supporting the need for a detailed study of CO_2 ablation of silica, presented in Chapter 4.

Chapter 3

MACHINING STATION

3.1 Introduction

This chapter describes the precision machining station developed for fabrication of micro-optics by CO_2 laser ablation of silica. There is a number of issues the machining station must address to fulfill the requirements of machining regimes presented in Chapter 5. The laser must deliver stable and repeatable long term (>10h) operation. The facility has to provide an accurate control over the temporal profile of laser pulse and its energy, $< \pm 1\%$, delivered in a beam of well defined parameters. The positioning system must guarantee the placement of laser spot with resolution at least 10 times better than its size.

A distinctive feature of the system, in comparison to the machining facilities used by other researchers studying rapid prototyping of planar micro-structures [53, 37, 54], was the spatio-temporal synchronisation between arbitrary position of laser spot and firing time, all under computer control. This feature allowed for spatially resolved accurate laser shooting in arbitrary locations with the resolution of positioning stages, as opposed to fixed mesh raster shooting, used extensively by others.

An acousto-optical modulator (AOM) has been added to the machining system to produce pulses with duration times shorter (<100 μs) than that of raw triangular CO_2 laser pulses. Except for improvement of pulse energy stability, the AOM allowed also for additional degree of freedom in a laser spot placement and possibility of additional pulse energy stabilisation by inclusion of single pulse energy stabiliser. Additionally, fine spot positioning (resolution 0.05 μm expected from calculations), along or transverse to then raster line direction, was achievable by controlling the

drive frequency of AOM in a narrow range over the digital interface. This feature, however, has not been utilised in the work described here.

A custom software has been written to drive the station and achieve the goal of flexibility. This chapter covers high level and hardware level software created to convert the machining station into the direct laser writer capable of producing arbitrary surface shapes within the limits of machining regimes, discussed in Chapter 5.

3.2 System hardware

The functional block diagram of developed system is depicted in Figure 3.1. The photograph of assembled system is shown in Figure 3.2. The system consists of CO_2 slab waveguide laser with beam circularising optics, acousto-optical modulator, beam expanding and delivery optics, high precision positioning tables and a PC, being the control center. The PC was responsible for managing the translation stages, AOM and laser timing according to a prescription contained in a special format, called later the laser spot distribution (LSD) file. The control software has been designed and developed to fully exploit the accuracy of positioning stages and at the same time to provide an easy and flexible interface for programming of arbitrary spot layouts.

3.2.1 CO_2 laser and optics

A commercial CO_2 slab waveguide laser was chosen for its glass machining capabilities [4]. The laser used was made by Lumonics, model 0630-920-00. It could deliver substantial amounts of energy per pulse (0-20 mJ) in a wide range of repetition frequencies, 0 Hz - 10 kHz, offering flexibility and high productivity. The laser produced pulses with peak power of ~100 W and the pulse duration could be varied by RF pulse timing in a wide range of duration times, from few tens of microseconds to a millisecond. However, the duty factor had to be kept lower than 50% to maintain stable laser output and to avoid possible damage of resonator mirrors or electrodes forming a waveguide.

The output beam had to be circularised and cleaned to obtain near-Gaussian TEM_{00} mode profile. A schematic view of optical setup responsible for that task is displayed in Figure 3.3. The circularisation was carried out by a set of three

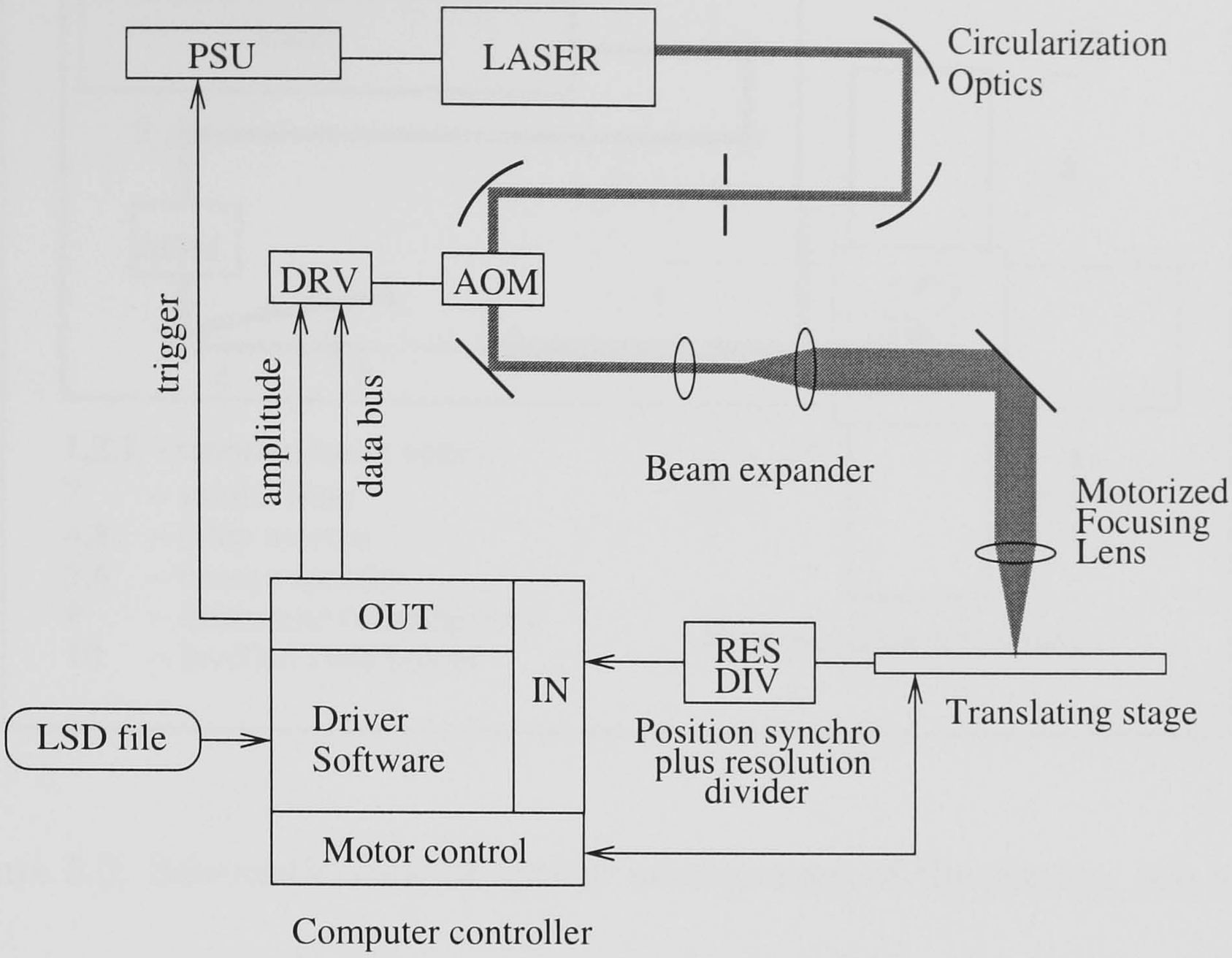

Figure 3.1: Block diagram of the machining system. Details described in text.

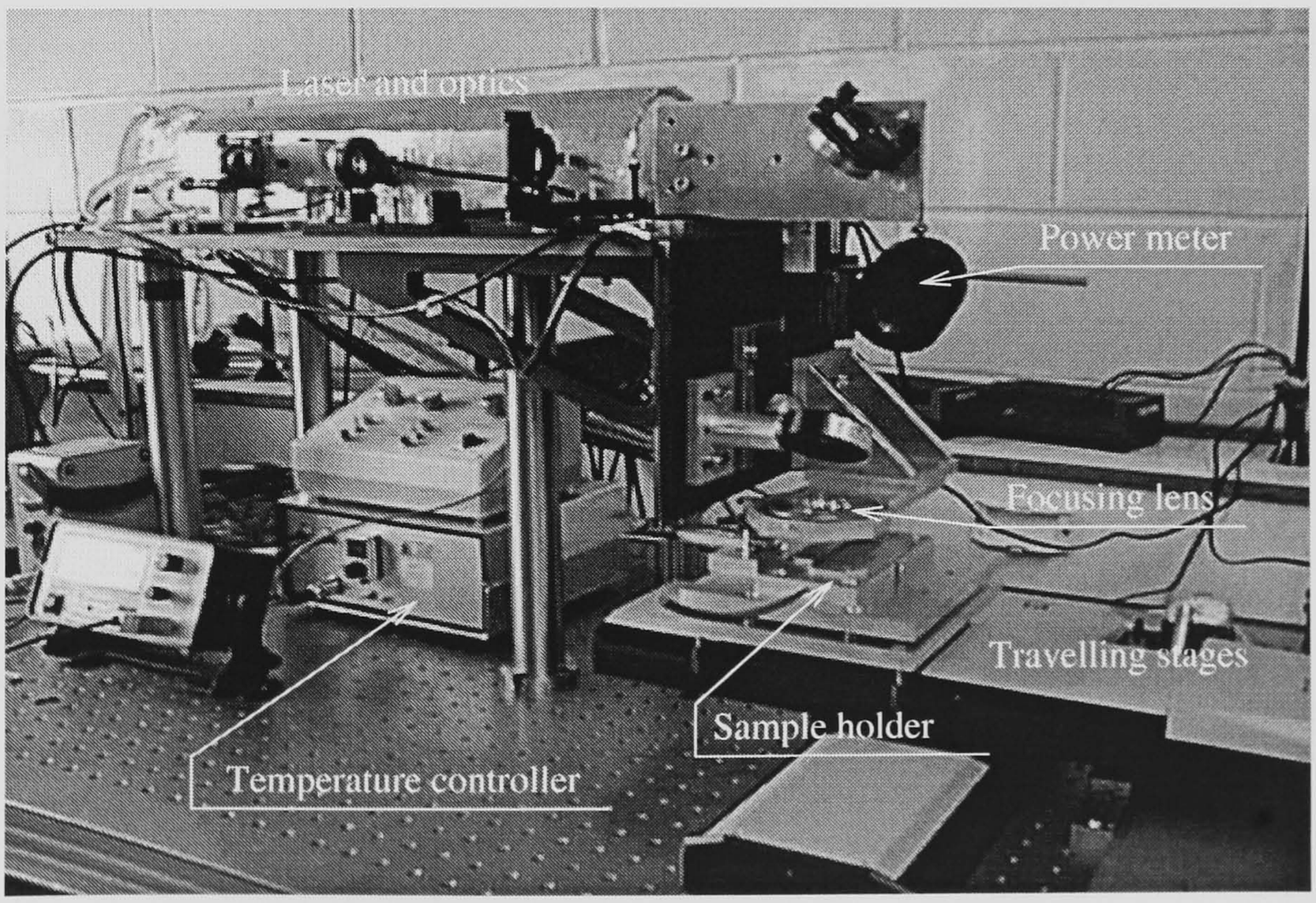

Figure 3.2: Photograph of the system.

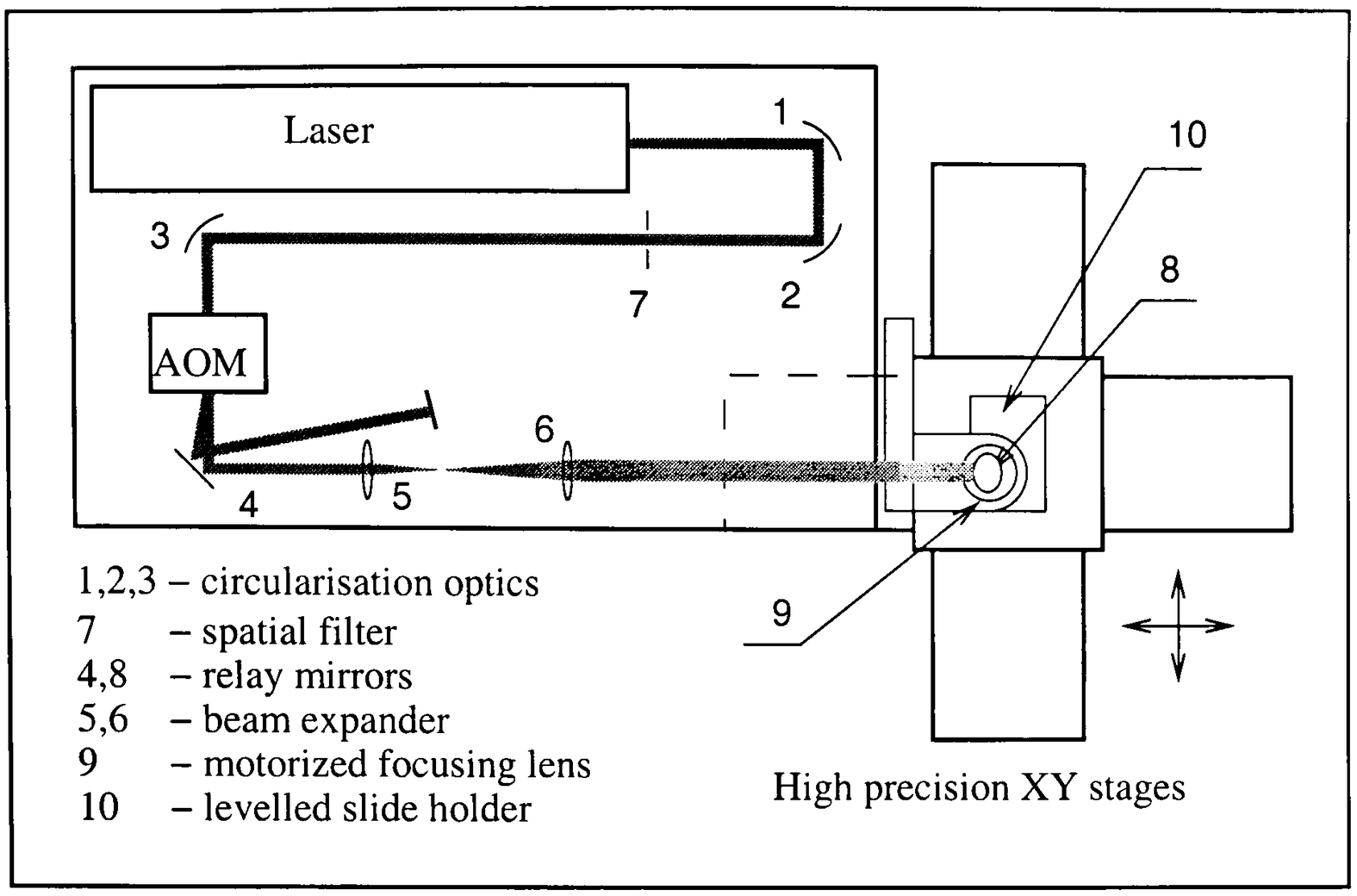

Figure 3.3: Schematic view of optical arrangement of the station, top view.

carefully adjusted concave spherical mirrors, 1 2 and 3, with radii of curvature 1 m. Although the circularisation could be carried out with just two mirrors, three mirrors were used to additionally fold the beam and make an efficient use of space on the laser board.

High frequency components of beam profile were removed by the spatial filter 7, consisting of two adjustable knife edges. The already clean and well circularised beam of quality M^2 <1.2 propagated through the acousto-optical modulator and confocal beam expander, consisting of two meniscus 1" diameter ZnSe lenses, foci $f_1 = 1.5$" and $f_2 = 5$", thus setting the expansion ratio to 3.33. The expanded beam was relayed onto an aspheric 1" diameter ZnSe lens of focal length f = 1.5" to produce 47 μm diameter $(1/e^2)$ spot on the target. The spot diameter has been measured using two methods that relied on assumptions of near-Gaussian, axially symmetric beam profile: knife egde and thermal paper methods. Both methods produced nearly identical results with accuracy of 5%.

3.2.2 Acousto-optical modulator

Germanium crystal based, acousto-optical modulator (AOM), model AGM-406B1M made by IntraAction Corp, provided an accurate control over the temporal laser pulse shape and intensity (see Section 3.3). AOM allows for precise dispensing

of laser pulse energy. The stable raw CO_2 laser pulses of rather long ~100 μs duration time and inherently triangular shape (see Figure 3.4) could be chopped by the modulator to produce shorter pulses of quasi-square temporal profile, which were found to be advantageous to raw triangular ones with respect to ablation threshold [4]. The intensity of chopped pulses could be accurately adjusted to the desired level of irradiance. Pulse energy stability could also be boosted by using AOM in conjunction with pulse fluence meter, which would control either amplitude of AOM driver signal or act as a fast and accurate electronic shutter. Besides the apparent advantages, the AOM limited the transmitted optical power to 30 W average to avoid thermal lensing in germanium and subsequent laser beam instability. It was not a limitation after all, since the laser power necessary for ablation and polishing of silica glass, covered in Chapters 4 and 6 was less than 8 W average.

AOM could additionally modulate the spot location on the workpiece by changing the beam deflection, which could be in turn achieved by changing the drive frequency. The driver, IntraAction Corp model VGE-4030, was endowed with the digital interface, allowing for computer control over AOM frequency and effectively over the beam deflection. As little as 0.05 μm of positional accuracy could be realised by using that feature of the AOM.

3.2.3 High precision positioning system

After early experiments on a previous machining rig [4] equipped with stepper motor stages, I've concluded that DC motor powered stages would be more appropriate for the precision machining station. Excellent motion smoothness, jostle-free operation, maximum translation speed of 50 mm/s and motion range of 20 cm was delivered by a pair DC motor stages, manufactured by Physik Instrumente, model M-521.DD, with resolution of 100 nm assured by built-in optical encoders. The third axis traveling stage, model M-126.PG with 2.5 cm travel range and 0.1 μm accuracy, was used to finely position the focusing lens above the target surface. The translation stages were driven by the motion controller card based on C-482 chip (Precision Motion Devices), plugged into PC data bus.

In order to achieve the goal of synchronisation between laser firing and instantaneous spot position, the software that executed a sequence of prescribed laser spots needed a high speed feedback on instantaneous position of laser spot to trigger the

laser in prescribed locations. This kind of performance could only be achieved by exploiting the characteristics of PC interrupt system, triggered by the digital signal from the optical encoders (see Section 3.4.2).

Repeatable and robust fixing of the workpiece to the stack of traveling stages was necessary to avoid accidental change of position during precision machining. The dedicated slide holder has been designed to accommodate the silica substrates, available in a standard format of 1"×3" microscope slides. The holder was firmly attached to a stack of traveling stages through a levelling table.

3.3 Controlling the laser pulse energy

The control over the laser pulse timing was primarily the task of AOM. Fine pulse length and intensity tailoring was made possible, allowing for a detailed study on ablation of silica (see Chapter 4). The optical pulses as short as ten microseconds were achievable, with minimal rise and fall times of couple of microseconds, defined by the beam diameter and the propagation velocity of acoustic field in the germanium crystal. Figure 3.4 shows temporal profiles of typical microsecond pulses obtained just by RF discharge pulse length control. Fine pulses could be cut out with AOM from any part the raw optical pulse. In practice however, the timing of RF trigger and AOM signals had to be carefully chosen because the ignition of plasma in the laser exhibited ~18 μs delay, with respect to pulse trigger signal, together with up to ±2 μs of ignition jitter. In order to minimize the effect of jitter on the resultant pulse energy stability and to assure minimal duty factor of generated pulses to increase laser stability (see Section 3.3.1), the "house" shaped pulses were chopped out from the raw laser pulses, as shown in Figure 3.5.

There is a maximum pulse repetition frequency limit ~800 Hz, above which the pulse energy starts to increase with increasing frequency. Such behaviour was most probably caused by the technical imperfection of the laser power supply, since the laser energy is known to drop with increasing pulse frequency due to the temperature rise of the gas mixture comprising the active medium. Figure 3.6 summarizes the measurements showing the dependence of pulse energy on pulse repetition frequency (PRF).

The early machining trials with the machining system have shown that laser stability was compromised by signature scanning and related pulse energy instabil-

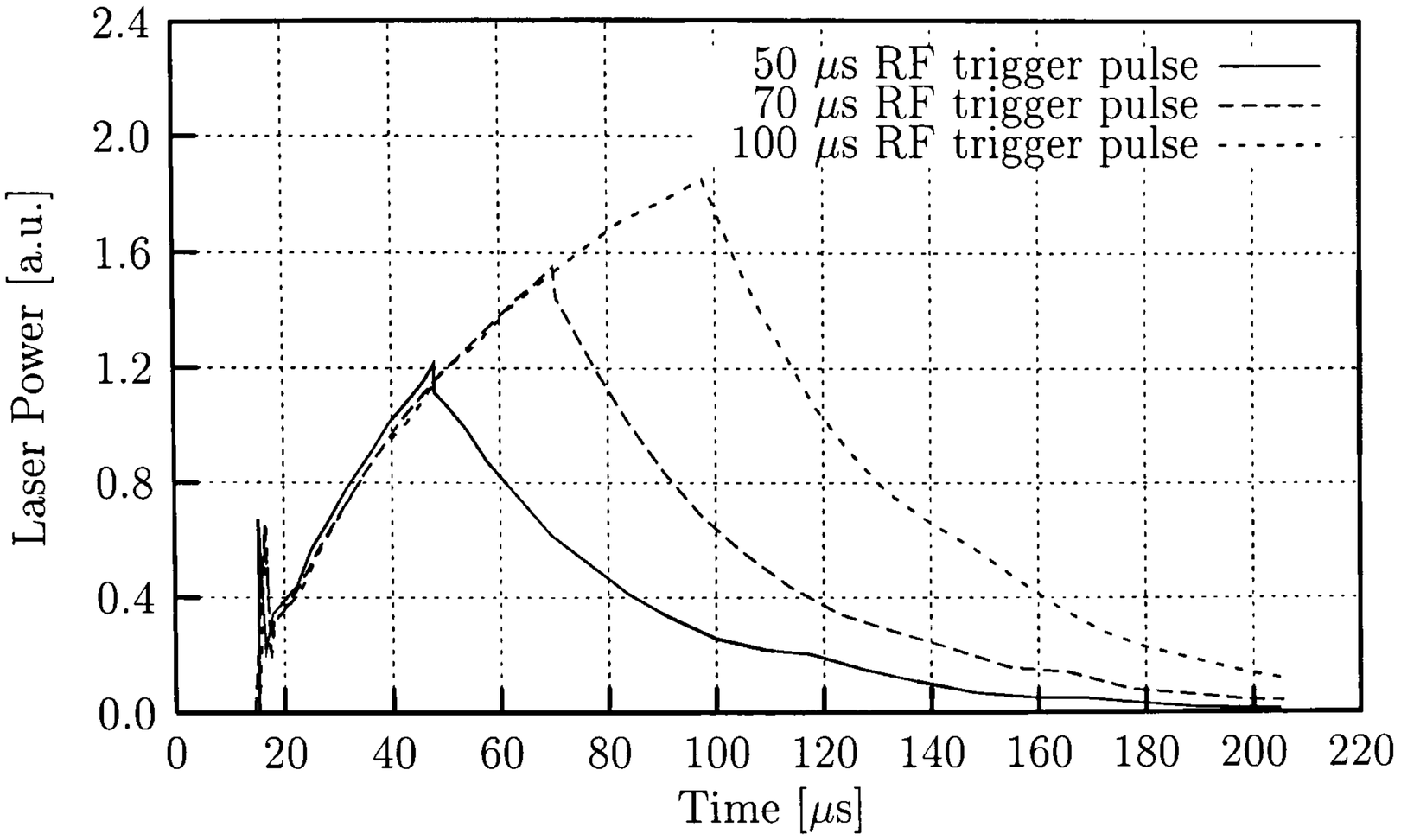

Figure 3.4: Typical temporal profiles of a laser pulse. Pulse length controlled only by RF duration time.

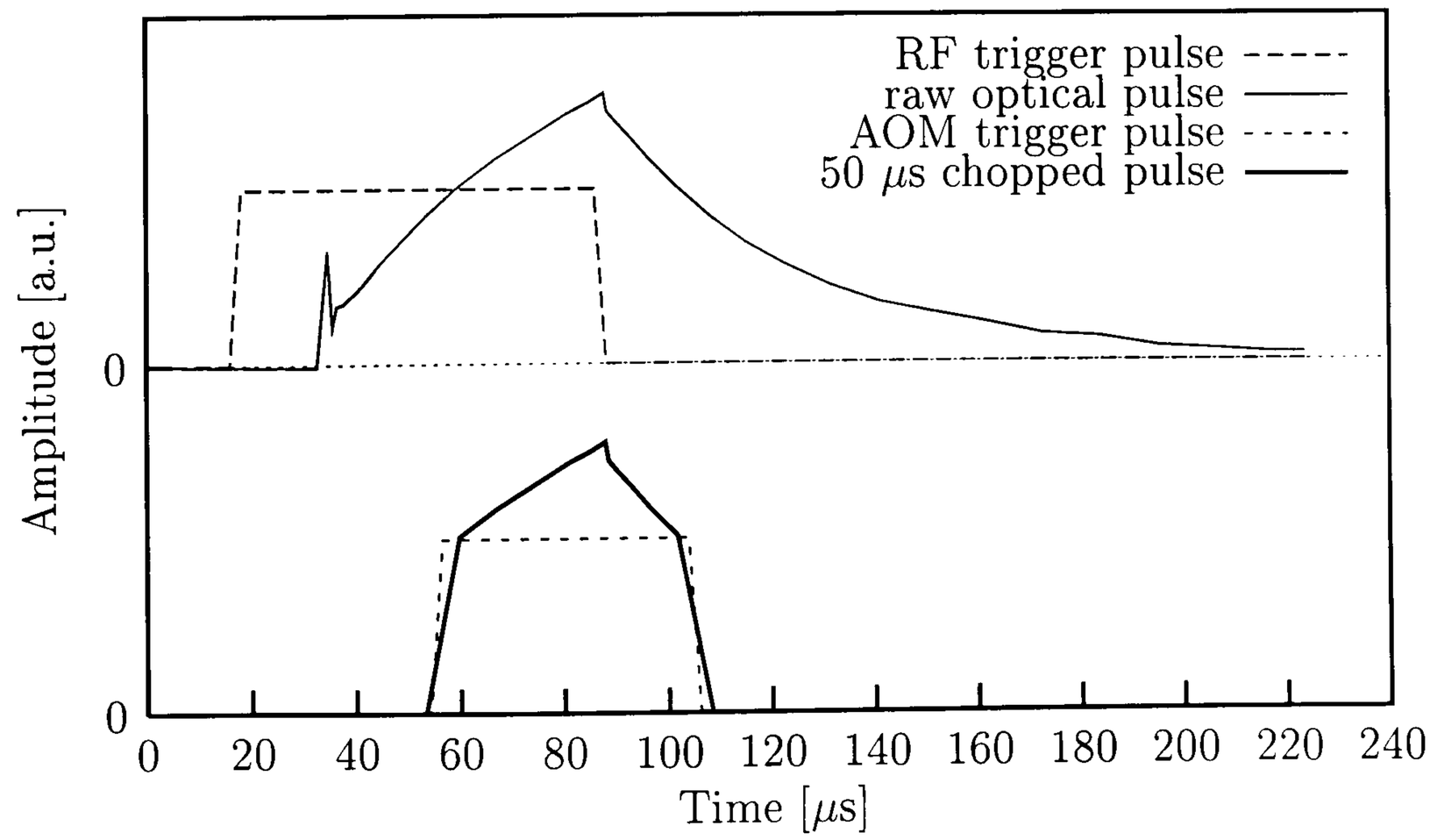

Figure 3.5: Shaping of a raw, triangular laser pulse into quasi-square one by AOM.

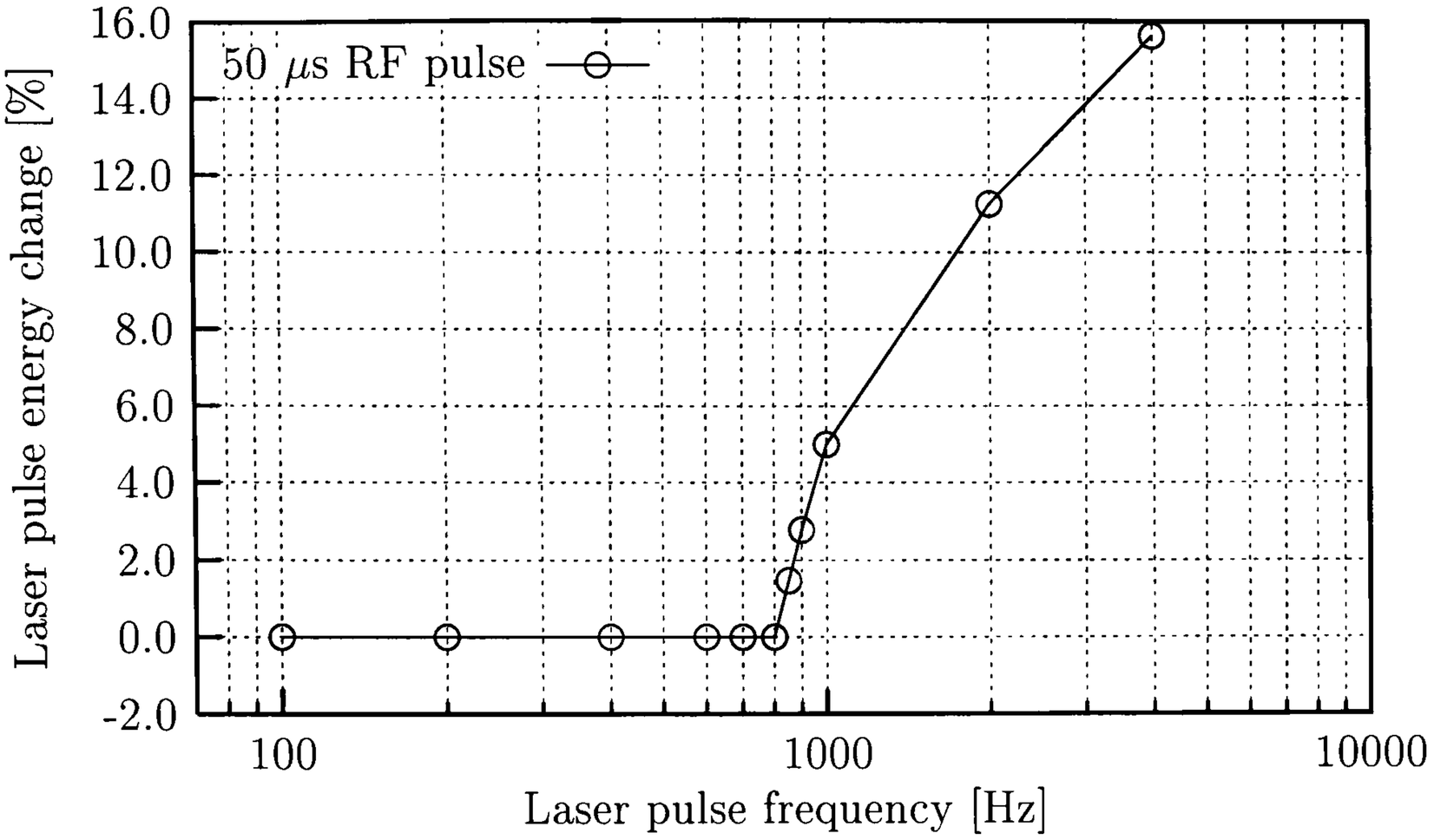

Figure 3.6: Pulse energy dependence on pulse repetition rate.

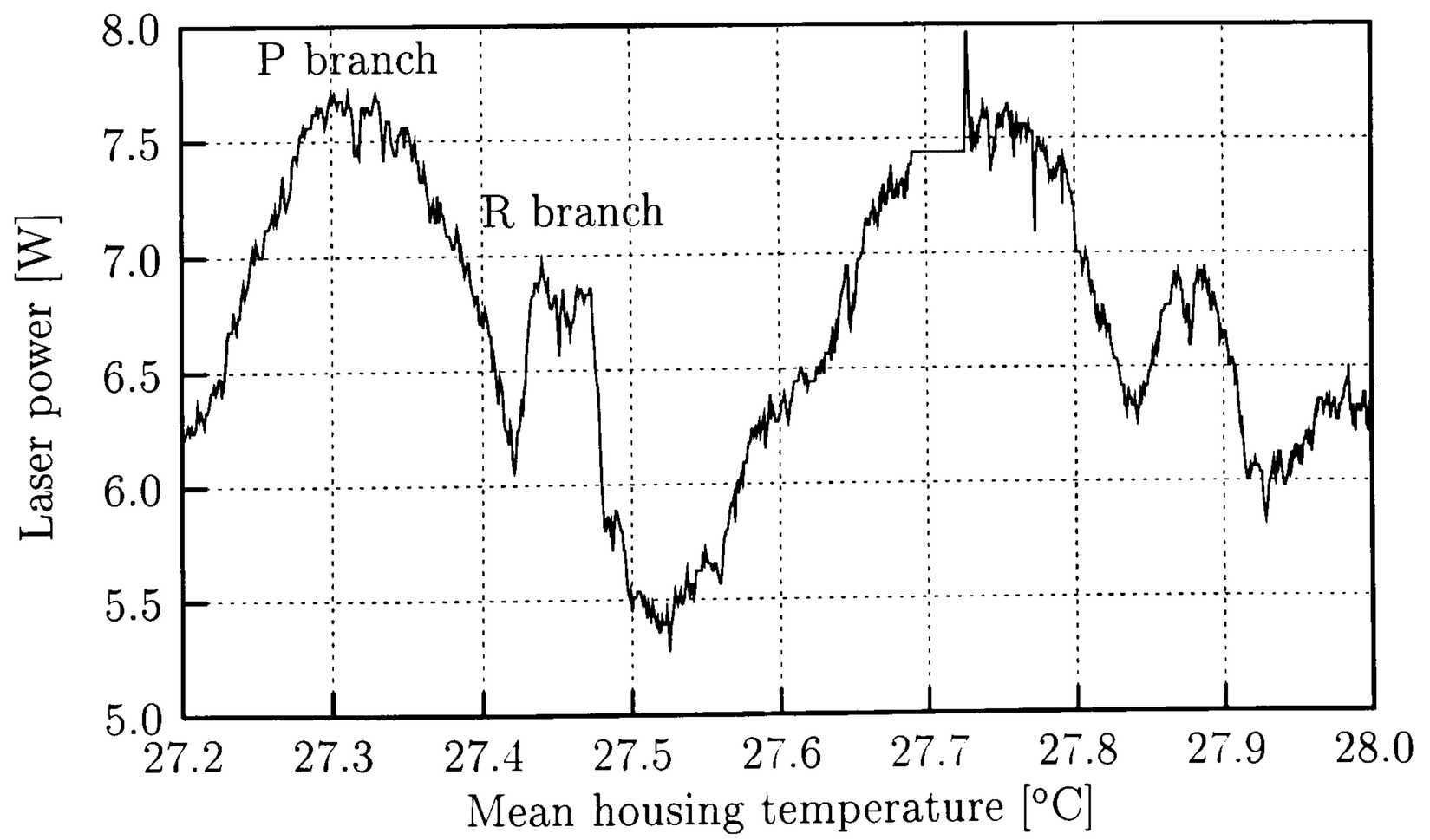

Figure 3.7: Laser power versus mean housing temperature.

ity, caused by temperature variations of laser housing. Multi-point measurements of housing temperature have been carried out to assess the extent of thermal sensitivity of laser power. A significant variation of maximum 16% (see Figure 3.7) occurred in a small temperature interval of ~0.5 °C. Additionally, laser line hopping caused changes in a spot position, due to a presence of acousto-optical modulator acting as a diffraction grating. The variation of power was bad enough, the uncontrolled modulation of spot position in order of tens of microns was unacceptable. The laser needed to be thermally stabilised.

3.3.1 Thermal sensitivity of a resonator

An aluminum tube housing is a characteristic feature of many commercial slab waveguide CO_2 lasers. The resonator mirrors are attached to the flanges in the ends of the tube. Thermal expansion of tube by $\lambda/2$ changes the length of resonator by the same amount, causing a full laser signature scan, where λ is a laser wavelength. The experimental data (Figure 3.7) have confirmed that the laser scanned the whole signature with mean housing temperature change $\Delta\overline{T}_h \approx 0.44$ °C, according to the equation below:

$$\Delta\overline{T}_h = \frac{\lambda}{2}\,\frac{1}{L\ k_{Al}}$$

$$L = 0.5\ \text{m}$$

$$k_{Al} = 24\ \mu\text{m K}^{-1}\ \text{m}^{-1}$$

$$\lambda = 10.6\ \mu\text{m}$$

where L stands for the resonator length and k_{Al} is an expansion coefficient of aluminum. The experiment has also shown that $\Delta\overline{T}_h$ stability <0.04 °C for the laser of that length is required to prohibit line hopping and to assure power stability $< \pm 1\%$

3.3.2 Distributed mean temperature sensing

Mean temperature of laser housing $\overline{T}_h$ influences the resonator length, thus a distributed sensor is necessary to measure that temperature directly. There are many possible implementations of the idea, starting from a metallic wire that can be wound around the object under measurement, multiple temperature to current sen-

sors connected in parallel, many semiconductor diodes connected in series, ending on NTC thermistors connected in series. The last option is of most importance for it is very easy to implement and offers high sensitivity, typically 4%/°C. High nonlinearity of thermistors is not a problem after all, since the sensor is intended to work in a very small temperature range, couple of degrees Celsius. Moreover, most of available integrated temperature controllers, such as Hytek HY5650 [55], accommodate NTC thermistor as a temperature sensor.

The number and distribution of measurement points influence the sensor performance. High quantity of such points ensures the accurate estimation of $\overline{T}_h$, but for practical reasons this number can be limited. Propagation velocity of thermal front ν_p and thermal time constant τ_d of single thermistor (both can be measured) determine the practical maximum distance between measurement points d_{max}:

$$d_{max} = \nu_p \cdot \tau_d$$

It is important to choose sensors with reasonably small thermal time constant to obtain fastest response, smallest transient errors and optimal distance between the individual sensors.

3.3.3 Development of high accuracy temperature stabiliser

I have designed and developed a high accuracy temperature stabilising system that significantly reduced the impact of housing temperature change on laser stability. Figure 3.8 depicts the important blocks of device. The first stage of temperature stabiliser consisted of commercial, recirculating chiller, model M-33 manufactured by ThermoNeslab, which assured the temperature stability of liquid better than 0.1°C. Heat removal capacity was sufficiently higher than the maximum anticipated power dissipation in the laser electrodes. The chiller also effectively diminished the strength of thermal coupling between the laser electrodes and the housing.

Second stage of the stabiliser comprised of custom design, precision temperature controller, based on the integrated temperature controller HY5650, capable of 0.01°C stability. The controller was designed to operate in a heating regime for simplicity sake. A heating cable (50W max) was wound around the tube to supply it with a right amount of heating power under controller's command. The chilling power, necessary to maintain thermal equilibrium, was provided by a steady state heat flow from the tube toward the terminal flange, being in good thermal contact

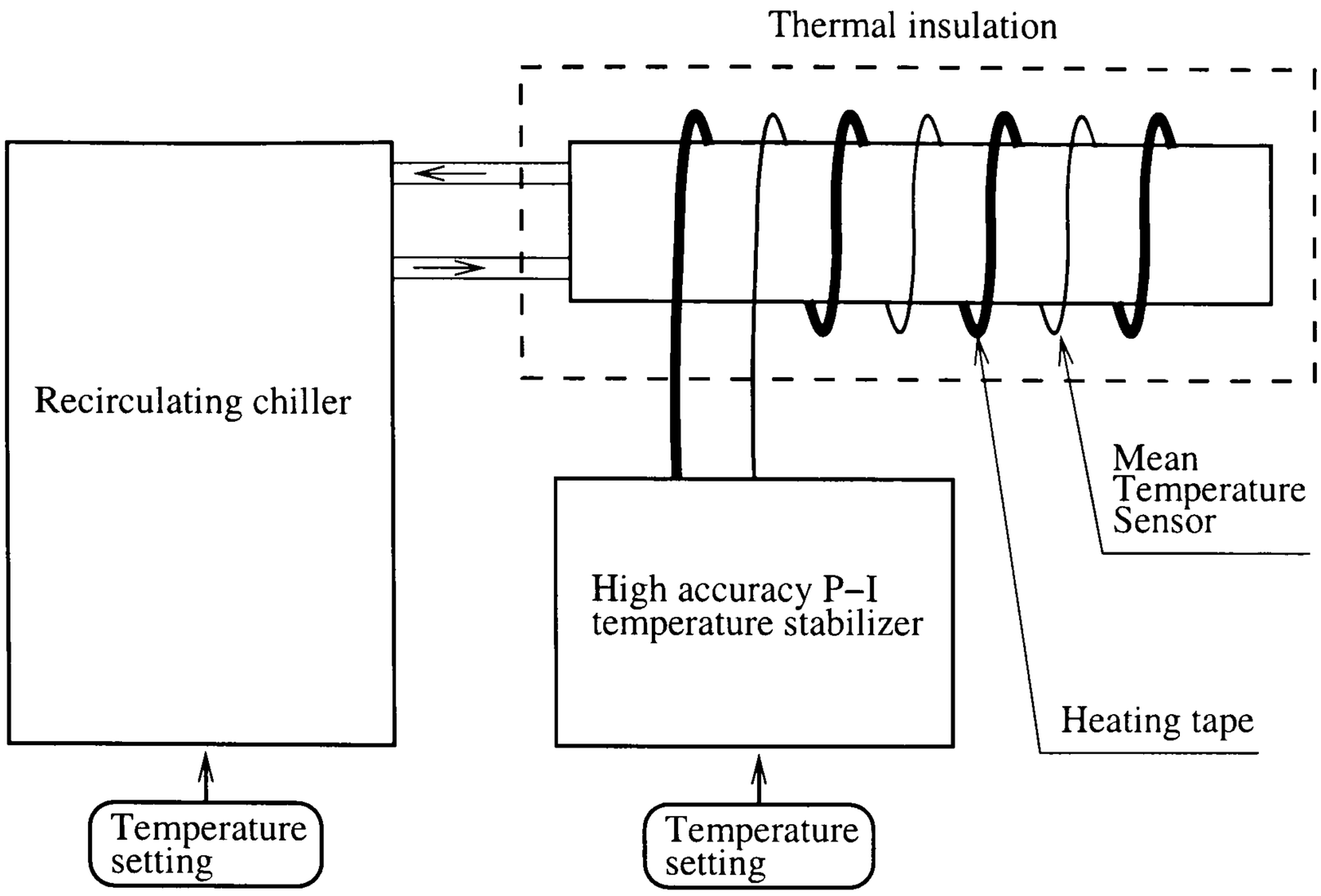

Figure 3.8: Block diagram of laser temperature stabiliser.

with a chilling liquid. It was achieved by setting the chiller temperature lower than the target mean tube temperature. The amount of heat flowing could be easily adjusted by chiller temperature setting to keep the controller in the middle of output range. The whole laser was thermally insulated to prevent the ambient temperature fluctuations from disturbing the controller balance.

The stability experiments, carried out to assess the performance of stabilising system, have yielded 24 hour power stability better than ±1% provided the ambient temperature did not change more than ±4°C. Spectral line selection was possible by the controller temperature setting. Short term power stability of the system (15 min after laser start) depended on the laser duty cycle and was better than ±2% for duty cycle up to 15%.

3.4 Flexible direct laser machining software

This section describes the software I've developed to implement the idea of flexible machining system, which aimed at rapid prototyping of arbitrary surface shapes in a raster scan regime with overlapping craters. I've divided the task of writing surface shapes into several stages, as shown in Figure 3.9:

- Conversion of input surface shape data into a raster of crater locations, know-

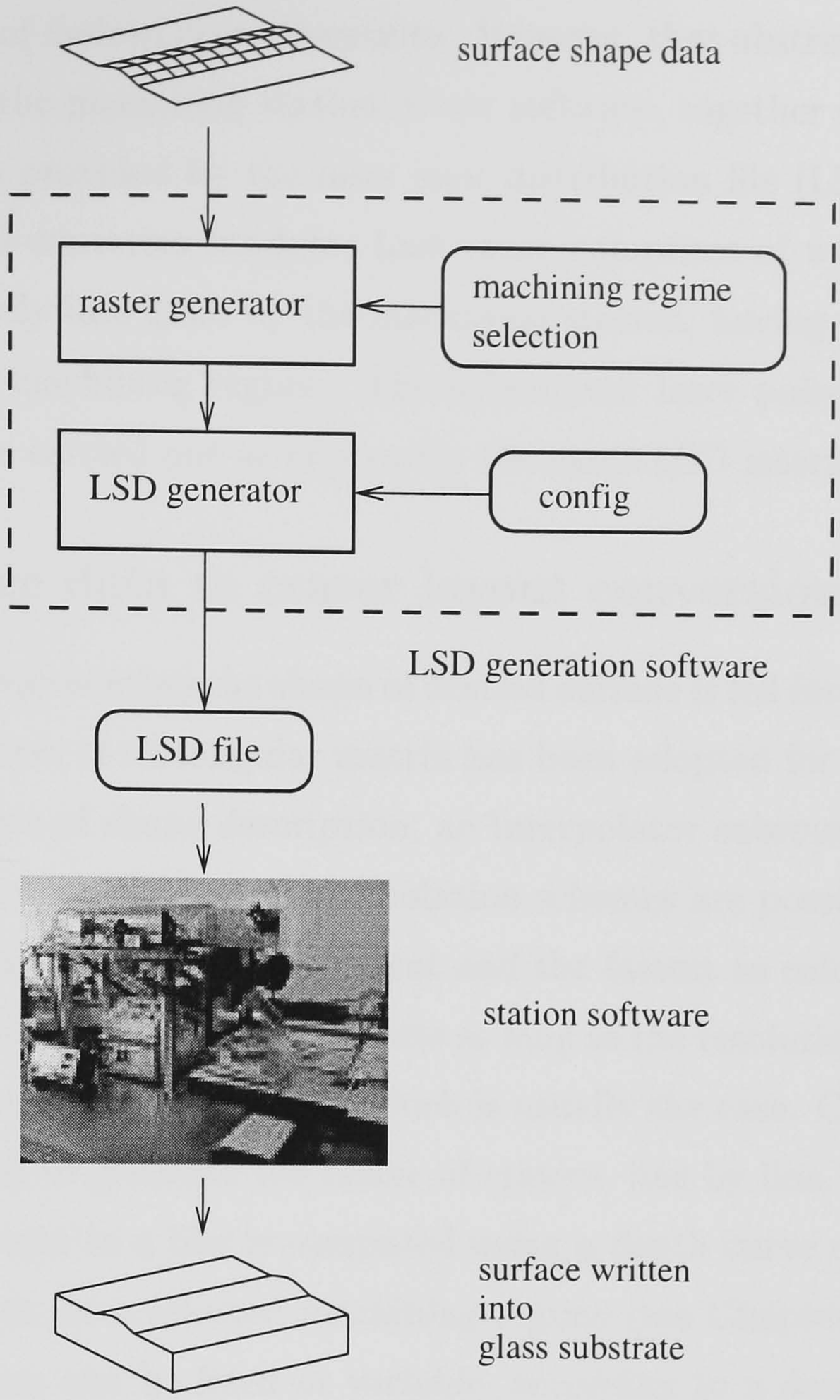

Figure 3.9: Block schematic of system software.

ing the overlapped material removal characteristics, see Chapter 5.

- Generation of laser spot distribution file (LSD), to provide a link between the calculated crater layout and the machining station
- Writing the craters at the locations prescribed in the LSD file

Designed surface data has to be converted it into a raster of laser spots that would reproduce the desired surface shape. This is achieved by calculating the spacing between craters, line by line, knowing the material removal dependence on the crater distribution, called a machining regime. The study on machining regimes is presented in Chapter 5. The process is independent from hardware peculiarities and requires the knowledge of input data and the characteristics of machining regime to

generate a raster of desired crater locations. However, that abstract raster of craters must be fed into the machining station driver software, together with configuration data. The link is provided by the laser spot distribution file (LSD), generated by the raster to LSD converter module. Last stage comprises of writing of that spot distribution directly into glass by the machining station, having set the laser pulse energy of chosen machining regime. The subsequent laser polishing, described in Chapter 6, can be carried out using exactly the same LSD interface.

3.4.1 Surface data to crater layout conversion

The input data, representing the shape of desired surface is fed into the raster generator module. A form of rectangular matrix has been adopted for convenience. Due to a discrete nature of shape description, an interpolator subroutine adds continuity to the surface data. Different interpolation schemes are possible. Quad-planar interpolation is the simplest to implement and the fastest to calculate. The quad-planar interpolation gives very good results as long as the resolution of shape matrix is kept smaller or equal to crater size, which is usually the case. Continuous surface data are then used to generate the raster of craters, line by line. The actual spacing of adjacent crater in a line is computed using a depth curve obtained from the calibration surfaces for a selected machining regime (see Chapter 5). The spacing between raster lines can be fixed or variable, according to a demand for depth of machining. This parameter has been fixed throughout the experiments.

The generated raster needs an encapsulation in a format understood by the driver software that controls the machining station. The conversion into the LSD format is a job of LSD generator module. LSD file defines the position of raster scan lines and their content. Each raster line section contains a number of prescribed laser firing positions. Configuration parameters, such as translation speed, axes acceleration, positioning tolerance and more, can also be specified globally or for individual line. The LSD generator module has a knowledge of machining system limitations, such as pulse repetition frequency limit, resolution of traveling stages, dimension units, resolution division factor, et cetera, to be able to determine whether the settings specified can be actually executed by the machining station.

I've chosen a structured text format for LSD file to keep the project flexible, since the works on the hardware and software development were being carried out in parallel and new features were constantly being added to the specification of

the LSD file. The binary format would be definitely more disk-space efficient, but it was not a concern after all. The software described has been written in Scilab environment, available on General Public License agreement from INRIA Group [56] for many platforms, including Microsoft Windows.

3.4.2 Driver software

The driver programme was very important for the success of the system. It was responsible for an accurate placement of laser spots under the prescription contained in LSD format. Simple example of working LSD file is shown in Figure 3.11. The structure of software is shown in Figure 3.10. A simplified description of operations, carried out by the driver programme under the command of LSD file, is supplied below.

On startup, the configuration parameters are extracted from LSD file by a parser module. The hardware parameters are set, ie motion controller PID filter parameters, motion parameters of traveling axes, etc. After the setup the driver enters a printing loop that lasts until the last line is written. The stage module provides a command interface between the main body of driver program and the traveling axes. The interface between the stage module and the motion controller card installed in the computer (C-482 chip based, manufactured by PMD) has been delivered by the C libraries supplied with the traveling stages by the manufacturer.

Line printing consists of monitoring the instantaneous position of axis 1 (X direction) and comparing it real-time with a position register containing the coordinate of next laser spot in the current raster line. The driver knows the exact, momentary position of active axis thanks to the programming technique assuring high speed link between the encoder and the software position register. Parallel printer port gives a direct access to the interrupt system of PC, most powerful instrument of processor control. The digital output of optical encoder, producing a pulse per 100 nm of translation, triggers the parallel port interrupt to update the software position register, thanks to a custom interrupt handling routine. The update, which takes less than 5 μs to complete, is very fast in comparison to straight forward technique of polling the motion controller's position register, which takes milliseconds.

This approach allows for full synchronisation in a speed range 0-15 mm/s at maximum resolution, 0-30 mm/s and 0-60 mm/s when resolution division by factor of 2 and 4 is carried out electronically by resolution divider. In case when the maxi-

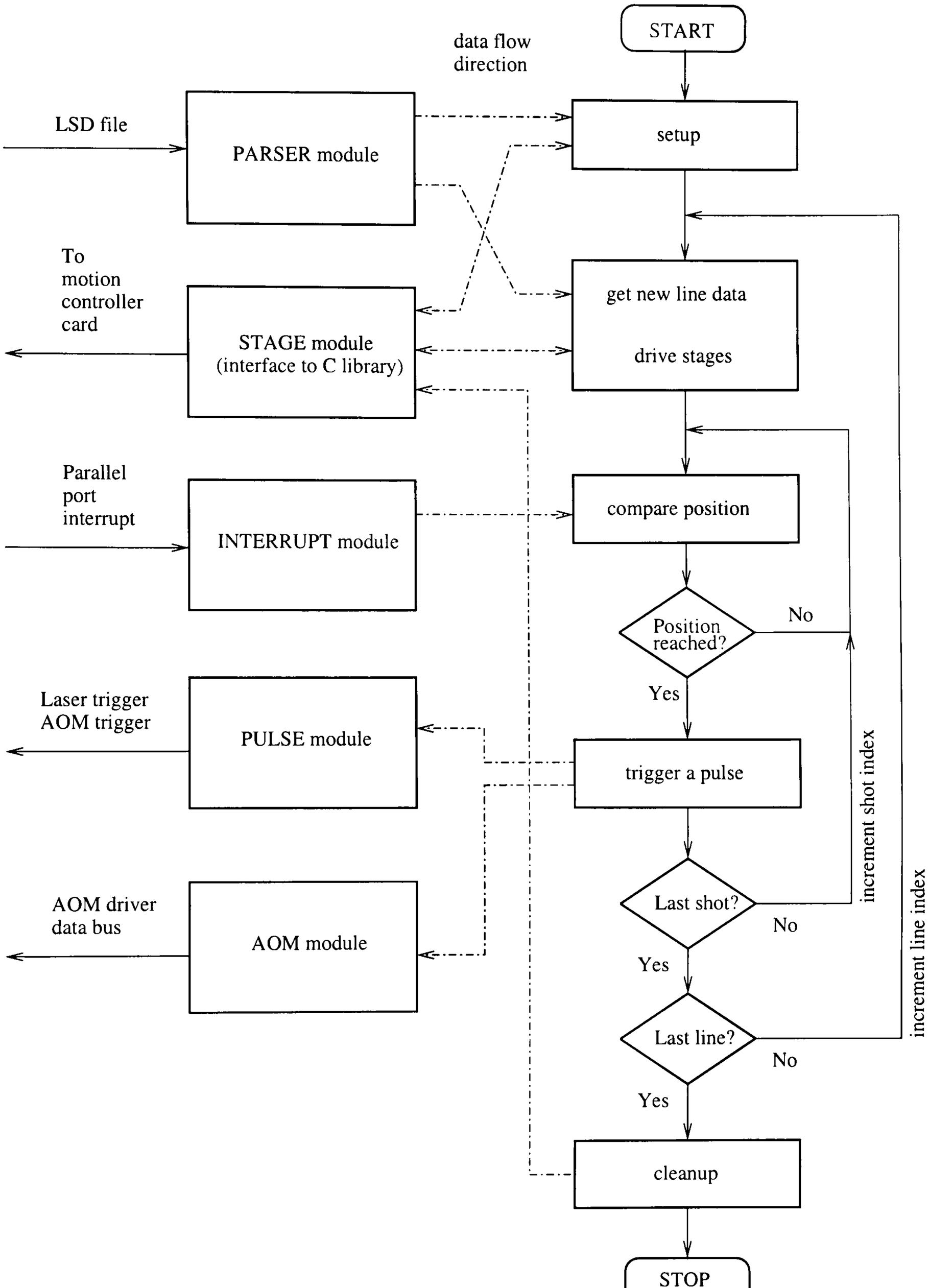

Figure 3.10: Block schematic of driver programme. The STAGE module incorporated the library of function calls, provided by the manufacturer, needed to communicate with motion controller card.

```
default              ;default machine setup section
speed=200000         ;default translation speed of the raster line (X direction) (steps per sec)
ret_speed=400000     ;return speed for raster line (unidirectional cutting only) (steps per sec)
runway=40000         ;runway required for speed build-up and stabilisation (steps)
t_l=40               ;default laser pulse duration produced on every occurence of "pos" keyword
aom=1                ;produce AOM pulses on every occurence of "pos" by default
single=1             ;enable unidirectional cutting (bidir disabled)
scale_pos=10         ;scaling factor for axis 1 (X direction) (steps per micron)
scale_line=10        ;scaling factor for axis 2 (Y direction) (steps per micron)
pos_err_1=30         ;allowable position error of axis 1 (X direction) (steps)
pos_err_2=1          ;allowable position error of axis 2 (Y direction) (steps)
pos_err_3=3          ;allowable position error of axis 3 (Z direction, lens) (steps)
res_div=1            ;resolution division setting (must match hardware setting)
enddefault

;raster section, numbers in microns

line=0 pos=0 pos=750 pos=1500 endline
line=250 pos=0 pos=125 pos=750 pos=1250 endline
line=500 pos=0 pos=250 pos=750 pos=1000 endline
line=750 pos=0 pos=375 pos=750 pos=1125 endline
line=1000 pos=0 pos=500 pos=750 pos=1250 endline
line=1250 pos=0 pos=625 pos=750 pos=1375 endline
line=1500 pos=0 pos=750 pos=1500 endline
```

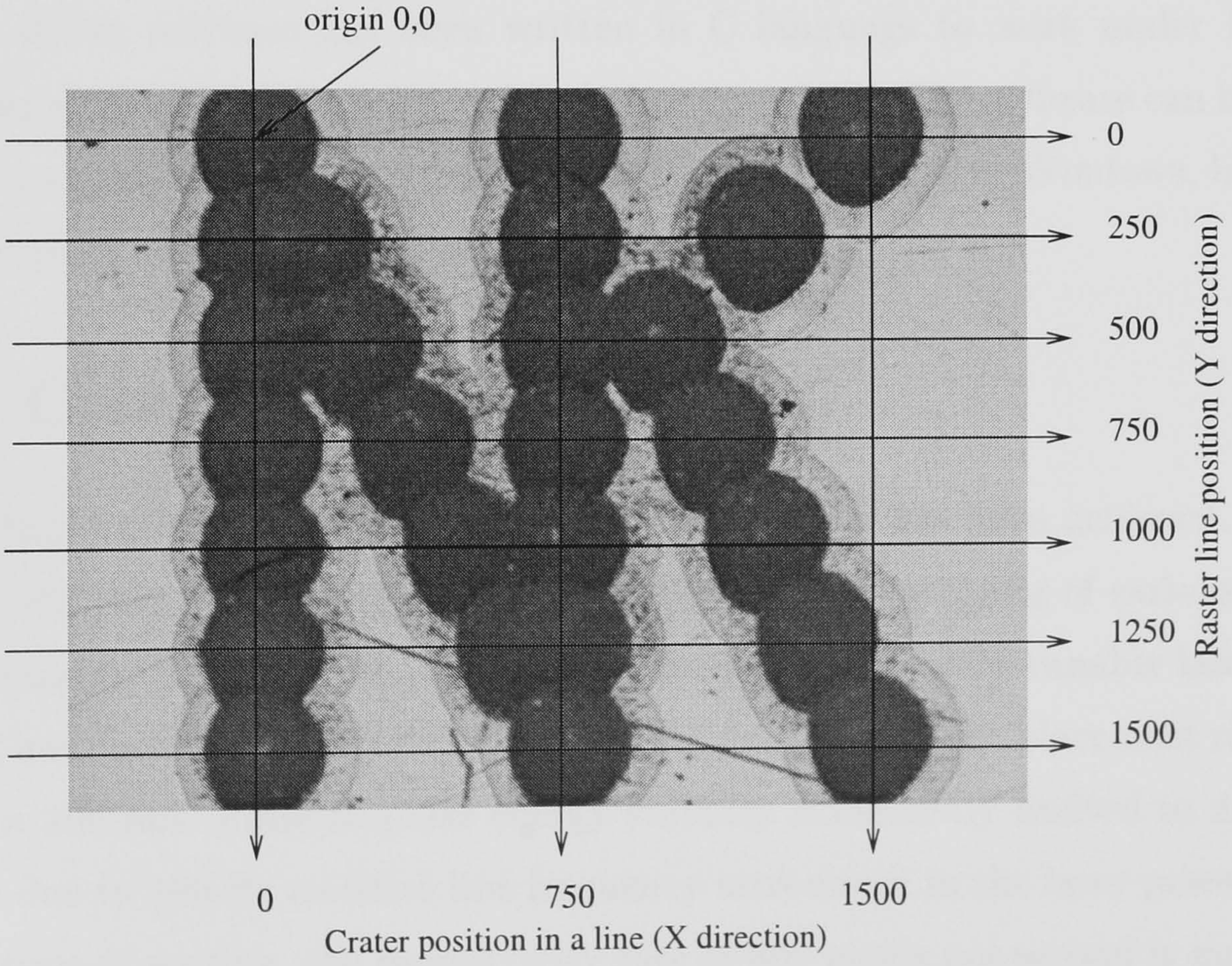

Figure 3.11: Contents of simple LSD file describing the crater layout needed to print author's initials. On the photograph below, the actual pattern printed in Perspex. Crater diameter ~300 μm. Dimensions in μm.

mum resolution and high >60 mm/s translation speeds are required, the resolution reduction can be avoided by using the AOM to finely position the spot under computer control with resolution better than 0.05 μm. This technique can then provide accurate synchronisation between laser spot and the instantaneous position of laser spot in a wide range of translation speeds.

The software register is used to quickly determine, in a timescale of half a microsecond, whether the new shooting position has been reached. When the position is reached, the driver triggers the software pulse module or external pulse generator, as needed. The system can directly control the acousto-optic modulator frequency over the digital interface, allowing for additional fine laser spot positioning. The monitoring of spot position continues until the last crater in the line has been written. After that the new line is read from the file by the parser module and the axis 2 (Y direction) is positioned with an acceptable error prescribed in LSD file. The procedure of monitoring the current spot position in the new line is then repeated until all raster lines are written.

The driver software has been written in C language to work under MS-DOS operating system, for simplicity and real-time operation. The software can be ported to modern multitasking operating systems, such us Linux and Windows, but it is a separate programming project on its own.

3.5 Conclusions

The objective of building the flexible machining center has been achieved. The developed software interface has enabled flexible rapid-prototyping of various kinds of continuous-profile structures. The station operated spectrally tunable laser source with 24 hour power stability better than $\pm 1\%$ and offered spot placement resolution of 100 $\times$ 100 nm. Pulse-to-pulse energy stability is currently limited to $\pm 2\%$ fluctuation due to 100 Hz rectified line frequency introduced in the laser power supply. At the time of writing, the productivity rate of 800 pixels per second is guaranteed with the above stability. An improvement of the productivity by factor of three can be expected when the laser pulse energy is controlled better than $\pm 1\%$ at all allowed pulse repetition frequencies. It can be achieved by developing an AOM-based pulse energy dispenser. This technical difficulty must be overcome before the station can fully exploit its currently dormant potential of >2000 pixels per second.

Chapter 4

MACHINING OF SILICA WITH CO_2 LASER

4.1 Introduction

A goal of this chapter is to present a detailed study of material removal dynamics and to verify the applicability of CO_2 laser ablation of silica for precision machining of refractive micro-optical elements (ROE). A need for the study was prompted by a lack of reliable, detailed data necessary to identify the optimal conditions for production of ablation craters. The knowledge was needed for the rapid prototyping regimes, studied in Chapter 5. The study of ablation involved determining the ablation threshold, material removal rates, crater topography and the role of laser pulse duration, irradiance level and laser spot size. This chapter addresses the issues that are important from a viewpoint of precision machining, such as the accuracy and repeatability of material removal, the sensitivity of ablation characteristics to the laser wavelength, the extent of melt displacement and the following surface quality.

There is a number of issues that makes CO_2 ablation of silica attractive for rapid manufacturing of micro-optics. Strong optical absorption in 8-11 μm band and exceptional smoothness of ablated surfaces (see Section 4.7) are the factors rendering the CO_2 laser the best suited ROE fabrication tool amongst the lasers mentioned so far (see Section 2.5 p.54). High rates of material removal per pulse, an order of magnitude greater than in case of UV and ultrafast laser ablation of silica [4], allow for rapid machining of structures deeper than 10 μm. CO_2 lasers can be operated at high pulse repetition frequencies up to tens of kHz, which yield high

material removal rates 1-10 μl/h, comparable with a performance of other capable methods (see Section 5.2) such as ink-jet printing of polymers. In the end, CO_2 lasers are by far the most practical devices operating in a range of wavelengths corresponding to infrared optical absorption of glasses, with respect to low cost of ownership, low cost of operation and available output power.

4.2 Experimental methods

An experimental technique, which facilitates reliable, repeatable and accurate measurements of the ablation craters, has been developed for the study on CO_2 laser ablation, presented in this chapter. A usual difficulty one faces when dealing with measurements of ablation characteristics is a need for accurate profiling of ablation craters, preferably with sub-micron accuracy. This can be done by atomic force microscopy (AFM), which is accurate down to a fraction of nanometer. Although very accurate, it was too slow and too unreliable (problems associated with tip contamination, sample positioning etc.) to be of practical importance when a vast number of craters had to be characterised. DekTak^{TM} stylus profiler has proved itself to be a better suited tool for quick and reliable data acquisition. It was accurate down to 10 nm and did not suffer, like AFM, from the contamination problem. A radius of stylus tip was only 2.5 μm, an order of magnitude smaller than the smallest crater produced in a course of experiments. The tip size practically did not affect the profile measurements.

The machining system, described in Chapter 3, was used throughout the experiments to deliver stable laser power in a selected spectral line of CO_2 laser. A wide range of laser pulse durations 10$-$300 μs has been used. AOM has been used to shape raw laser pulses into quasi-rectangular in time domain (see Section 3.5 p.69), since rectangular pulses have been found to be advantageous over pulses of any other shape with respect to the machining threshold.

An accurate control over the crater position, provided by the machining facility, allowed for writing of craters arrays. A number of linear arrays of evenly spaced craters, each array corresponding to particular pulse settings of interest, was ablated in a silica sample and subsequently characterised.

A difficulty associated with stylus positioning could be overcome by exploiting the crater repeatability in each array. The whole line of many identical and evenly

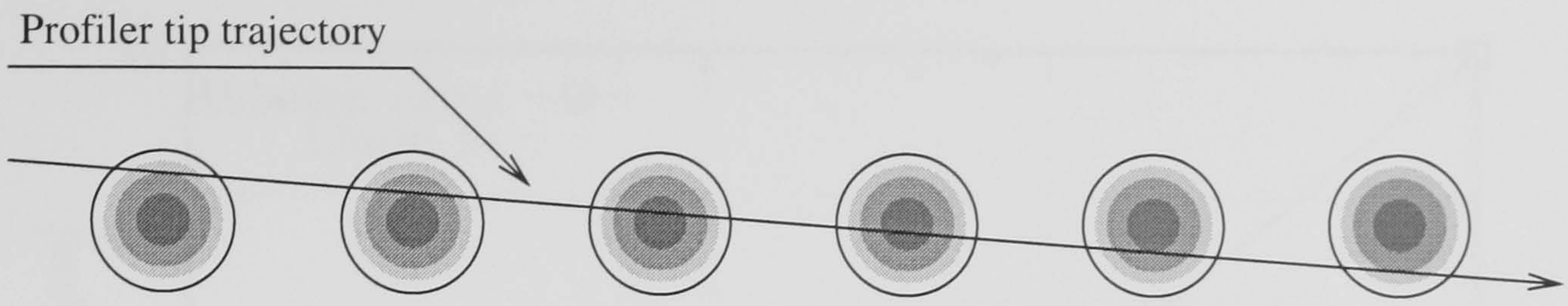

Figure 4.1: Illustration of crater profiling method using a stylus profiler.

spaced craters was scanned at a very small inclination angle (see Figure 4.1), thus producing a kind of tomographic record of single crater. The amplitude of peaks in this record, corresponding to a depth of slice, was modulated by an envelope of axial crater profile. The true depth could be then easily found by fitting the peaks with appropriate fitting function. A choice of fitting function was not critical, since a rate of change of envelope was small due to a small inclination angle of the scan. Gaussian fitting function, being the closest resemblance of crater shape, was used to find the depth of ablated craters.

4.3 Ablation curves

Many craters, produced with different laser pulse settings within the machining window of silica (see Figure 2.18 p.62), have been characterised. All the measurements of crater depth versus axial fluence have yielded the machining curves of characteristic shape, which is shown in Figure 4.2. The curves consisted of three main sections, a neutral section I (no material removal), a nonlinear section of ablation onset II and a linear part of constant gradient III.

In real circumstances, a change in the crater geometry towards deep craters frustrated the ablation [4] due to internal reflections occurring on crater walls inclined more than 45° with respect to a surface of a silica sample. Such angle corresponds to 0.5 depth-to-crater ratio, which has been taken as a limit for an allowable crater aspect ratio. The ablation curves have thus been characterised only up to $\sim$10 μm of crater depth at spot diameter 47 μm to avoid the effect.

The shape of obtained curves does not follow the logarithmic dependence known

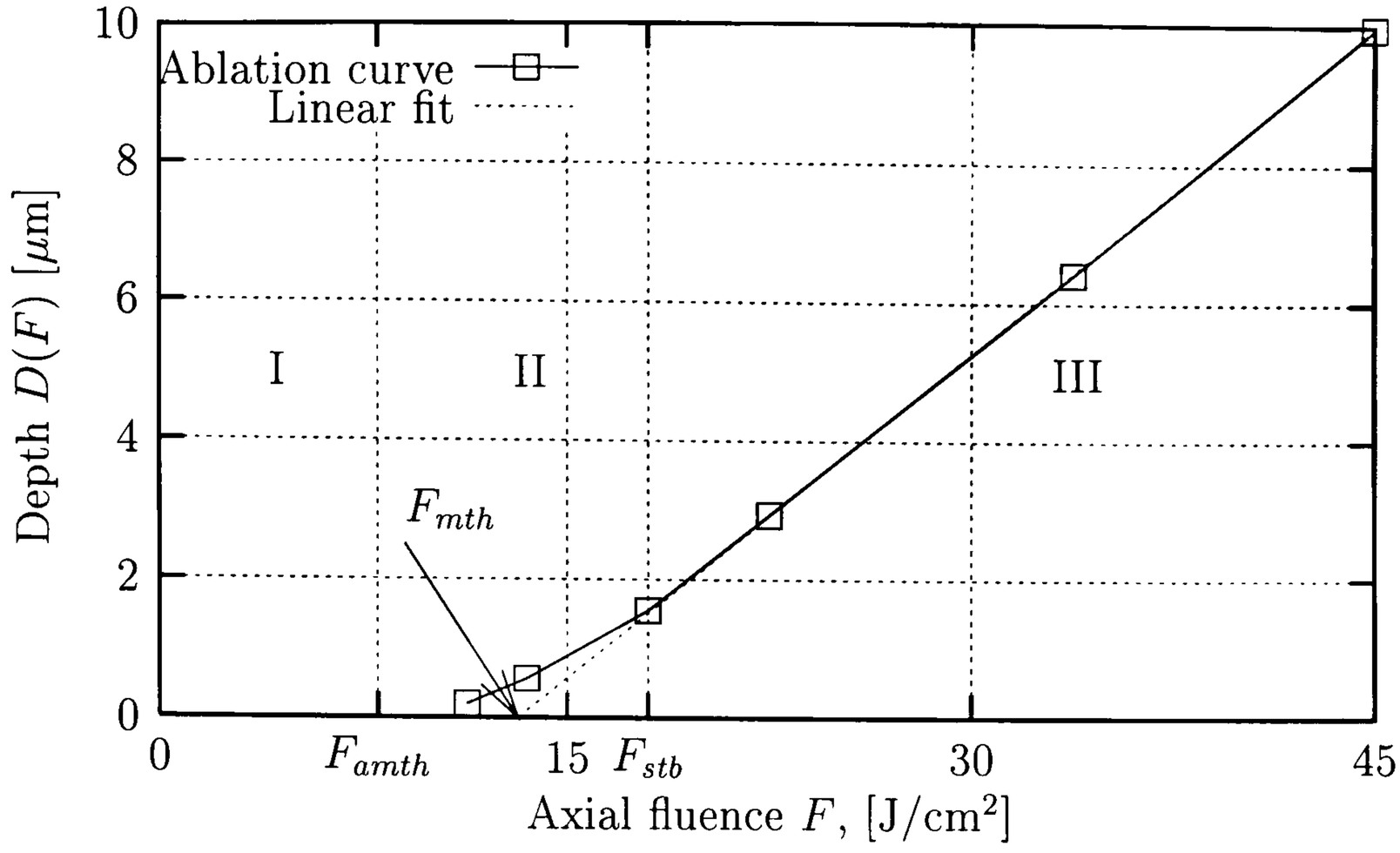

Figure 4.2: Crater depth versus axial fluence, pulse duration 50 μs, spot diameter 47 μm, laser line P-14. Typical ablation curve.

from previous studies on UV ablation of polymers [57, 58]:

$$D_{UV} = \frac{1}{\alpha} \ln \left(\frac{F}{F_{mth}} \right) \tag{4.1}$$

where α is the absorption coefficient, F is a pulse fluence and F_{mth} is a machining threshold fluence. Striking linearity of ablation curves and an absence of incubation suggest different mechanisms responsible for the material removal in comparison to UV ablation of polymers. In case of CO_2 ablation of silica at ~0.5-1 MW/cm^2, the material is removed in a smooth, non-explosive, evaporative regime, as discussed in Section 2.5.3 p.56. It resembles the *quasi-stationary vaporisation regime*, in which the laser energy is spent for heating up the material and delivering the latent heat of vaporisation into the superheated layer of the material [59], according to Formula 4.2:

$$I_o(1 - R) = \nu_F \, \rho \, (C_{sp} \, \Delta T + L_H) \tag{4.2}$$

where I_o stands for an irradiance incident onto the sample, the reflectance R, surface recession velocity ν_F, density ρ, heat capacity C_{sp} and latent heat of evaporation L_H. Although this description fits the substances that have sharply defined melting point, such as metals, it is shown in Sections 4.5 and 4.7 that with little modification the quasi-stationary vaporisation it can be used to describe CO_2 ablation of silica.

The transition points I-II and II-III can be expressed mathematically in terms

of threshold values of fluence:

$$\begin{aligned} 0 < F \leq F_{amth} \quad &: \quad D(F) = 0 \,, \quad \frac{dD(F)}{dF} = 0 \\ F_{amth} < F \leq F_{stb} \quad &: \quad D(F) > 0 \,, \quad \frac{d^2D(F)}{dF^2} > 0 \\ F > F_{stb} \quad &: \quad D(F) > 0 \,, \quad \frac{d^2D(F)}{dF^2} = 0 \end{aligned} \tag{4.3}$$

where F_{amth} and F_{stb} are the adiabatic ablation threshold and stabilisation threshold accordingly. A rate of material removal can be then defined as:

$$F_{stb} < F < F_{nonlin} \quad : \quad R_m = \frac{dD(F)}{dF} \tag{4.4}$$

Only one parameter from above three can be derived from the experimental data with an acceptable accuracy, the material removal rate R_m, a slope of linear part of the curve. Section 4.5 links R_m with material constants. An estimation of depth of highly mobile layer of superheated glass, based on the measured R_m, is carried out in Section 4.7.

An artificial parameter, a machining threshold F_{mth} obtained numerically by extrapolation of linear section III (see Figure 4.2), was introduced to facilitate simple linear approximation of ablation curve. All subsequent references to the "machining threshold" are made with respect to that artificial parameter.

4.4 Measurements of machining threshold

Laser pulse duration, spot size and radiation wavelength were the parameters of ablation curves, obtained in a series of experiments designed to explore the characteristics of CO_2 laser machining of fused silica. The machining threshold versus these parameters is studied in this Section. A first wave of experiments was conducted using early version of machining system, which was not yet equipped with the precision temperature stabiliser. The system suffered from $\pm 4\%$ short term power variation, as a consequence of thermal instability of the chiller. Although the output power was badly modulated, the spectral stability was unaffected during the experiments. In spite of these technical difficulties, the agreement between early and later experiments was very good.

4.4.1 Irradiance threshold of ablation

A state of ablative material removal can be maintained only when a rate of energy deposition in a thin surface layer exceeds the rate of heat dissipation by thermal conduction and radiation. Following this reasoning, an irradiance threshold I_{th} must exist, below which the ablation cannot build up. The influence of radiative heat loss in the irradiated zone can be usually neglected, since the radiation flux at temperature range 1000-3000 °C (evaporation temperature of many materials) is sufficiently smaller than the laser irradiance. The heat flux required to activate the ablation is a function of thermal properties of material, a rate of energy deposition and a geometry of interaction zone.

A calculation of I_{th} for fused silica and its experimental verification has been carried out by Markillie *et al.* [4]. The threshold irradiance has been calculated for a semi-infinite slab of silica with thermal conductivity k, thermal diffusivity K and absorption coefficient α, irradiated by a Gaussian source with spot size ω:

$$I_{th} = \frac{2\ k\ T_o}{(1-R)} \left[\int_0^{2\sqrt{K\ t}} \exp\left(\frac{\alpha^2\beta^2}{4}\right) \mathrm{erfc}\left(\frac{\alpha\beta}{2}\right) \alpha\beta \left(1 + \frac{2\beta^2}{\omega^2}\right)^{-1} d\beta \right]^{-1} \tag{4.5}$$

The entity $\beta = 2\sqrt{K\ t'}$, where t' is a time variable during the laser pulse. The values of material constants have been quoted at 1400 °C, since the silica parameters vary significantly with temperature. The value of threshold surface temperature T_o was found from the vapour pressure data [48] to be 2700 °C. Figure 2.18 (p.62) compares the experiment [4] with calculations using Equation 4.5. Good agreement between the experiment and simple model has been found.

It has been concluded in [4] that in case of CO_2 laser ablation of silica one deals with a region of heating intermediate to a surface heating (depth of heat affected zone (HAZ) governed by heat conduction, characteristic depth $2\sqrt{K\ t}$) for long laser pulses >100 μs and a volume heating (depth of HAZ determined by α^{-1}) for short pulses. For a good control over ablation it is then beneficial to use short laser pulses of possibly highest irradiance to minimize the radial heat flow from the melt zone. There is, however, a limit imposed on the maximum value of irradiance, as shown in Figure 2.18, due to a vapour pressure driven violent melt ejection process [4].

The melt ejection is an undesired effect because it reduces the control over material removal. The studies, carried out in the remaining part of chapter, used pulses of irradiance not exceeding 1.2 MW/cm^2 to avoid melt expulsion. Section 4.9

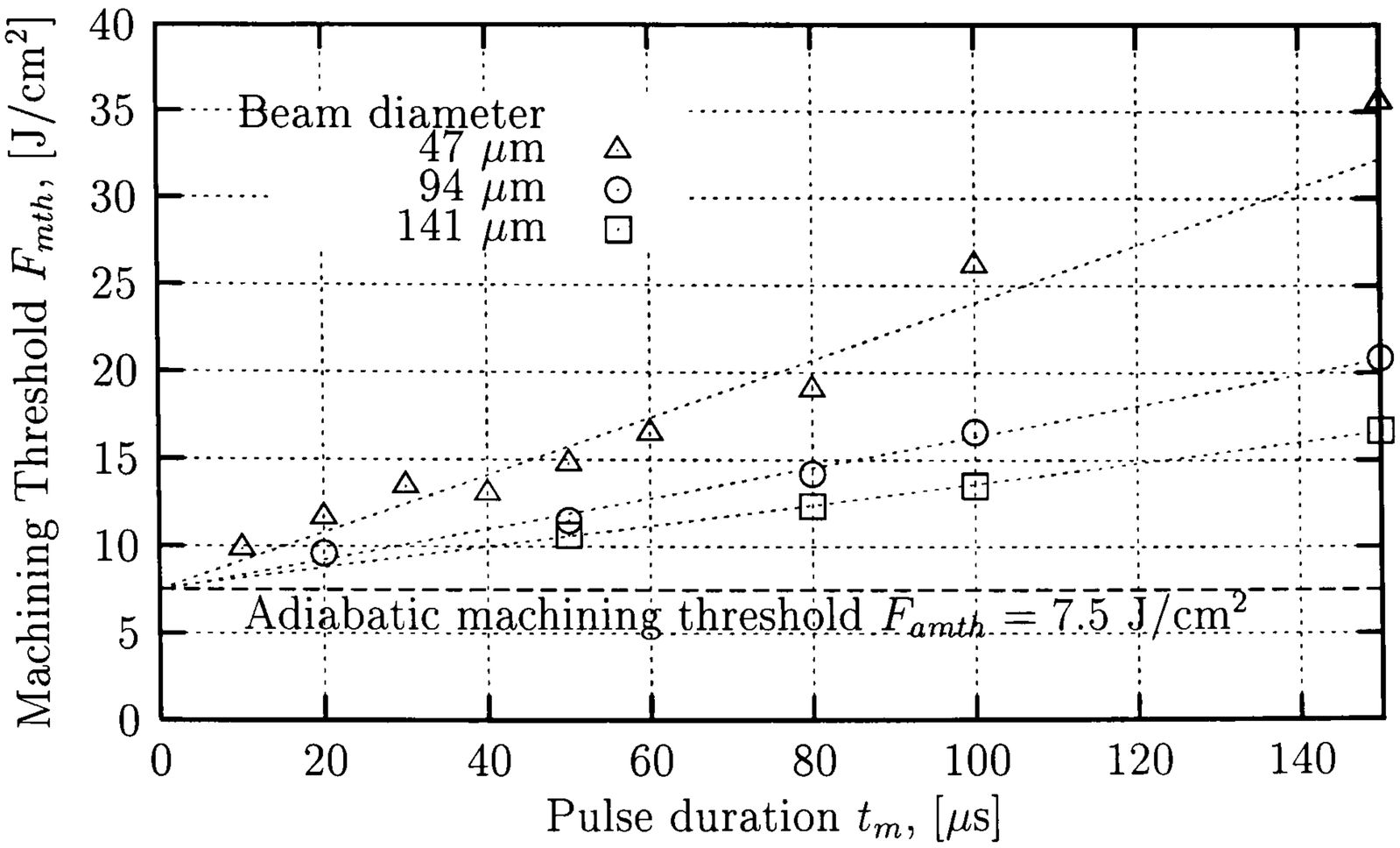

Figure 4.3: Machining threshold F_{mth} versus pulse duration, spot diameter as a parameter. Measured for a wavelength P-14 (10.53 μm).

investigates the profiles of ablation craters to identify the optimal pulse parameters that provide lowest possible machining threshold and the minimal deformation of crater profile due to the melt displacement under vapour pressure.

4.4.2 Fluence threshold of ablation versus pulse duration

It is convenient to use a fluence to describe the ablation threshold, because it provides a direct measure of energy required to set off an ablation and pinpoints the interplay of many parameters influencing the material removal dynamics. The transition between surface and volume heating of silica with CO_2 laser can be shown on the example of machining threshold fluence F_{mth} versus pulse duration. Figure 4.3 shows the measured machining threshold F_{mth} as a function of pulse duration, with a spot diameter as a parameter. From Figure 4.3 it is clear, that the heat dissipation is significant in a timescale of a typical CO_2 laser pulse, causing approximately twofold increase in an amount of energy required to set off the ablation. The comparison is made with a value of adiabatic machining threshold $F_{amth} = 7.5$ J/cm^2 (duration time zero), obtained by a linear extrapolation of data to a point, where the family of curves cross. The heat loss from the interaction zone is practically suppressed by using pulses shorter than 5 μs, thus the volume heating of silica, determined by α^{-1}, dominates in such timescale. However, the occurrence of melt ejection would

reduce the applicability of such pulses to production of shallow craters only (see Figure 2.18, the machining region above ablation and below ejection thresholds is very narrow).

The geometry of interaction zone has a big impact on the value of F_{mth}, especially when the spot diameter and the absorption length α^{-1} (see Section 2.3.5 p.36) are comparable, the case of smallest spot size. As the spot diameter increases, the geometry factor quickly becomes insignificant, since the 1-D heat flow becomes dominant in a conduction of heat.

4.4.3 Fluence threshold versus irradiance

By plotting the fluence threshold versus irradiance it is easy to visualize an irradiance threshold below which there is no ablation for practical laser pulse energies. It has been done by representing the data from Figure 4.3 as a function of irradiance, calculated as F_{mth}/t_m and shown in Figure 4.4. It can be seen how the influence of heat conduction, draining the energy from the surface of material, reduces with an increase of incoming laser energy flux. It has been found from the experimental data that no appreciable ablation takes place for practical laser pulses of irradiance lower than 50 kW/cm^2, since the rate of energy deposition is insufficient to build up the necessary surface temperature in a timescale of that pulse. Although this range of irradiance is unsuitable for a well controlled ablation, it can be used for surface melting to polish the as-machined surfaces by surface tension driven viscous mass flow, described in Chapter 6.

Rapid reduction of the amount of energy needed to initiate ablation can be observed in a region 100−300 kW/cm^2, dependingly on the spot diameter used. In this region the rates of heat supply and heat diffusion are comparable. With further increase of irradiance above 300 kW/cm^2, the rate of heat supply outpaces the rate of conductive heat loss and the machining threshold becomes minimal and practically independent of the irradiance and ablation zone geometry, thus this condition favours a well controlled ablation.

4.5 Measurements of machining rate

The machining threshold describes the amount of fluence necessary to initiate material removal. To gain more complete picture of ablation dynamics, a measurement

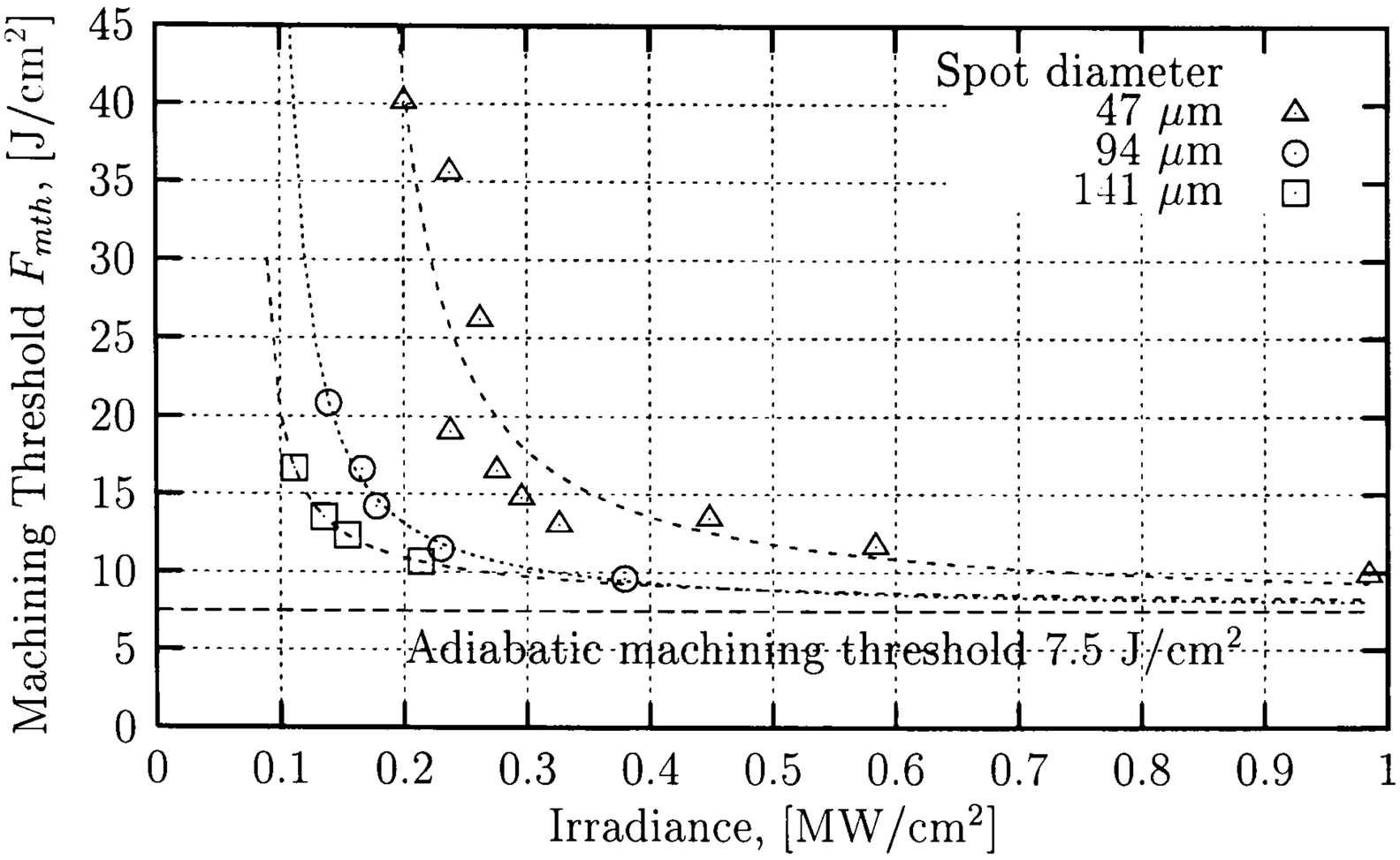

Figure 4.4: Machining threshold F_{mth} versus irradiance, beam diameter as a parameter. Measurements carried out for a line P-14 (10.53 μm).

of material removal rates has been carried out. In case of nano-second UV and ultrafast (pico-second, femto-second) ablation of silica, the material removal (or etch) rate is usually defined as a depth of material removed per laser pulse, quoting some particular pulse fluence [27, 36]. In case of CO_2 ablation of silica however, such definition of material removal rate is not useful since the ablation mechanism is different. As discussed in Sections 2.5.3 and 4.3, the evaporative regime dominates the removal process and the ensuing linear behaviour of ablated depth versus pulse fluence allows for introduction of different concept of machining rate. It has already been defined previously as the slope R_m of linear part of ablation curve (see Section 4.3), which describes the depth of removed material per unit fluence delivered. The parameter can be easily calculated from the acquired ablation data with reasonable accuracy.

An expression for R_m can also be derived analytically by making some simplifying assumptions. The quasi-stationary vaporisation regime ([29] Ch.5, [59] Ch.6) fits the process characteristics well, since the irradiance levels are too low for nonlinear effect to occur, such as plasma generation or vapour opacity. The issues concerning additional heat loss factors such as kinetic energy carried away in vapours, backscatter of vapour particles ([29] Ch.5) etc. have also been ignored.

In case of steady-state evaporation the surface recession velocity ν_F is defined

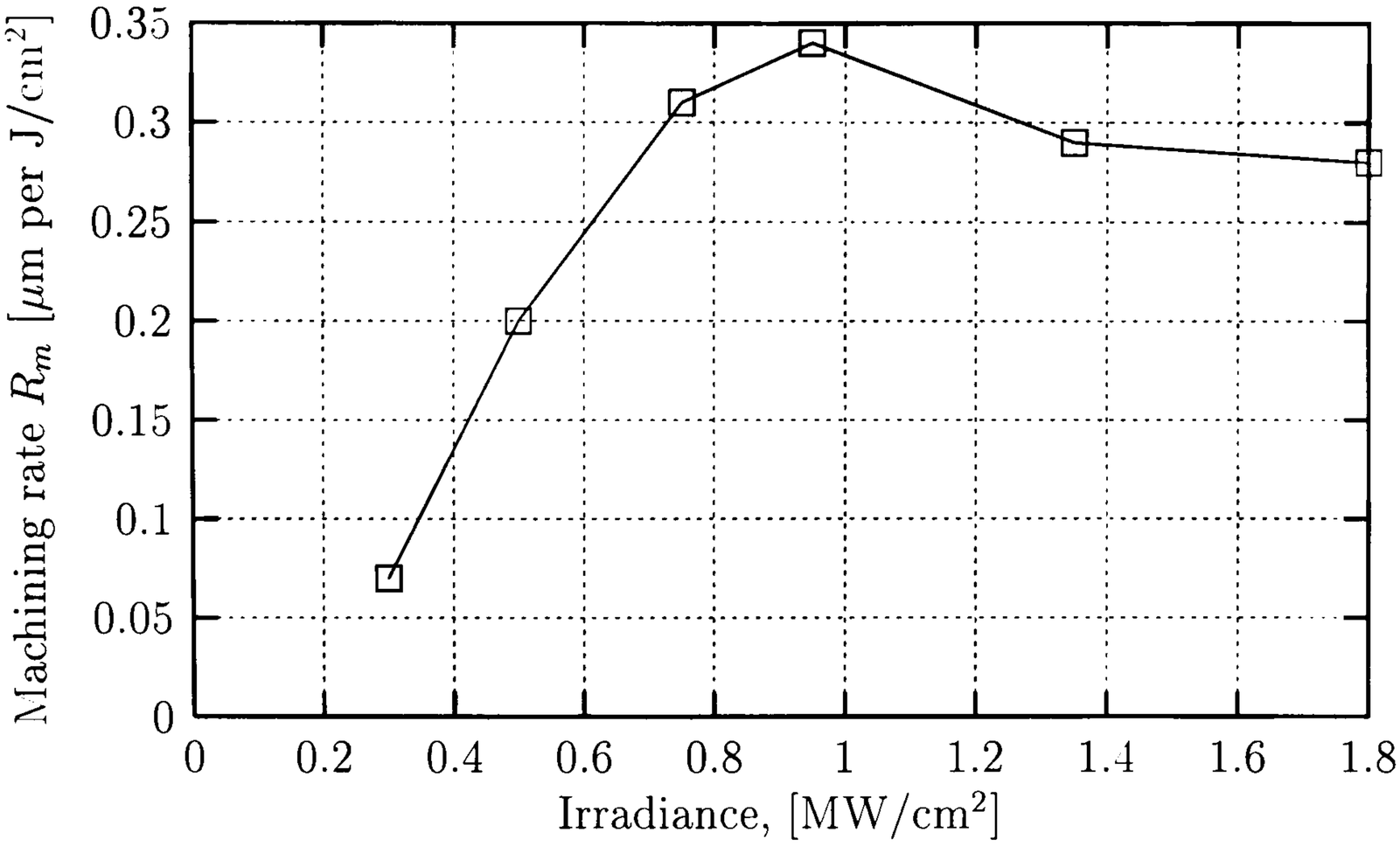

Figure 4.5: Machining rate R_m versus irradiance, 47 μm spot diameter, measured for a line P-14 (10.53 μm).

as:

$$\nu_F = \frac{I_o(1-R)}{\rho\,(C_{sp}\,\Delta T + L_H)} \tag{4.6}$$

where L_H is a latent heat of evaporation. The rate of material removal R_m is defined as the slope of ablation curve:

$$R_m = \frac{\Delta D}{\Delta F} = \frac{\nu_F}{I_o} \tag{4.7}$$

By combining Equation 4.6 and 4.7 one gets:

$$R_m = \frac{1-R}{\rho\,(C_{sp}\,T_o + L_H)} \tag{4.8}$$

The machining rate R_m depends only on material parameters. Equation 4.8 produces 0.47 μm (J/cm^2)$^{-1}$ of material removal rate after inputting the values of reflectivity $R = 0.15$ (line P-14, 10.53 μm) and heat capacity $C_{sp} = 1250$ J kg^{-1} °C^{-1} quoted at 1400 °C [4], a density $\rho = 2200$ kg m^{-3}, $\Delta T = 2700$ °C [48] and latent heat of vaporisation $L_H = 4.7$ MJ kg^{-1} [60]. The value calculated according to that simple model is only 30% larger than the measured one, as seen in Figure 4.5, even with ignored thermal flux, draining the energy from the heated zone, and strong temperature dependence of parameters involved. Evidently, the simple quasi-stationary model of evaporation can be applied to CO_2 laser ablation of silica.

In reality however, the heat dissipation in a material plays an important role in determining the value of R_m, which does in the end depend on the irradiance.

The drop of R_m for small irradiance (see Figure 4.5) can be explained by the heat conduction, which drains the energy deposited in the melt. This slope coincides with a sharp increase of machining threshold F_{mth} in this region of irradiance (see Figure 4.4). A slight drop in the range of high irradiance is not so easy to explain, because the influence of heat conduction is not so critical anymore. The vapour pressure is high enough in this region to displace the melt and frustrate the smooth ablation. The melt, displaced radially from the center of the crater, may lose some of its stored heat because of the reduced level of irradiance in the peripheries of beam profile. A thinner layer of superheated melt in the crater center may evaporate with a smaller rate because of additional heating of the solid, underlying the molten material, up to evaporation temperature.

Summarizing, the data shown in two Figures 4.4 and 4.5 describe the dynamics of CO_2 ablation of silica with different pulses and spot sizes. It is possible to find, based on the data and a study on crater topography (see Section 4.9), the optimal conditions for production of smooth near-Gaussian craters for purposes of rapid-prototyping regimes described in Chapter 5.

4.6 Accuracy of ablation process

The machining threshold F_{mth} is generally undesired from a point of view of precision fabrication, because it does not contribute to a material removal depth D:

$$D \simeq R_m \, (F_m - F_{mth}) \tag{4.9}$$

where F_m is a pulse fluence. As it is shown below, the depth error caused by a pulse energy instability can be amplified by the existence of threshold F_{mth}. It is easy to show that the relative depth error δD of ablated crater is associated with relative fluence error δF_m by:

$$\delta D = \delta F_m \, \frac{F_m}{F_m - F_{mth}} \tag{4.10}$$

F_{mth} ranges from 10 to 20 J/cm^2 (see Figure 4.2) for a typical CO_2 laser pulse. The total fluence F_m needed to ablate a crater with an aspect ratio smaller than 0.5 (for the reasons discussed in Section 4.3) is less than 45 J/cm^2 (see Figure 4.2). Hence, the fraction from Eq. 4.10 is always higher than one. It is especially large for shallow craters, machined by pulses that only slightly exceed the machining threshold.

If one considers the depth removal error ΔD in absolute measures. one finds that it does not depend on the target depth of ablated crater:

$$\Delta D = R_m \, \Delta F_m \tag{4.11}$$

To achieve a sub-micron machining accuracy comparable to that of UV and ultrafast ablation of silica (<0.2 μm per pulse), the pulse fluence must be controlled with an accuracy <1 J/cm^2, which corresponds to relative fluence error of <2% for typical laser pulses. Such pulse stability has been delivered by the machining station, described in Chapter 3, in a long term. In short term however (pulse to pulse), the fluence error <4% has been observed and this technical difficulty still awaits a solution. These fluence variations have appeared on the as-machined surfaces as low spatial frequency ripples of peak-peak amplitude <0.4 μm (see Chapter 5).

The slope of ablation curve just above F_{amth} (see Figure 4.2) suggests the lowered rate of material removal R_m in that region of fluence. The machining error ΔD can be thus smaller for shallow craters than for deeper ones, relaxing the requirement for production of deep craters to minimize the machining error.

The machining accuracy can be improved by finding a regime where the material removal rate R_m is small, for example using 9−9.5 μm wavelength that addresses peak absorptivity of silica (see Figure 2.7). The reflectivity in that wavelength region is nearly five times higher than at ∼10.6 μm currently investigated. A five-fold improvement in machining accuracy can be then expected by switching into the 9−9.5 μm band, which is covered by CO_2 lasers (see Section 4.8).

4.7 Assessment of melt depth

A knowledge of thickness of highly mobile melt layer is important for an assessment of maximum roughness of surfaces machined by overlapped ablation craters (see Chapter 5). The quasi-stationary vaporisation mode can be used to estimate the thickness of evaporating melt in strongly absorbing substances with sharply defined melting temperature, such as metals. The significant drop of viscosity that occurs in these materials at melting temperature, determines the sharp boundary between the solid and the melt. The expression describing the melt depth [29] has a form:

$$x_m \simeq \frac{K}{\nu_F} \ln\left(\frac{T_{lv}}{T_{sl}}\right) \tag{4.12}$$

where T_{sl} and T_{lv} are melting and evaporation temperatures respectively. In case of glasses however, such estimation is not applicable since they do not exhibit sharp melting point temperature (see Figure 2.4 p.31). The depth of molten material can be estimated from the length of thermal diffusion, taking place in a timescale of typical CO_2 laser, in conjunction with the viscosity data. Such estimation has been carried out in [4] and produced a depth of $\sim$4 μm.

It is possible to harness the quasi-stationary evaporation regime to estimate the depth of mobile, superheated material from the measured material removal rate R_m. A difficulty related to an absence of sharply defined melting point for silica can be overcome by exploiting the fact of volume heating of thin layer of glass. An irradiation of the thin layer, depth of which is comparable to an absorption length α^{-1}, produces highly mobile melt of superheated material (>3000 °C [4]) of similar depth. The degree of superheating, due to a long pulse timescale of slab waveguide CO_2 laser, is insufficient to cause violent volume evaporation, addressed in literature as vapour or phase explosion [45, 29]. It is safe to assume nearly constant temperature in the melt layer as a result of balance between a heat input from the laser beam and a heat loss in a form of vapour energy [29]. It is also possible that the melt depth x_m does not exceed the absorption length α^{-1} in an ablation front swiftly advancing into the silica (the calculation result from Eq. 4.6 shows that the surface recession velocity, 0.1−0.3 m/s for a typical CO_2 laser pulse, is higher than propagation velocity of thermal front). The derivation of expression for R_m is then possible, bearing in mind the assumptions. Figure 4.6 illustrates the derivation conditions. The light of intensity I_o, illuminating the material at normal incidence, undergoes reflection on the surface of reflectivity R. The intensity of refracted light decays according to Beer-Lambert law with an extinction factor determined by absorption coefficient α:

$$I(x) = (1 - R)\ I_o\ \exp(-x\ \alpha) \tag{4.13}$$

Thus the absorbed power density inside the material becomes:

$$g(x) = (1 - R)\alpha I_o\ \exp(-x\ \alpha) \tag{4.14}$$

Let's now consider already developed stable ablation front moving into the material with a constant velocity ν_F. The heat loss from the melt by the thermal conduction and radiation has been neglected for simplicity sake. The volume of molten material

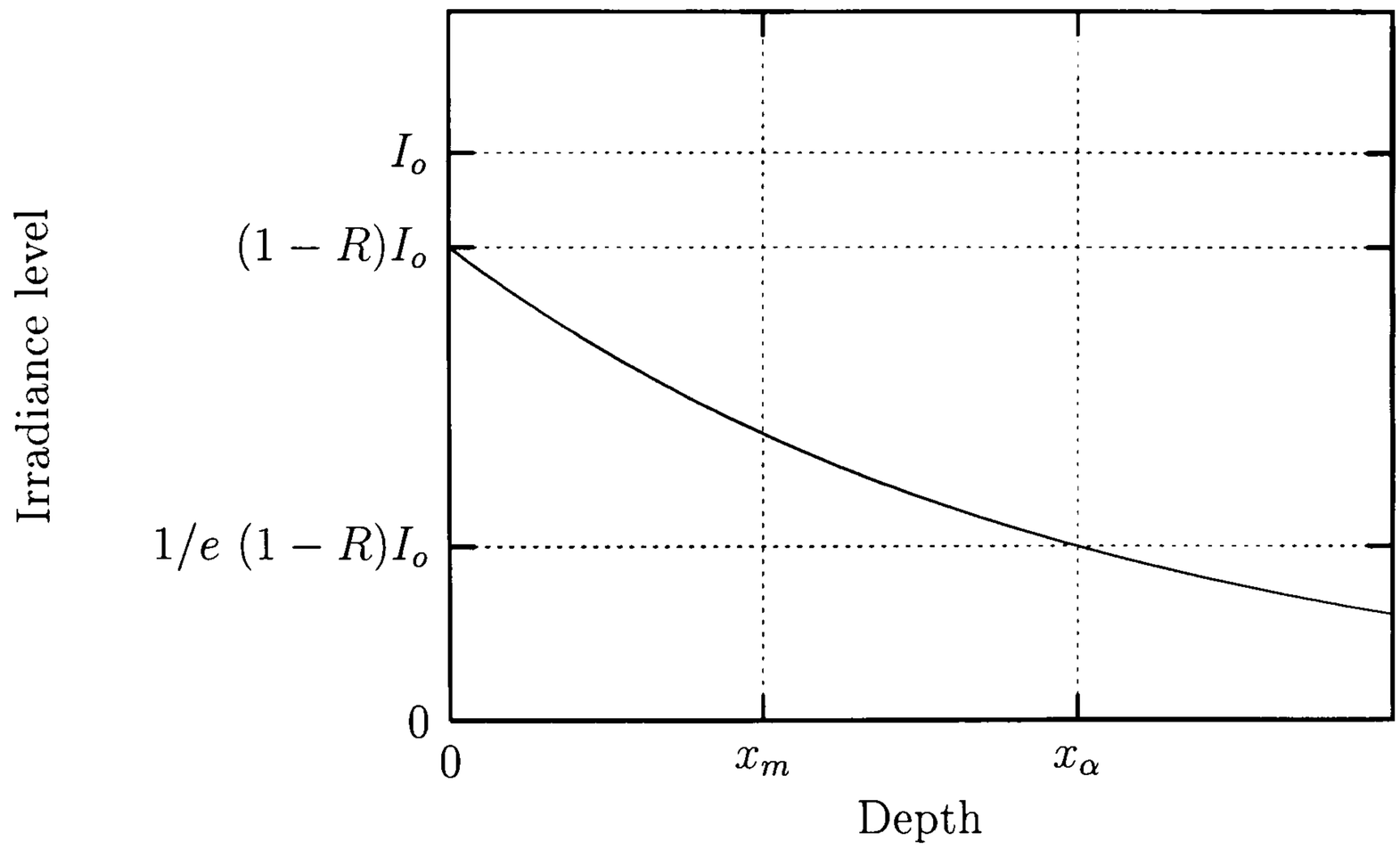

Figure 4.6: Illustration to the derivation of formula for material removal R_m

V_m of thickness x_m evaporates with a rate:

$$\frac{\partial V_m}{\partial t} = \frac{P}{L_H\ \rho} \tag{4.15}$$

where P stands for a power absorbed in the volume V_m, L_H is a heat of evaporation of material and ρ is a density. The power P absorbed in the volume V_m:

$$\begin{aligned} P &= V_m\ g_{mean} \\ g_{mean} &= \frac{1}{x_m} \int_0^{x_m} g(x)\ dx \end{aligned} \tag{4.16}$$

By exploiting the identity 4.17 it is possible to relate the rate of volume change to a rate of change of melt thickness:

$$\frac{\frac{\partial V_m}{V_m}}{\partial t} = \frac{\frac{\partial x_m}{x_m}}{\partial t} \tag{4.17}$$

Propagation velocity ν_F of ablation front can be derived from Eq. 4.16, 4.17 and 4.15:

$$\nu_F = \frac{\partial x_m}{\partial t} = \frac{g_{mean}\ x_m}{L_H\ \rho} \tag{4.18}$$

By inserting the result of integration from Eq. 4.16 into Eq. 4.18 one gets:

$$\nu_F = \frac{(1-R)\ I_o}{L_H\ \rho} \left(1 - \exp(-x_m\ \alpha)\right) \tag{4.19}$$

The final expression for R_m can be obtained by combining Equations 4.7 and 4.19:

$$R_m = \frac{(1-R)}{L_H\ \rho} \left(1 - \exp(-x_m\ \alpha)\right) \tag{4.20}$$

The estimation of melt depth is possible from the rearranged form of Equation 4.20, knowing the material constants and the measured value of R_m:

$$x_m = -\alpha^{-1} \ln\left(1 - \frac{R_m \; L_H \; \rho}{1 - R}\right) \tag{4.21}$$

Equation 4.21 produces plausible result for the P-14 line, because the thermal diffusion length $\tau = \sqrt{D \; t_m}$, amounting to 9 μm for 50 μs pulses [45], is comparable with the absorption length α^{-1}. It must be also borne in mind that the depth of removed material in a timescale of that pulse can be as high as $\sim$10 μm. Rapid advance of ablation front effectively compresses the thermal front propagating into the material, thus the influence of thermal diffusion is reduced. Heat loss that inevitably takes place due to a radial flow from the ablation zone and the heat expenditure needed to warm up the underlying "cold" material, tend to reduce the depth of evaporating layer x_m and the material removal rate R_m. Equation 4.21 is immune to that effect because the melt depth is calculated from the measured value of R_m, which already is a result of interplay between these factors.

The absorption length for the wavelengths in a close proximity of silica absorption peak at 9.2 μm can be as little as 0.1 μm [45], almost two orders of magnitude smaller than τ. Equation 4.21 would thus yield the underestimated depth of superheated layer, even if the compression of thermal front was assumed.

After taking into account the absorption length for the line P-14 at high temperatures [25] α^{-1}=4 μm, surface reflectivity 0.15, latent heat of vaporisation [60] L_H=4.715 MJ/kg and measured machining rate 0.31 μm/J/cm^2, Equation 4.21 produces x_m=2.5 μm. The result agrees well with a measurement of ejected fiber diameters [4], which were found to be approx. 4 μm. The calculations also agree with the observed heights of crater rims, shown in Section 4.9.

The fact that follows the calculations is that the maximum expected value of surface roughness, related to the melt displacement, can be as much as 2.5 μm peak-peak. The AFM study of as-machined surface condition, presented in Section 5.6.2 p.141, has confirmed the finding.

The presence of molten layer is also responsible for excellent smoothness of ablated surfaces. Surface irregularities can be effectively smoothed out by the surface tension driven mass flow, which has been applied for laser polishing of as-machined surfaces (see Chapter 6). As the calculations and experiments show, very effective polishing of sub-micron size features of melt layer (see Figure 6.1 p.151) can take

place in a matter of few microseconds of the melt cool-down (see Section 4.11.1 on cooling rate of ablation site). The polishing action is significantly suppressed when ablating with UV or ultrafast lasers, due to very thin heat affected zones (~300 nm) and much higher cooling rates of ablation site. These factors lead to a much worse surface morphology than in case of CO_2 lasers.

4.8 Spectral sensitivity

The study, presented in Section 4.5, has shown that the surface reflectivity R influences the dynamics of machining (Eq. 4.8). R determines the coupling efficiency of CO_2 light into silica, thus it directly influences the values of machining rate R_m and threshold F_{mth}. The reflectivity of silica varies with temperature and the wavelength of incident radiation (see Figure 2.8 p.40). The effect of temperature change on reflectivity can be qualified as static, since the melt temperature remains roughly (~3000 °C) constant during developed ablation process (section III of machining curve from Figure 4.2), thus it is the wavelength that determines the dynamics of material removal.

4.8.1 Machining threshold change with wavelength

The machining threshold is primarily determined by the absorption depth α^{-1}, the reflectance R and thermal properties of material. The amount of fluence necessary to bring the surface temperature up to an evaporation point is proportional to the absorption depth. To discuss the impact of absorption length on the value of machining threshold alone, the *specific machining theshold* F_{sp} has been introduced here as:

$$F_{sp} = F_{mth}\ (1 - R) \tag{4.22}$$

which describes the amount of fluence deposited *inside* the surface layer, irrespective of reflectance R.

An approximate expression for *adiabatic specific threshold* F_{asp} can be derived assuming the material properties do not depend on temperature. The threshold amount of fluence that increases the surface temperature up to a point of evaporation can be written as:

$$F_{asp} \simeq \int_0^\infty \rho\ C_{sp}\ \Delta T(x)\ dx \tag{4.23}$$

where $\Delta T(x) \simeq \Delta T_e \ \exp(-\alpha_{eff}\ x)$. After integration of RHS Eq. 4.23 one gets:

$$F_{asp} \simeq \rho\ C_{sp}\ \Delta T_e\ \alpha_{eff}^{-1} \tag{4.24}$$

which links the *effective absorption depth* α_{eff}^{-1} with an amount of energy needed to raise the surface to an evaporation point. In case of silica Equation 4.24 yields $F_{asp} =$ 26 J/cm^2 with material constants quoted at 1400 °C [4] and absorption length $\alpha^{-1} =$ 35 μm at room temperature for a 10.53 μm wavelength [25]. The value obtained is almost four times larger than the measured $(1-R)\ F_{amth} = 6.3$ J/cm^2, $R = 0.15$ at 10.53 μm (see Section 4.4). The difference comes from the fact the absorption depth in silica drops with temperature, from 35 μm at room temperature down to <4 μm near 1800 °C (see Section 2.3.5 p.36). However, the reverse calculation is possible based on the experimentally measured F_{asp}. Equation 4.24 produces $\alpha_{eff}^{-1} = 8.6$ μm, which agrees well with experimental findings. The adiabatic specific threshold F_{asp} can be used as a tool for ablative measurements of absorption coefficient of strongly absorbing materials.

Bearing in mind the above, F_{asp} can be calculated as a function of wavelength from available data on complex refractive index. The obtained curve shall be a horizontally flipped version of extinction coefficient data shown in Figure 2.7 on page 39. In case of absorption peak of silica near 9.6 μm, α^{-1} can be as little as 0.1 μm at room temperature. Hence large reduction of F_{asp} can be expected at this wavelength, over an order of magnitude in comparison to 10.53 μm. In reality the adiabatic conditions are not satisfied for typical ~50 μs CO_2 laser pulses (see Figure 4.3) and some heat diffusion occurs. However, the decrease of F_{asp} may be compensated by the increase of reflectivity R, as far as a value of F_{mth} is considered. Nevertheless, the ratio $\frac{F_m}{F_m - F_{mth}}$ from Eq. 4.10 may approach unity. A switch into the 9-9.6 μm band promises higher accuracy of machining than at ~10.6 μm currently used (see Section 4.6).

4.8.2 Machining rate change with wavelength

The machining rate R_m is determined primarily by the material constants and surface reflectivity (Eq. 4.8). It should be thus possible to quantify the spectral behaviour of R_m from the reflectivity data shown in Figure 2.8 p.40 quoted at room temperature. Near five-fold reduction of R_m is expected by switching from 10.53 μm wavelength to 9.6 μm, which corresponds to peak 80% reflectivity of

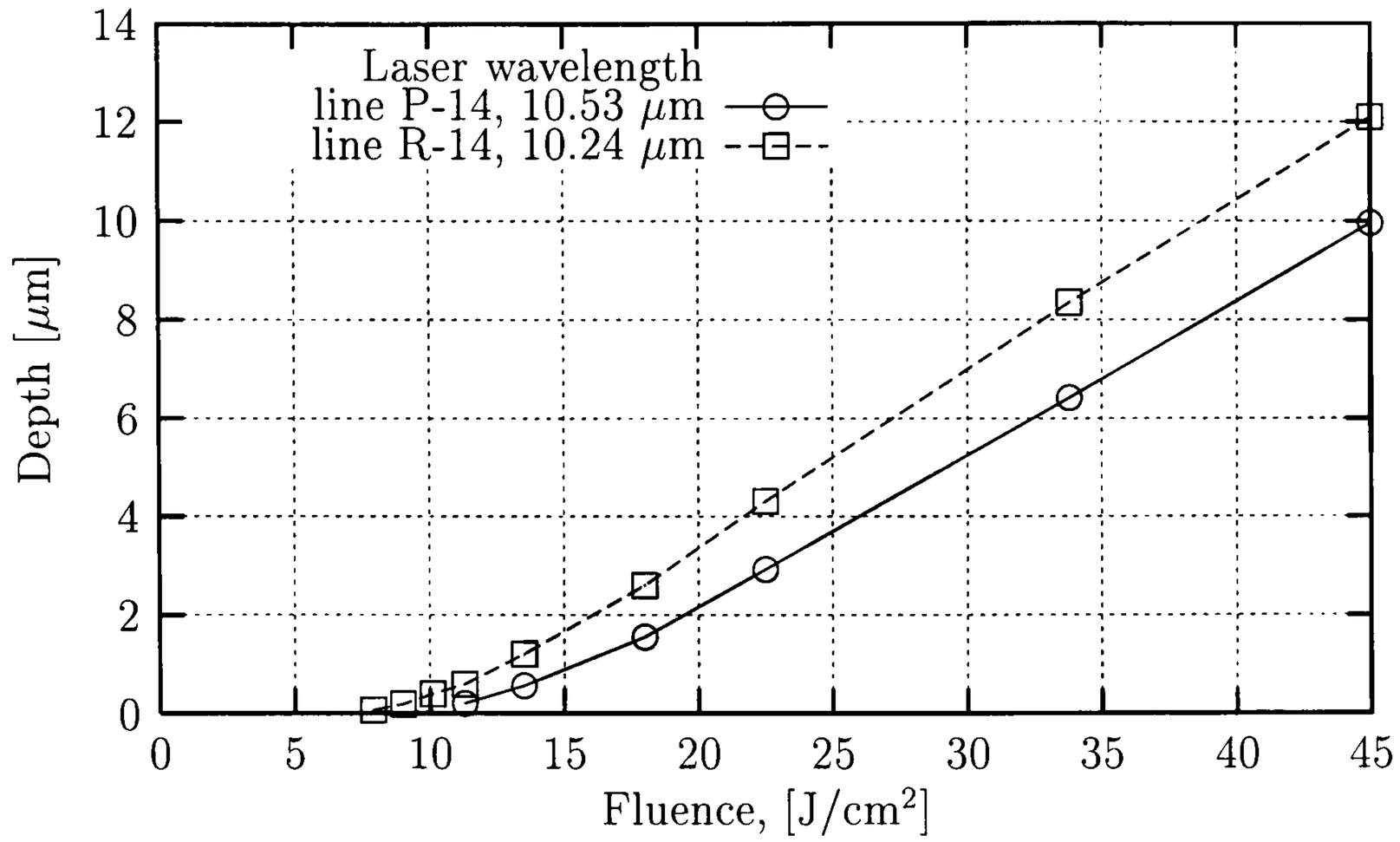

Figure 4.7: Comparison of machining curves obtained for different laser lines, P-14 and R-14, 50 μs pulse duration and 47 μm spot diameter.

silica. Five-fold enhancement of machining accuracy can be then achieved solely by a wavelength adjustment (see Section 4.6). The question arises whether room temperature reflectivity holds at high temperatures created in the ablation zone. It is very probable that the reflectivity at 9.6 μm drops significantly due to surface texturing and vapour interface, as in case of metals [29]. An additional experimental study is then required to quantify the behaviour of R_m in the 8-10 μm spectral range of interest.

4.8.3 Sensitivity of ablation to laser signature scan

Laser instability in spectral domain may lead to non-repeatable material removal that compromises the machining accuracy of target optical structures. Such event is very likely to occur when operating commercial slab waveguide CO_2 lasers. To quantify the effects of laser line change on machining rate and threshold, two ablation curves have been measured using two selected CO_2 wavelengths, P-14 and R-14, chosen to simulate a full scan of laser signature. Line selection was possible thanks to precision temperature controller, described in Section 3.3.3 p.72.

Figure 4.7 shows two machining curves obtained for lines P-14 and R-14 of CO_2 spectrum, wavelengths 10.24 and 10.53 μm correspondingly, using pulse duration time 50 μs. The curves differed significantly both in threshold and machining rate,

Laser line	F_{mth} $\left[\frac{\text{J}}{\text{cm}^2}\right]$	R_m $\left[\frac{\mu\text{m}}{\text{J/cm}^2}\right]$
P-14 (10.53 μm)	13.1	0.31
R-14 (10.24 μm)	9.9	0.35
Change [%]	−26%	+12%

Table 4.1: Material removal rate and machining threshold for two CO_2 laser lines.

as shown in Table 4.8.3, resulting in over 1 μm of depth removal difference. It was clear from the experiment that spectral stability had to be assured to fulfill the requirements of precision machining.

The reduction of machining threshold F_{mth} agrees with an idea outlined in Section 4.8.1. The interesting fact is that the machining rate R_m has increased with decreasing wavelength, which contradicts the considerations from Section 4.8.2. There is a need for a study of R_m versus wavelength to gain better understanding of spectral behaviour of machining rate.

4.9 Optimal crater shape

Crater profiles, being the by-products of depth measuring technique, allowed for a study of crater topography as a function of machining conditions. This section studies the extent of melt displacement that occurs during ablation and aims to identify a range of optimal machining parameters that produce craters of undisturbed profiles for the purposes of machining algorithms described in Chapter 5.

It was known from previous work [4] that irradiance above certain threshold $I_{eth} \geq 1.6$ MW/cm^2 spot radius $\omega = 27$ μm was capable of driving an ejection of molten material from the melt pool in a form of fibers. This effect has been recognized as badly affecting the resultant crater profile and compromising the process control. The melt ejection can be avoided by reduction of irradiance below the fiber ejection threshold. Pulse duration time must be then increased to assure a delivery of required amount of fluence. As an outcome, a compromise had to be sought between low threshold of short pulses ($\leq$10 μs) and good quality of craters machined by longer pulses ($\leq$ 100 μs).

Crater profile versus pulse duration. A large number of craters have been produced with varying machining conditions. The pulse width varied from 10 to

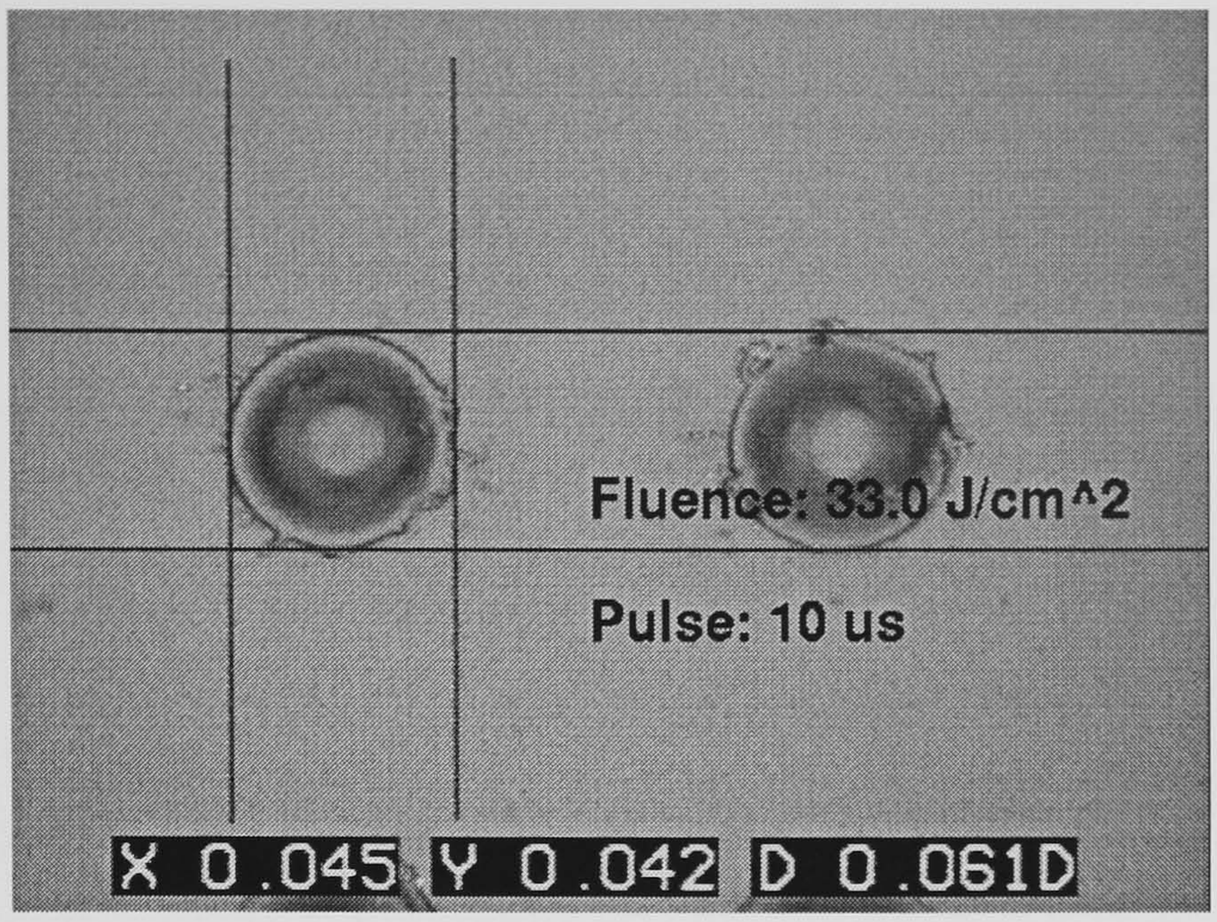

1)

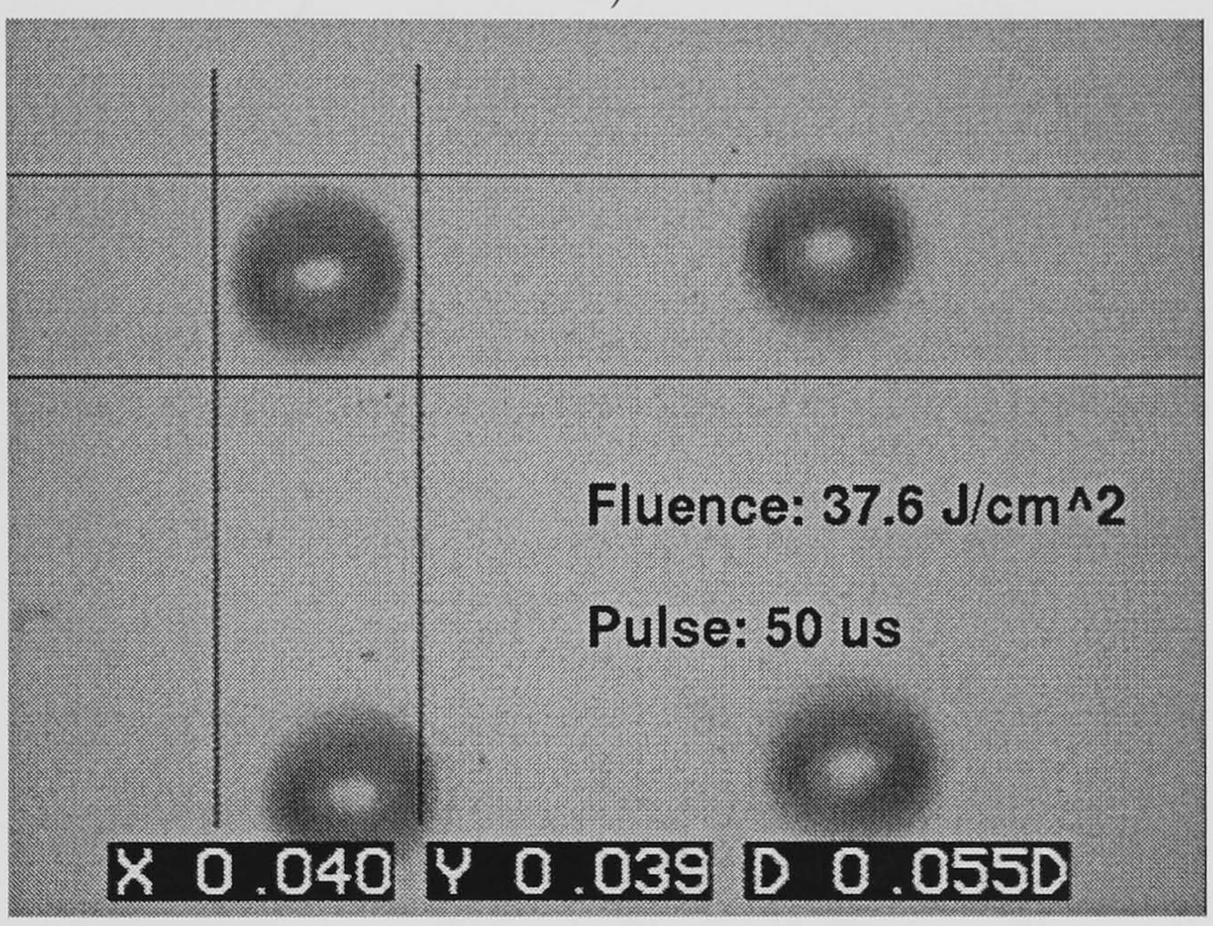

2)

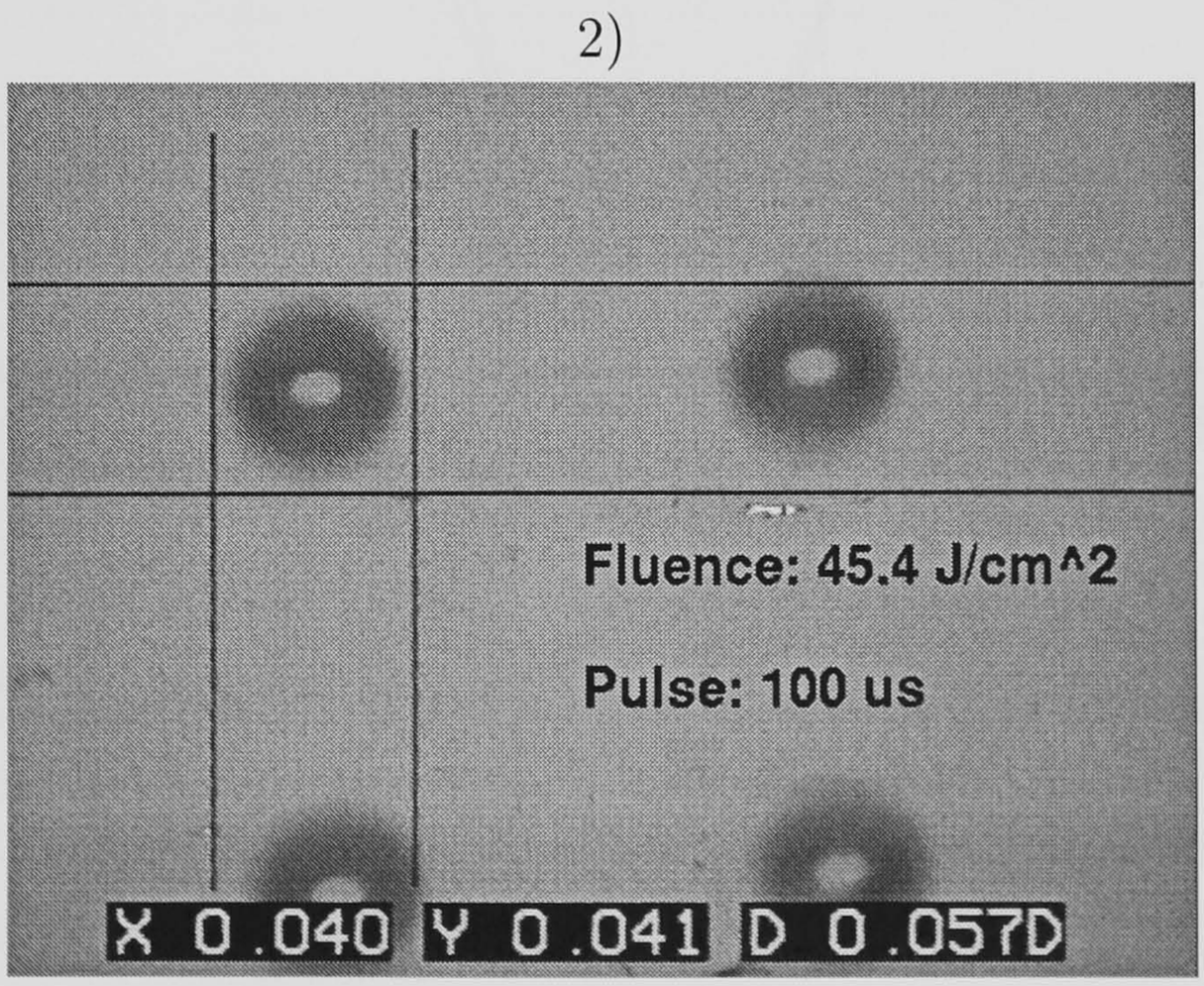

3)

Figure 4.8: Photographs of craters of comparable depth made with laser pulses of different duration time, as indicated in each photo. Digital readout in millimeters.

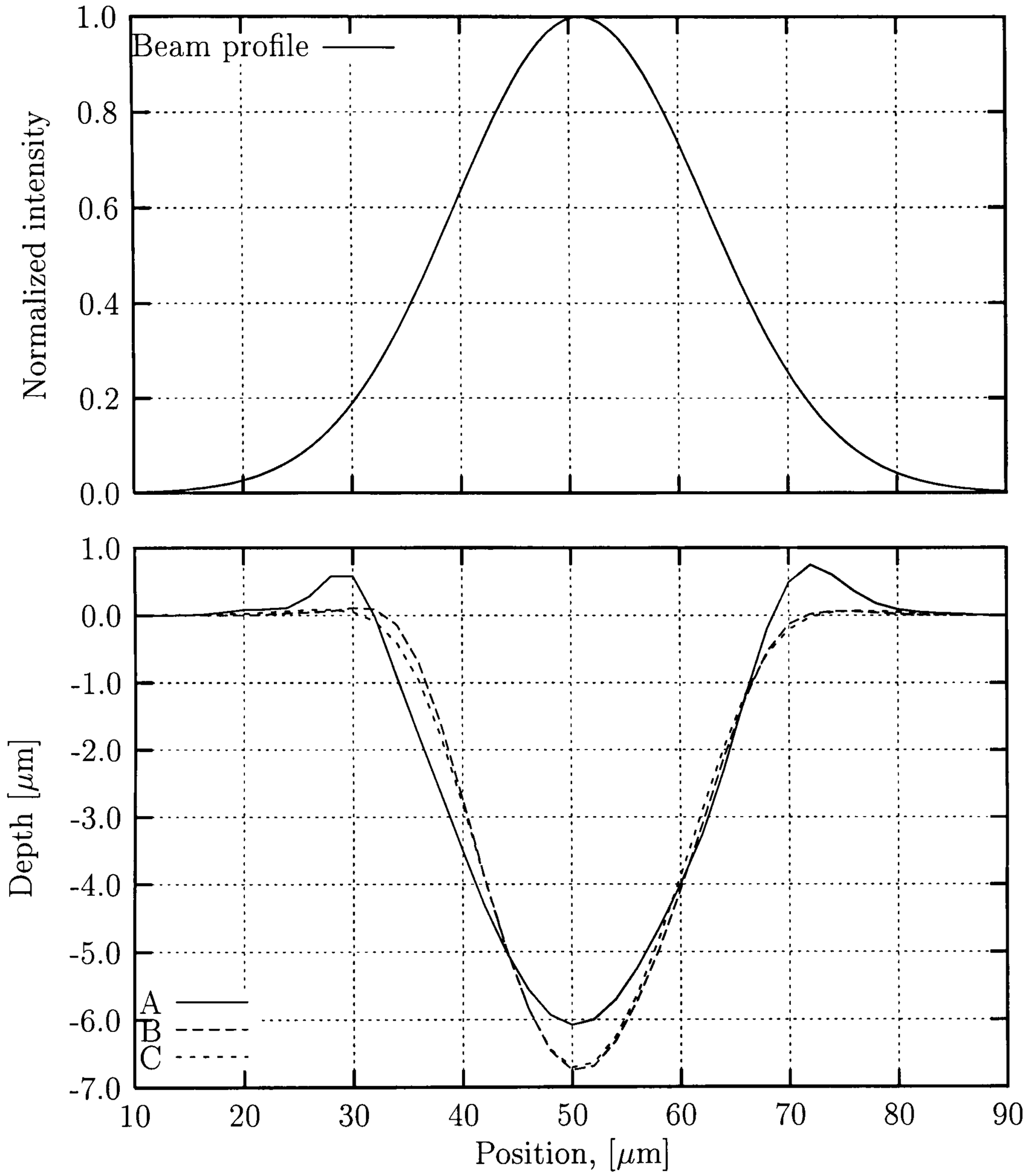

Figure 4.9: Profile comparison of craters from Figure 4.8 produced by a single laser pulse, beam diameter 47 μm. The craters were made with pulses: A) pulse duration 10 μs, fluence 33 J/cm^2, B) 50 μs, 37 J/cm^2, C) 100 μs, 45 J/cm^2. Beam profile included for comparison. Rim height clearly higher for short pulses.

300 μs, the irradiance level varied from 0.4 to 1.6 MW/cm^2. A whole area of machining window, shown in Figure 2.18 p.62, has been covered. Most attention has been directed towards short 10−80 μs laser pulses, since they provide lowest machining threshold (see Figure 4.3). Figure 4.8 shows the micrographs of craters produced by single pulses with various duration times and fluences, as indicated in each photograph. Figure 4.9 shows the measured profiles of craters shown in Figure 4.8. A comparison of influence of laser pulse duration on the crater profile has been carried out with craters of arbitrarily chosen depth 6.5 μm.

10 μs pulses (the irradiance only slightly lower than fiber ejection threshold) produced craters surrounded by the rims of displaced molten material (see Figure 4.8, Photo 1)). The rim height was in some cases as much as 1.8 μm. As the pulse length increased, the irradiance level dropped. The pressure of vapours followed the drop of irradiance and the extent of melt displacement was reduced, which manifested as a drop of rim height. The rim practically disappeared ($<$ 100 nm) for pulse duration times greater than 50 μs.

Substantial difference between crater profiles for 10 μs and 50 μs has been observed. The walls of craters obtained with 10 μs pulses seemed to be pushed apart, in comparison to craters produced by longer pulses, and a crater rim has been created. The onset of melt ejection is responsible for the presence of distinctive crater rim, since the irradiance ($\sim$3 MW/cm^2) exceeded the melt ejection threshold (see Figure 2.18) reported in [4].

The rim can also be observed around craters made with 50 μs pulses, but in this case the irradiance fell below melt ejection threshold. The low rim ($<$100 nm) was produced in the area of non-zero beam profile, where the softened material was plastically deformed by the piston action of vapour pressure. For pulse duration longer than 50 μs the formation of rim does not practically take place.

In general, the crater diameter was smaller than that of incident beam. It can be explained by the dependence of machining threshold on irradiance (see Figure 4.4). Machining threshold varies along the beam profile, thus the onset of ablation in the areas further away from the beam centre is more delayed. This effect can be described as crater tapering. The smooth crater edges can also be explained by the irradiance dependent machining threshold, since it varies in a smooth manner.

4.10 Optimal machining conditions

In the light of results from Sections 4.4, 4.5, 4.9 and practical aspects of operating the CO_2 slab waveguide laser, I've chosen the 50 μs pulse length as optimal for precision machining of silica. Good crater quality yet small machining threshold (13 J/cm^2 at spot radius ω =24 μm) can be achieved by application of 50 μs pulses with fluences not exceeding 45 J/cm^2.

4.11 Considerations on processing speed

The machining algorithm, described in Chapter 5, utilized an overlap of individual craters as a way of removing layers of material. The overlap of craters creates thermal coupling between the adjacent interaction zones by means of residual heat that is not fully diffused in a time between laser pulses. This thermal memory effect may effectively lower the machining threshold for the next overlapped crater, provided the time interval between consecutive shots is sufficiently small.

The experiment has been carried out to find the characteristic timescale and magnitude of the effect. A number of craters has been produced by directing two identical laser pulses into the same location on the substrate, with prescribed time interval between them. Subsequently, the depth of resultant double-shot crater has been measured. The pulse settings used were the same as given in Section 4.10, pulse fluence 28 J/cm^2, machining threshold 13 J/cm^2, craters 21 μm diameter and 5 μm deep.

The relative depth D_R of double-shot craters was calculated with respect to a depth of single-shot reference craters. The allowed range of D_R values was 2 to 2.8–2.9. D_R should be exactly 2 for large temporal separation between the pulses, assuming the removal mechanism is ideally subtractive. In reality however, D_R was smaller than 2. Such behaviour was an outcome of modification of ablation site geometry and related increase of machining threshold as seen by the second pulse. It is another issue to bear in mind when considering the overlap of craters for machining of micro-structures (see Chapter 5). The maximum possible value of D_R was ~2.8-2.9, when two consecutive 50 μs laser pulses merged into a single 100 μs pulse and 13 J/cm^2 of threshold fluence usually lost contributed to machining.

Figure 4.10 shows the relative depth of double-shot crater as a function of pulse separation. For pulse separation larger than 5 ms full dissipation of residual heat

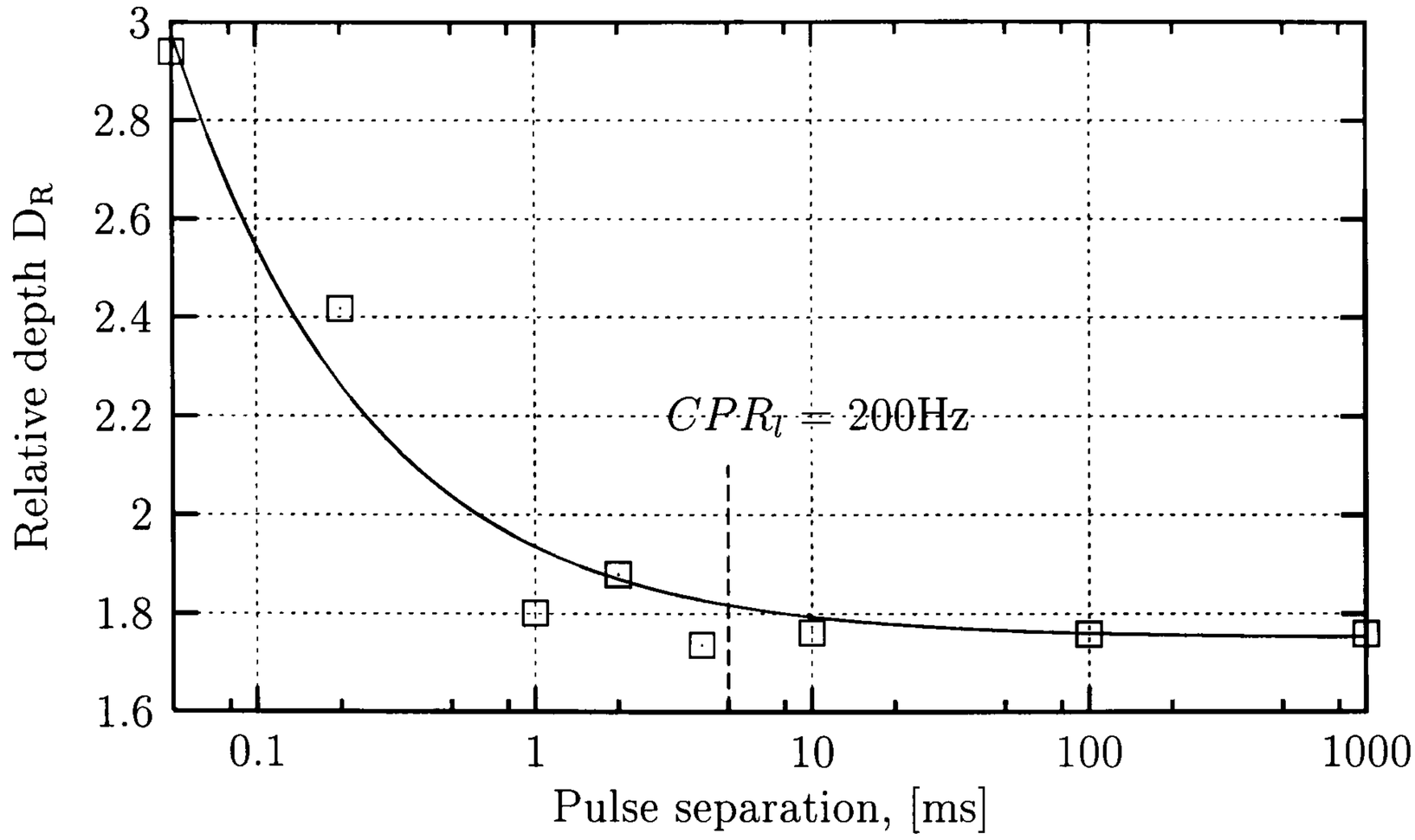

Figure 4.10: Relative depth D_R of a crater made by two laser pulses as a function of temporal separation between them. D_R calculated with respect to a depth of reference single-shot crater. Laser pulse length 50 μs, fluence 28 J/cm^2. CPR_l is a limit of crater production rate below which thermal coupling is negligible.

from the crater site has been recorded, the depth ratio was constant and nearly 2. A natural 200 Hz limit of crater production rate CPR_l has thus arisen, below which an independence of machining conditions between one laser pulse and another could be assured. In spite of apparent disadvantage, the effect of threshold reduction may be utilized to improve linearity and increase machining efficiency of overlapped regime, as shown in Chapter 5.

4.11.1 Cooling rate of ablation site

It is possible to calculate the initial cooling rate of heat affected zone from the measured relative crater depth D_R. The double-shot crater depth difference between 50 μs and 200 μs data points amounts to ~2.5 μm. The amount of fluence F_l necessary to ablate such depth is ~8 J/cm^2 (see Figure 4.5 p. 89). The fluence F_l = has apparently leaked out from the heat affected zone of arbitrary depth $X_a = 35$ μm (CO_2 laser absorption depth at room temperature), thus reducing it's temperature by ΔT ~1000 °C (Equation 4.25) in a timescale of 150 μs, C_{sp} is a heat capacity and ρ is a density of silica.

$$\Delta T = \frac{F_l}{\rho \, C_{sp} \, X_a} \tag{4.25}$$

The cooling rate was then ~6 °C/μs. As shown in Section 2.4.4 p.52, the measured cooling rate is comparable with critical cooling rates of silicate glasses, above which a probability of cracking during or after ablation is high.

4.12 Conclusions

This chapter has provided quantitative answers on CO_2 laser machining of silica. The machining of silica without detrimental cracking has been shown. Material removal rate and machining threshold fluence have been measured and related to irradiance, pulse duration time and spot size. Optimal machining conditions that produce Gaussian like craters have been found (see Section 4.10). Optimal pulse length and fluence range, that produce smooth near-Gaussian craters, have been found to be 50−80 μs and 25−45 J/cm^2 correspondingly. It has been also shown that spectrum and power stability of the source better than 2% was essential to assure levels of accuracy needed for precision machining of optical elements.

It has been shown that depth removal accuracy ~200 nm, comparable to that of UV and ultrafast ablation, is achievable in the current machining system. Further improvement of depth accuracy is expected by enhanced stabilisation of pulse fluence to better than 1 J/cm^2 (currently achieved fluence stability). Besides the additional stabilisation of pulse fluence, it seems that the accuracy can be further improved by ablation in 9.0-9.6 μm wavelength band, easily addressable with CO_2 lasers. Substantial reduction of machining rate (~eight-fold) is expected in this wavelength region. Machining resolution of <100 nm can be thus achieved by changing the wavelength alone.

It has been demonstrated that CO_2 ablation of silica produces surfaces of exceptional smoothness in comparison to ablation with other lasers relevant to precision micro-fabrication. The excellent smoothness has been associated with the presence of thin 2−3 μm layer of low viscosity material. However, such melt layer promotes cracking in other silicate glasses that possess high thermal expansion coefficient.

Chapter 5

RAPID PROTOTYPING OF ARBITRARY SURFACES

5.1 Introduction

The aim of the study presented in this Chapter is to explore the possibilities of precision machining of arbitrary surface shapes in silica by overlapping single shot craters in a raster scan regime. Different variants of raster scan regimes have been investigated to learn about dependence of process control, productivity and accuracy on machining conditions such as raster organisation, laser pulse parameters, single shot crater profile and material characteristics. Subsequently, the variations of machining regimes have been characterised and their performance assessed, leading to a development of empirical model of material removal and creation of the original system that made the rapid prototyping of arbitrary surface shapes possible. In the end, a fabrication of optical elements to a computer generated prescription is presented together with a quality assessment of resulting surfaces.

5.2 Background

Diffractive (DOE) and refractive (ROE) optical elements accompany the lasers to transform and customize their output to suit a particular application, for example efficient launch into optical fibres, optical interconnects or aperture filling. These elements are responsible for exploiting a potential of lasers, thus a manufacture of DOEs and ROEs has drawn a lot of attention of many researchers in the last two decades.

In the seventies and early eighties the methods for fabrication of micro-optics

were limited to resist-based techniques such as photolithography (PL), electron beam lithography (EBL) and the reactive ion etching (RIE). They were developed primarily for the manufacture of VLSI electronics [61, 62, 63, 64]. The PL and EBL techniques exploited a sensitivity of polymer-based photoresists to UV light and an electron beam of suitable energy. PL method used a set of photolithographic masks to expose the selected areas of the resist to UV light. EBL technique was designed to produce photolithographic masks but was later adapted to write the patterns directly into photoresists.

PL and EBL methods used a thin $\sim$10 μm layer of photoresist created on a SiO_2 substrate by spin coating. After UV exposure through a set of masks or in an electron beam writer, the latent photoresist relief had to be developed. Chemical etching and dry etching methods were used to remove the affected parts of the photoresist to reveal the desired surface pattern [65, 61]. The developed pattern could be used with RIE technique for a direct transfer of the resist profile into the SiO_2 substrate. The desired shape could also be etched in a resist alone by exploiting the dependence of etch rates on the dose of UV light or electron beam. The resultant relief could be then used directly as a micro-optical device or its shape could be transferred into a Ni mould or shim for mass replication by hot embossing or moulding [66].

These techniques perfectly suited a preparation of moulds for mass production of optical devices such as holographic security labels, used on bank cards for example, but performed poorly when small batches of optical elements were needed, i.e. for prototyping purposes of a developing business. The preparation of a set of masks, required for the photolithography, was very time consuming and expensive part of the fabrication cycle. Depending on the number of masks required (from one for 2-level binary diffractive element, to N for 2^N-level device), the preparation could take from weeks to months [61]. In a dynamically expanding photonics business of today such a long timescale is unacceptable.

An invention of half-tone and gray-scale mask technologies has reduced to one the number of lithographic masks necessary for production of large N and continuous-profile DOEs and ROEs. Half-tone masks were produced by electron beam writing of sub-micron size, binary patterns of variable density in standard metal-coated masks used for VLSI photolithography. Gray-scale masks exploited properties of special high electron beam sensitive (HEBS) glasses [61]. The transmittance of

these glasses could be locally varied, dependingly on the local dose of the electron beam.

Although the preparation and fabrication cycles could be greatly reduced with half-tone and gray-scale photolithography, a complicated manufacturing process exploiting PL and EBL remained. The optical devices could be made mainly in polymers with a profile dynamics limited to a few microns. RIE technique was capable of producing optical devices directly in the substrates such as SiO_2, but very small etch rates practically limited the profile dynamics to single microns. In spite of the fact that the etching of deep structures (6-10 μm) in SiO_2 was possible [64], the fabrication time of custom optical element was still long because of the need for a full set of N photolithographic masks.

In the late seventies and early eighties a direct electron-beam writing of patterns in resists seemed to be a suitable tool for fabrication of custom, continuous-profile optical devices thanks to high lateral resolution 0.05 μm. A fabrication of optical devices using this technique has been reported by Fujita *et al.* [67]. However, the proximity effect (scattering of electrons in a bulk of resist leading to undercuts and overall resolution reduction from 0.05 μm to $\sim$1 μm) has rendered EBL unattractive. Continuous profile writing by EBL posed basically too much technical difficulties leading to expensive vacuum technology and fabrication time penalty of highly sophisticated writing algorithms that were needed for a calculation of proper beam doses and for a compensation of proximity effect. Historically, it seems to be the first rapid-prototyping-like technique for manufacturing of optical elements, however without much further success.

The end of EBL surface profiling was sealed by Gale *et al.* [53] by using a UV laser for an exposure of photoresist instead of an electron gun. There were no problems related to the proximity effect and no need for vacuum environment. Feature size resolution 0.5-5 μm was easily achievable, enabling fabrication of efficient, multilevel and continuous profile DOEs. The true rapid prototyping has become possible, since the time needed to produce the desired micro-structure was less than a day. However, the devices could be produced only in polymer-based resists with maximum structure depths limited to less than 10 μm.

The nineties were the decade of intensive research on laser ablation of various materials by a range of deep UV, UV, visible, near-infrared and infrared lasers. The findings on ablation of polymers and other transparent materials have opened new

possibilities for further enhancement of rapid-prototyping techniques for manufacture of micro-optics. UV lasers have been shown to be capable of clean ablation of polymers [54, 37, 68, 36, 35]. The roughness of resulting surfaces was reported to be 1-15 nm, thus comparable with surface condition of conventional optics.

Behrmann *et al.* [37] have demonstrated an excimer laser based micromachining system dedicated to rapid prototyping of DOEs. The fabrication of four-level, computer generated hologram (CGH), consisting of 512x512 array of 5 μm pixels, could be accomplished in only 20 minutes. The structure was written in a 10 μm thick layer of polyimide on silica substrate. The method utilized a raster scan regime with a spot size of $\sim$1 μm.

Jitsuno *et al.* [54] have shown a successful correction of surface shape of polymer sample for precise phase control, using an excimer ArF laser. This technique was also raster scan based. A phase correction with accuracy $\pm 0.2\lambda$ ($\lambda = 632.8$ nm) has been demonstrated.

In many applications however, like high power laser diode optics, inorganic optical glasses are superior to the polymers in terms of stability and durability. Laser machining of glasses poses technical difficulties, since these materials are transparent in near UV and visible range of radiation, covered by most industrially relevant laser sources [28]. Fused silica has an energy band-gap of $\sim$9.3 eV equivalent to 133 nm wavelength, thus even F_2 laser radiation (157 nm, currently shortest wavelength available from a practical laser) is not efficiently absorbed (absorption coefficient $\alpha = 10$ cm^{-1}). However, F_2 lasers have been shown to cleanly ablate fused silica without cracks, flaking and excessive surface roughness [28]. Material removal rates of 0.1-0.2 μm per pulse at repetition frequency from single to tens of Hz have been reported.

In a visible and near infra-red band only ultrafast lasers can deliver the necessary levels of irradiance that could induce two photon absorption and creation of colour centres in glasses to increase the absorption of light (see Section 2.5, p. 54). A significant amount of research work, dedicated to nano-, pico- and femto-second processing of materials, has been carried out in the last decade [28, 43, 26, 27, 69]. Visible femto-second laser machining of soda lime glass, barium borosilicate and fused silica glasses has been studied by Krüger *et al.* [43] and the machining rates were found to be in a range of 0.2 μm per pulse for silica and 0.4 μm for soda lime. The problem with ultrafast machining of glasses is the quality of resultant

surfaces [28, 43, 26], which undergo micro-patterning, cracking and flaking. These as-machined surfaces were far from optical quality. However, very precise laser shaping of glasses by short wavelength and ultrafast lasers is possible. With improved productivity and resultant surface quality, these technologies have the potential to become the leading precision laser shaping tools of the future.

The infrared lasers, such as CO_2, offer an alternative to UV and ultrafast lasers in a field of micro-machining of glasses. Most glasses strongly absorb CO_2 wavelengths (see Section 2.3.5, p. 36) with absorption lengths from a fraction to hundreds of microns. However, the 10.6 μm wavelength imposes a restriction on a minimum feature size of the machined structures. Additionally, the larger heat affected zones increase the risk of undesired residual stresses that are critical for the performance of miniature optical devices [47, 70, 32]. CO_2 lasers are thus unsuitable for fabrication of fine feature DOEs, but perform pretty well in machining of continuous-profile ROEs with feature size bigger than 100 μm. So far, CO_2 lasers have been successfully applied to direct machining of fiber lenses [71] fiber couplers and tapers [72] and microlenses in fused silica [4, 5, 73]. It has been also shown that CO_2 lasers offer large machining rates (1-10 μm of removed depth per shot, few pico-litres per shot) which are an order of magnitude greater than for other lasers discussed. They also produce ablation sites of exceptional smoothness. The above arguments, combined with kHz range pulse repetition frequencies, make the CO_2 laser machining highly competitive in the field of rapid prototyping of sub-millimeter size ROEs, such as brightness restoring micro-optics discussed in Chapter 7.

The direct maskless machining with CO_2 lasers can even keep up with a performance of ink-jet printing technique, which is renowned for high productivity and flexibility. Ink-jet printing is capable of dispensing spheres of fluid polymers from pico to nano-litres of volume at very high rates, ranging from 0-25000 droplets per second for droplet-on-demand devices [74]. The resolution of ink-jet rapid-prototyping is limited by a minimum droplet diameter (controllable from ~15 to 200 μm), thus the method is also limited to the fabrication of ROEs. ROE can be accurately fabricated by controlling the density of droplet deposition on the target substrate. The surface tension of the viscous epoxy smoothes out the raster pattern and reduces the surface roughness down to a level of optical finish. An additional step is required to accomplish the printing stage. The freshly printed polymer structure has to be UV cured and baked in 110 °C to form a rigid final product [75]. A

fabrication of planar waveguides and efficient polymer refractive microlenses, with diameters ranging from 50 μm to few mm, has been reported [76, 75]. The method has also been applied for the collimation of light from single emitters comprising a high power diode laser bar [75]. Hemispherical micro-lenses (200 μm diameter) were printed onto a glass slide fixed above the diode laser bar. A test of sustained operation (45 hours) at high-power levels delivered by diode laser bar has shown that an optical stability of polymer micro-optical elements is much worse than that of inorganic glasses (total output power drop 0.3W out of 20W). To date, however, no detailed study on aging of polymers illuminated with high power diode lasers has been reported. So far, the CO_2 ablation of silica is advantageous to ink-jet printing with regard to the optical stability of fabricated micro-optics.

5.3 Material removal by overlapping craters

Previous work done on laser processing of silica [4] has shown that it is possible to remove a layer of material in a controlled manner by raster scan machining. The advantage of pulsed laser ablation over the CW variant is the reduction of melt depth and suppression of melt displacement. The lifetime of the ablation site following the pulsed irradiation with the CO_2 laser is more than an order of magnitude shorter than in case of CW scanning in typical experimental conditions. The reduced amount of heat and suppressed thermal diffusion result in a thinner and less mobile layer of molten material. By overlapping the identical craters in a raster scan mode it is possible to quickly cover large areas of the substrate and to control the local depth of resultant surface by appropriate the crater layout in the raster pattern. The question how to accurately control the depth of resultant surface and which way of achieving that is advantageous, has been left unanswered. This work aims at answering the question in a quantitative fashion.

5.3.1 Ideal subtractive model

From Chapter 4 we know that is it feasible to produce smooth circular craters that follow a near-Gaussian profile. It is possible to carry out theoretical derivation of local layer depth as a function of local overlap of such craters, making assumptions of a Gaussian crater profile and an ideal subtractive material removal in the overlapped ablation sites. Figure 5.1 illustrates the definition of local overlap of unit Gaus-

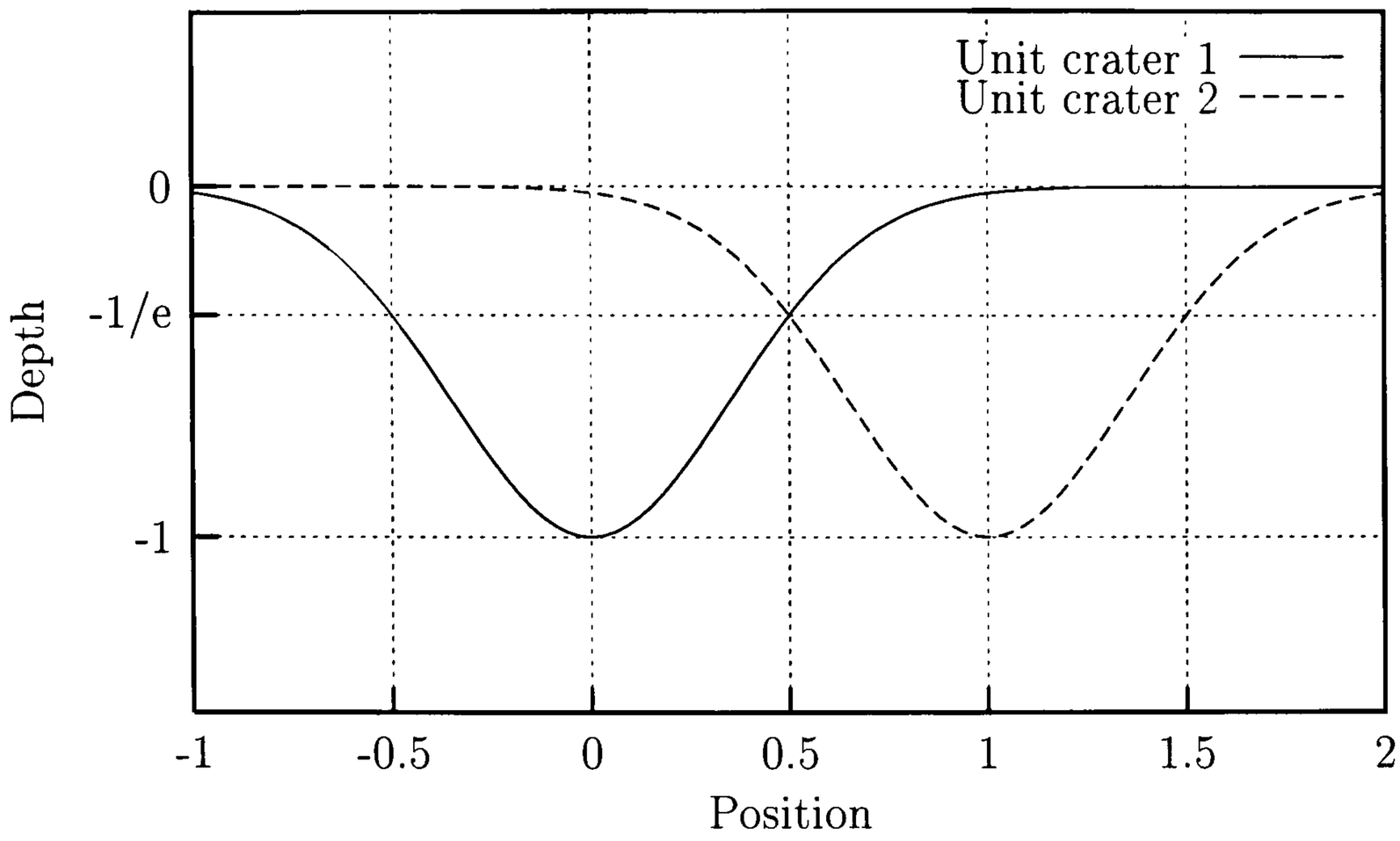

Figure 5.1: Illustration of unit overlap $x_o = 1$ between adjacent unit craters. Unit overlap means that two identical craters are placed one $1/e$ diameter apart.

sian craters in an attempt to normalize the following calculations. Equation 5.1 describes a profile of Gaussian crater with unit depth and unit $1/e$ diameter:

$$\mathrm{C}(x, y) = -\exp\Big(-4\,(x^2 + y^2)\Big) \tag{5.1}$$

By overlapping such craters with overlaps x_o and y_o in orthogonal directions, a layer of material of depth D would be removed:

$$\mathrm{D}(x, y, x_o, y_o) = \sum_{n=-\infty}^{\infty} \sum_{m=-\infty}^{\infty} \mathrm{C}(x - n \cdot x_o\ ,\ y - m \cdot y_o) \tag{5.2}$$

The approach leads to a calculation of family of material removal curves, shown in Figure 5.2, describing the dependence of mean normalized depth ND (relative to a depth of a single crater, which is unity) versus normalized crater overlap in X and Y direction:

$$\mathrm{ND}(x_o, y_o) = -\frac{1}{4\ x_L\ y_L} \int_{-x_L}^{x_L} \int_{-y_L}^{y_L} \mathrm{D}(x, y, x_o, y_o)\ dx\ dy \tag{5.3}$$

where $x_L \to \infty$ and $y_L \to \infty$. These curves describe the case of ideal subtractive material removal, thus the maximum performance of overlapped machining regime. Large machined depth can be expected from the regime, promising single pass machining of structures with depth dynamics of few tens of microns.

A departure from that behaviour can be expected in practice due to existence of machining threshold, as discussed in Section 5.4.5. A series of experiments has

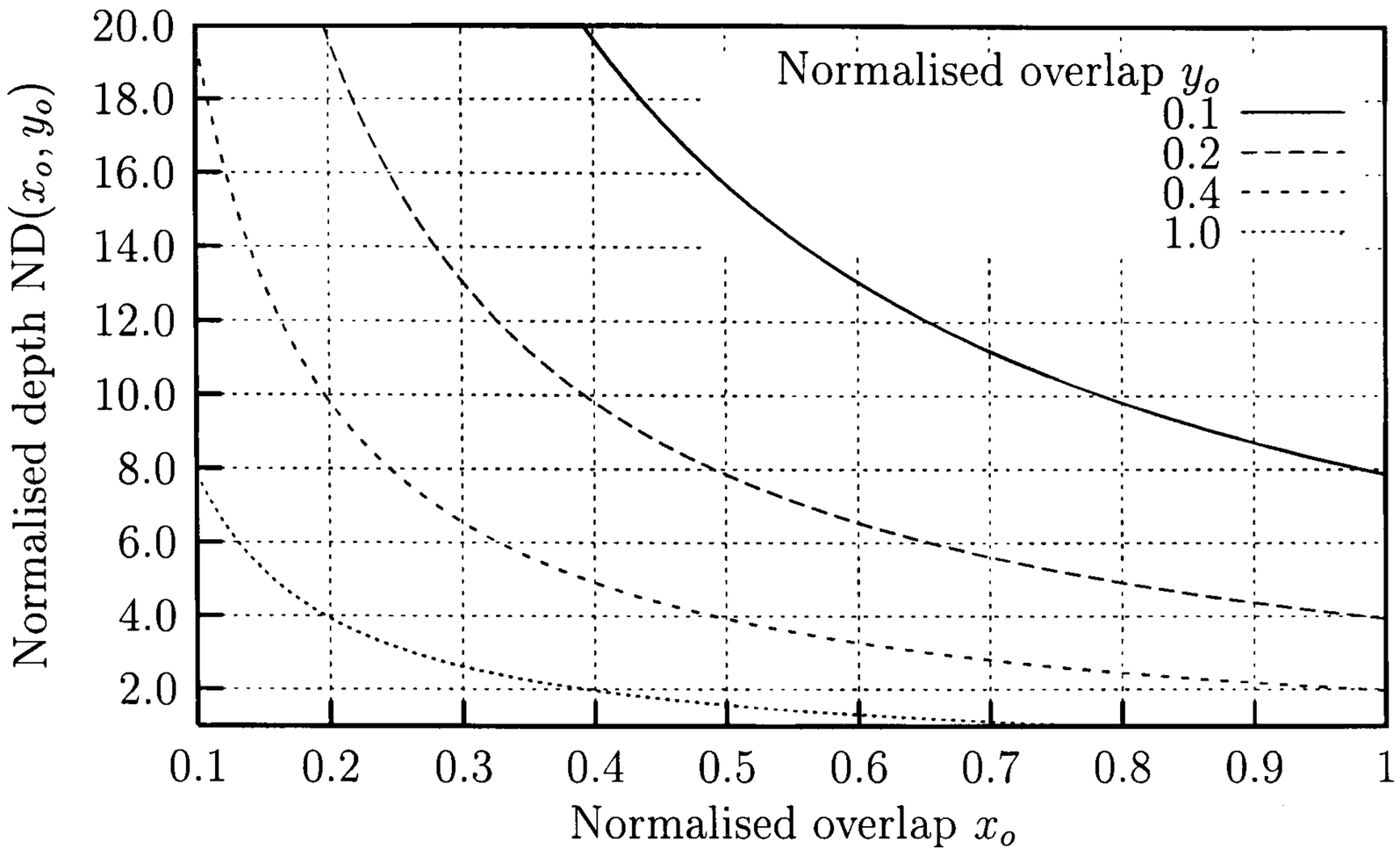

Figure 5.2: Theoretical material removal curves, calculated from Eq. 5.3.

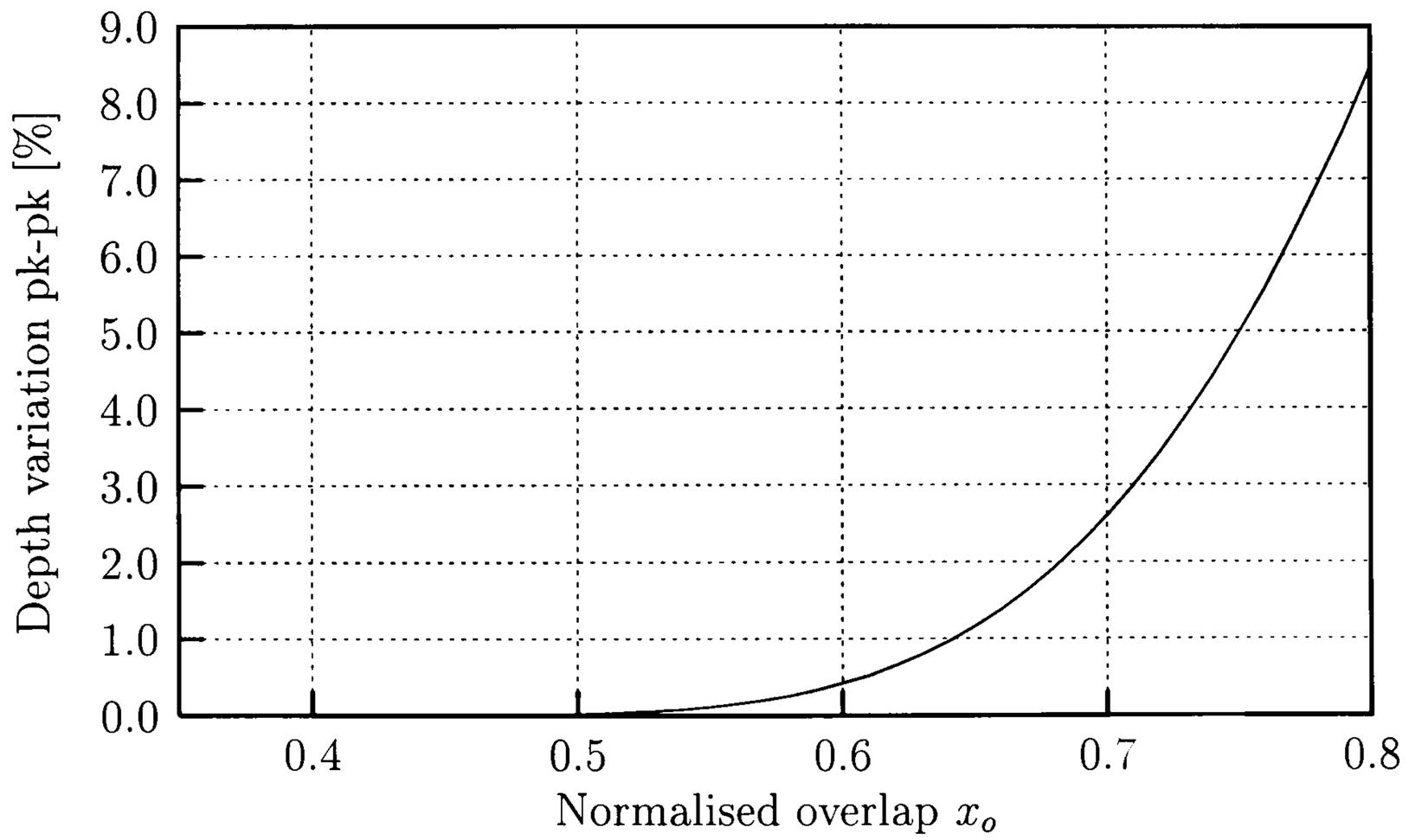

Figure 5.3: Depth variation of a groove created by the overlapped Gaussian craters, relative to the depth of single crater.

been carried out to calibrate the process (see Section 5.5). The surface roughness can also be assessed by the ideal machining model. Figure 5.3 shows relative amplitude of ripples on the bed of simulated groove as a function of crater overlap. Calculations indicate that it is theoretically possible to produce smooth surfaces provided the normalized overlap is smaller than 0.5. In practice however, as shown in Section 5.6.2, the roughness of as-machined surface is the outcome of residual micro-debris production and melt displacement taking place during ablation.

5.4 Development of regimes for fabrication of arbitrary surfaces

There are many possible variations of the raster scan method. A most straitforward solution is to organise the laser spots in a rectangular mesh of fixed pitch. The depth control can be achieved by appropriate fluence modulation per pixel. Such technique has been successfully used by many researchers [53, 37, 35] for machining of binary and continuous-relief, micro-optical elements. However, the need for a very precise control over an absolute value of laser pulse energy in order to control the cutting depth is a drawback of this technique.

The distinctive feature of slab waveguide CO_2 lasers is the possibility of asynchronous pulsing in a wide range of pulse repetition frequencies, from hundreds Hz to few kHz. Bearing in mind the above, I've decided that it's more beneficial to study the method that enables broader and more systematic investigation of machining regimes and at the same time avoids excess technical development: the raster scan technique with variable overlap between craters created by pulses of fixed energy. The strategy is depicted in Figure 5.4. In this case only long term laser stability and fine resolution of translation stages are required for an accurate control over the cutting depth. The data obtained in the study can also be used to characterise the technique based on fixed raster scan writing. It can be achieved by an investigation of machining characteristics as a function of pulse fluence.

There are technical limitations and physical effects that must be taken into account when considering the applicability of raster scan machining, such as the characteristics of laser operation (see Section 3.3 p.68) and the limitation of crater production rate $CPR_l = 200$Hz due to the thermal memory effect (see Section 4.11 p.102). Variable overlap between adjacent craters, needed for a depth control, re-

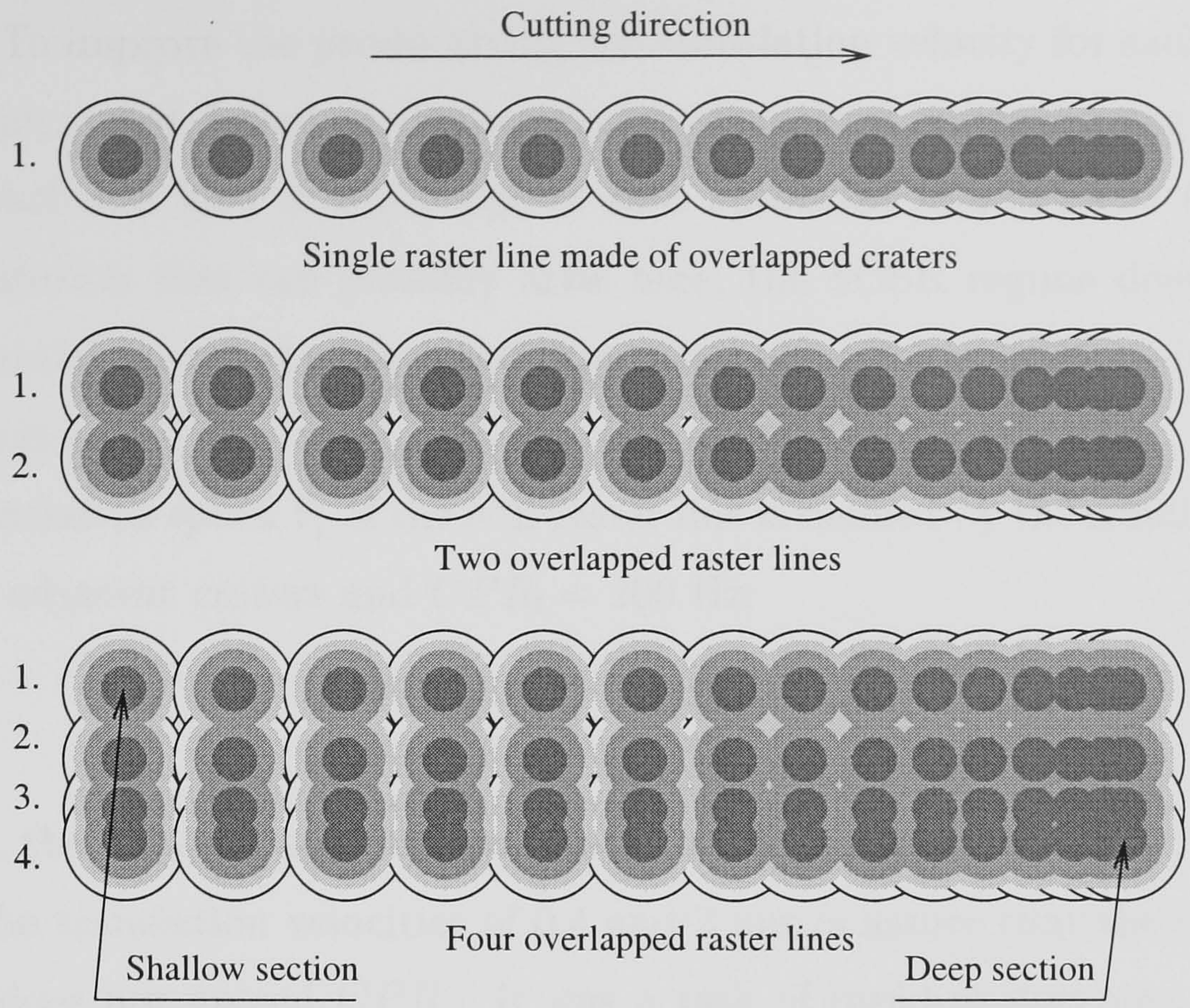

Figure 5.4: Illustration of raster scan machining technique with the variable overlap of ablation craters. The overlap between craters can be arbitrarily varied in orthogonal directions of the raster to implement the depth control.

quired an aperiodic laser firing within a frequency range defined by the raster scan setup, such as translation speed of the substrate and the crater layout. Unfortunately, the pulse energy of the laser used varied with the frequency above a threshold value of 800 Hz, as shown in Figure 3.6 p. 70. Another thing to bear in mind was a thermal memory effect (see Section 4.11 p. 102), which reduced the machining threshold of sequentially overlapped craters. The effect could be avoided by limiting the crater production rate (CPR) down to 200 Hz, as the experiment presented in Section 4.11 has shown.

5.4.1 Slow machining regime of optimised translation speed (SOSR)

The slow cutting regime was chronologically the first to be studied. CPR was kept below 200 Hz to avoid thermal coupling of adjacent ablation sites, thus this machining regime was inherently unproductive. The translation speed of the substrate was defined by the smallest crater spacing (deepest section of the surface, as depicted in Figure 5.4), thus in most cases of practical crater spacing the speed was limited to

0.4 mm/s. To improve the productivity, the translation velocity for each raster line had to be calculated, based on the knowledge of smallest crater spacing and CPR_l. Such approach has lead to a concept of *slow optimised speed regime* (SOSR). To avoid a confusion that can possibly arise here, the SOSR regime does not imply that the translation speed of the substrate varies along the raster line, it is actually kept constant.

The translation speed V_i of the i-th raster line is defined by the smallest distance d_i between adjacent craters and $CPR_l = 200$ Hz:

$$V_i = d_i \cdot CPR_l \tag{5.4}$$

In practice, the minimal and maximal crater overlaps encountered are 2 μm and 10 μm, thus the translation velocities of 0.4 and 2 mm/s assure that the crater placement rate does not exceed CPR_l. It was a task of rapid-prototyping programme (see Section 3.4) to calculate the translation speed for every individual raster line, knowing the frequency limit and smallest distance between adjacent craters in each raster line.

In spite of the fact that the SOSR was unproductive, it provided an insight into the real characteristics of rasterized material removal. It also helped to specify the range of optimal parameters, such as crater overlap and crater depth, providing good depth control and little machining debris.

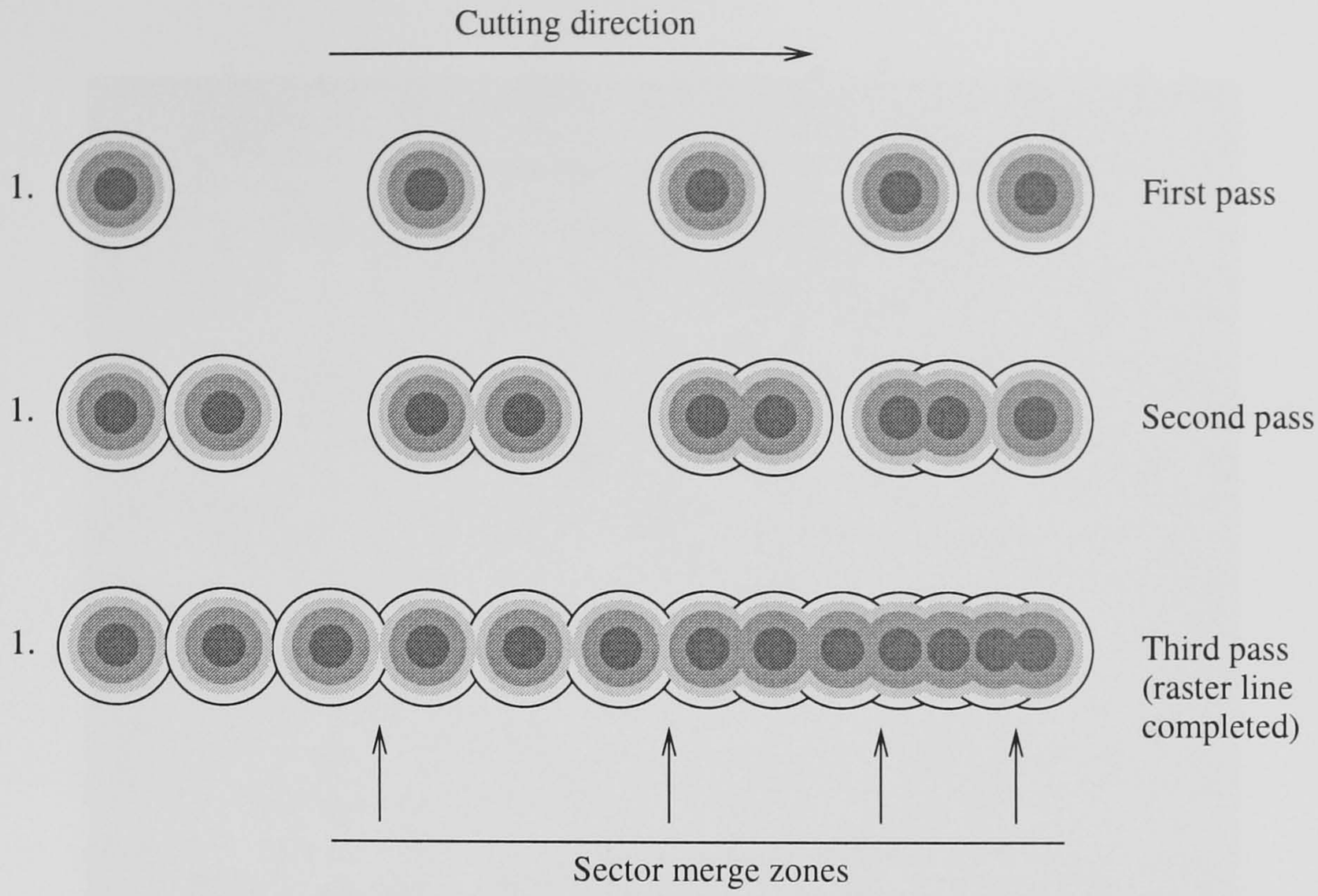

Figure 5.5: Illustration of the interleaved raster scan machining with overlapped craters. An example of interleaving of every fourth crater. Three passes are then required to write a full raster line.

5.4.2 Fast interleaved machining regime

The limit of crater placement rate, described in Section 5.4.1 can be lifted by the *interleaving* technique of placing the craters far apart from each other. Each raster line is divided into a number of sectors, which are also cut sequentially but experience much lower crater production rate. The craters in each sector are thus thermally separated even if the actual CPR is increased beyond CPR_l. The technique is illustrated in Figure 5.5. An overhead of additional passes per line can be compensated by the increase of translation speed. However, an experiment has shown that seamless merge of the interleaved zones does not take place, since the characteristics of material removal depends significantly on the geometry of ablation site (see Section 5.4.5 for analysis of cutting front geometry). An increase of machining threshold in the merge zones takes place and the ridges, few microns high, are created, as seen in Figure 5.6. These unwanted morphological features have ruled out the usefulness of interleaving for the fabrication of smooth, continuous-profile structures. The formation of ridges does not occur during ordinary sequential cutting, because the ablation site topography is practically unchanged from one laser shot to another, for a fixed spacing between craters.

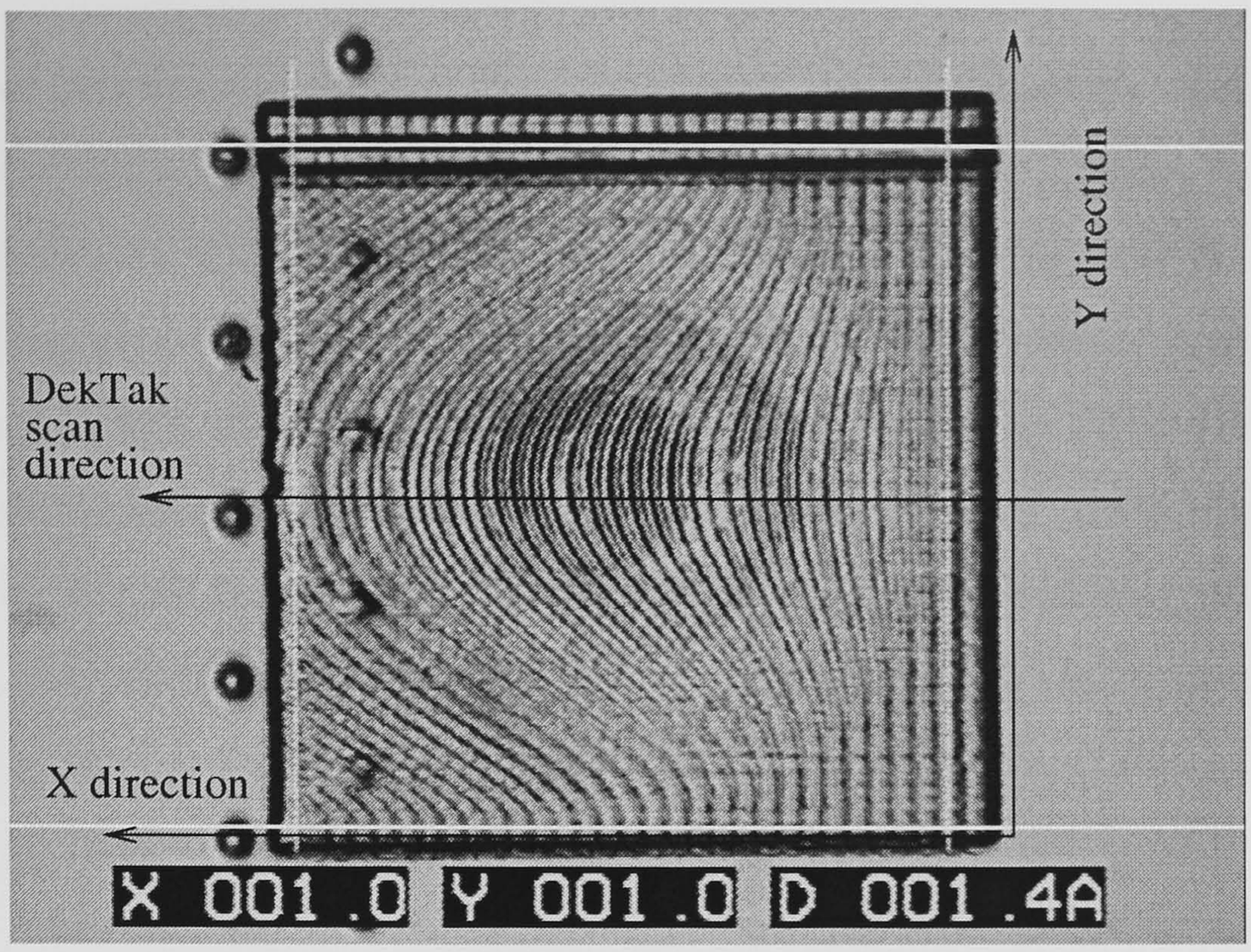

Figure 5.6: Micrograph of the as-machined microlens made with interleaving of every fourth crater. Lens diameter 1 mm, sag 10 μm. Distinctive ridges have been created in the merge zones, giving rise to ± 2 μm roughness. CPR=500 Hz in deepest sections. X axis corresponds to the raster scan direction. Digital readout in mm.

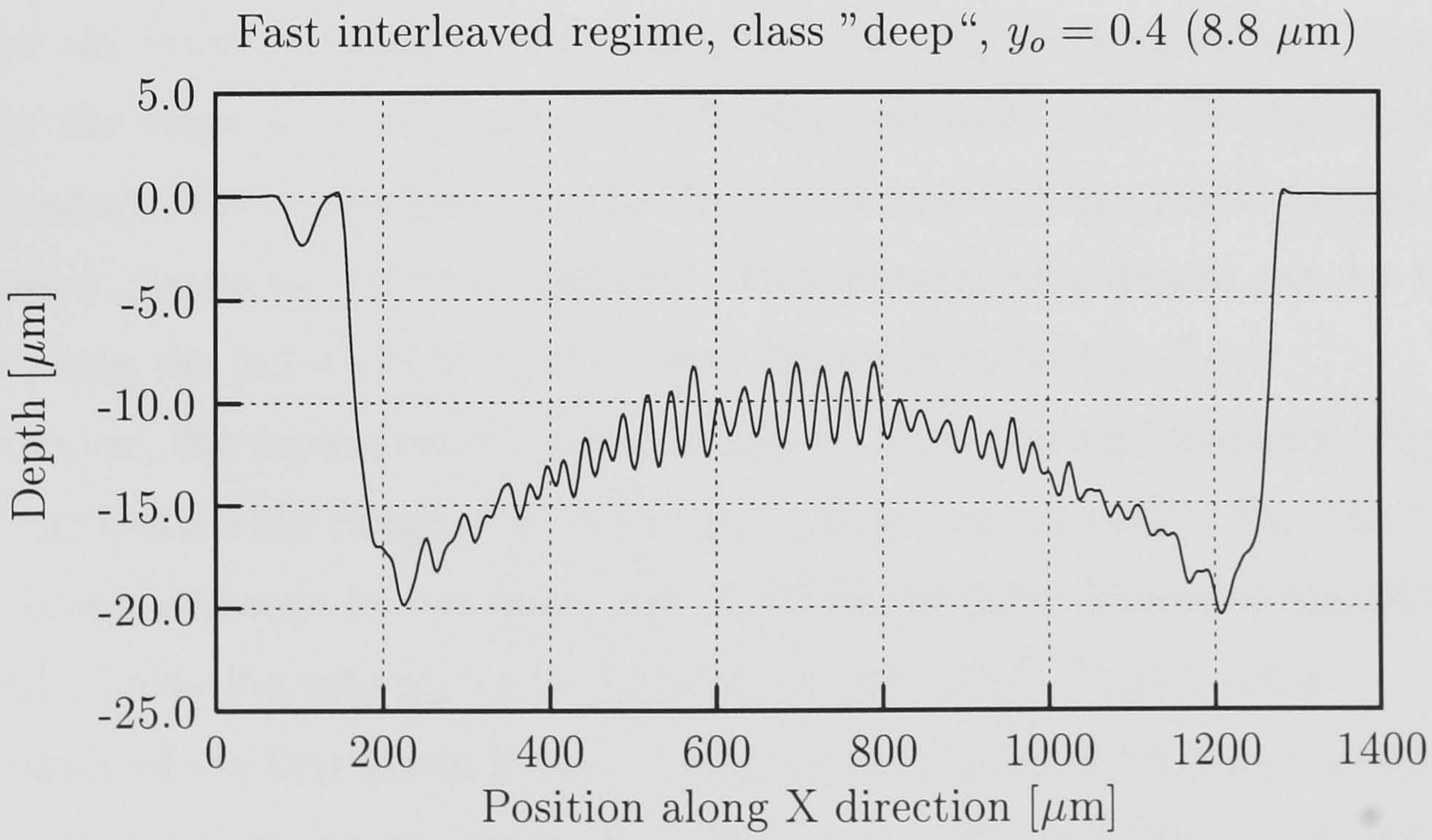

Figure 5.7: DekTak^{TM} profile of the microlens from Figure 5.6. The peak-peak amplitude of the ridges is as much as 4 μm. The machining conditions are explained in more detail in Section 5.5.

5.4.3 Fast machining regime of fixed translation speed (FFSR)

The failure of fast interleaved machining regime to boost the productivity has raised a question whether the thermal coupling could be turned into advantage. Section 5.5 p.124 demonstrates that the increase of machining depth range can be achieved by allowing the crater production rate to exceed the frequency limit of thermal memory effect. In contrast to the SOSR and the interleaving regimes discussed earlier, the *fast fixed speed regime* (FFSR) allows for the reduction of machining threshold. Now, it is the translation speed V of the raster line and the global, minimal crater overlap d_{min} (smallest spacing between craters in a whole of raster lines comprising the structure) that determine maximal crater production rate CPR_{max}, which may exceed the thermal memory limit CPR_l:

$$CPR_{max} = \frac{V}{d_{min}} \tag{5.5}$$

The translation speed has now to be *fixed* for all raster lines, because CPR depends on the crater spacing. It is thus important to assure the same CPR for all areas of the same crater spacing. The FFSR is thus intrinsically more productive than SOSR.

Thermal memory effect can be used to compensate for the increased machining threshold on the slopes of cutting front, as discussed later in Section 5.4.5. The smaller the crater spacing in the raster line, the bigger the developed depth and steeper the angle of cutting slope seen by the next laser spot. On the other hand, the memory effect is stronger in the deepest sections of machined surface, where the crater production rate is highest. This natural mechanism can be used to compensate the influence of cutting angle discussed in Section 5.4.5.

However, the dependence of pulse energy on laser pulsing frequency (Figure 3.6 p.70) has limited the range of allowed pulsing frequencies to 0-800 Hz. The minimal 4 μm crater distance in the raster line and 800 Hz limit determine the maximum allowed translation velocity to be 3.2 mm/s, as shown in Section 5.5.2.

In spite of the limitation, it was possible to obtain the machining characteristics for the translation speeds larger than 3.2 mm/s. The velocities of 10 mm/s and 20 mm/s (2.5 kHz and 5 kHz maximum crater production rate on minimal 4 μm pitch) have been studied thanks to the technique described in Section 5.4.4. These regimes of high scanning velocity offer high productivity and increased machining dynamics, they do however approach the mode of CW laser ablation, which has

been concluded undesirable. It is especially apparent on the example of 20 mm/s scan velocity (see Section 5.5.2), where ablation of deep sections nearly approaches the CW limit.

5.4.4 Stabilisation of laser pulsing frequency

All of the cutting regimes discussed so far utilized the modulation of crater production rate CPR to control the overlap between adjacent craters in the raster line. The available range of CPR was dictated by laser stability and was limited to 0-800 Hz (see Figure 3.6). It was also not recommended to pulse the laser in such a wide range of frequencies. The range of pulsing frequencies can be minimized by inserting idle laser pulses in the raster line. It can be accomplished during the generation of LSD file, containing the information on desired crater layout. Raster lines were being filled up with idle laser pulses (energy of these pulses was directed into a beam dump by AOM) to maintain quasi-constant laser firing rate. Filling ratio m is a number of equal sections d_s the smallest crater spacing d_{min} in the raster line is divided into:

$$d_s = \frac{1}{m}\, d_{min} \tag{5.6}$$

The task of the programme was to find the smallest spacing d_{min} and to monitor the spacing between the adjacent craters in each raster line and try to fit an integral number of sections d_s in between the craters. The result of such operation is a narrower range of laser pulsing frequencies and increased laser pulse repetition frequency, which is desirable when cutting below the $CPR_l = 200$ Hz limit, as in case of SOSR regime. The range of PRF is then defined as:

$$\begin{aligned} PRF_{min} &= CPR_{max} \cdot \frac{m^2}{m+1} \\ PRF_{max} &= CPR_{max} \cdot m \end{aligned}$$

It is thus possible to run the laser in a range 450−600 Hz ($m = 3$) while the crater production rate can vary from practically zero to 200 Hz. The bigger the m the narrower the PRF range. In practice however $m = 3$ has been found to be optimal, since PRF did not exceed 800 Hz limit.

Exactly the same technique can be applied to the FFSR regime. The problem that arises is the nonzero range of PRF, which may exceed the 800 Hz limit. The 3.2 mm/s FFSR did not allow that to happen. The faster regimes 10 mm/s and 20 mm/s, suffered from PRF caused pulse energy instability and could not be used

for cutting of continuous surfaces. It was possible, however, to obtain calibration curves thanks to the technique described in this Section.

5.4.5 Cutting front considerations - influence of polarisation and machining threshold

The way of removing the material by the overlapped craters is unavoidably associated with the creation of an inclined cutting front. Since the laser ablation takes place mostly on the slope, which can be as steep as 45°, the irradiance reduction as well as the polarisation effects play an important role in the dynamics of cutting.

Increase of machining threshold on cut slopes. The irradiance drop causes the increase of machining threshold and reduction of material removing rate (see Sections 4.4 and 4.5). This is the primary mechanism behind the departure of the machining curves, presented later in Section 5.5, from the ideal ones displayed in Figure 5.2. However, the influence of laser polarisation cannot be ignored either, since the cutting slopes approach the Brewster angle (refractive index $n \simeq 2.2$ for silica at 10.6 μm wavelength), at which the polarisation effects are most distinctive:

$$\alpha_B = \tan^{-1}(n),\ \alpha_B = 65.5^\circ \tag{5.7}$$

Figure 5.8 shows the cross-sections of grooves created by a series of evenly spaced, ideal Gaussian ablation craters. The profile of a single crater is supplied for comparison. The cut depth depends on the crater spacing, and the slope angle, as seen by the next laser spot, depends on the groove depth. Figure 5.9 displays the dependence, obtained numerically from Equation 5.2. The critical angle α_{sc} exists, above which the machining threshold F_{mth} exceeds the laser pulse fluence F_m and no material removal takes place. For typical machining conditions, given in Section 4.10 p.102, the angle can be found by reading the value of threshold irradiance I_{mth} for a threshold fluence equal to F_m from Figure 4.4 p.88:

$$\alpha_{sc} = \cos^{-1}(I_{mth}|_{F_m} \cdot \frac{t_m}{F_m}) \tag{5.8}$$

where t_m is the pulse duration. The calculation yields $\alpha_{sc} = 65.7^\circ$, which accidentally coincides with the value of Brewster angle α_B. In practice, the α_{sc} has not been reached, as seen in Figure 5.9. The smallest relative crater spacing used in the experiments was 0.1 for the practical conditions from Section 4.10 p.102. The

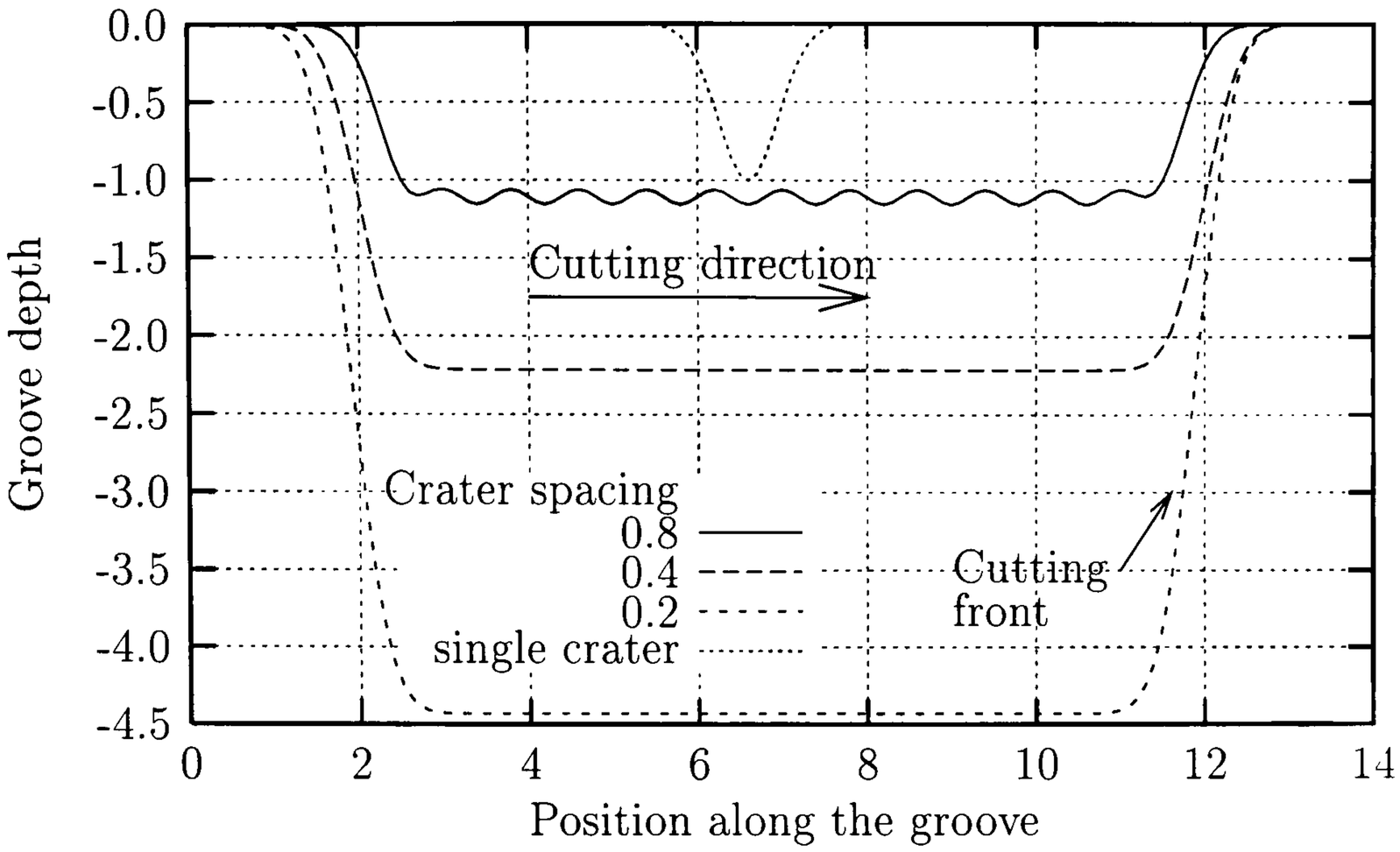

Figure 5.8: Cross-sections of grooves made by overlapping, unit Gaussian craters. The smaller the crater spacing, the steeper the cutting front. Single crater shown for comparison.

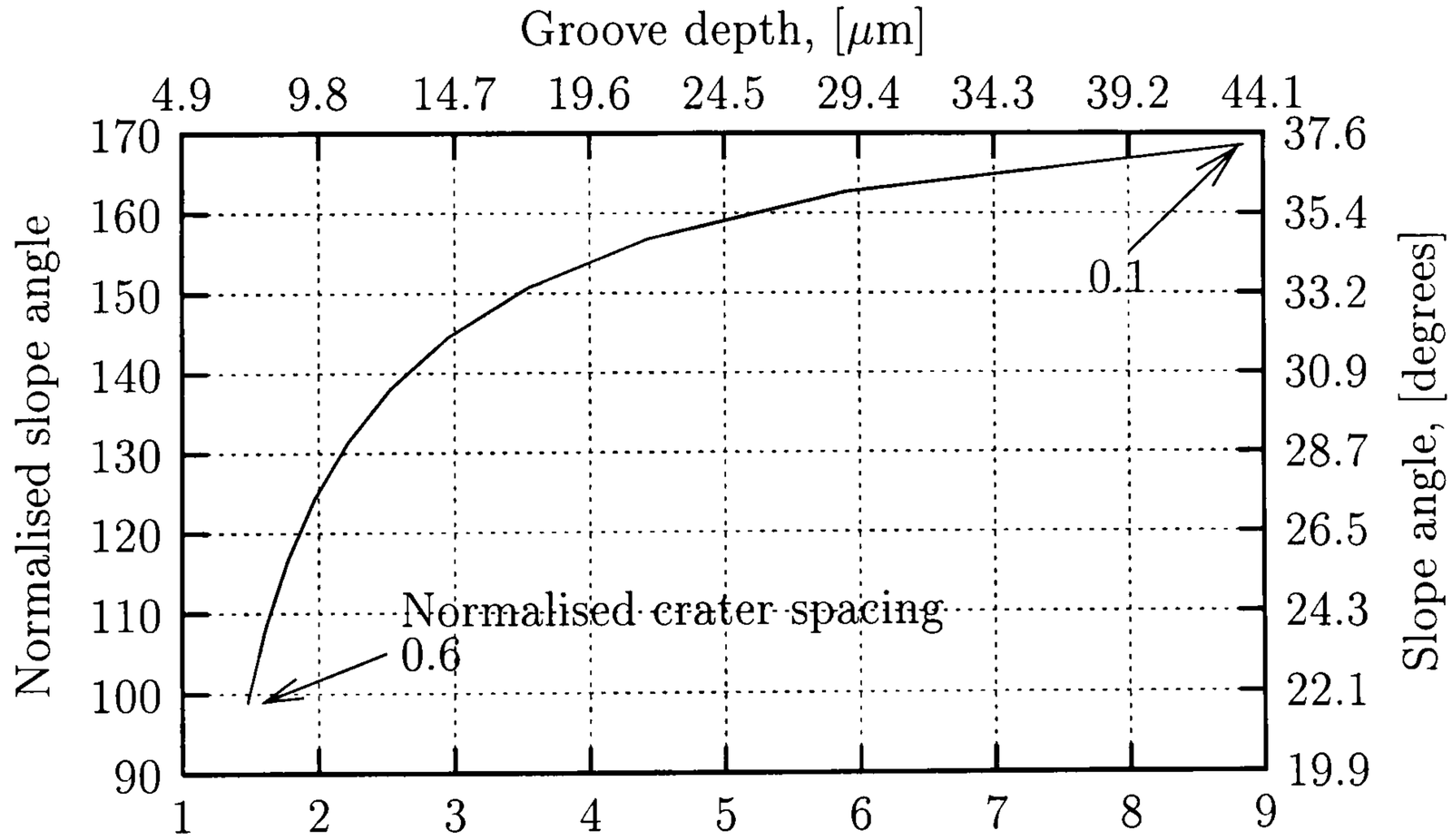

Figure 5.9: Cutting front angle experienced by a center of the next laser spot while cutting the groove. Calculated for the crater parameters from Section 4.10 p.102, diameter 22 μm and depth of 4.9 μm. Groove depth was normalized with respect to the single crater, slope angle was normalized with regard to the crater aspect ratio.

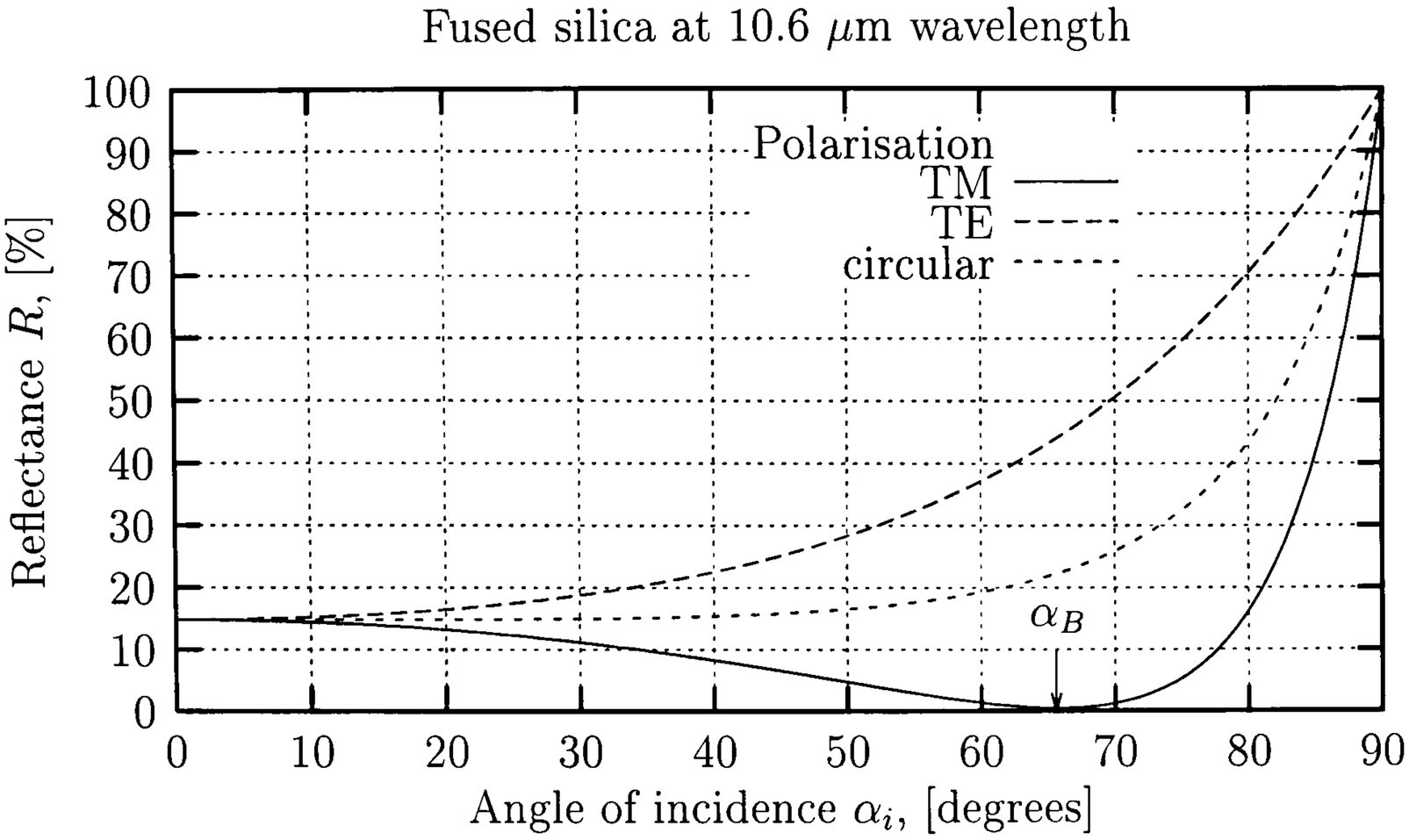

Figure 5.10: Reflectance R of silica at 10.6 μm wavelength for two polarisations TM and TE as a function of incidence angle α_i. The complex refractive index n' is $2.3+i0.3$

influence of polarisation is thus much weaker than the impact of the slope angle on a value of irradiance.

The calculations have been carried out assuming no thermal coupling between adjacent laser pulses. The critical angle α_{sc}, and the achievable cut depth, can be bigger if thermal coupling is allowed, as shown in Section 5.5.2. Since the machining threshold is reduced to zero, now the value of threshold irradiance $\sim$200 kW/cm^2 alone determines the maximum value of α_{sc}, as seen in Figure 4.5 p.89. The angle α_{sc} is now 69°.

Influence of polarisation. The reflectance experienced by the polarised laser beam depends strongly on the incidence angle α_i, as shown in Figure 5.10. The reflectance R for TM and TE (Eq. 5.9 and 5.10) polarisations has been calculated from the Fresnel equations (Ref. [77] p.112) as a function of incidence angle α_i.

$$R_{TM} = r_{TM} \cdot r^*_{TM}, \quad r_{TM} = \frac{n' \cos\alpha_i - n_i \cos\alpha_t}{n' \cos\alpha_i + n_i \cos\alpha_t} \tag{5.9}$$

$$R_{TE} = r_{TE} \cdot r^*_{TE}, \quad r_{TE} = \frac{n_i \cos\alpha_i - n' \cos\alpha_t}{n_i \cos\alpha_i + n' \cos\alpha_t} \tag{5.10}$$

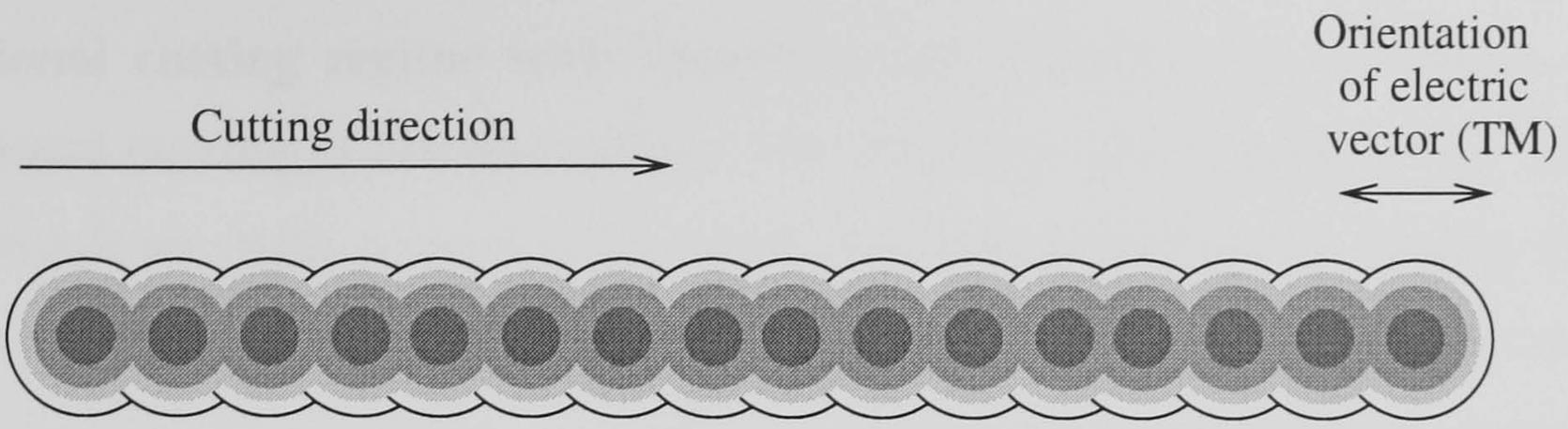

Figure 5.11: TM-polarised laser beam allows for better coupling of light in case of groove cutting.

where n_i is the refractive index of air, $n' = n + ik$ is the complex refractive index of silica and α_t is related to α_i by Formula 5.11.

$$\cos^2 \alpha_t = 1 - \frac{n_i^2}{(n')^2} \sin^2 \alpha_i \tag{5.11}$$

As can be seen in Figure 5.10, TM polarisation is optimal for groove cutting, since the coupling of laser light into the material increases with the angle of incidence. The grooves cut with TM polarisation will be deeper and narrower than those cut with TE polarisation. Figure 5.11 illustrates the experimental setup that utilizes the TM-polarised laser beam.

The fabrication of arbitrary surfaces differs from single groove cutting, since the overlap of many grooves is now necessary. The resultant cutting slope has now two orthogonal components of the incidence angle, which are the function of crater and groove spacings. The reflectance R may now occupy the region in Figure 5.10 between the TM and TE characteristics. It complicates the situation, but is not critical since the slope angle does not usually exceed α_{sc}. If the circular polarisation of the beam was provided, the reflectance would increase only by 5% in the anticipated range of cut slopes. In the experiments, however, the TM polarisation has been used, as illustrated in Figure 5.11, because a similar behaviour to that of the circular polarisation can be expected in most situations, where orthogonal components of α_i are similar. Nevertheless, the problem of polarisation can be ignored by calibrating the cut depth, as described in Section 5.5.

5.4.6 Unidirectional vs bidirectional cutting

The influence of polarisation is not critical for the machining of arbitrary surfaces, as shown in Section 5.4.5, but may contribute to additional surface roughness if

bidirectional cutting regime with linearly polarised beam is considered. During bidirectional cutting of the flat surface, the longitudinal component of a normal to the cutting front (with respect to the scan line) changes sign with cutting direction. The symmetry of cutting conditions is undisturbed as long as the beam polarisation is aligned with the scan line. In practice however, the polarisation vector is not perfectly aligned and slightly different reflectance for two cutting directions can be expected.

This problem can be solved by using the circularly polarised beam. However, a simpler solution is also possible in a form of unidirectional cutting with TM polarised beam. The experiments have shown that such mode does not infer productivity penalty since the return velocity of the translation stage can be much higher than the scan speed. The unidirectional cutting has been used for production of micro-structures in this thesis.

5.5 Experimental characterisation of machining regimes

Whichever machining regime is chosen it must be calibrated to obtain real machining curves. The types of studied regimes are listed in Table 5.1. The overlap x_o

See Section	Regime type	Velocity [mm/s]	Max. CPR [Hz]	x_o range	y_o range
5.5.1	SOSR	0.4 - 2.8	200	0.1 - 1.0	0.1 - 1.0
	FFSR	3.2	800	0.2 - 1.0	0.2 - 0.5
5.5.2	FFSR	10	2500	0.2 - 1.0	0.2 - 0.5
	FFSR	20	5000	0.2 - 1.0	0.2 - 0.5

Table 5.1: Characteristics of studied regimes. CPR stands for the crater production rate.

corresponds to the crater separation in the raster line while the overlap y_o specifies the separation of raster lines. These entities have been presented here in a normalized form to provide a link to the theoretical machining curves shown in Figure 5.2.

Depth class	Depth C_d [μm]	$1/e$ Diameter $C_\varnothing$ [μm]	Aspect ratio [%]	Fluence F_m $\left[\frac{\mathrm{J}}{\mathrm{cm}^2}\right]$
shallow	1.30	19.5	6.6	17.3
medium	2.10	20.5	10.2	20.8
deep	4.90	22.1	22.1	27.9

Aspect ratio defined as $\frac{\text{Depth}}{\text{Diameter}} \cdot 100\%$

Table 5.2: Classes of crater depth. All craters made with minimal spot diameter of 47 μm.

It is easy to convert the normalized notation of crater spacing x_o and raster line spacing y_o into the engineering units X_o and Y_o:

$$X_o = x_o \cdot C_\varnothing \ [\mu\mathrm{m}] \tag{5.12}$$

$$Y_o = y_o \cdot C_\varnothing \ [\mu\mathrm{m}] \tag{5.13}$$

where $C_\varnothing$ is the crater diameter, as shown in Table 5.2. In a similar way, the normalized depth ND from Figure 5.2 can be converted into the depth D of the resultant surface knowing the crater depth C_d:

$$\mathrm{D} = \mathrm{ND} \cdot C_d \tag{5.14}$$

The influence of crater depth on a character of machining curves has also been investigated. Three classes of crater depths were defined (as shown in Table 5.2) to facilitate the analysis. The "shallow" craters were made with a fluence just slightly above the machining threshold. The "deep" craters were close to optimal since the fluence required was well above the machining threshold and below the upper limit of crater aspect ratio 0.5. It has been shown that an interference of light reflected from the walls of deep crater (aspect ratio >0.5) was responsible for departure from a near-Gaussian crater profile [4].

In order to measure the real machining curves, a set of step, terrace-like structures per each regime have been computer generated and written into silica substrate (see Figures 5.13 and 5.12) together with the reference craters. The fabricated structures have been subsequently measured by DekTak^{TM} profiler with accuracy

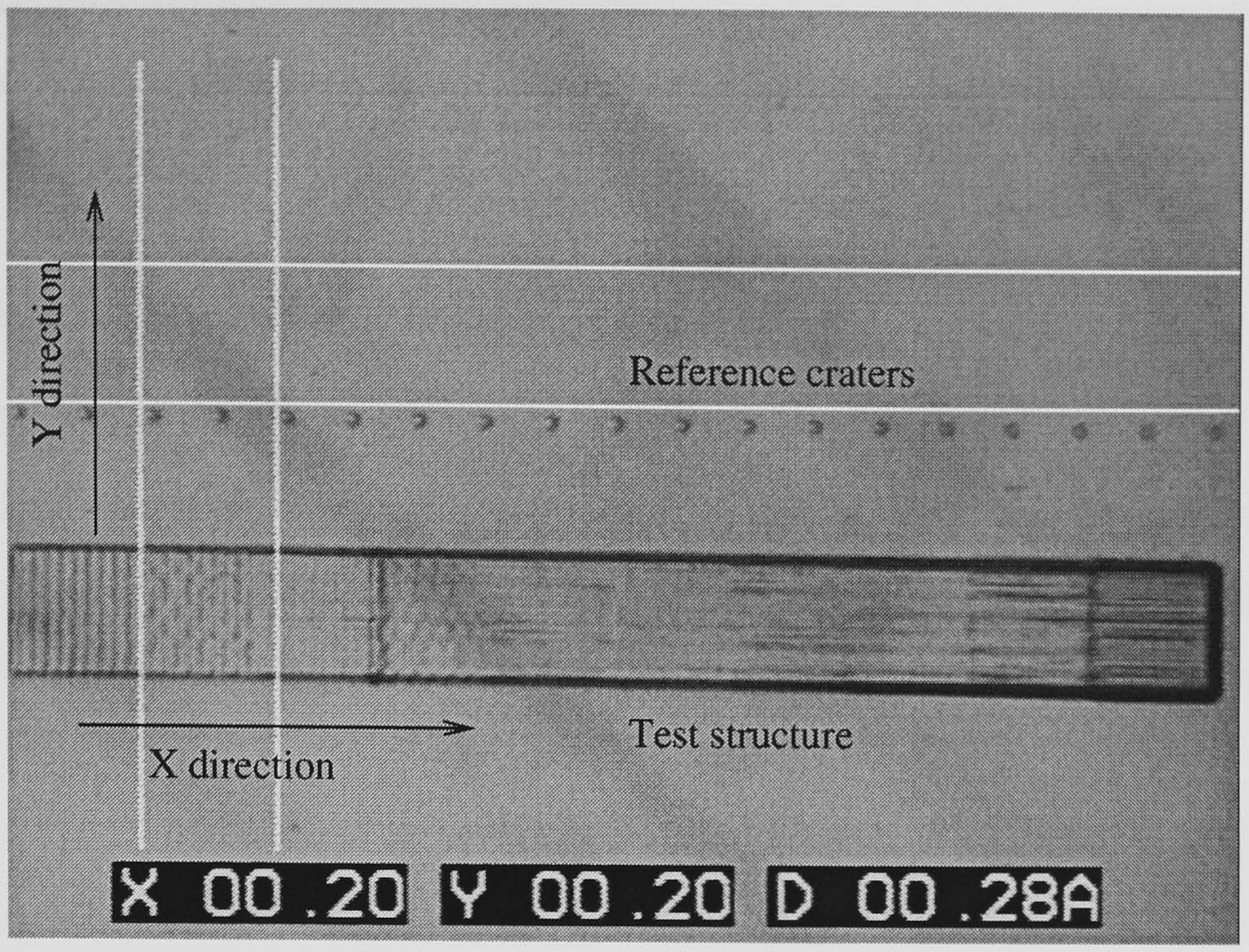

Figure 5.12: Micrograph of the calibration structure, digital readout in millimeters. The reference, single-shot craters (depth class "deep", 4.90 μm deep and 22 μm diameter) are visible above the structure, which consists of 25 horizontal raster lines, spaced by 8 μm. Each of ten 200×200 μm sections corresponds to a different x_o, as indicated in Figure 5.13. The structure has been machined using the SOSR regime.

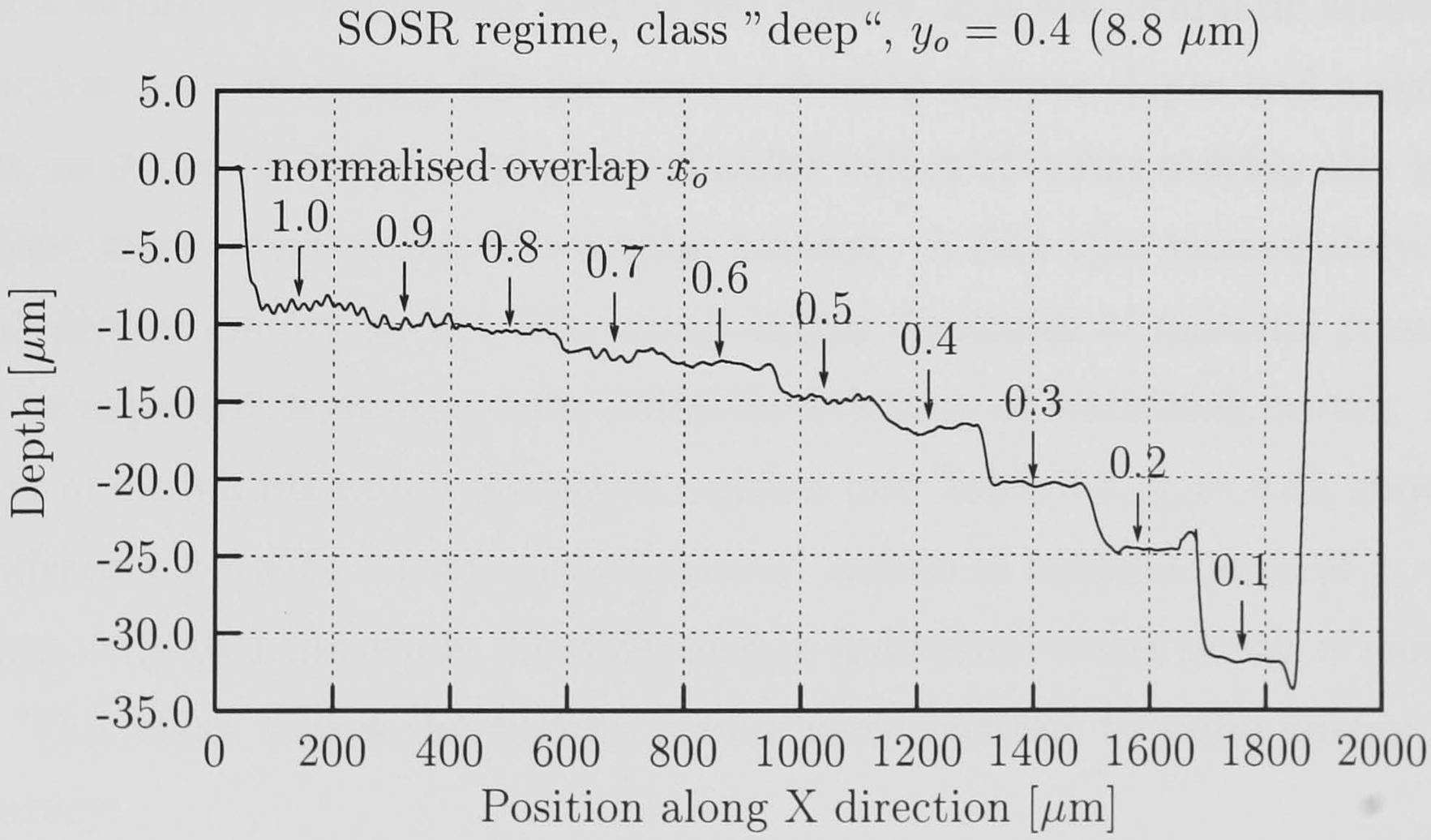

Figure 5.13: Measured profile of the calibration structure. Normalized overlap of raster lines $y_o = 0.4$ corresponds to 8 μm spacing. Normalized crater spacing ranges from 0.1 to 1.0 with 0.1 increment (2.2 to 22 μm).

better than ±0.1% (±10 nm) and the acquired data has been normalized for direct comparison with ideal material removal from Equation 5.3. The experimental data is presented in Sections 5.5.1 and 5.5.2.

5.5.1 Calibration of SOSR regime

SOSR regime was the first one to be characterised and analyzed. Test structures covered a full range of reasonable values of x_o and y_o overlap, ranging from 0.1 to 1.0, enabling direct comparison between theoretical expectations and experimental results. Due to a large amount of collected data the comparison is presented in a number of Figures 5.14 to 5.19 for greater clarity.

It has been pointed out in Section 5.3 that overlaps bigger than 0.7 do not produce smooth surfaces. Except for proving that the experiments have also shown that the overlaps smaller than 0.2 give rise to increased production of machining debris and reduction of machining repeatability.

The measured curves depart significantly from the ideal machining characteristics. The difference is inversely proportional to the value of crater overlap and proportional to the crater aspect ratio. The suspected mechanism behind that behaviour is an increase of machining threshold (see Section 5.4.5). It arose due to two main factors: lower level of irradiance on the machined slope, being a product of a sequence of previously overlapped craters, and also dramatic alteration of interaction zone geometry. Deeper craters develop steeper slopes and amplify the effects, as it can be seen on the plots. Smaller values of crater overlap also increase the slope angle, thus acting in a similar manner. A fact that immediately follows is that deeper craters do not offer much higher dynamics of material removal, as could be expected, leading to substantial linearisation of machining curves. A comparison of machining range of studied regimes (see Table 5.3, $y_o = 0.5$), shows that the difference between "deep" and "medium" classes in optimal range of x_o overlap amounts only to 1 μm while the difference in individual crater depth is more than 50%. This effect makes the cutting regime more immune to pulse energy setting inaccuracy.

The overall productivity is then a compromise between the maximum machining dynamics and maximum separation between raster lines. The bigger the separation between the raster lines the smaller is the number of lines necessary to write the desired shape. However, the separation too big may result in excess surface roughness

and the reduction of depth dynamics. If line spacing is too small, the productivity penalty and excessive amounts of machining debris may counterbalance the gain in depth dynamics. In the light of results presented in Table 5.3, I've concluded that 0.3-0.5 range of overlap y_o and "deep" craters are optimal for machining of surfaces in SOSR regime.

Spacing between lines (y_o) [μm]	Min. depth ($x_o = 0.7$) D_{min} [μm]	Max. depth ($x_o = 0.2$) D_{max} [μm]	Machining range $D_{max} - D_{min}$ [μm]	Comment
		Crater depth class "deep"		
(0.6) 13.3	8.20	20.54	12.34	
(0.5) 11.0	9.25	23.54	14.29	Highest productivity
(0.4) 8.8	10.88	23.64	12.76	
(0.3) 6.6	13.68	26.41	12.72	
(0.2) 4.4	17.41	29.72	12.31	Lots of debris
		Crater depth class "medium"		
(0.6) 12.3	3.49	10.65	7.16	
(0.5) 10.2	4.36	17.66	13.30	Highest productivity
(0.4) 8.2	5.09	18.02	12.93	
(0.3) 6.1	6.78	20.61	13.83	
(0.2) 4.1	9.43	17.57	8.14	Debris
		Crater depth class "shallow"		
(0.6) 11.7	2.06	6.44	4.38	
(0.5) 9.7	2.63	10.65	8.02	
(0.4) 7.8	3.09	12.48	9.36	Highest productivity
(0.3) 5.8	4.31	14.18	9.87	
(0.2) 3.9	5.44	15.05	9.61	Little debris

Table 5.3: Performance of SOSR regime - a summary. Highest productivity is defined as a compromise between maximal machining depth range and minimal number of raster lines necessary (maximal y_o). Crater depth classes are described in detail in Table 5.2.

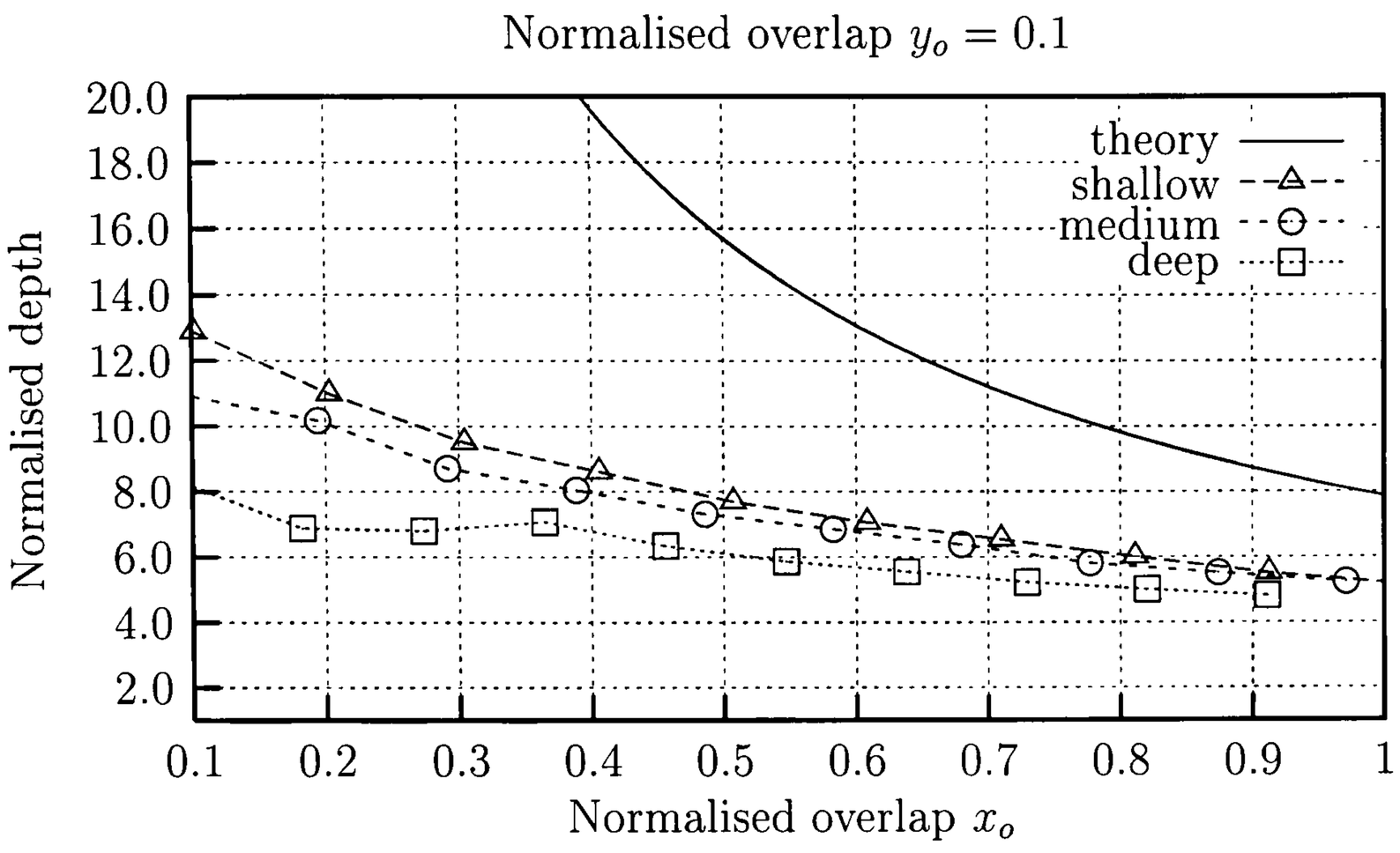

Figure 5.14: Machining curves of SOSR regime, $y_o = 0.1$.

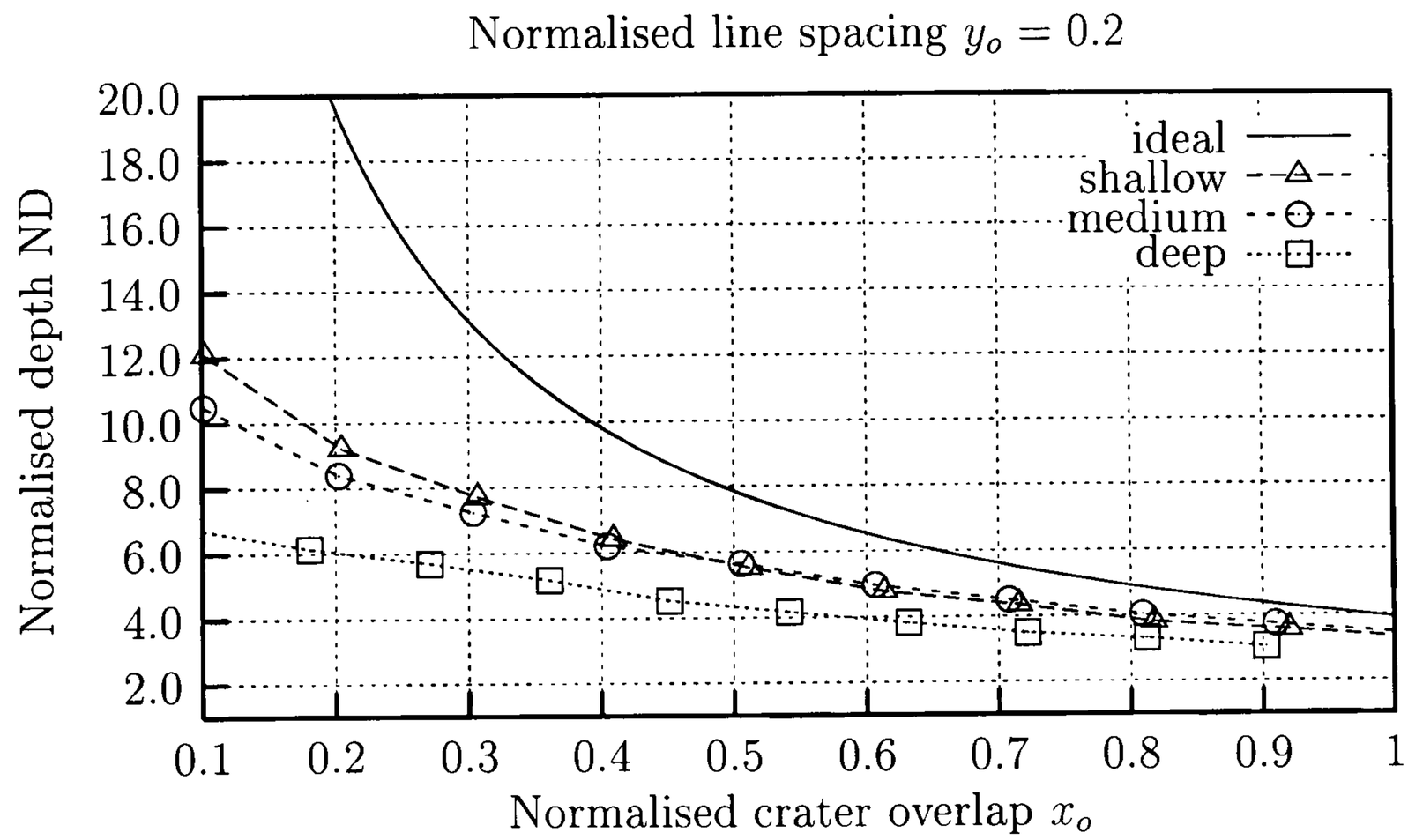

Figure 5.15: Machining curves of SOSR regime, $y_o = 0.2$.

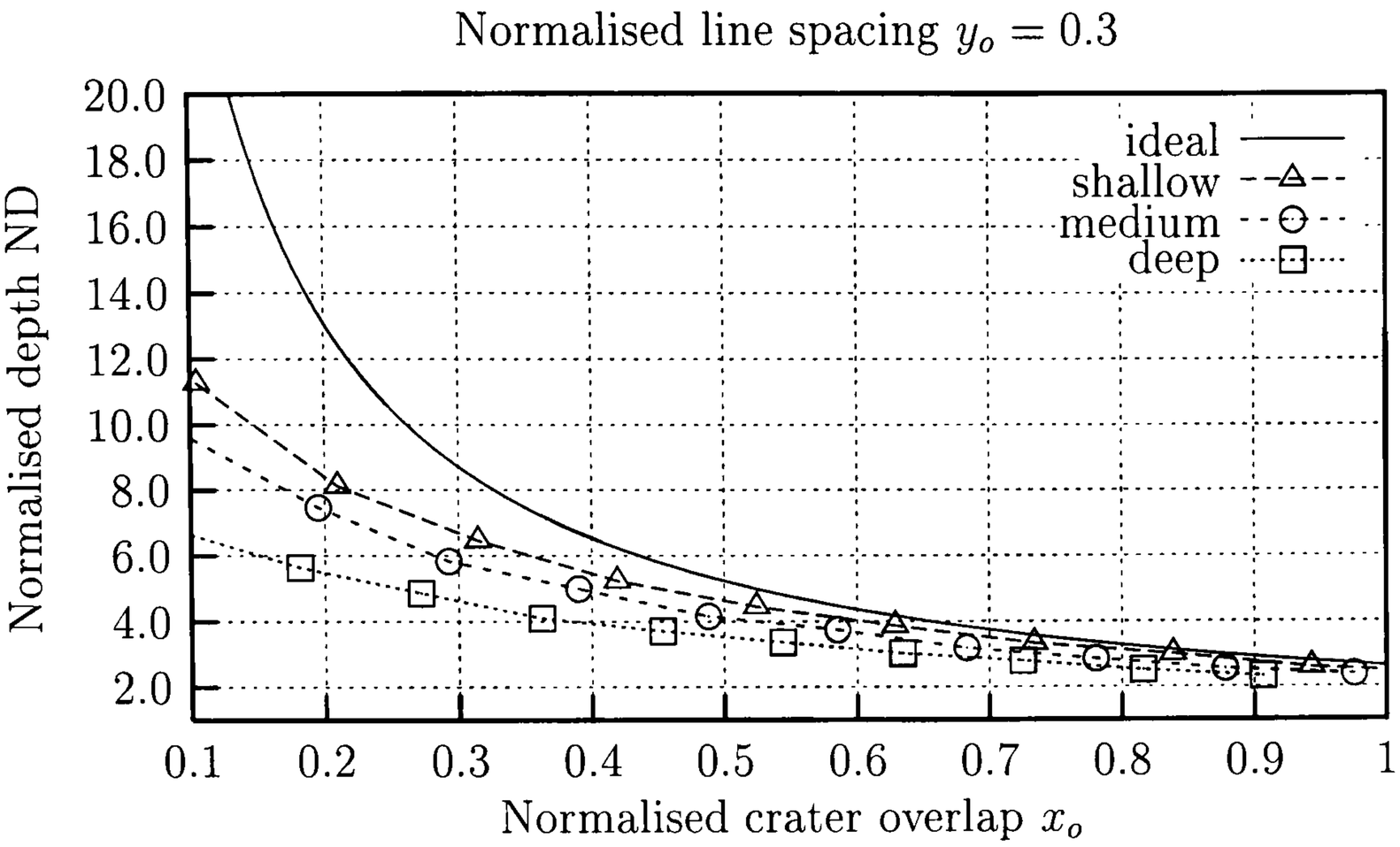

Figure 5.16: Machining curves of SOSR regime, $y_o = 0.3$.

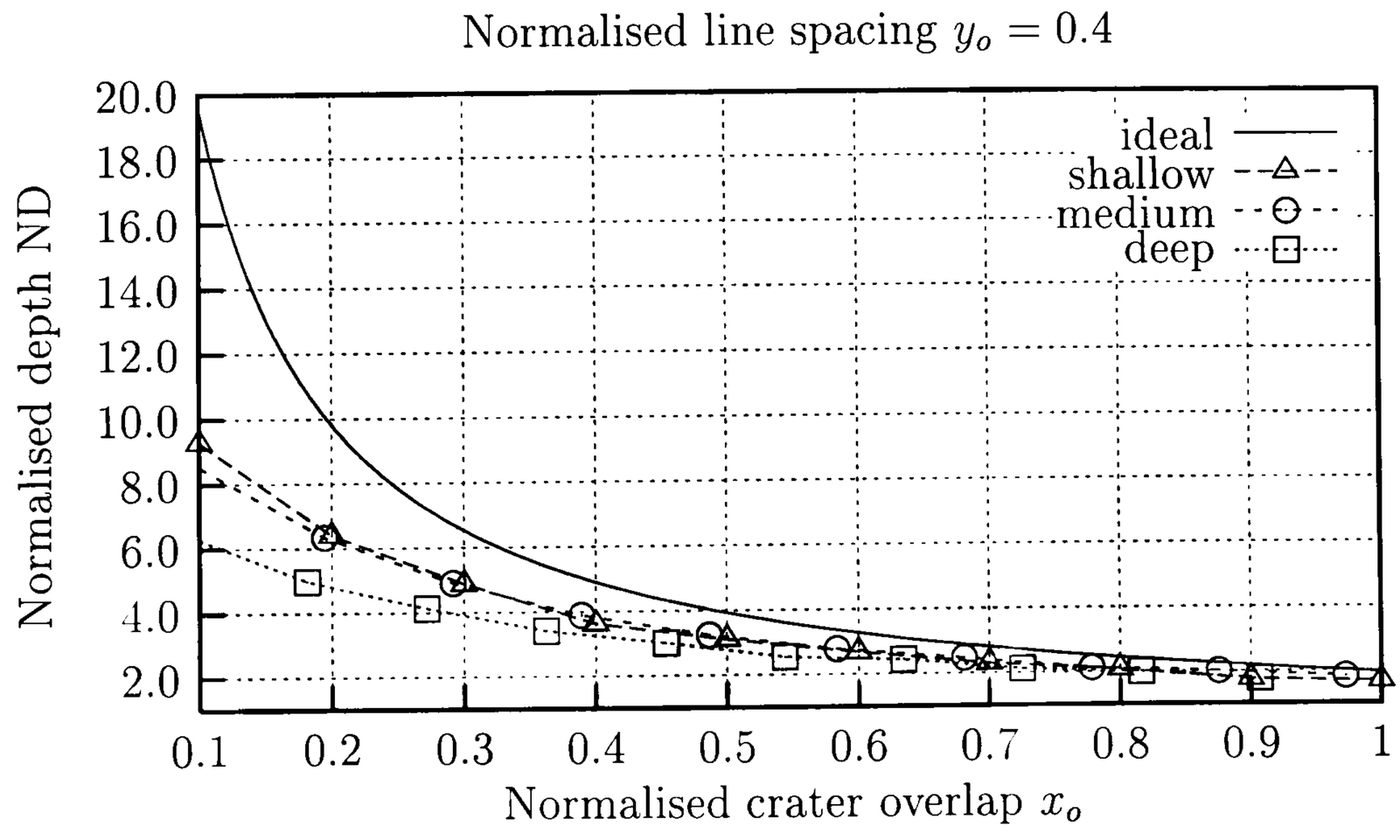

Figure 5.17: Machining curves of SOSR regime, $y_o = 0.4$.

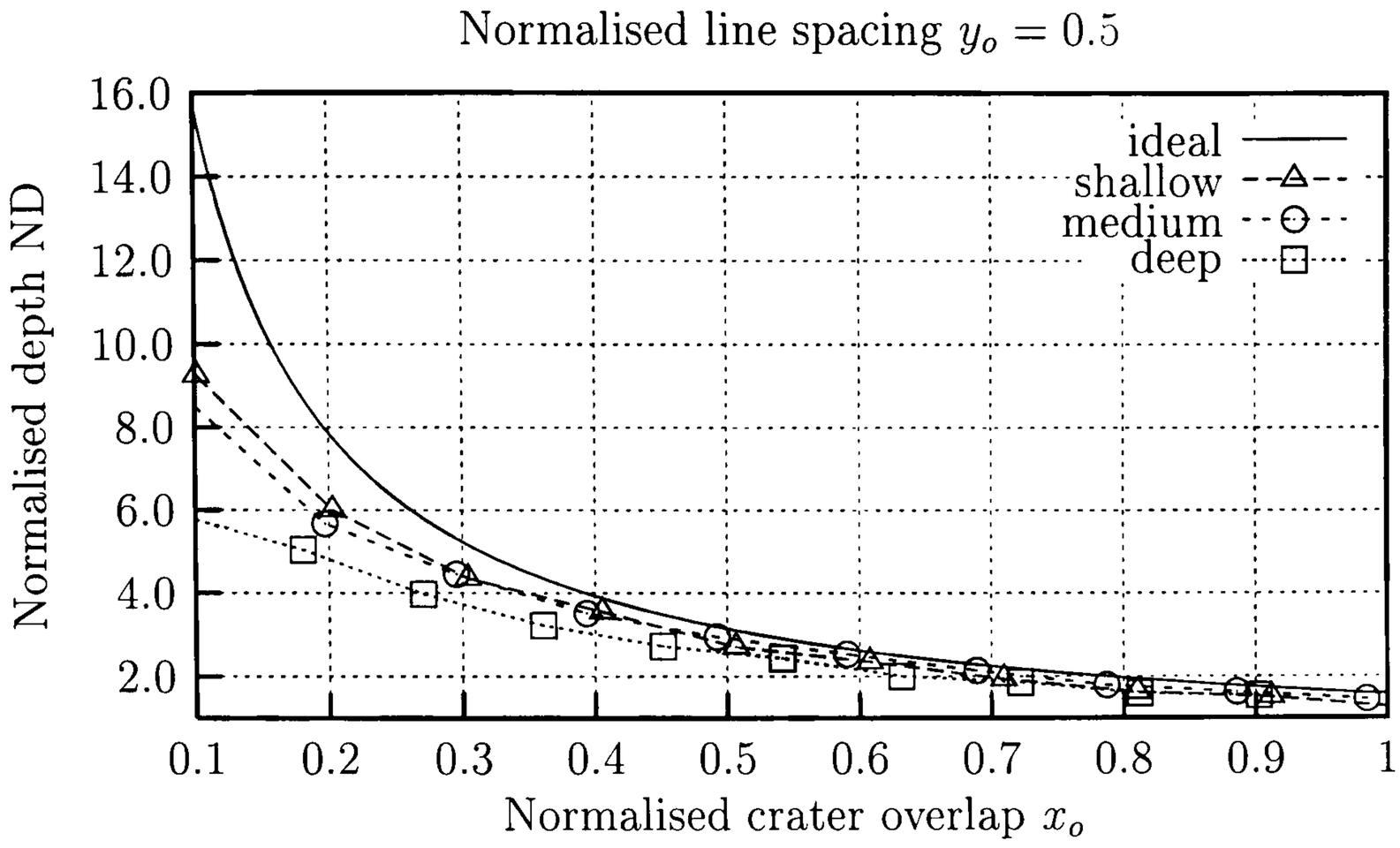

Figure 5.18: Machining curves of SOSR regime, $y_o = 0.5$.

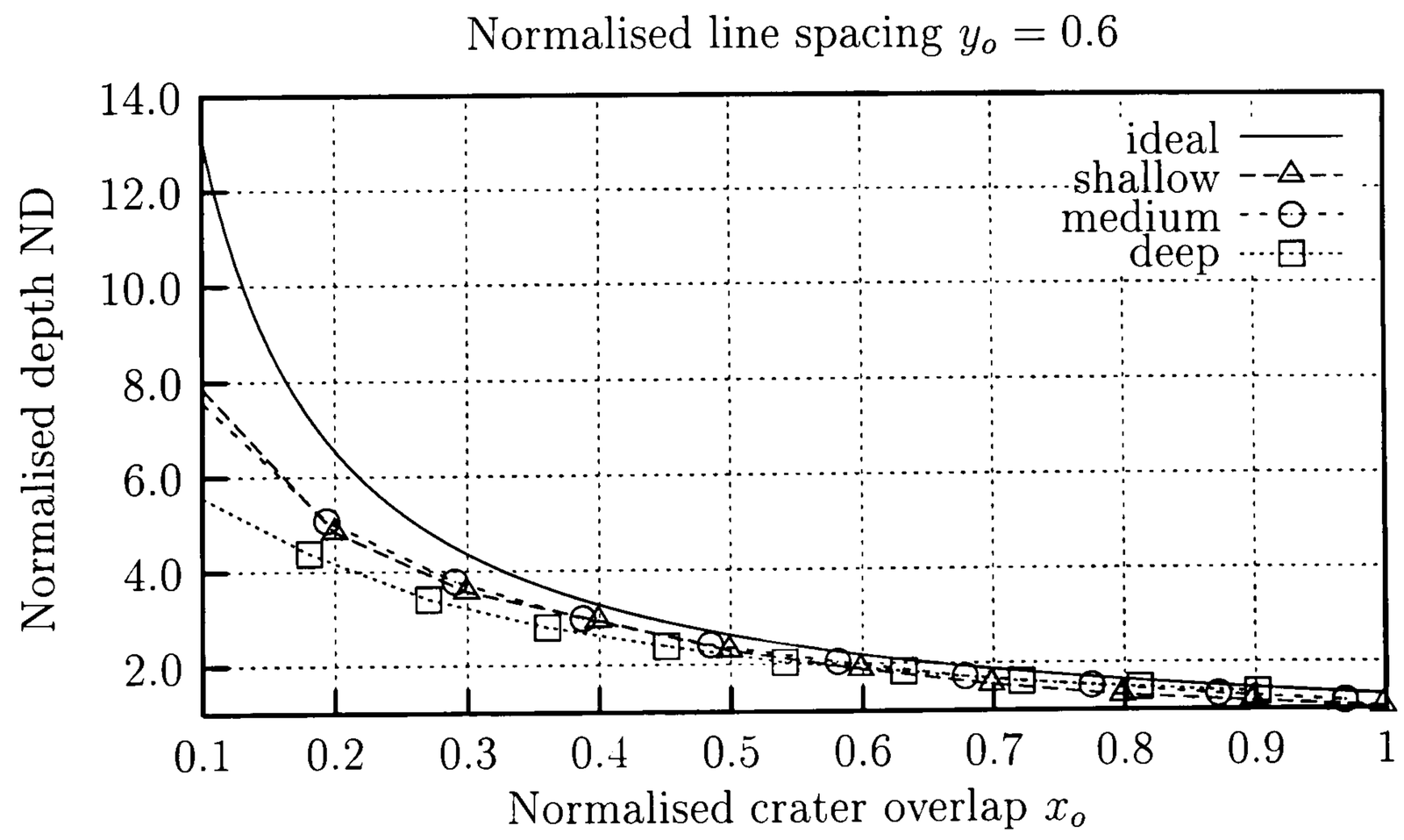

Figure 5.19: Machining curves of SOSR regime, $y_o = 0.6$

5.5.2 Calibration of FFSR regime

The productivity target of 1000 pixels per second on 10 × 10 μm grid can be achieved by fixing the translation speed to 10 mm/s or above. Thermal coupling between overlapped craters plays a significant role in a dynamics of material removal. Stable laser operation can be guaranteed even above the 800 Hz limit (see Figure 3.6 p. 70) by appropriate choice of crater overlap in the calibration structure, allowing for a fill-up of raster line with idle laser shots that are not directed onto the substrate but maintain constant pulse repetition rate (see Section 5.4.4). Three different translation speeds have been studied (see Table 5.1), 10 mm/s, 20 mm/s and 3.2 mm/s. The first one corresponds to 1 kHz on 10 μm by 10 μm grid, second one increases the shooting frequency twofold and the last one assures that laser pulsing limit of 800 Hz is not exceeded.

Figures 5.20 to 5.25 display the measured calibration curves of FFSR regimes with the crater depth as parameter. The characteristics of SOSR regime are included for comparison. A substantial reduction of machining threshold can be observed on the curves obtained for the regimes that exceed 200 Hz pulsing frequency limit (see Section 4.11 p.102). Figures 5.20 to 5.22 show that experimental machining curves of 10 and 20 mm/s regimes nearly follow ideal ones, suggesting the increase of machining threshold has been fully compensated and by the thermal coupling between craters. Figures 5.23 to 5.25 show that the ideal limit has even been exceeded when shallower craters were used for machining.

In an extreme case (pulsing frequency $1/t_m$ - CW mode) the threshold F_{mth} can be reduced to zero. The amount of pulse energy normally used up for overcoming the threshold could be then used for machining. The ratio

$$\mathrm{MEF} = \frac{F_m}{F_m - F_{mth}} \tag{5.15}$$

can be used to quantify maximal machining enhancement factor (MEF) due to threshold reduction. In case of all real craters MEF > 1, thus the material removal is super-subtractive provided the threshold reduction takes place. The effect of super-subtractive machining is especially strong when shallow craters are used for machining. In spite of apparent disadvantage, the machining with shallow crater is worth a further study because of a possibility of production of smooth surfaces with little residual debris and sufficient annealing effect. There is a possibility of making the laser polishing step (see Chapter 6) redundant.

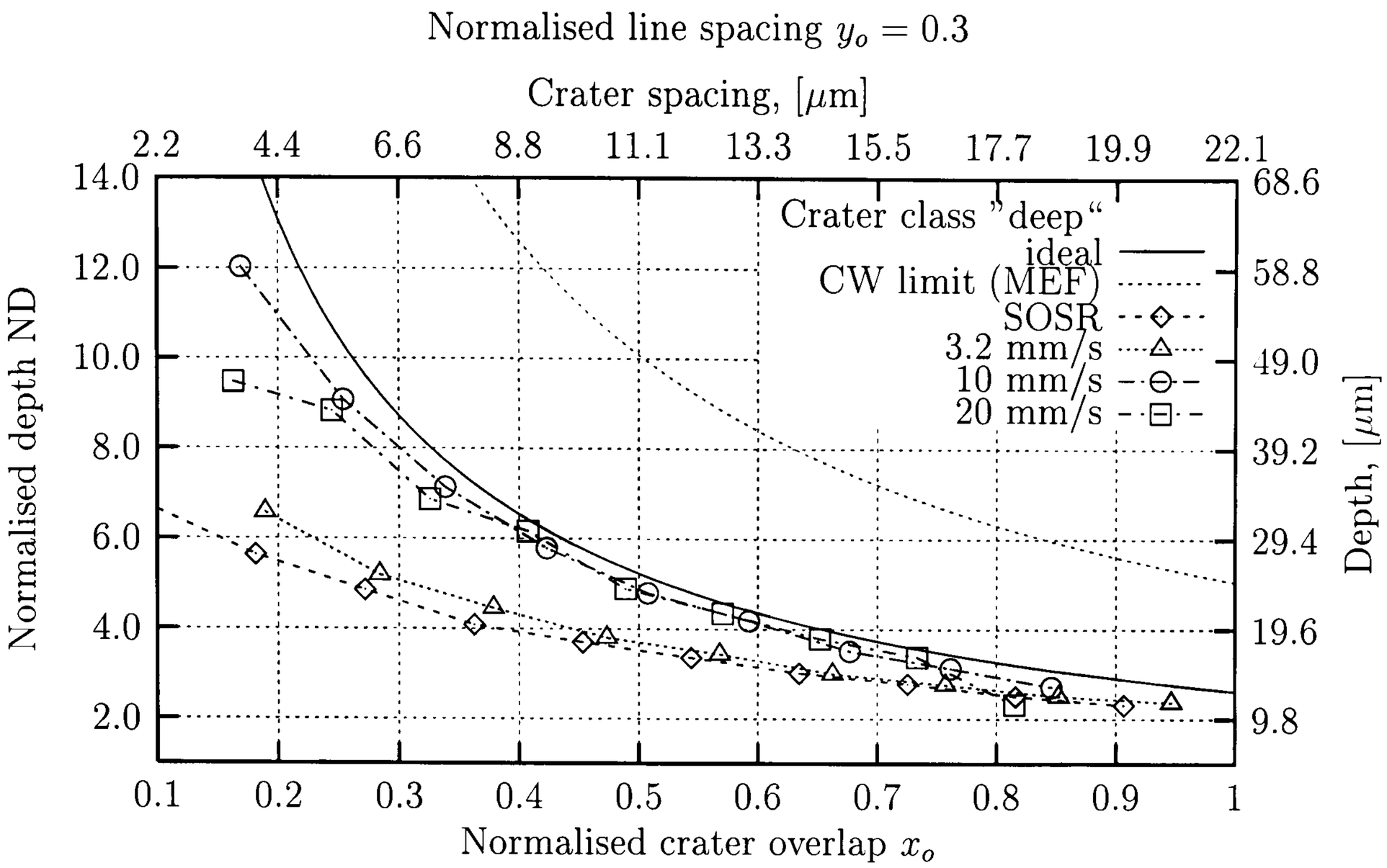

Figure 5.20: Machining curves of FFSR regime, $y_o = 0.3$, crater class "deep".

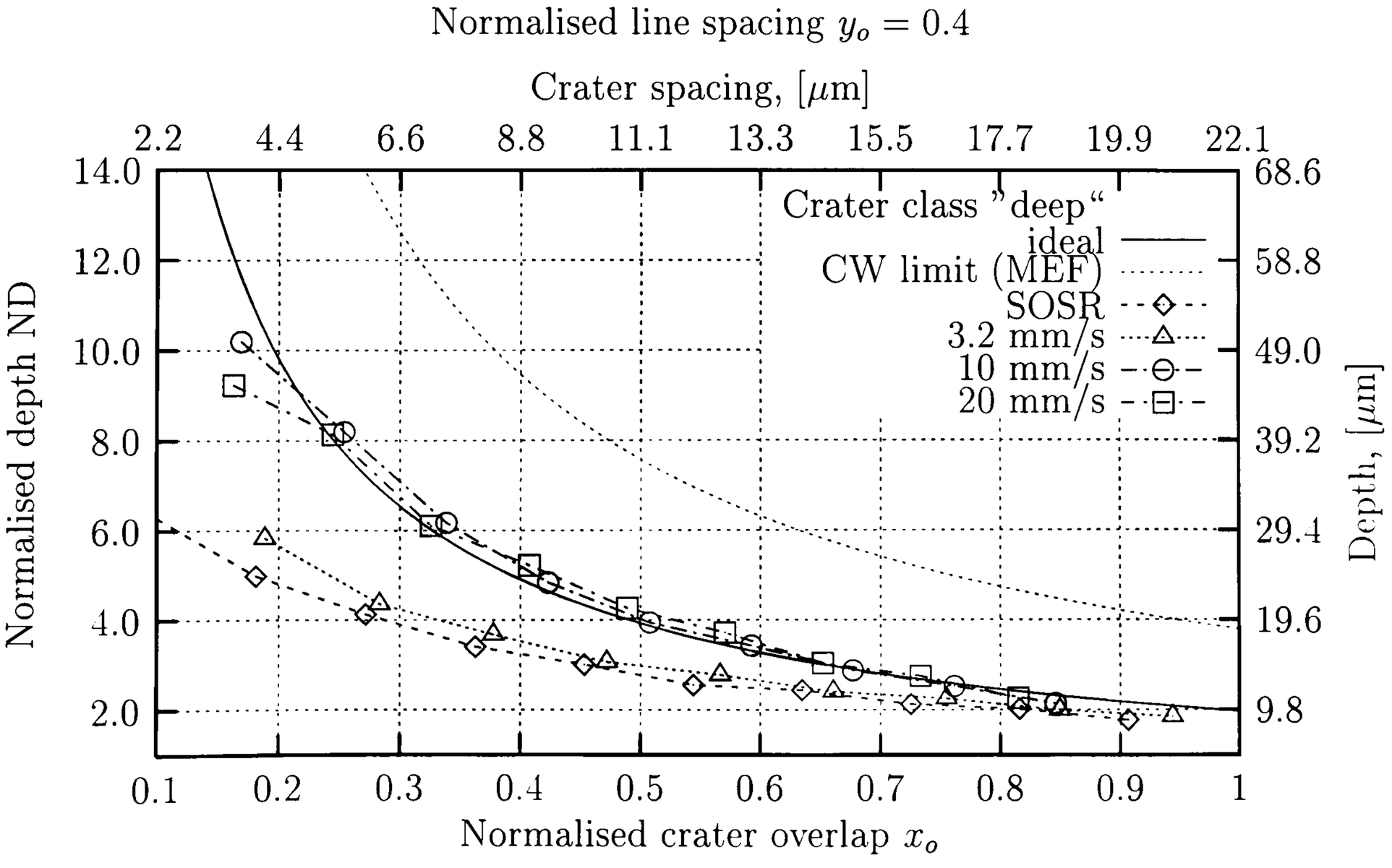

Figure 5.21: Machining curves of FFSR regime, $y_o = 0.4$, crater class "deep".

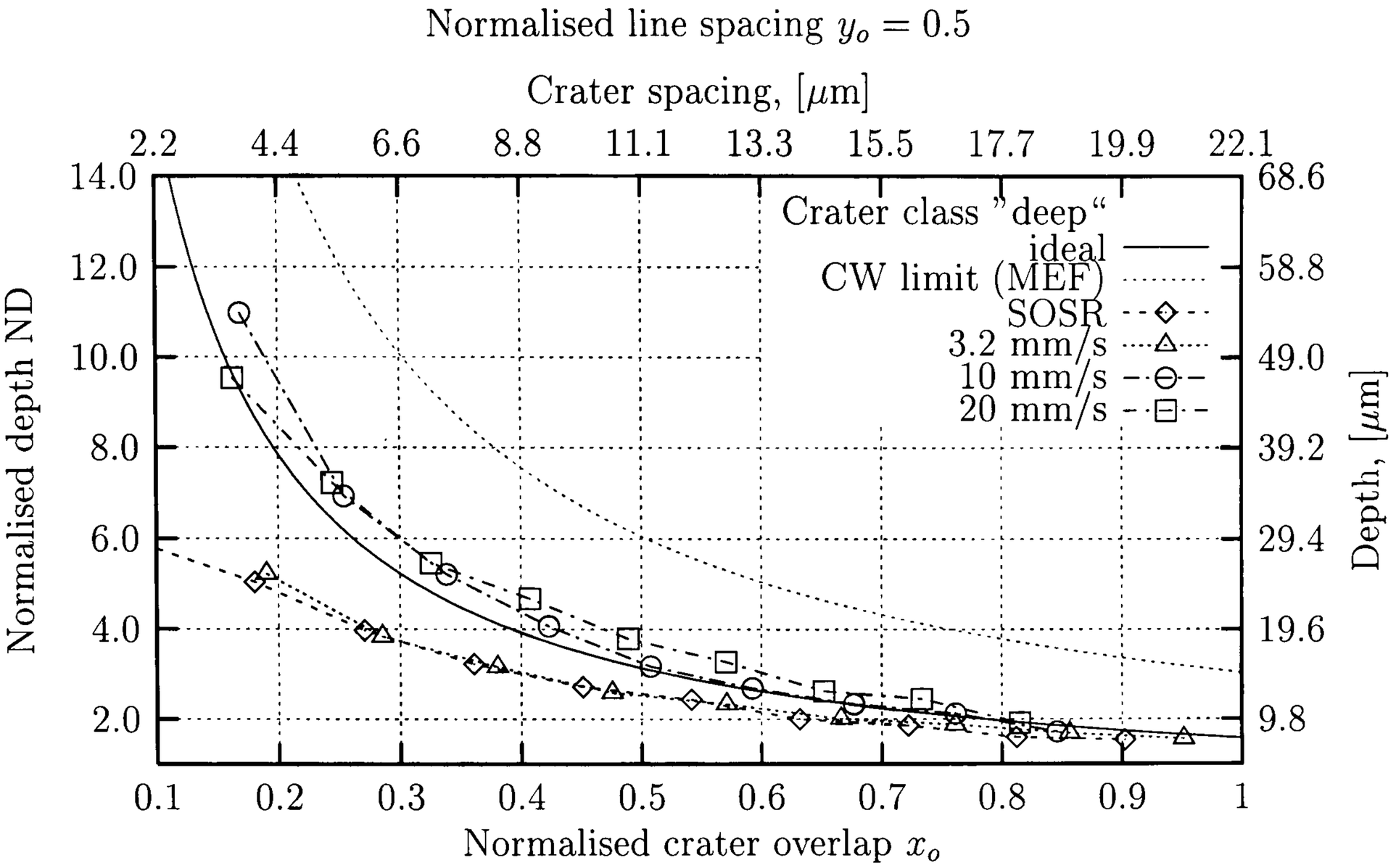

Figure 5.22: Machining curves of FFSR regime, $y_o = 0.5$, crater class "deep".

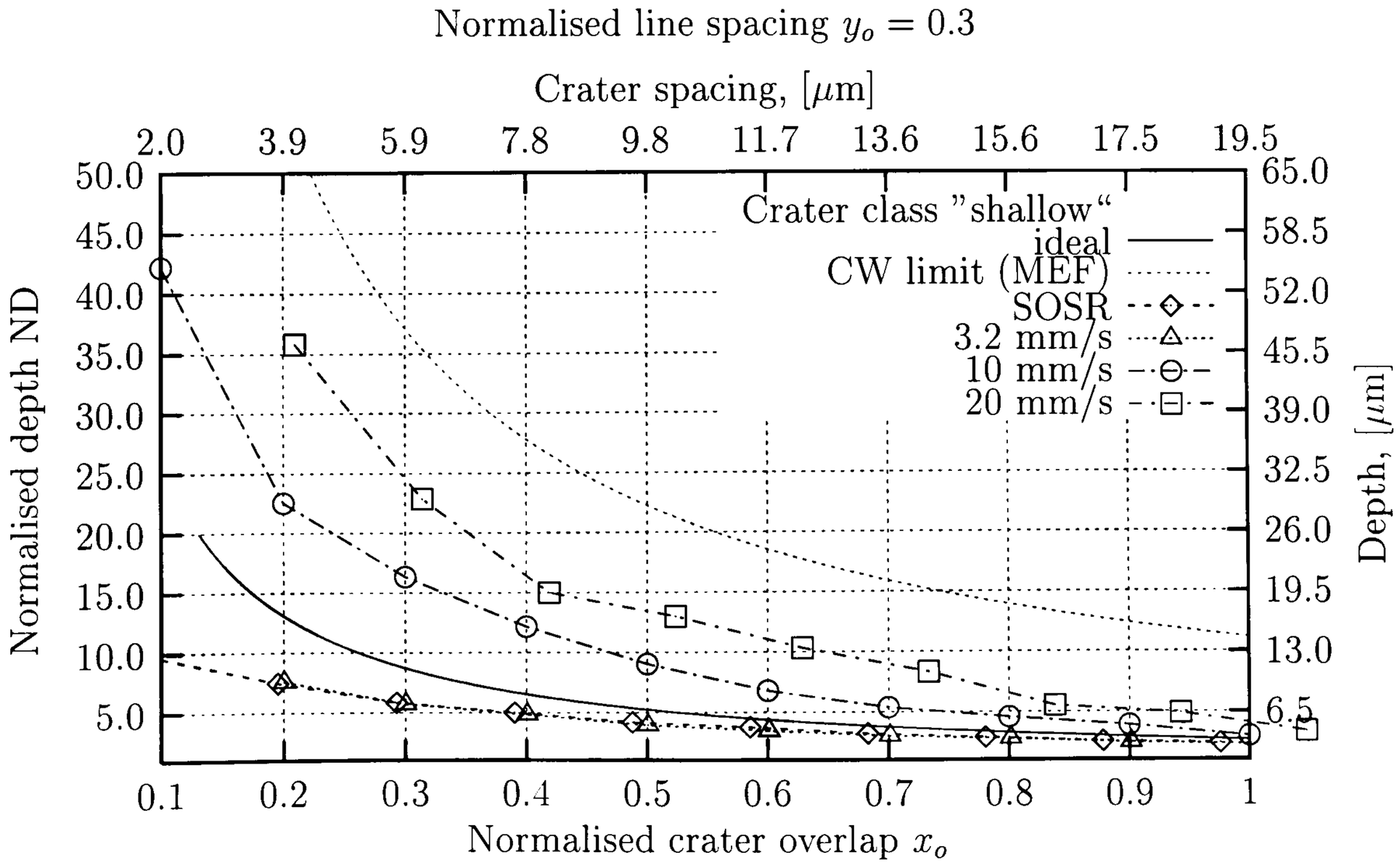

Figure 5.23: Machining curves of FFSR regime, $y_o = 0.3$, crater class "shallow".

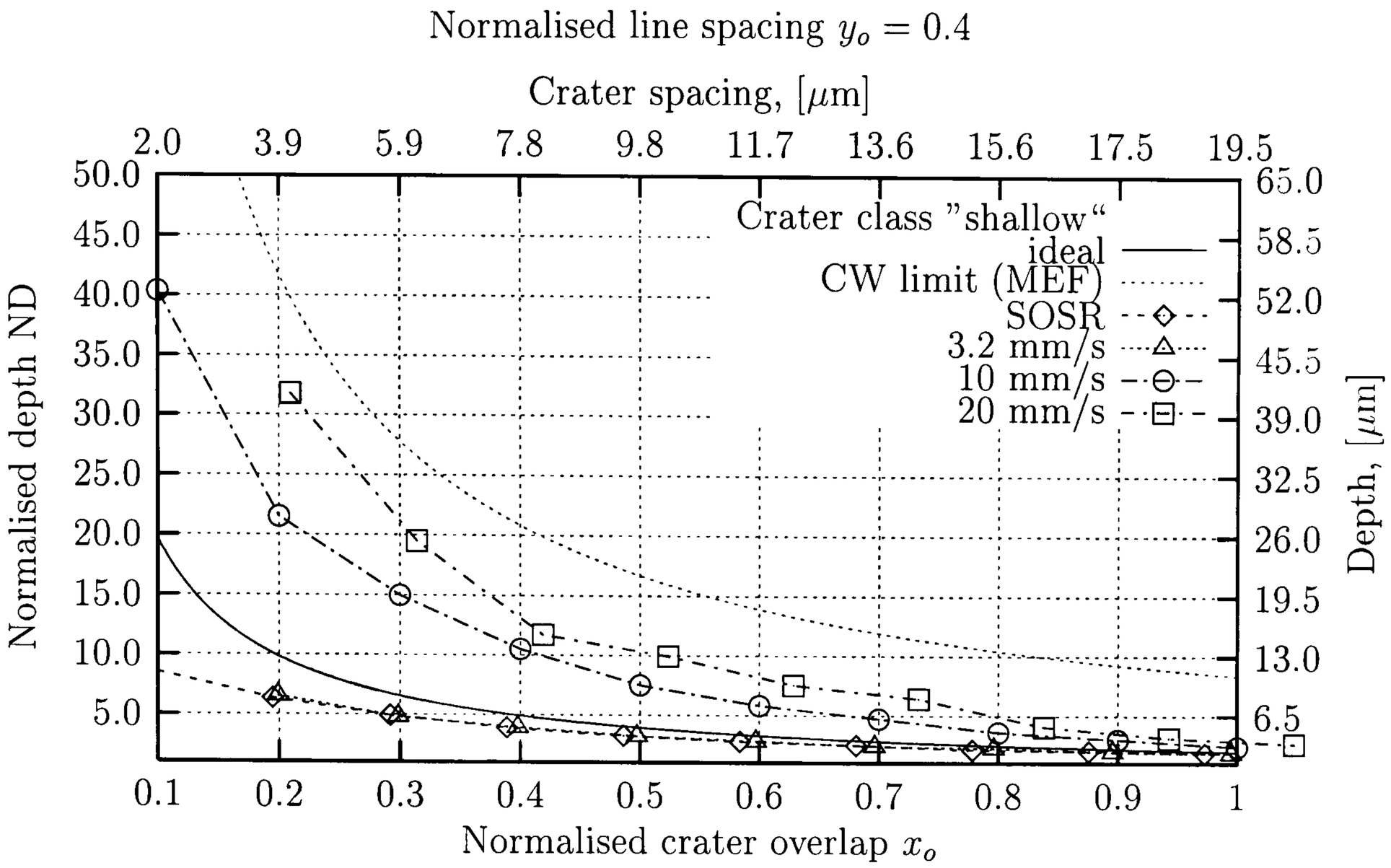

Figure 5.24: Machining curves of FFSR regime, $y_o = 0.4$, crater class "shallow".

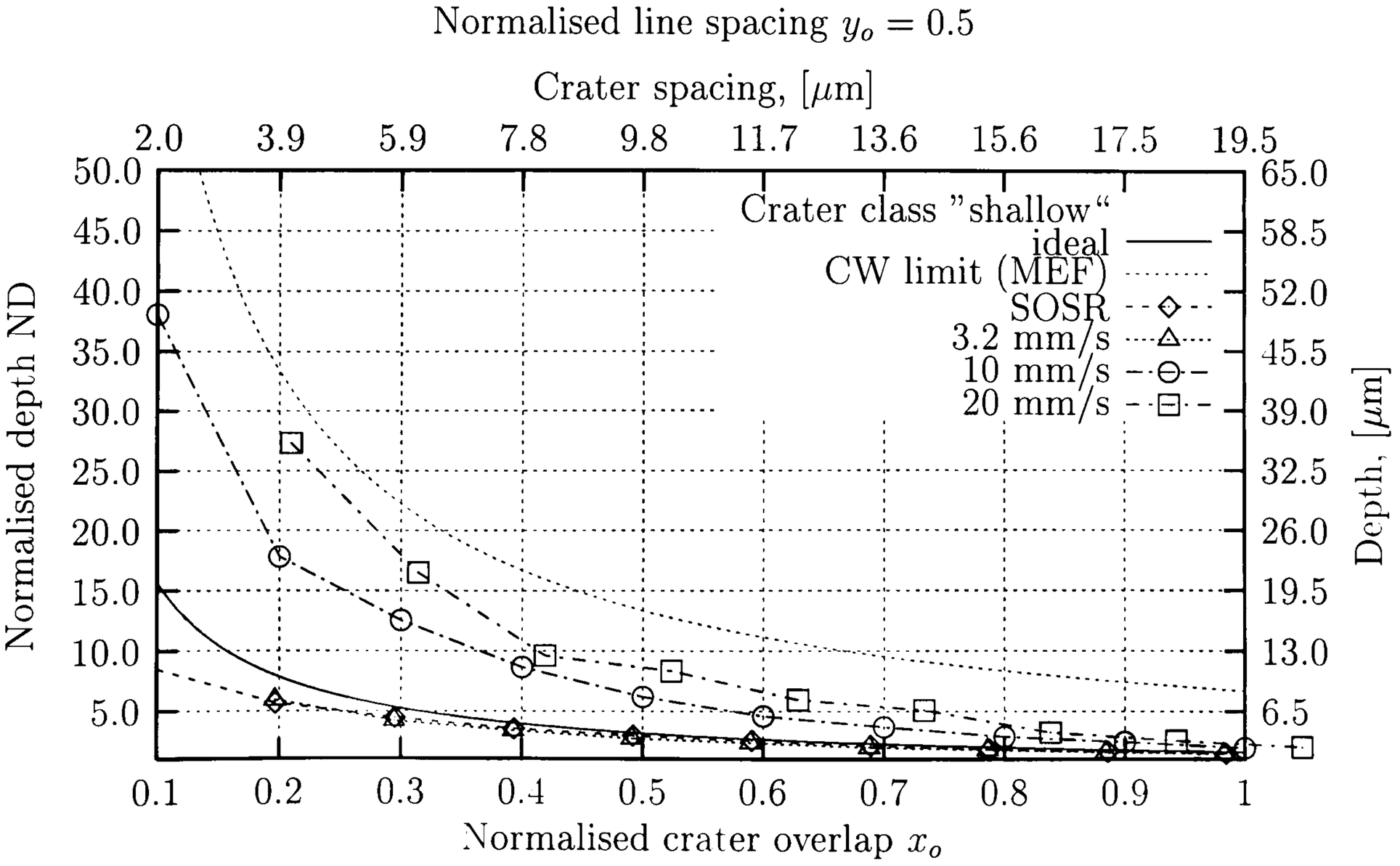

Figure 5.25: Machining curves of FFSR regime, $y_o = 0.5$, crater class "shallow".

5.6 Fabrication of test optical elements

Many elements have been machined in a course of the project, such as prisms, cylindrical and spherical lenses. All of these elements shared similar characteristics with regard to the machining accuracy and final surface quality. Maskless direct writing of prescribed surface shapes into silica is demonstrated below on an example of spherical microlens. This shape challenges the machining in X and Y directions and is easy to characterise both by profilometry and optical imaging.

A map of spherical lens, 1 mm of diameter, 10 μm of height and radius of curvature 12.505 mm, has been computer generated and subsequently converted into a file printable by the machining system. It has been done by the especially developed, rapid-prototyping programme that used experimental calibration data to calculate and generate the crater layout according to prescribed surface map. The calculation has been carried out using the characteristics of SOSR regime, class "deep", overlap $y_o = 0.4$ (see Section 5.5). Generated crater layout has been written into silica substrate and resultant as-machined surface, shown in Figure 5.26 has been measured by the DekTak^{TM} profiler. Figures 5.29 and 5.28 depict the profile analysis in two orthogonal directions, indicated as across and along the direction of raster lines.

5.6.1 Machining accuracy

The as-machined surfaces follow the prescribed spherical shape with worst case accuracy $\pm$500 nm. There is a number of issues deteriorating machining fidelity (in order of importance):

- the amplitude of residual machining ripple, found to be as much as $\pm$800 nm (see Section 5.6.2),
- $\sim$5% modulation of pulse energy occurring in the system, responsible for as much as $\pm$200 nm error,
- energy setting inaccuracy, adding an error less than $\pm$100 nm.

Laser micro-polishing, studied in detail in Chapter 6, can efficiently remove the machining pattern and improve the machining accuracy to $\pm$200 nm. This figure is the outcome of pulse energy modulation, which translates into medium and low spatial frequencies that unfortunately fall just outside laser polishing bandwidth.

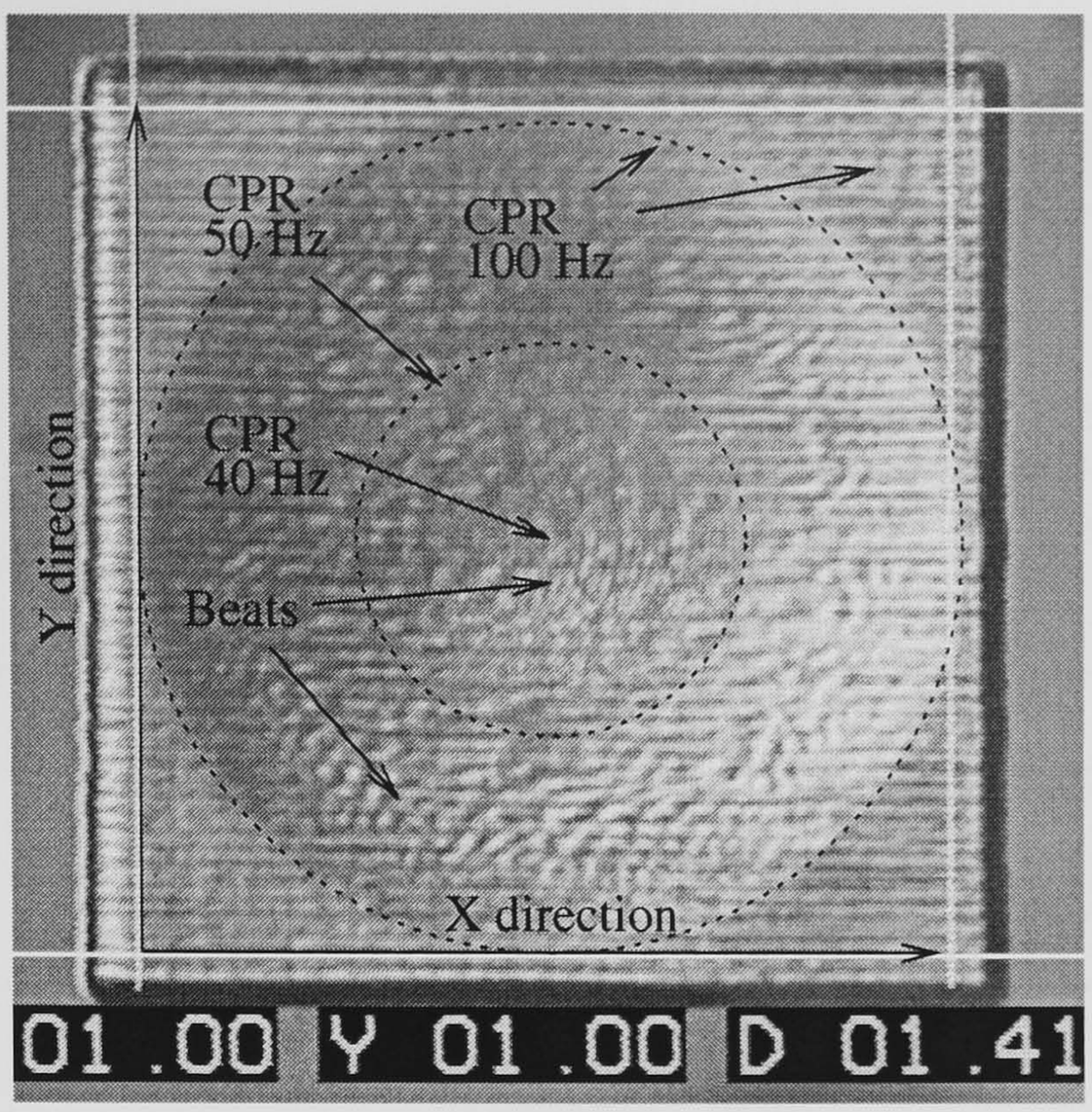

Figure 5.26: Micrograph of the as-machined microlens, 1 mm diameter, 10 μm sag, 12.505 mm radius of curvature. Digital readout in mm. Raster lines along X direction. The circular regions, as indicated, of distinctive low frequency ripples are the result of beat between crater production rate (CPR) and the frequency of parasitic modulation of pulse energy, found to be ~100 Hz.

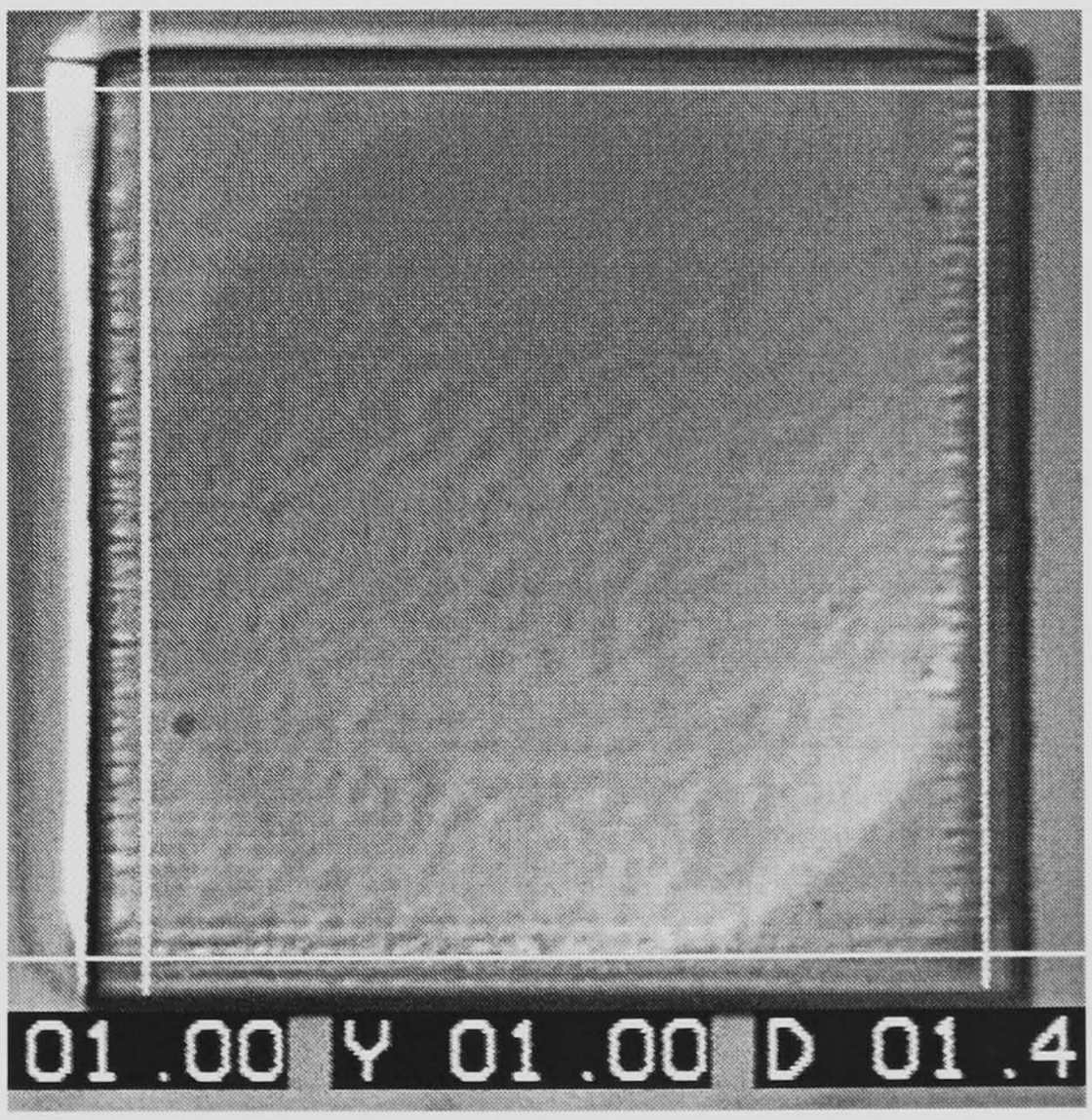

Figure 5.27: Micrograph of laser polished microlens. Digital readout in mm. Laser polishing according to regime D, see Section 6.3.3 in Chapter 6. Removal of machining ripple is visible. Remaining low frequency ripples are the result of parasitic pulse energy modulation.

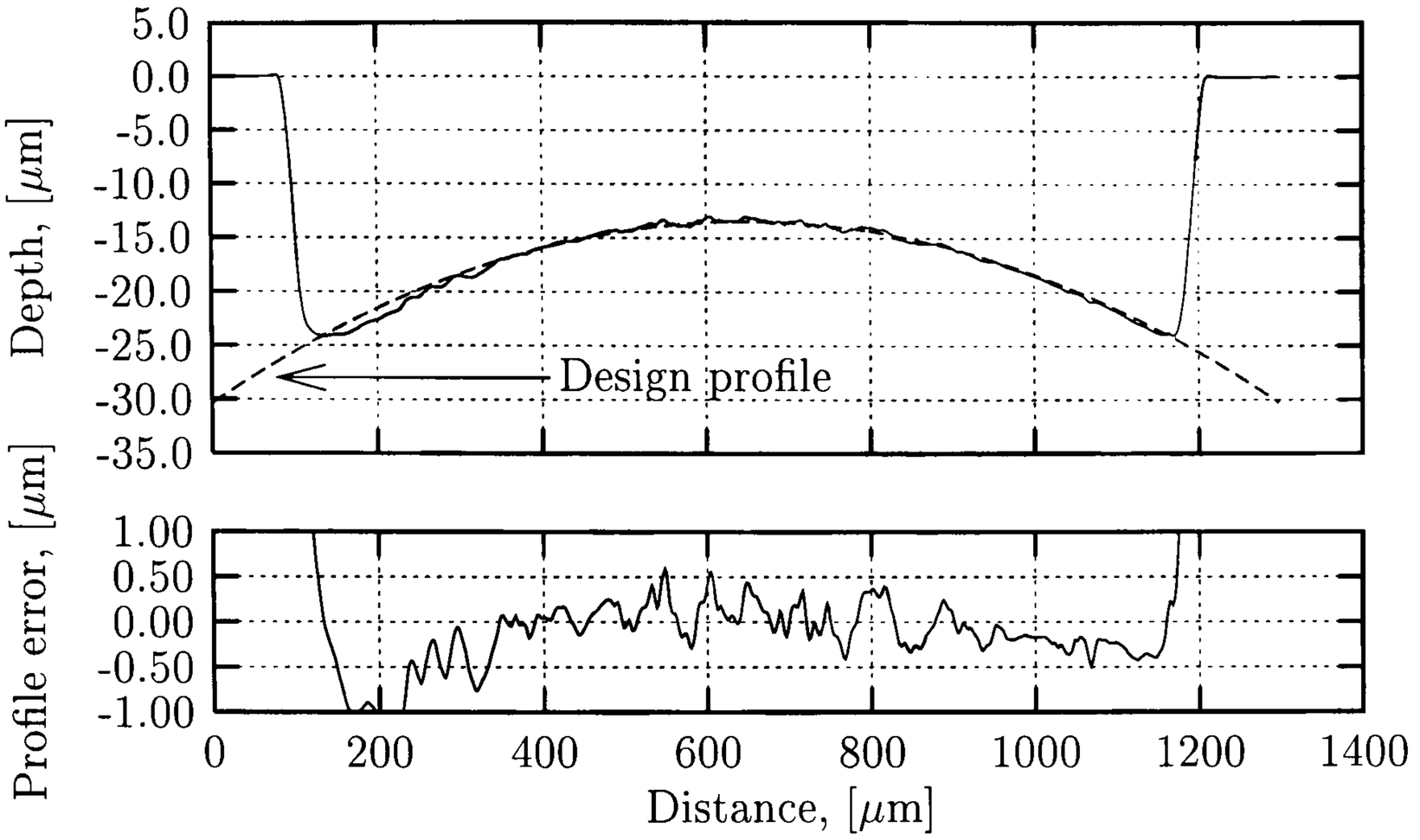

Figure 5.28: Profile of the as-machined spherical microlens from Figure 5.26. The plot below shows the discrepancy between measured and design profiles. Taken along the raster lines (X direction), through the center of the microlens.

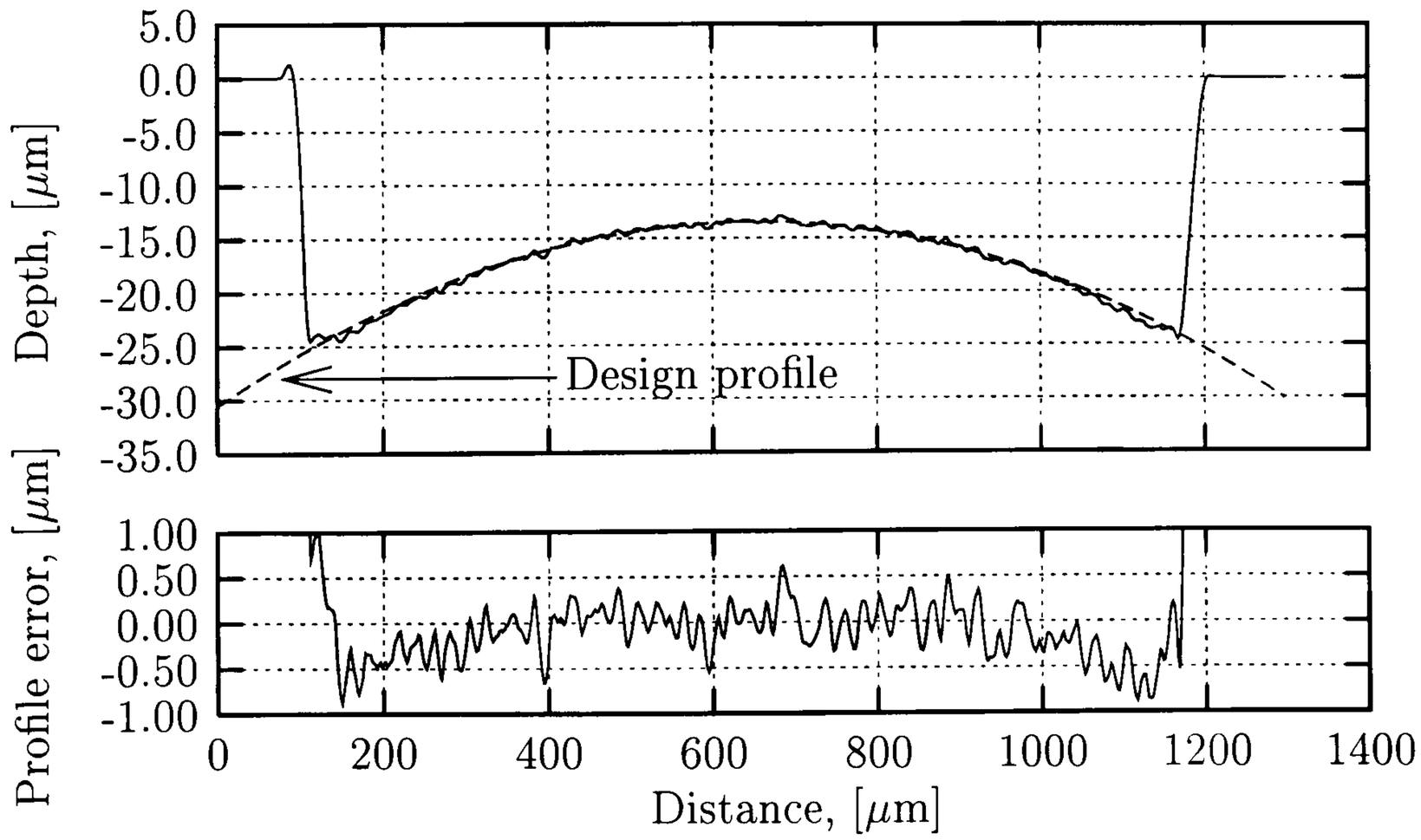

Figure 5.29: Profile of the as-machined spherical microlens from Figure 5.26. The plot below shows the discrepancy between measured and design profiles. Taken across the raster lines (Y direction), through the center of the microlens.

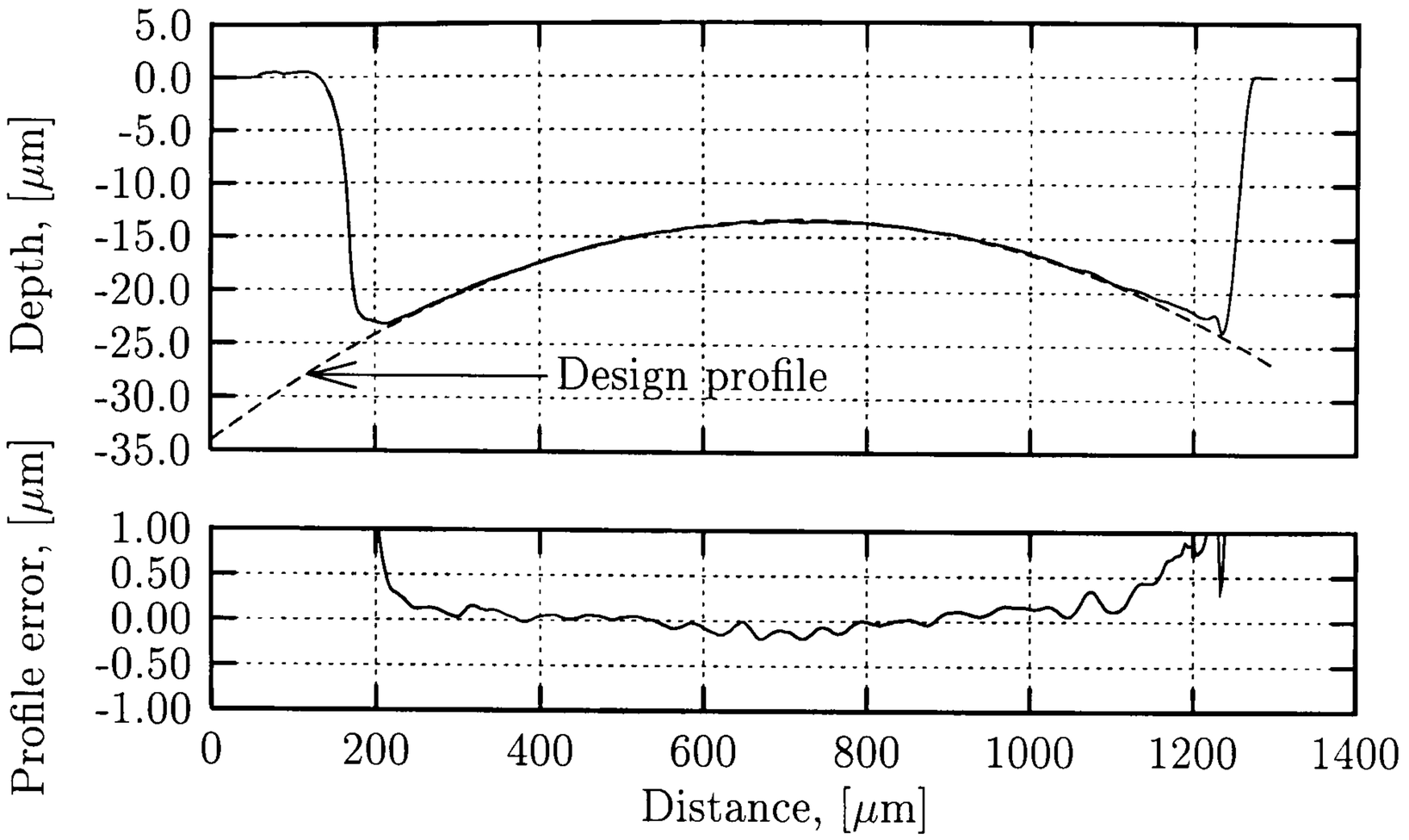

Figure 5.30: Profile of laser polished spherical microlens from Figure 5.27. The plot below shows the discrepancy between measured and design profiles. Taken along the raster lines (X direction), through the center of the microlens.

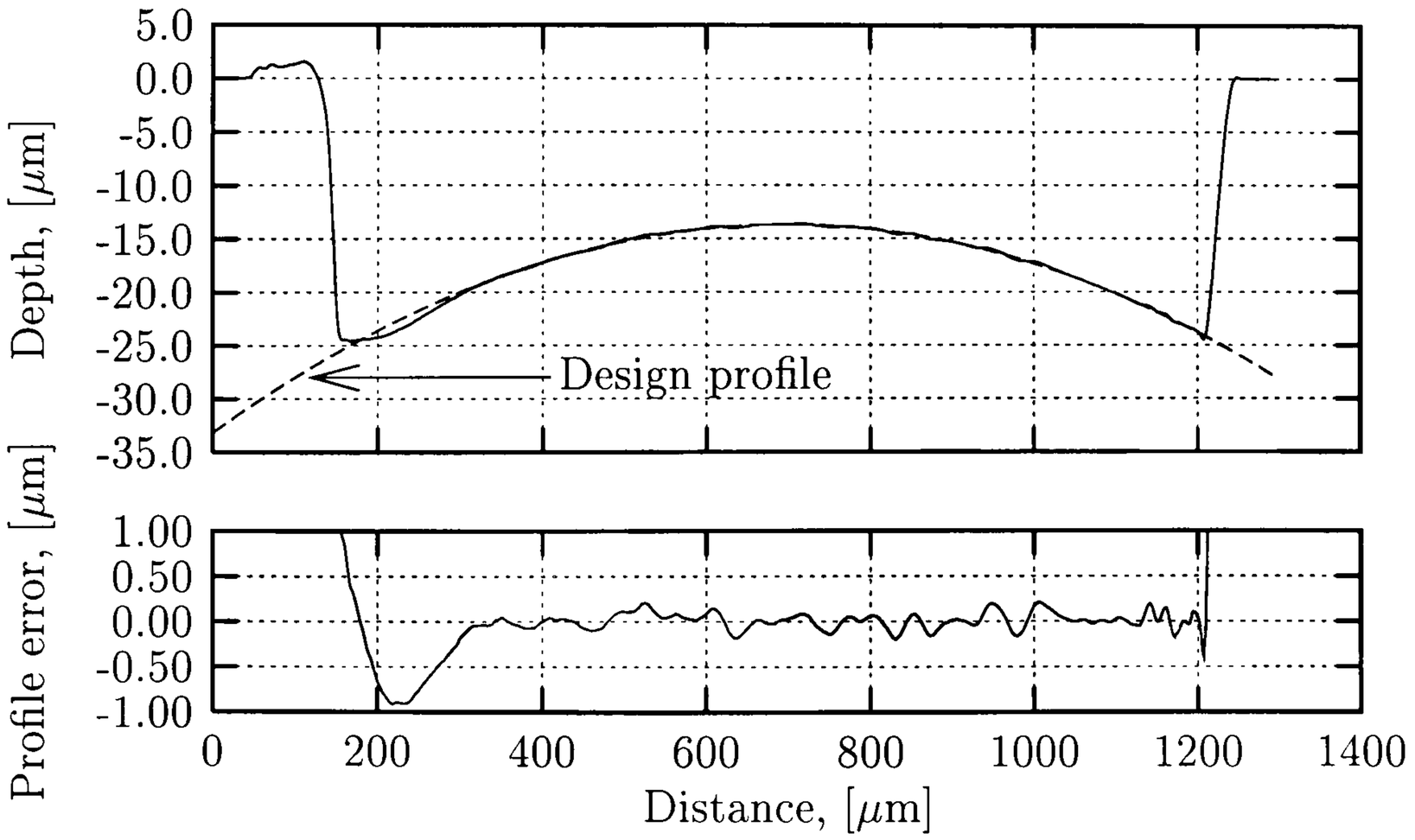

Figure 5.31: Profile of laser polished spherical microlens from Figure 5.27. The plot below shows the discrepancy between measured and design profiles. Taken across the raster lines (Y direction), through the center of the microlens.

The ripples visible in Figure 5.27 and in profile error (Figures 5.30 and 5.31) are the products of that unwanted pulse energy modulation. However, with careful calibration and laser pulse stability below 0.1% it seems feasible to achieve the machining fidelity in order of ± 50 nm. Such accuracy corresponds to less than $\lambda/10$ for visible wavelengths.

5.6.2 As-machined surface quality

The as-machined surface is modulated with residual ripple caused by melt displacement under the vapour pressure. The spatial frequency of these ripples corresponds to a separation between craters in the raster line in one direction and the separation between lines in the other. The amplitude of these undulations depend on the separation between craters (see Figure 5.3 p.112). In practice however, the roughness does not fall to zero with decreasing separation between individual craters. The thickness of the mobile melt that can be displaced under the vapour pressure during the ablation has been found to be ~3 μm (see Section 4.7). It sets the maximum amplitude of the ripples to ±1.5 μm, which has been confirmed by the atomic force microscopy. Additional factor reducing the quality of as-machined surfaces is a presence of machining microdebris, which is the product of resolidification of silica vapours. These sub-micron size particles can be partially molten into the surface or can stick to it by adhesion.

Figure 5.32 shows the image of as-machined surface, 10 μm × 10 μm raster of craters made by 20 μs laser pulses, obtained with atomic force microscope. 20 μs pulse duration has been deliberately chosen to produce the worst-case surface roughness, since the substantial melt displacement is caused by the pulses of that timescale (see Figure 4.9 p.100). The peak-peak amplitude of ripples is as much as ±1.5 μm, but does not fall below ±0.5 μm even with longer > 50 μs laser pulses.

The machining pattern acts as an effective diffraction grating, while the debris gives rise to efficient scattering of light. Figure 6.10 p.163 shows the speckle pattern obtained with He-Ne laser beam passing through the as-machined surface. The bright vertical and horizontal lines are the result of diffraction on a pattern of orthogonal raster lines, while the wide specular field is a product of scattering on microdebris sticking to the surface. The ripples and microdebris cause substantial scattering of light (~30-50% of power left in zeroth order) that practically excludes an application of the as-machined element. Low scatter optical finish must

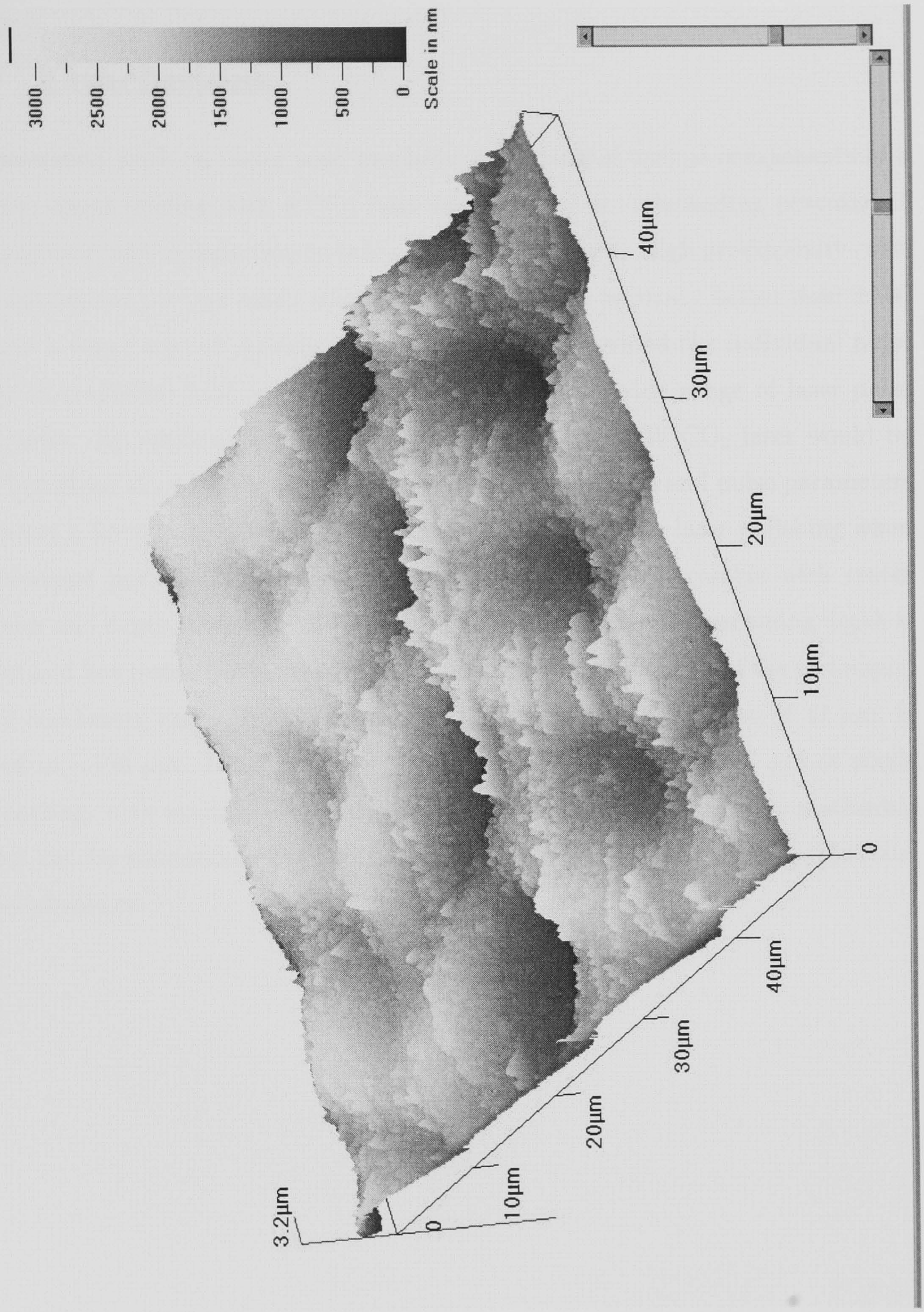

Figure 5.32: AFM image of as-machined surface.

be restored to assure minimum transmission losses. A study on a laser polishing technique capable of achieving that goal is presented in Chapter 6.

5.7 Conclusions

The presented work on raster scan precision machining of optical components in a one step direct writing with a CO_2 laser has outlined an outstanding potential of the technique with comparison to other methods discussed. High productivity rates >16 minutes per cm^2 are easily achievable together with accuracy better than ± 100 nm over a range tens of microns of machining depth provided the individual pulse energy is controlled with accuracy better than 1% in a wide range of laser pulse frequencies. An application of low power, DC discharge, CW CO_2 laser would be more beneficial since it's easier to precisely control laser beam and pulse parameters and select a laser line, while slab waveguide laser is better for laser polishing when high average powers are required. The machining range is scalable with crater diameter and depth, thus further optimisation is possible if more machining depth is needed and less resolution is acceptable. The minimum feature size of the technique, at full machining range dynamics and minimum obtainable spot size of 47 μm, is limited to $\sim$100 μm. The available cut depths can be as much as 100 μm at single pass cutting, with available depth dynamics of few tens of microns. The machining scheme can be successfully applied to fabrication of sub-millimeter size, refractive optical elements.

Chapter 6

LASER MICRO POLISHING

6.1 Introduction

This chapter is dedicated to a study on the application of CO_2 laser for surface smoothing of micro-optical components, machined in the fused silica. There is a need for a post-machining surface treatment, which would eliminate the raster scan surface relief and restore the optical quality of as-machined surfaces. Much attention has been directed in the past towards CO_2 laser polishing of conventional "bulk" optics, but to my knowledge no detailed study on CO_2 laser polishing of micro-optical components has been carried out so far.

Following sections reviews the polishing methods known to produce optical quality surfaces, such as traditional abrasive polishing, fire polishing and modern variations of these techniques, like magnetorheological finishing, chemical and laser polishing. The considerations of applicability of these methods for polishing of sub-millimeter scale, optical elements of arbitrary shapes, are presented here.

There are basically two mechanisms of glass polishing for removal of machining marks and giving the products their final optical quality finish [78]. One involves material removal by abrasives and the second exploits the capability of glasses to flow under stress or surface tension, resulting in a mass redistribution and the reduction of surface roughness.

6.1.1 Abrasive polishing

In many variations of abrasive polishing of conventional optics, the workpiece is forced to a physical contact with a polishing tool, separated by a liquid film of suspended abrasive micro-particles, usually metal oxides [18, 21]. These particles

cause material removal as well as plastic flow of glass on a micron and sub-micron scale, resulting in surface roughness much lower than the abrasive grain size. The chemical composition of both glass and abrasive play a significant role in the resulting optical and chemical properties of polished glass surfaces. Usually, a number of polishing stages (requiring abrasives of different characteristics) is necessary to give the raw product an optical finish, adding to a complexity of technique. Summarizing, the method requires the physical contact between polishing tool and the workpiece, making it suitable only for a large scale "bulk" optics in a limited range of shapes.

New powerful methods of optical finishing have emerged that practically eliminate the inflexibility of conventional polishing of bulk optics. Don Golini *et al.* [79] have reported commercially available magnetorheological finishing (MRF) technology. The MRF process uses magnetorheological fluid as a polishing tool, which adheres to the surface of a spherical wheel rotating in an electromagnet gap. A gradient of magnetic field causes the fluid to develop high stresses when in contact with the workpiece surface, effectively removing the surface material and polishing it down to an optical quality. This sub-aperture polishing tool does not wear and can be very accurately controlled with regard to viscosity ($\pm 1\%$) and magnetic field. Optical quality finish and additional correction of any shape is possible under computer prescription in a matter of minutes, with accuracy of $1/4\ \lambda$ and surface roughness of 1 nm rms.

Takino *et al.* [80] have reported a similar method, with respect to flexibility and accuracy. The atmospheric pressure RF-plasma chemical vaporisation machining (CVM) with a pipe electrode has been applied to figure a workpiece surface with accuracy of $1/5\ \lambda$, also under computer control. However, the productivity was inferior to that of MRF, reaching few hours for shape correction of 90 mm diameter optics.

6.1.2 Fire polishing

The disadvantage of physical contact and possible chemical interactions between the abrasive and the workpiece was avoided by the fire polishing. This method exploited the thermally activated surface mass flow, driven by the surface tension. The polishing process consisted of controlled-rate heating and cooling steps in a furnace. At high temperature, chosen above the glass transition point, the reduced

viscosity of material permitted a substantial mass transfer in a thin layer of material under surface tension, in a practical timescale. To prevent the cracking of product during and after the treatment, the heating and cooling rates had to be properly chosen to avoid thermal fracture and generation of internal stresses. A control over the process was limited to baking time and temperature settings, dependingly on the material and a particular shape of optical element.

Although this method could be used to polish any arbitrary surface shapes, the thermal characteristics of material determined the limit on process throughput and the dimensions of optical component. In case of the small, optical element, all its volume could be heated up above the softening point of glass, resulting in undesired global modification of shape.

The fire polished optics also needed to be cooled at very slow rates to prevent the freezing of internal stresses caused by thermal gradients combined with strong dependence of viscosity on temperature (see Section 2.4.3 p.50 on thermal stresses and Section 2.4.4 p.52 on annealing). The frozen stresses impair the optical performance of glasses (see Section 2.3.4 p.33 on stress-optical effect) and also may cause cracking of the polished element. The annealing of bulk optics takes hours, so the technique is most suitable for mass production.

Fire polishing however does not have to be limited to furnace method only. Methods utilizing scanning heat source using pure oxy-hydrogen flame have also been used. Veiko [81] has applied a small H_2 plasma jet to smooth out the surface of millimeter-size cylindrical lenses made of fused silica, which were simultaneously machined by the CO_2 laser.

6.1.3 Laser polishing

A solution to the problem of low productivity and inflexibility has been found by combining laser technology and fire polishing. The application of laser allowed for precise control over the amount of heat delivered to a layer of material of controlled depth. The desired temperature distribution could be thus induced in timescales much shorter than that defined by the thermal diffusion of heat occurring in the furnace, thus the technique improved process control and productivity.

The CO_2 laser has been shown to be capable of glass polishing thanks to strong absorption of its radiation in glasses. A successful polishing of large area optics has been reported by Vega *et al.* [51]. There are, however, thermal fracture lim-

itations to the laser polishing of brittle materials like glasses, which may crack if the stresses introduced during fast melting and resolidification are not relaxed by preheating [32]. Fused silica fortunately withstands the stress buildup, thanks to its very low expansion coefficient with comparison to other glasses. It can be laser processed without the preheating stage.

An idea of applying the CO_2 laser for polishing of optical glasses has met with an interest of a number of researchers. The first work on CO_2 polishing of fused silica is believed to be addressed by Temple *et al.* [49] in late seventies and early eighties. It investigated the reduction of optical damage threshold (caused by nanosecond 1064 nm laser pulses) by a CO_2 laser treatment of mechanically polished silica surfaces. The experimental technique was based on large spot (TEM_{00} mode, 4mm $1/e^2$ spot radius) CW laser scanning with translation speed ~5 cm/s and irradiance 0.3-0.6 kW/cm^2. The laser spot created the traveling red-hot zone with a dwell time of <1 second. The substantial reduction of damage threshold was observed for the laser treated areas in comparison to just mechanically prepared ones. The polarimetric measurements have also been carried out to assess an influence of post-process, residual stresses on the optical transmission of treated surfaces. It has been shown that the stress-induced wavefront distortion, measured with 632.8 nm wavelength, was practically negligible if the polishing process was carried out properly.

Thermal stress limitations, imposed on laser polishing of optical glasses, have been outlined by Xiao an Bass [32]. They have studied laser polishing of various glasses like Zerodur, BK-7, Pyrex and fused silica. The experimental technique they've used was similar to that used previously by Temple *et al.* [49] with an addition of oven, which allowed for preheating the samples up to 400 °C. They have shown that it is the thermal expansion coefficient that mainly determines the ability of glasses to resist cracking during and after laser treatment. Only fused silica and Pyrex have been successfully polished and these glasses have the lowest expansion coefficient among the tested ones.

Laguarta *et al.* [50] and Vega *et al.* [51] have carried out an extensive study on application of CO_2 laser for polishing of bulk optics made of conventional glasses, like K or BK crowns. The cracking has been avoided by preheating the samples uniformly up to the temperature near the glass transformation point (viscosity 10^{14} Pa·s, ~500 °C for most conventional glasses, see Table 2.5 p.32), which reduced a build-up of thermal stresses during and after laser polishing. This solution allowed

for successful processing of optical glasses that would otherwise crack [32]. A large beam of uniform distribution has been used to irradiate the glass surfaces with irradiance in a range 50-235 W/cm^2 and processing times 0.4-2 s. The authors have found that timescale of the surface flow, taking place in a layer of 25 μm depth and viscosity 10^3 Pa·s, was less than several tenths of second for the transition from ground (1-10 μm initial roughness) to polished state of the surface (1 nm roughness).

The influence of beam non-uniformities on the glass surface morphology has been assessed by Ocaña *et al.* [52]. It has been shown that peak-patterned beam intensity distribution may lead to a development of significant temperature variation across the surface. The viscosity of glasses is strongly dependent on the temperature, approximately an order of magnitude per 100°C (see Figure 2.4 p.31). Short pulse irradiation with a non-uniform beam may then create local melt zones of viscosity high enough to allow for mass flow under surface tension in a timescale of that pulse, introducing unwanted surface modulation with the spatial frequencies of the beam non-uniformity.

The work done so far revolved around laser polishing of bulk optics. There is no report, to my knowledge, on analysis of performance and applicability of laser polishing in a scale of micro-optical elements. I believe this Chapter will have succeeded in delivering the evidence of the potential offered by the CO_2 laser for polishing of silica micro-optics.

6.2 Surface relaxation under surface tension

Laser polishing of silica can be carried out by exploiting the surface tension driven mass flow. At this stage, it is necessary to gain an insight into the mass flow dynamics to design and carry out meaningful laser polishing experiments. The characteristic timescales of polishing in a melt zone defined by the laser beam parameters can be estimated with an aid of theoretical model described below, which applies Newtonian viscous flow dynamics.

6.2.1 Newtonian viscous flow model

White *et al.* [82] have carried out the work on planarisation of glass surfaces of micro-electronic structures. The CVD deposited, borophosphosilicate glasses have been used as interlevel layers of dielectric material in semiconductor structures. Heat activated, viscous flow under the action of surface tension has been used for smoothing out sharp edges of these layers to promote good metallization. The analysis of the process has led them to a derivation of useful formula describing the amplitude reduction of sinusoidal surface undulation with a period λ as a function of material parameters (surface tension γ, viscosity η), melt dimensions (initial undulation amplitude A_i, average melt depth h) and flow time t.

$$A_f = A_i \exp\left(- k_1 \frac{1}{\lambda^4} t \right) \quad \text{, where} \quad k_1 \cong 4\pi^2 \frac{\gamma}{\eta} h^3 \tag{6.1}$$

The Equation 6.1 has been derived with simplifying assumptions of $\lambda > h > A_i$, constant value of surface tension γ, constant viscosity η throughout the average fluid depth h and an absence of surface tension gradients and gravitational effects. Formula 6.1 has been experimentally verified and the value of flow constant k_1 has been found in a course of experiments with fusible borophosphosilicate glasses (BPSG), thus excluding its direct application to fused silica. Nevertheless, the model describes the relationship between the parameters involved, providing directions and clues for the analysis of flowing of silica.

Equation 6.1 can be used to estimate the timescale necessary for substantial flowing of fused silica, if only the values of η, γ and h are known. In the experiments carried out by White *et al.* [82], the viscosity η was determined by the furnace temperature and h was defined directly by the thickness of deposited glass. The viscosity could also be assumed constant throughout the depth h, since long (>1

hour) flow time t assured the temperature uniformity of the micro-structure.

In case of laser polishing however, the temperature distribution is determined by the absorption depth of laser radiation and the extent of thermal diffusion taking place in the timescale of polishing. The temperature distribution is thus intrinsically nonuniform and dynamic and the precise definition of thickness h and viscosity η turns out to be problematic. However, it is possible to estimate the range of thickness h knowing the softening point temperature of silica ($\sim$1667 °C, $\eta = 10^{6.6}$ Pa·s, see Table 2.5 p.32) and the absorption depth of CO_2 radiation at low temperatures ($\leq$30 μm [25]) and the fact that surface temperature cannot exceed $\sim$2700 °C to avoid mass loss through evaporation (see Section 2.5 p.56). The softening point is regarded as an onset of plasticity, thus it is plausible to assume that no significant mass flow can occur in the material above this viscosity in the timescale of laser polishing. Since the avoidance of additional material removal was one of the goals of laser polishing, the melt temperature could not exceed 2700 °C (see vapour pressure data, Figure 2.16 p.60) to avoid mass loss. Following the reasoning, the minimum value of viscosity ($\eta = 10^3$ Pa·s at 2700 °C) can be found with the aid of extrapolated characteristics from Figure 2.17 p.61.

The lower limit of h is defined by the absorption length of CO_2 wavelength in silica, yielding $\sim$30 μm. The upper limit can be found from the steady-state temperature distribution ($t \to \infty$) in 1 mm thick silica slides, which have been used for the experiments. The assumption of surface temperature $\sim$2700 °C and the maximum viscosity of $10^{6.6}$ Pa·s ($\sim$1667 °C, softening point) above which no flow occurs, gives the maximum value of $\sim$200 μm.

The unavailability of data on surface tension of silica can be explained by high temperatures needed to carry out the measurements. However, a representative value $\gamma = 300$ mJ/m^2 can be estimated from the convergence of surface tension data for binary silicate glasses [19].

I've taken the intermediate values of thickness $h = 50$ μm and average viscosity $\eta = 10^5$ Pa·s for the calculation of spatial frequency response of laser polishing, according to Equation 6.1, with the flowing time as a parameter. Figure 6.1 displays the result of calculations. The timescale necessary for 10 fold decrease of the amplitude of surface waviness, corresponding to 10 μm machining ripple (spatial frequency 100 lines/mm), ranges from milliseconds upwards. The magnitude of the calculated timescale is coherent with experimental observations made by other

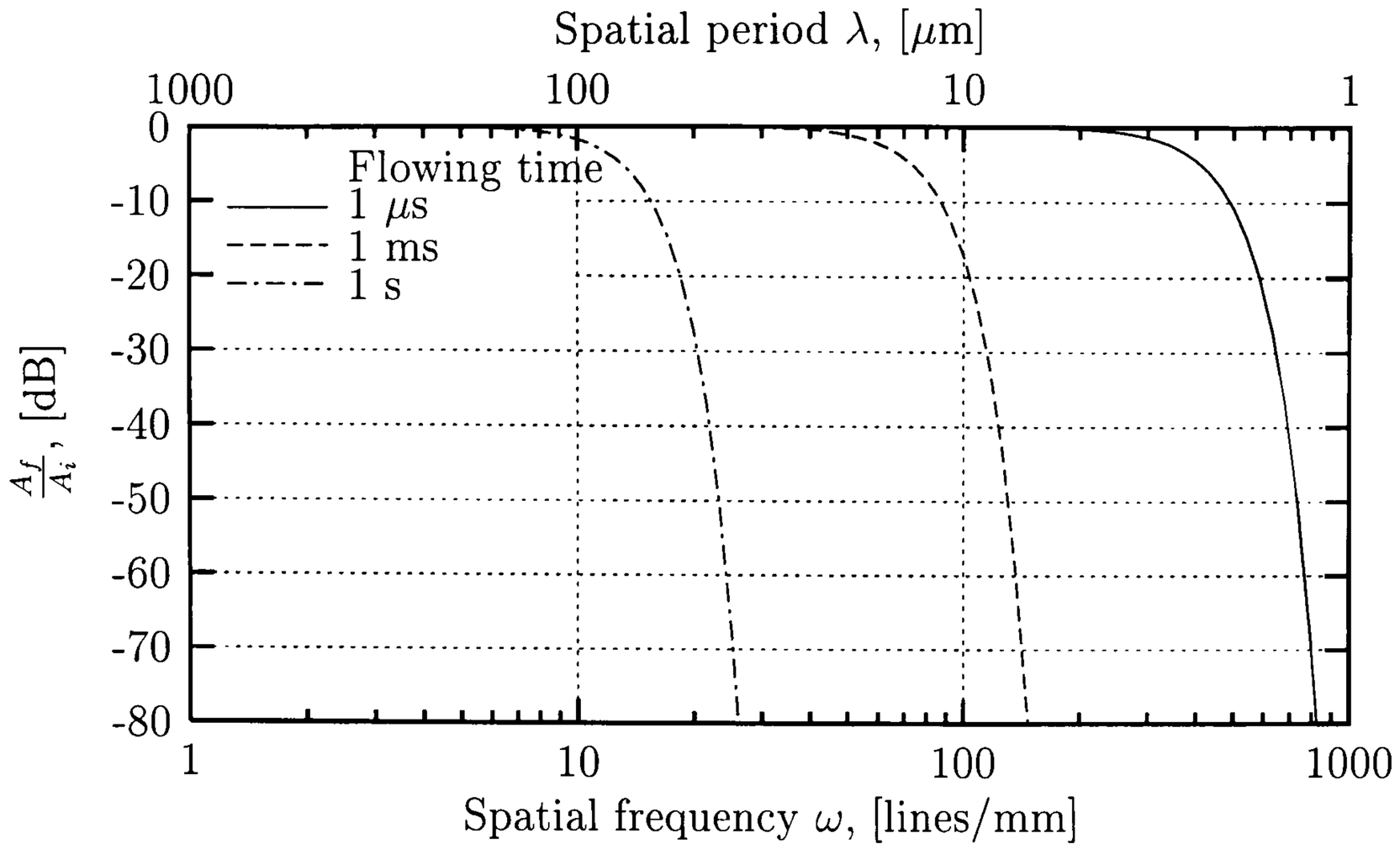

Figure 6.1: Theoretical prediction of frequency response of laser polishing. Calculated from Eq. 6.1 with $h = 50$ μm, $\eta = 10^5$ Pa·s and $\gamma = 300$ mJ/m^2.

researchers (see Section 6.1.3). Strong dependence of transfer function A_f/A_i on the spatial frequency $\omega = 1/\lambda$ is predicted. The curves, shown in Figure 6.1, indicate that high performance, low-pass filter behaviour can be expected, with sharply defined cut-off frequency. This extraordinary selectivity is of great significance for the polishing process, allowing for controllable removal of high frequency patterns without a global modification of shape.

From the characteristics in Figure 6.1 it is clear that sub-micron ($\omega > 1000$ lines/mm) features can be highly attenuated in a matter of microseconds. The described polishing mechanism is thus also responsible for exceptional smoothness of ablation craters, described in Chapter 4. The presence of thin layer ($\sim$3 μm) of highly mobile, molten glass during the CO_2 ablation (see Section 4.7 p.91), combined with the flow time in order of tens of microseconds (determined by the cooling rate of ablation site $\sim$6 °C/μs, see Section 4.11 p.102), results in very effective polishing action.

6.3 Experimental study on CO_2 micro-polishing of silica

Summarizing the findings from Section 6.2, the characteristics of surface tension driven smoothing of surfaces is determined by material properties, such as viscosity and surface tension of liquid silica, melt zone dimensions and the flow time (later called also the dwell time). The advantage of using a laser for the polishing is that spatio-temporal parameters (melt zone dimensions, dwell time) can be easily controlled by laser beam settings and the laser wavelength. The beam diameter sets a feature size limit on the polishing process by confining the melt zone area.

From the characteristics, shown in Figure 6.1, it is clear the melt zone diameter can be as small as ~100 μm without affecting the polishing bandwidth. This localized micro-polishing approach allows for a substantial reduction of laser power necessary to carry out the smoothing process, leading to much lower heat load of micro-optical component and excellent capabilities of process control. Additionally, the uniformity of beam profile is no longer an issue [52], since the polishing action is confined to a very small area of melt zone while the overall irradiance uniformity is assured by the overlap of many such melt zones in a raster scan regime.

The laser can also control the value of viscosity, exploiting the strong temperature dependence of that parameter (see Figure 2.17, p. 61). It can be simply done by delivering right amount of heat into the melt zone. The melt depth, determined primarily by the absorption length α^{-1} for CO_2 wavelengths, can be controlled to some extent by the thermal diffusion taking place in a dwell time. In the end, the devitrification (see Section 2.4.2 p.48) can be suppressed due to a very short lifetime of the melt zone.

The smoothing performance, predicted theoretically in Section 6.2, can be experimentally assessed by the measurement of spatial frequency response, having laser beam settings and dwell time for parameters. This knowledge allows for analysis, optimisation and subsequent application of laser polishing for the restoration of surface quality of as-machined optical elements, as described in Chapters 5 and 7.

6.3.1 Methodology

A measurement of spatial frequency response of laser polishing requires sophisticated experimental techniques. Having carried out pilot experiments on laser

polishing of abraded silica surfaces I've concluded, that in order to get meaningful results in spatial frequency domain, the polishing should be done on prescribed test surfaces with spatial frequencies of interest. The test shape, containing spatial frequencies in a range 2 - 500 lines/mm, has been computer generated and converted into a file printable by the machining station. The boundaries of the spatial frequency domain have been dictated by the tip radius (2.5 μm) of a DekTak^{TM} profiler and maximum anticipated size of features that should remain unaffected by laser polishing (>100 μm).

A number of such surfaces has been written into silica substrate (see Figure 6.2) allowing for a detailed study of frequency response. The test surfaces of the same shape were used for all laser polishing experiments described in this chapter. The correlation between different samples and the ability to detect the material removal threshold were the natural consequences of the method.

The tip profiler has been used to acquire the shapes of polished and reference surfaces (Figure 6.3). Fast Fourier Transform (FFT) analysis with Gaussian data window has been applied to the measured profiles to calculate the spatial frequency response for each test surface. Frequency aliasing effect has been avoided since the tip radius of 2.5 μm has set a limit on maximum measurable spatial frequency, thus acted as an anti-aliasing filter for the chosen spatial sampling of 1 μm.

6.3.2 Experimental confirmation of theoretical predictions - millisecond timescale laser polishing

The study, presented in this section, aims to verify theoretical predictions from Section 6.2. The experiments described here have assessed the effectiveness of surface smoothing with single, sub-millisecond laser pulses, the longest that could be produced without a risk of laser damage.

The polishing pulse, produced with AOM by modulating the intensity of single laser pulse, consisted of two main parts: 100 μs melting pulse and a train of micro-pulses with adjustable duty factor, as shown in Figure 6.4. The melting pulse was designed to deliver an amount of energy needed to raise surface temperature up to a flow point (temperature at which the viscosity of material is sufficiently low that only surface flow takes place in a timescale of that pulse). The duration time of that pulse should be as long as possible for better control over laser heating, as mentioned in Section 4.4 p.84. The task of the following pulse train was to maintain

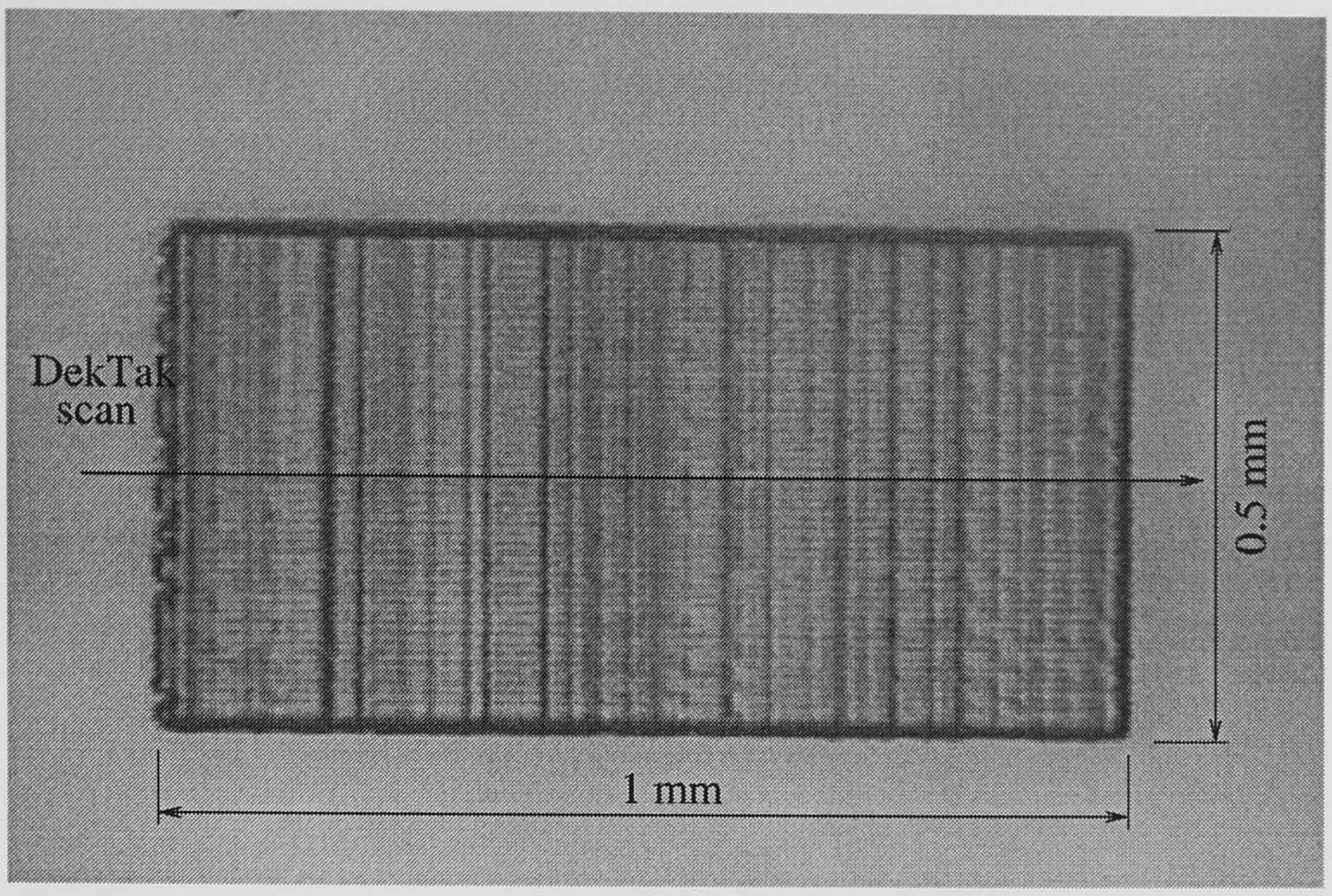

Figure 6.2: Micrograph of test surface used for laser polishing experiments. Dimensions 1 x 0.5 mm.

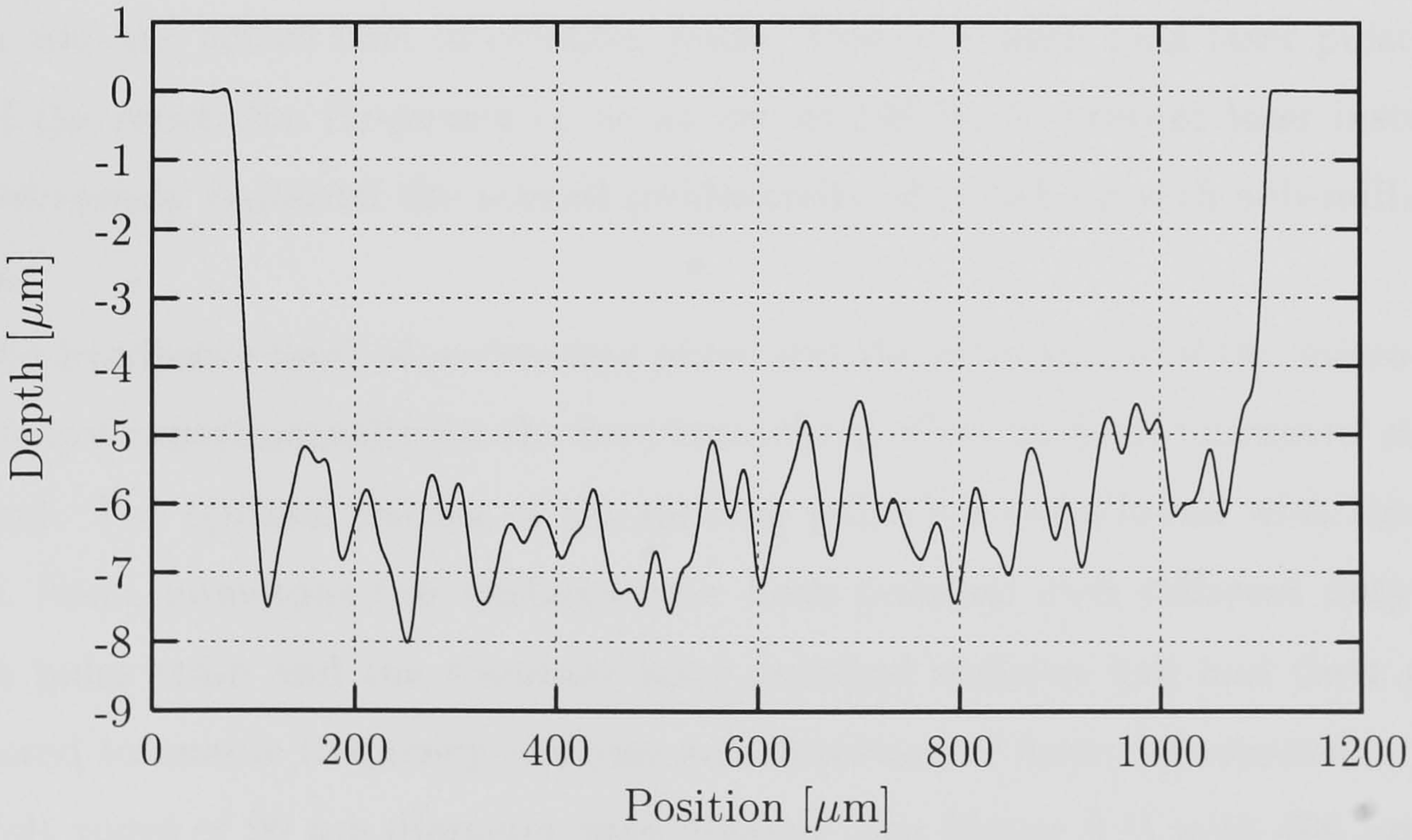

Figure 6.3: Typical profile of test surface from Figure 6.2 before laser polishing.

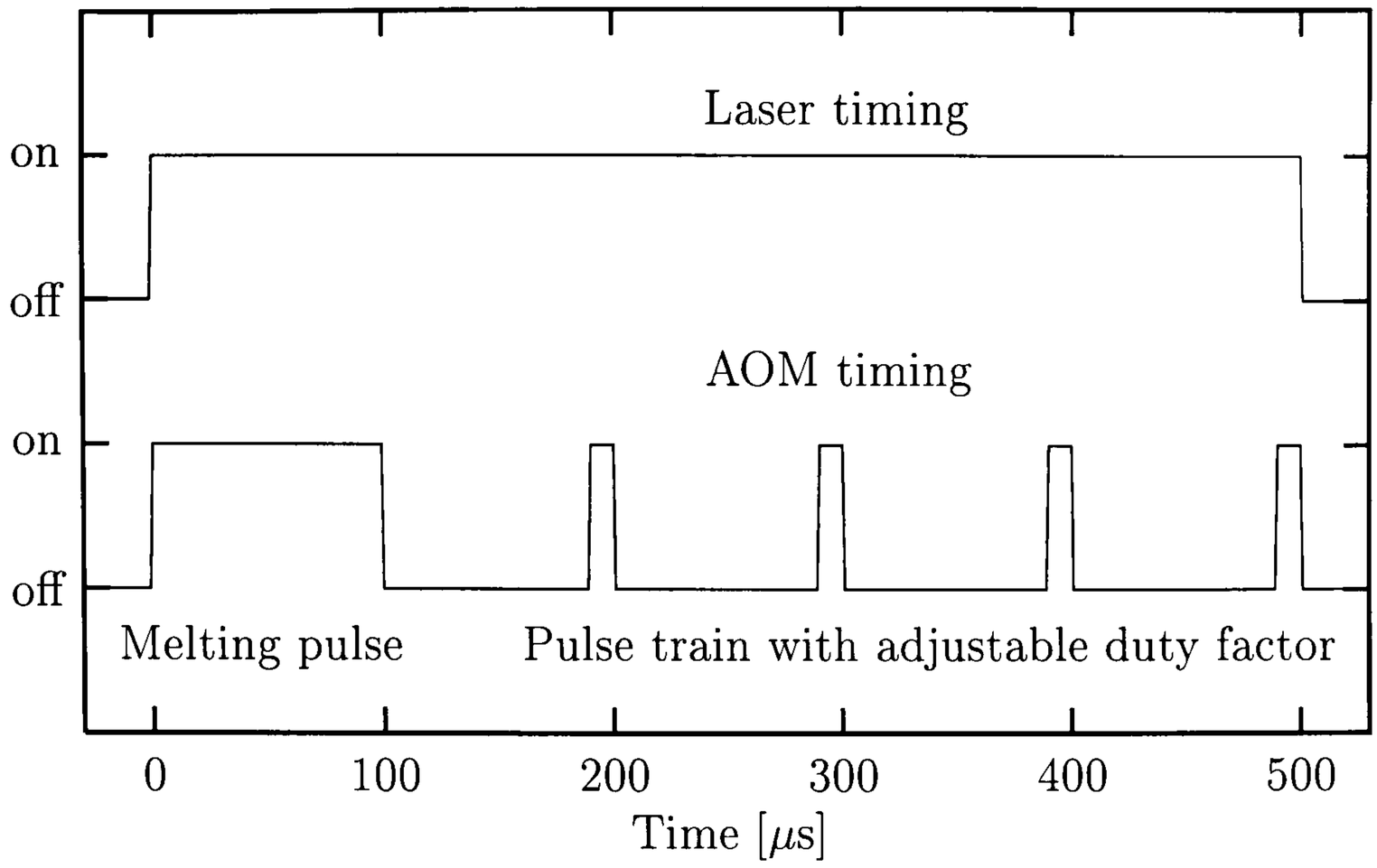

Figure 6.4: Complex pulse used for millisecond laser polishing, active part 400 μs. The energy of the pulse train was controlled by the prescribed duty factor.

high surface temperature without exceeding 2700 °C in order to avoid undesired material loss.

Maximum duration time of CO_2 laser pulse was limited to 500 μs due to a possibility of resonator damage. I've chosen melting pulse duration of 100 μs as a compromise between a good control over melting and maximum length of pulse train, which was the active part of complex pulse. However, such long laser pulses have forced the repetition frequency to be as low as 100 Hz to prevent laser instability. This obviously impaired the overall productivity of polishing with sub-millisecond pulses.

The irradiance level of preheating pulse and the duty factor of the micro-pulses were found experimentally for the best smoothing effect without unwanted material removal. The optimal fluence of the melting pulse has been found with the aid of AOM. Next, numerous test surfaces have been polished with different duty factor of the pulse train and the resultant laser polished surfaces had had their profiles measured to enable frequency analysis and detection of material removal.

Melt zones of 90 μm diameter were created (See Figure 6.5) with 400 μm beam diameter, the biggest spot size available due to a fluence limitation imposed by relatively short duration of preheating pulse. The melt zones were overlapped in a single line on 10 μm pitch to cover large area of the test surface in order to

facilitate profiling with DekTak. The other benefit of the overlap was the increase of dwell time from original 400 μs to 3.6 ms (factor of 9), allowing for achievement of desired millisecond polishing time. Thermal coupling between the melt zones has been avoided by the interleaving technique, similar to one described in Section 5.4 p.113.

The search for optimal polishing conditions with single, thermally decoupled laser pulses is summarized in Table 6.1. The acquired profiles of untreated and laser polished samples permitted the calculation of spatial frequency spectra, which are shown in Figure 6.6. Subsequently, the frequency response characteristics has been calculated as a ratio of polished and unpolished spectrum and the result is shown in Figure 6.7.

The experiment has proved that the laser polishing is capable of smoothing the surface in a certain bandwidth of spatial frequencies, without further machining, in a timescale of milliseconds, as anticipated by the theory. The curve from Figure 6.7 resembled the characteristics of low pass filter with a 3 dB cutoff frequency ~20 lines/mm, translating into feature size of 50 μm. I've chosen the attenuation at frequency of 100 lines/mm per pass A_{100} to be a figure of merit of the polishing process:

$$A_{100} = 20 \log \frac{A_i}{A_f(\omega = 100)}$$

That frequency corresponds to the maximum crater overlap of 10 μm, thus lowest possible, undesired spatial frequency introduced by the rasterized machining described in Chapter 5. For the optimal process presented in this section (regime code A), the value of A_{100} was 15 $\pm$5 dB per pass. However, the profile measurements have indicated that the removal of thin surface layer (less than 0.1 μm) took place. This figure could be an outcome of the measurement error associated with the presence of machining ripple and residual machining debris on unpolished test surfaces.

Regime code		A
Spot diameter	[μm]	400
Melt zone diameter	[μm]	~90
Peak irradiance	[kW/cm^2]	~60
Melting pulse fluence	[J/cm^2]	6.0
Pulse train fluence	[J/cm^2]	4.3
Pulse train duty factor	[%]	20
Frequency	[Hz]	100
Overlap	[μm]	10
Effective dwell time	[ms]	3.6
Depth removed	[μm]	<0.1

Table 6.1: Characteristics of optimal complex polishing pulse.

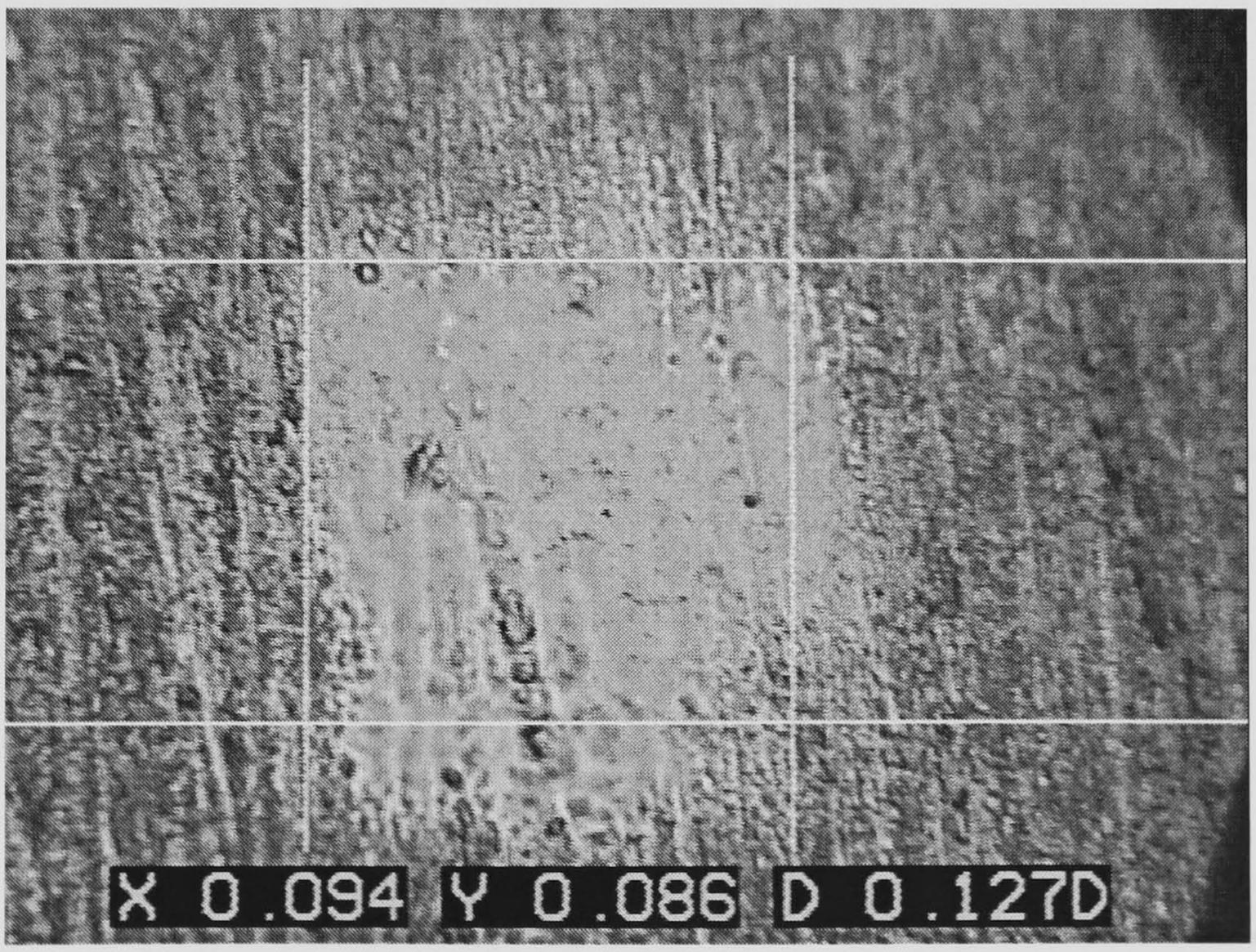

Figure 6.5: Micrograph of a melt zone on an abraded surface of a silica slide, digital readout in millimeters.

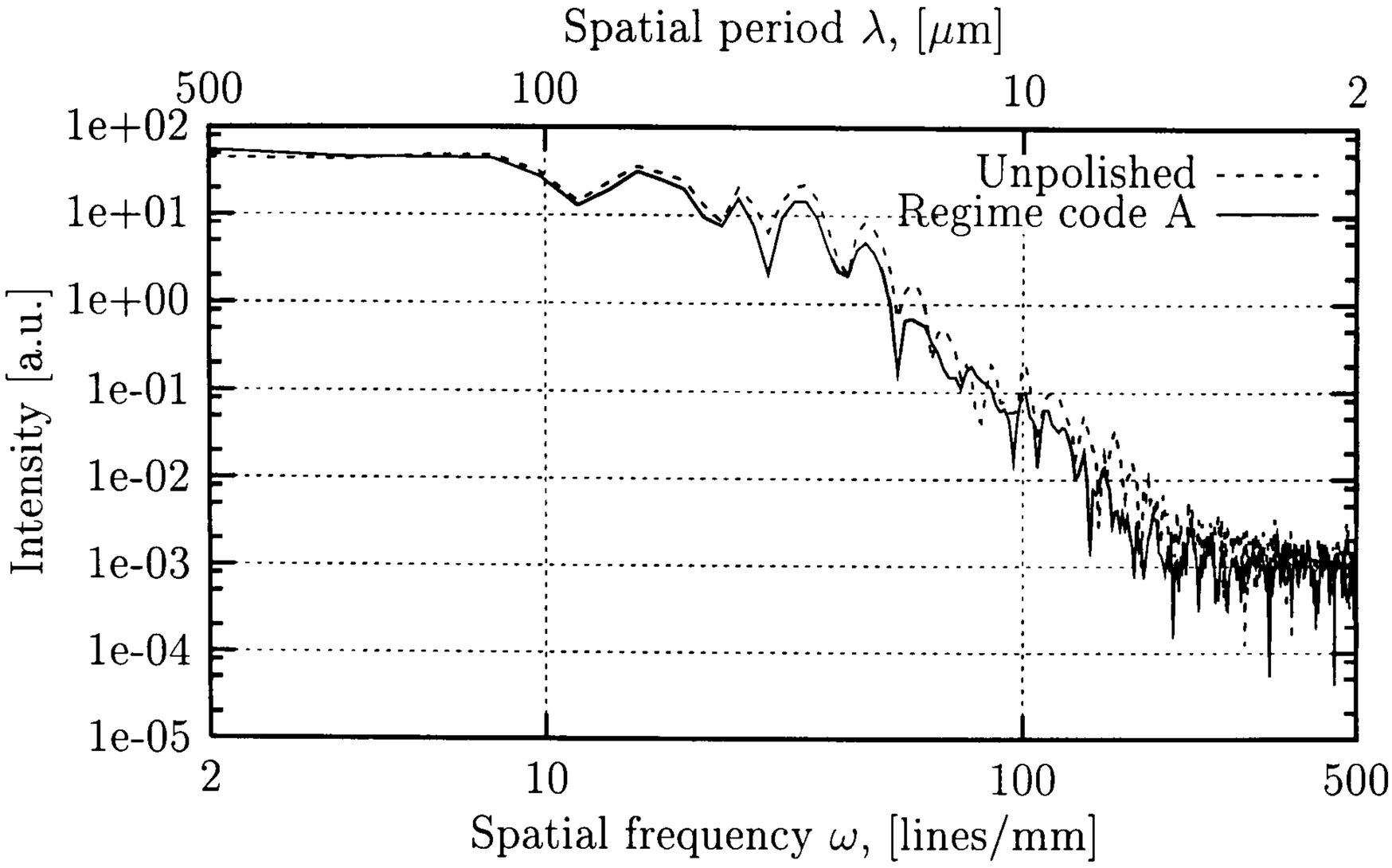

Figure 6.6: Frequency spectra calculated using FFT from the test surface profiles measured by DekTak. Test surface has been laser polished in conditions listed in Table 6.1 (regime code A).

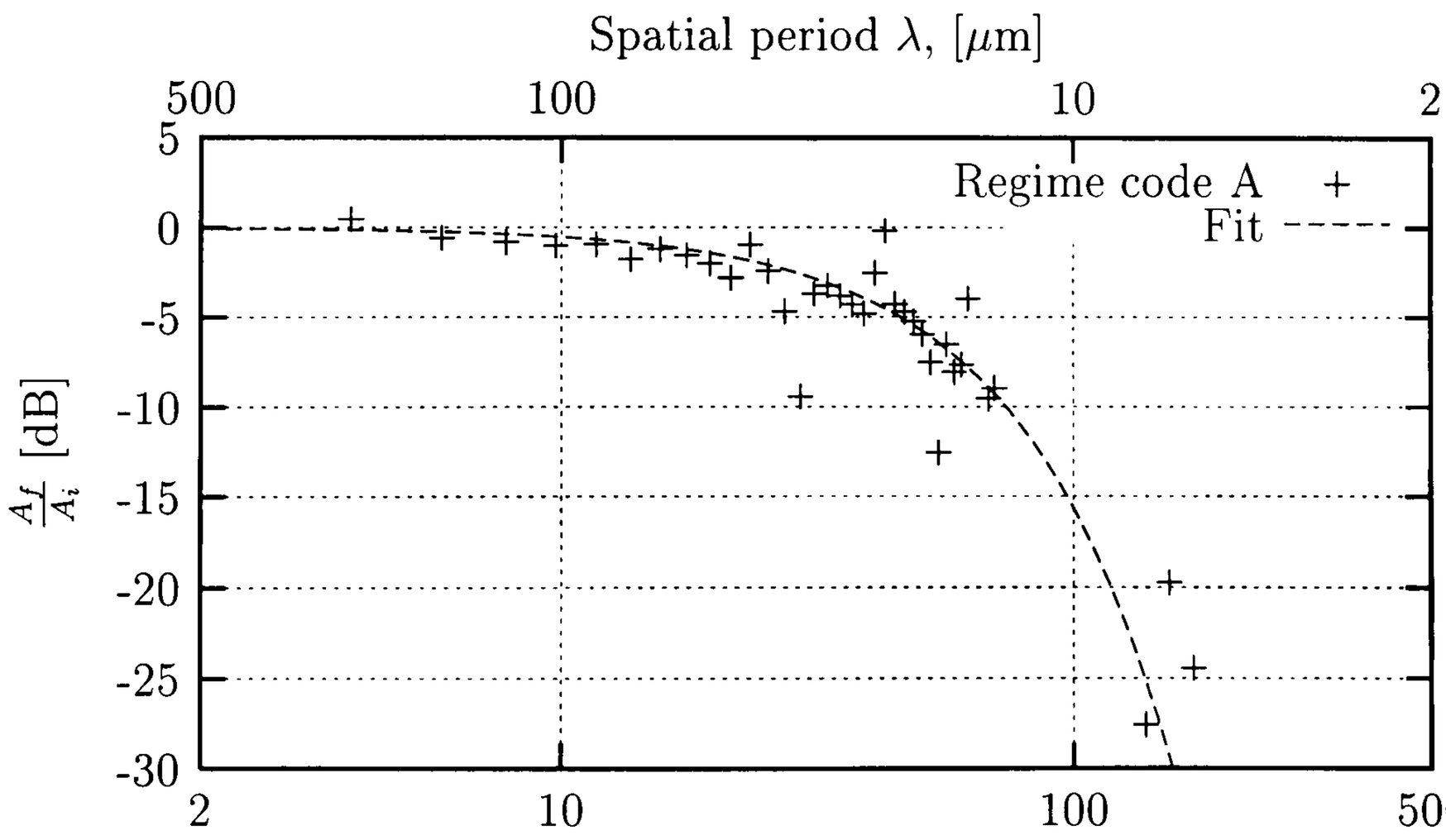

Figure 6.7: Frequency response of laser polishing with sub-millisecond pulses according to regime A, shown in Table 6.1. Calculated as a ratio of peak amplitudes selected from the frequency spectra from Figure 6.6. The reliability of measurements in the range ω >100 lines/mm is compromised by low signal to noise ratio.

Regime code		B	C	D
Spot diameter $1/e^2$	[μm]	800	800	1000
Melt zone diameter	[μm]	150	150	200
Mean irradiance	[kW/cm^2]	3.3	2.4	2.1
Peak irradiance	[kW/cm^2]	22	16	14
Average laser power	[W]	8.3	6.0	8.2
Fluence per pulse	[J/cm^2]	0.67	0.49	0.42
Frequency	[Hz]	5000	5000	5000
Overlap X	[μm]	2	1	1
Overlap Y	[μm]	10	10	10
Spot dwell time	[ms]	15	30	44
Effective dwell time t_{edw}	[ms]	225	450	880
Depth removed	[μm]	<0.1		

Table 6.2: Characteristics of raster scan polishing regimes.

6.3.3 Efficient raster scan micro-polishing

The potential of laser polishing of as-machined silica surfaces has been demonstrated. However, the performance needed to be improved to reach the level of practical importance, since the sub-millisecond laser pulses could not be produced with high repetition frequency necessary for high productivity. High frequency (quasi-CW) raster scanning with the pulses as short as 20 μs, maximum pulse repetition frequency of 5 kHz, has proved to be a much better solution. This method offers not only dwell times two orders of magnitude longer, promising hundred-fold increase of polishing efficiency, but also high rates of area coverage, ~16 cm^2/min, leading to substantial performance improvement. The 5 kHz frequency and 20 μs pulse duration (10% duty factor) have been chosen as a compromise between advantageous CW mode and stable laser operation.

Table 6.2 presents the parameters of studied polishing regimes. A set of samples per regime has been laser polished with varying pulse energy to find the point of maximum performance without material removal, similarly to experiments described previously in Section 6.3.2.

Figure 6.8 shows the measured frequency response of regimes B to D with a dwell

time t_{edw} as a parameter. The data points have been fitted with the theoretical curve, resembling the characteristics from Equation 6.1,

$$A(\omega) = \exp\left(K\ \omega^M\ t_{edw}\right) \tag{6.2}$$

where ω is a spatial frequency, K and M are fitting parameters. The results of fitting are shown in Table 6.4. The influence of frequency is weaker than expected from the theoretical model. It may be a result of nonuniform distribution of viscosity in the melt layer, which compromises the derivation conditions for Formula 6.1. The discrepancy can be also attributed to a non-Newtonian character of the mass flow.

According to theoretical considerations from Section 6.2, the control over the characteristics of spatial frequency attenuation can be achieved experimentally by controlling the effective dwell time t_{edw}. It has been confirmed by the experiments. However, it is the depth of softened material and the viscosity, due to its strong temperature dependence, that have the greatest impact on the resultant attenuation of spatial frequencies. Table 6.3 backs up the statement by comparing the sensitivity

Regime D

Fluence per pulse	[J/cm^2]	0.38	0.40	0.42	0.44	0.47
A_{100}	[dB/pass]	15±5	30±5	50±5	80±5	>100
Depth removed	[μm]	<0.1	<0.1	<0.1	0.1	1.1

Regimes A to D - max. performance

Effective dwell time t_{edw}	[ms]	3.6	225	450	880
A_{100}	[dB/pass]	15±5	35±5	50±5	80±5

Table 6.3: A_{100} sensitivity to pulse energy and dwell time. Polishing conditions for regimes A-D are listed in Tables 6.1 and 6.2.

of A_{100} to pulse energy and effective dwell time setting.

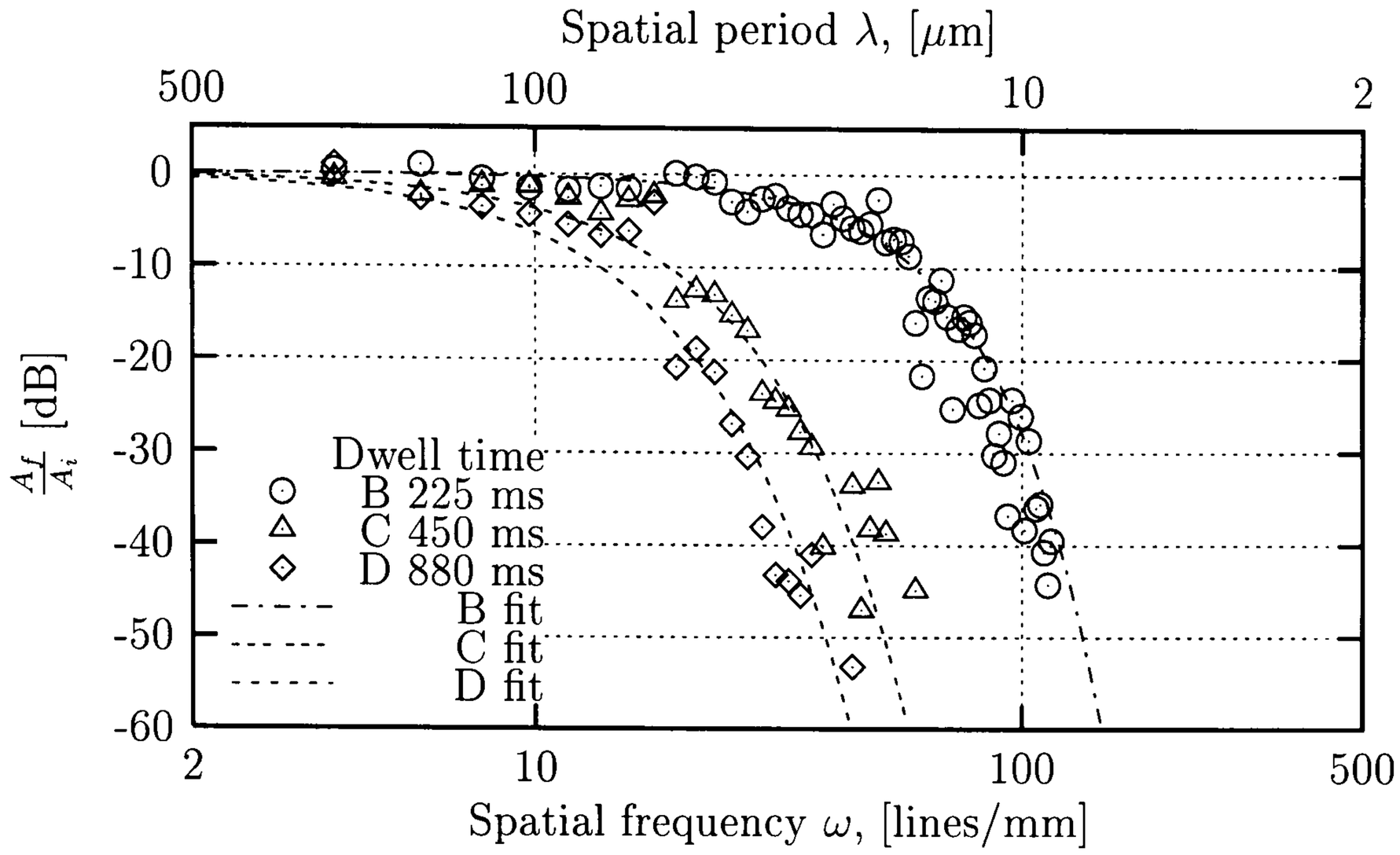

Figure 6.8: Comparison of frequency responses of different polishing regimes. Regimes indicated by code letters can be found in Table 6.2. The fitting parameters for the data fits, according to Eq. 6.2, can be found in Table 6.4.

Regime code		B	C	D
M		2±0.7	1.6±0.2	1.5±0.2
K	[mm^M/ms]	1.5±3.3	1.4±0.7	0.9±0.5

Table 6.4: Curve fitting parameters for the data shown in Figure 6.8.

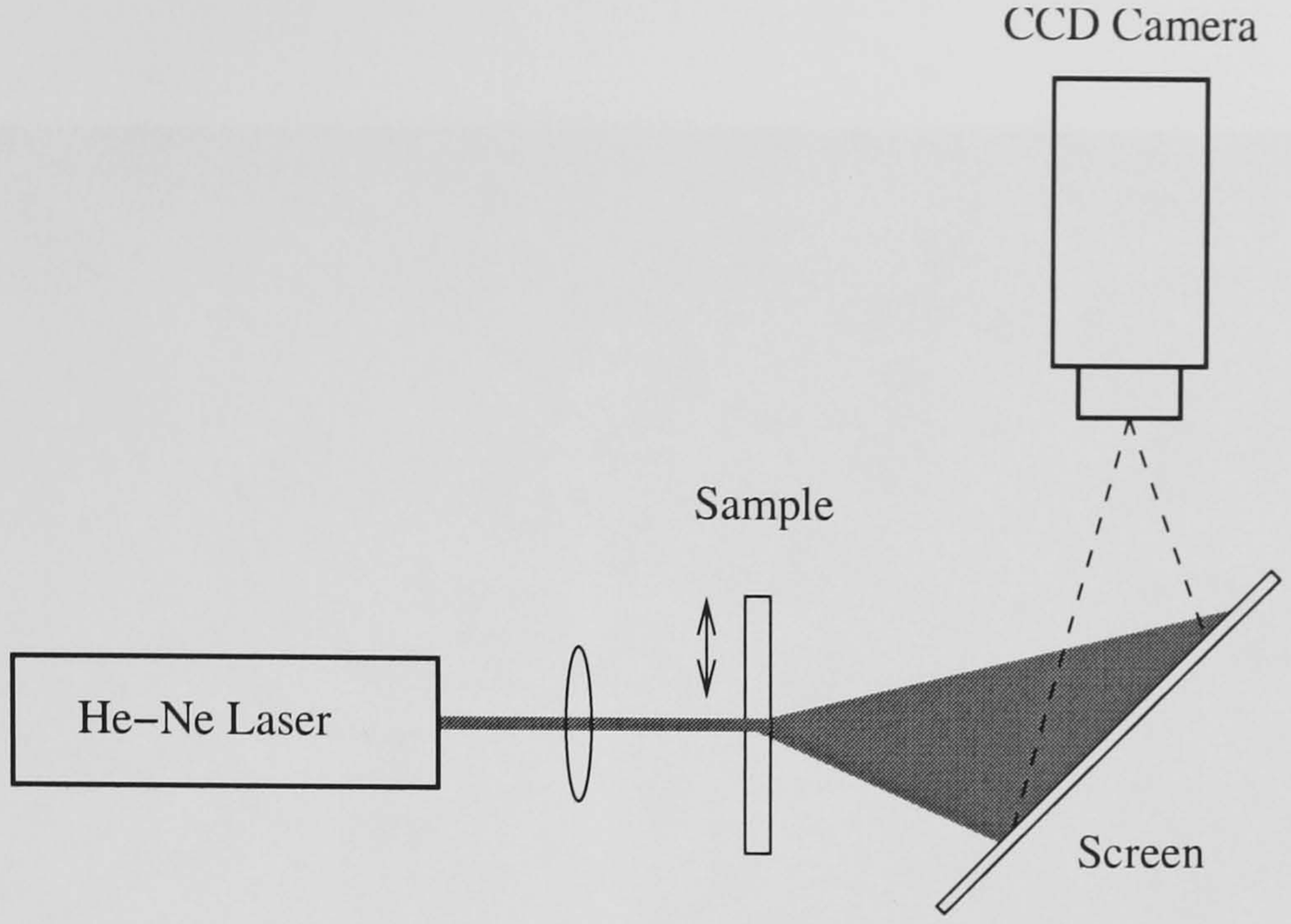

Figure 6.9: Schematic diagram of a setup used for the assessment of optical scattering.

6.3.4 Assessment of optical properties of polished surfaces

The as-machined surface is covered with a regular pattern of lines, being the result of raster scanning. These lines with micron-size spacing give rise to very efficient diffraction of light transmitted through such surface. Additionally, significant scattering occurs on the residual machining micro-debris, consisting of sub-micron size particles of resolidified silica vapours, which stick to the surface. The optical evidence of efficient suppression of these unwanted features by the laser polishing has been reported here. The discussion on the degree of residual, stress-induced birefringence is also presented in this Section.

Assessment of optical scattering. The scatter assessment setup is shown in Figure 6.9. The He-Ne beam, focussed down to 500 μm diameter, was normally incident onto the surface of sample. The transmitted beam was intercepted by a screen, which was monitored by a CCD camera. Using this simple setup it was possible to measure the transmittance of the sample with accuracy $\pm 2\%$ and, with less accuracy, the reflectance and a fraction of laser power lost to optical scattering. Additionally, it was feasible to acquire the images of scatter pattern.

Figure 6.10 shows a typical scatter pattern obtained on the as-machined surface with raster pitch 10×10 μm. The bright horizontal and vertical lines correspond to the diffraction on the grating created by orthogonal raster lines. Wide field of laser

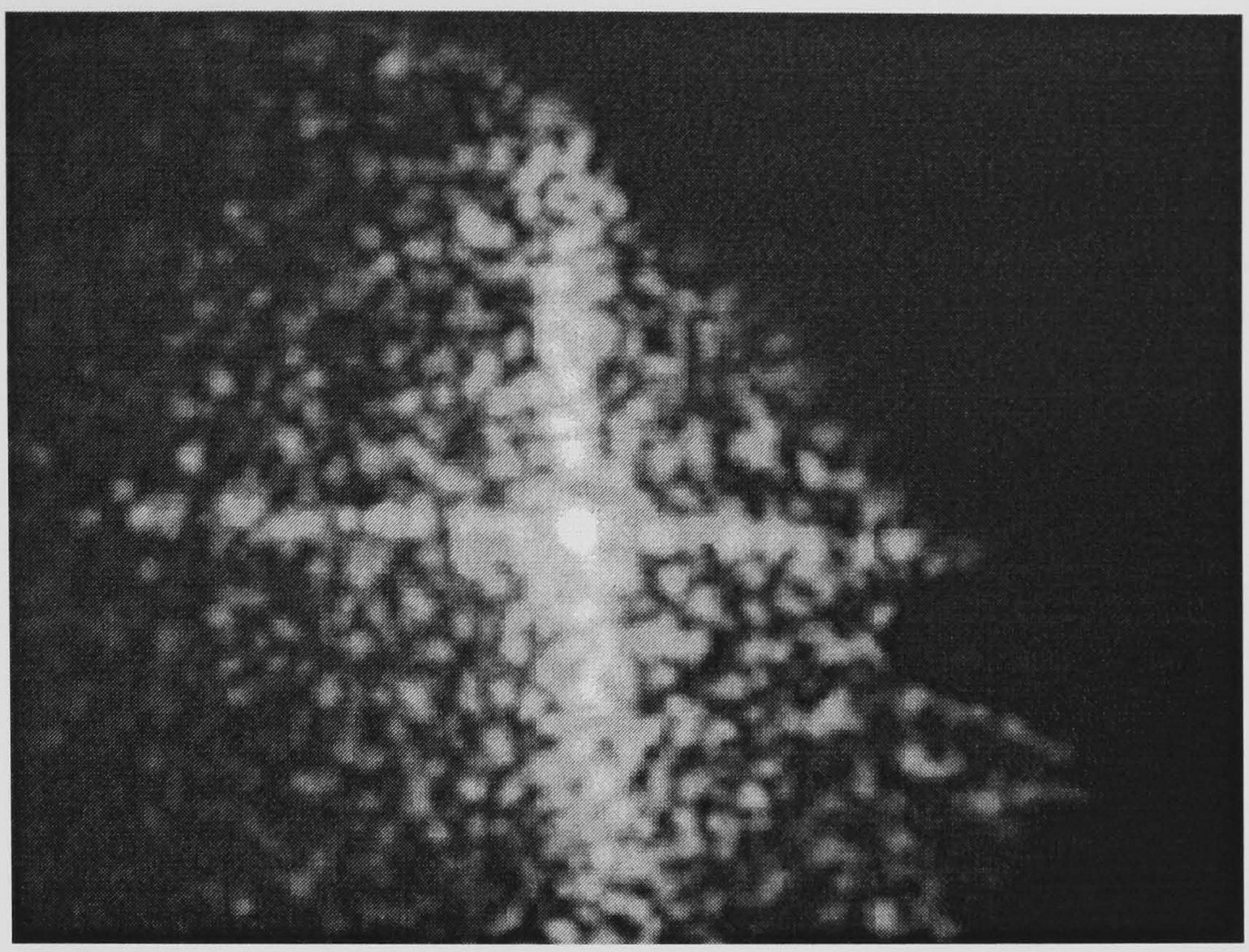

Figure 6.10: Scatter pattern on an as-machined surface. A part of the field has been shadowed by the sample holder.

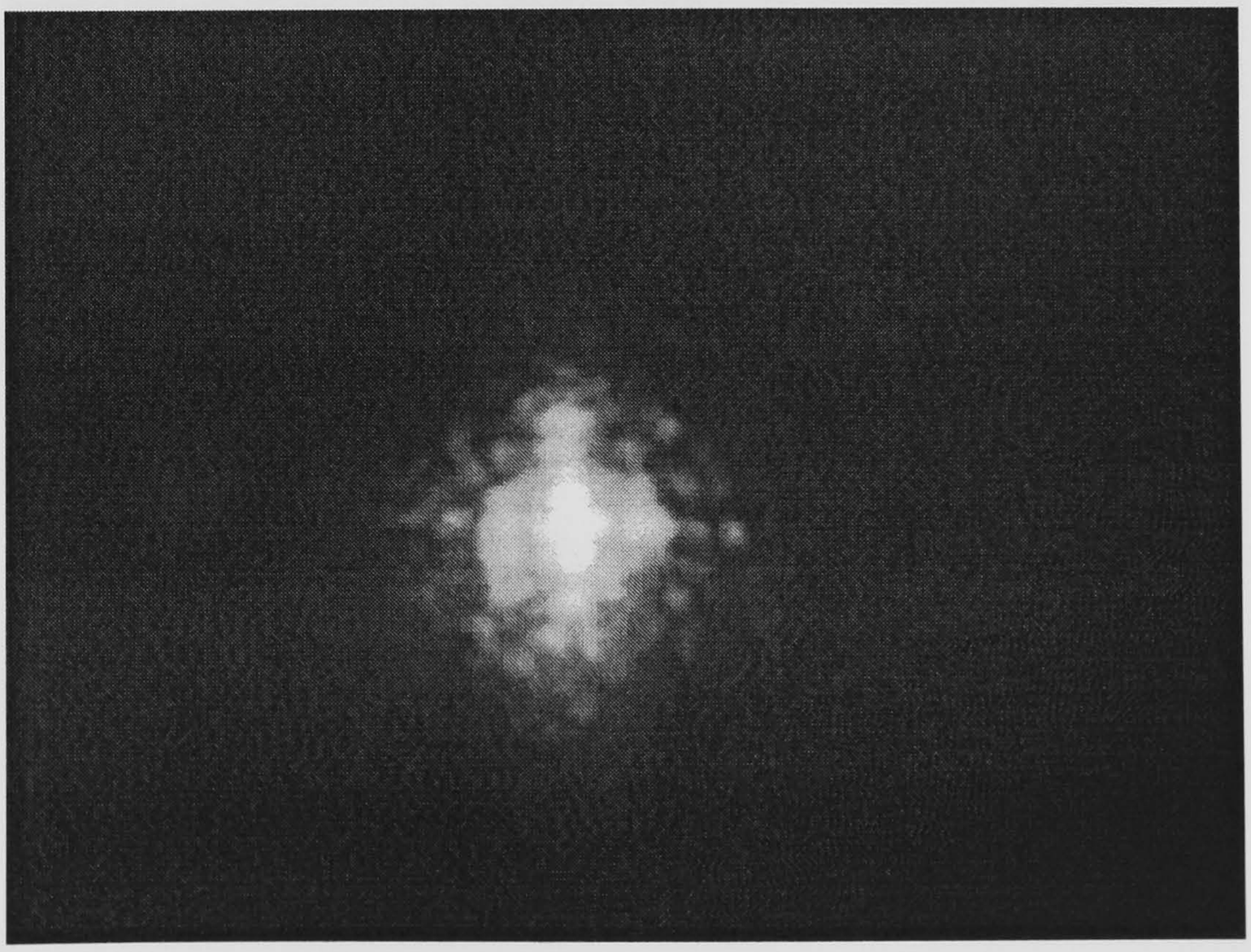

Figure 6.11: Scatter pattern after single pass polishing.

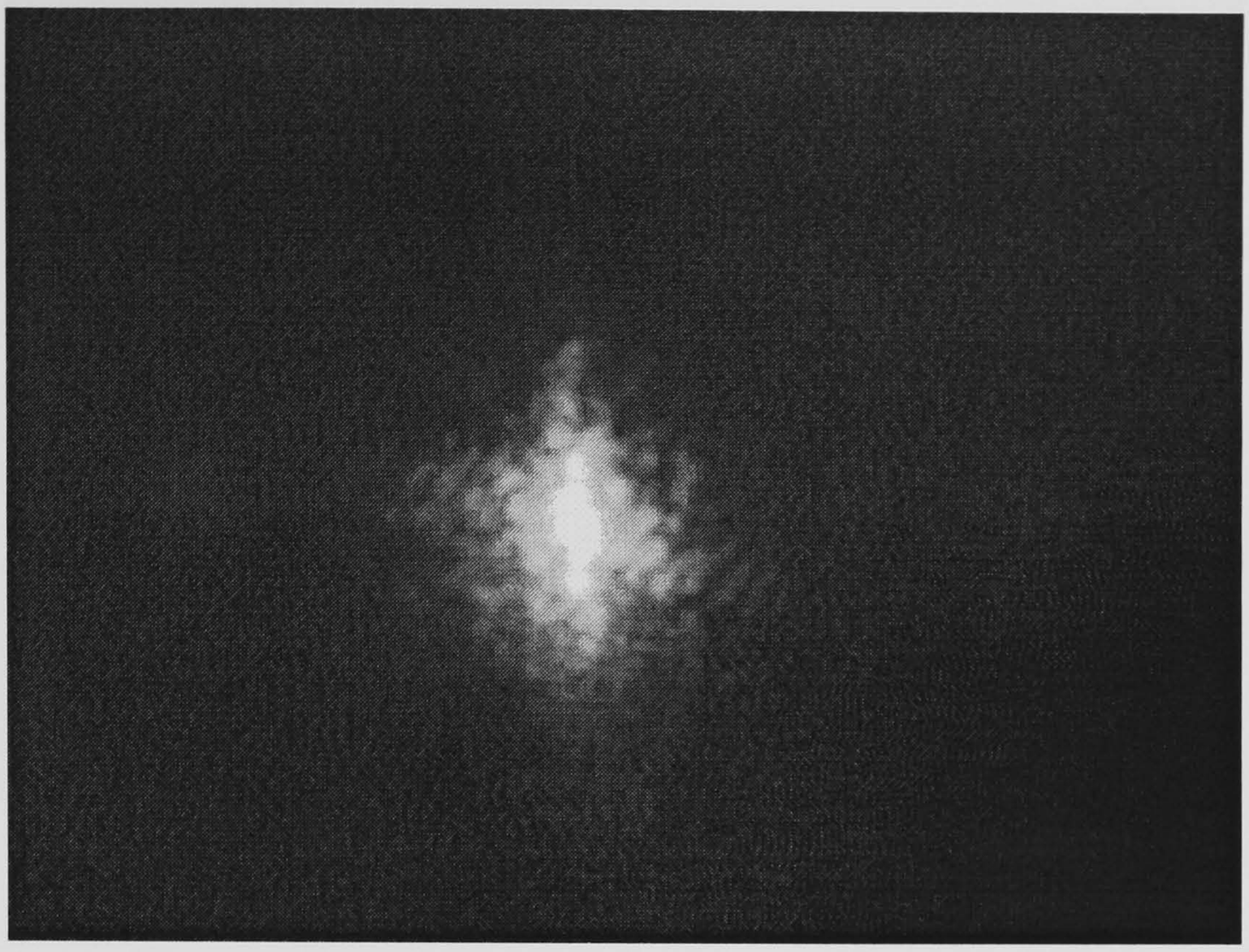

Figure 6.12: Scatter pattern after 2-pass polishing.

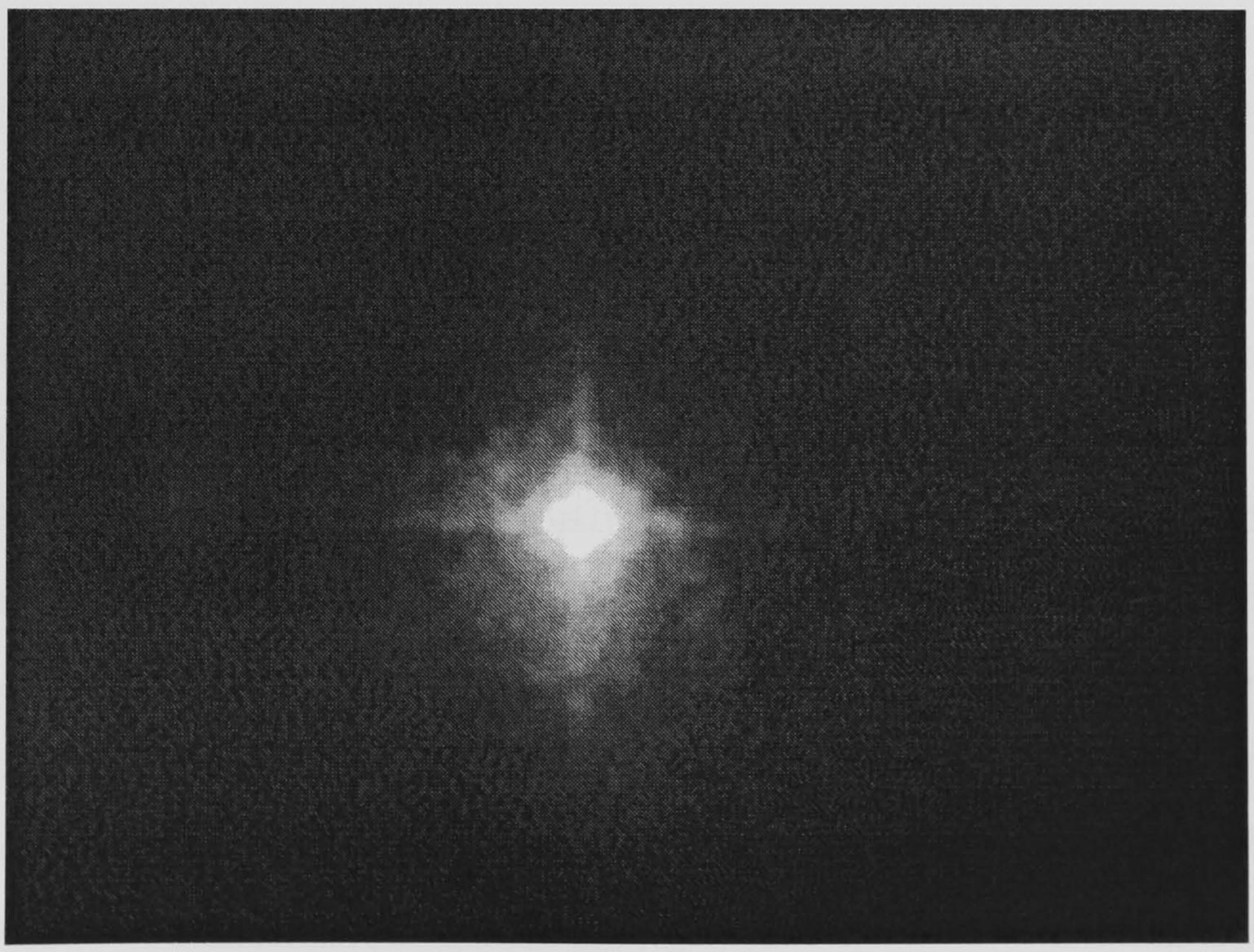

Figure 6.13: Scatter pattern after 4-pass polishing.

Figure 6.14: Undisturbed reference beam profile.

speckles is a product of forward scattering on the post-machining micro-debris.

Scattering efficiency measurements, carried out in the setup from Figure 6.9, have shown that nearly 50% of impinging laser power was diffracted away from the zeroth order in a form of higher diffraction orders and laser speckles. Next, the as-machined surface has been laser polished according to the regime B (see Table 6.2) with conservative fluence setting of 0.60 J/cm^2 and expected value of A_{100} in a range 10-20 dB/pass. Four consecutive polishing passes have been applied to the same test piece to observe the progress of surface smoothing.

Figures 6.11-6.13 show the gradual reduction of the intensity of diffraction orders and the area occupied by the laser speckles. First two passes have practically removed the micro-debris by evaporating it or melting back it into the surface. Subsequent two passes have continued to reduce the number and intensity of visible diffraction orders. The resultant beam profile from Figure 6.13 can be compared with the undisturbed reference spot, shown in Figure 6.14. The scatter efficiency measurements, carried out after the polishing sequence, have shown that the transmission was practically identical for the original unmachined silica surface and the laser polished one. However, the removal of high spatial frequency components has uncovered the remaining low spatial frequencies, being the product of pulse energy variation with the line frequency, introduced during the fabrication of the test piece.

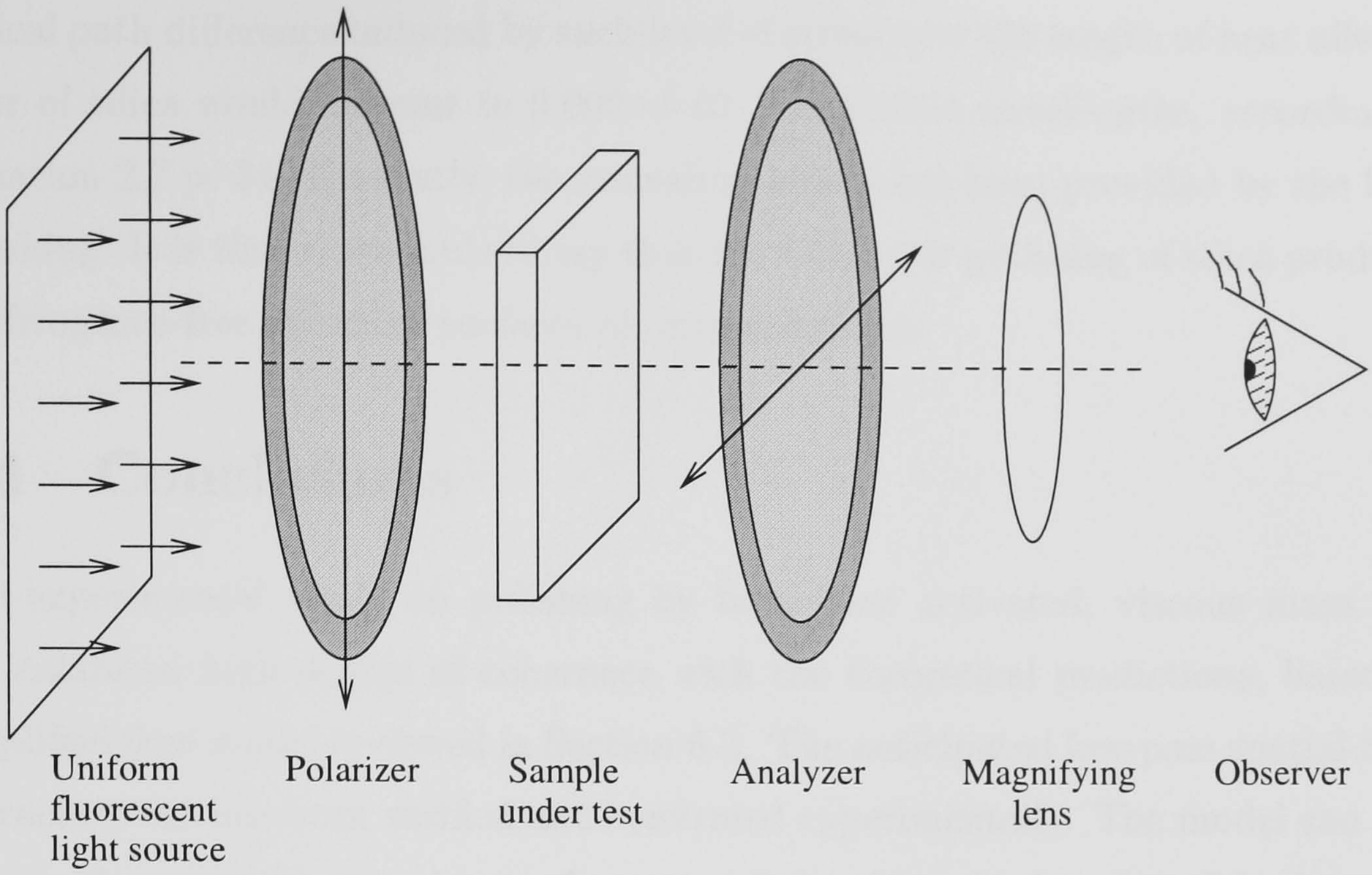

Figure 6.15: A schematic diagram of a simple setup used for polarimetric inspection of the laser polished samples.

The diffraction orders, near the zeroth order spot in Figure 6.13, are the signature of these low frequencies. It must be noted that there is no mark of polishing raster pitch 2×10 μm in the diffraction pattern.

Assessment of stress induced birefringence. Laser-polished microlens, shown in Figure 5.27 p. 138, has been inspected in the typical polarisation measurement setup depicted in Figure 6.15. No difference in appearance and colour has been observed between the laser polished and raw untreated areas, thus the optical path difference introduced in a thin layer of affected glass, estimated to be less than ~200 μm, must have been much less than $\lambda/4$.

The measurement result is consistent with the considerations on annealing of glasses presented in Section 2.4.4, p. 52. The expected maximum value of cooling rates during laser polishing of silica has been defined by the maximum surface temperature and the dwell time of a laser spot in the melt zone. In case of polishing regime D (see Table 6.2, p. 159, spot dwell time 44 ms), which has been applied to the tested microlens, the maximal cooling rate is ~0.04 °C/μs. Such rate would introduce residual stresses an order of magnitude smaller than practical strength of silica glass, according to the Formula 2.16 from Section 2.4.4, p. 52. The maximal

optical path difference induced by such level of stress over the length of heat affected layer of silica would amount to 0.002−0.02 λ at visible wavelengths, according to Equation 2.7 p. 34. Evidently, the annealing action has been provided by the laser polishing. It is thus reasonable to say that the CO_2 laser polishing of silica produces birefringence-free annealed surfaces of optical quality.

6.4 Conclusions

The experimental study on polishing by laser heat activated, viscous mass flow has exhibited high degree of coherence with the theoretical predictions, based on simplified flow model reviewed in Section 6.2. The anticipated low-pass spatial filter characteristics has been verified and confirmed experimentally. The model can also explain the excellent smoothness of crater walls in silica, produced by CO_2 ablation.

It has been shown that CO_2 laser can be also used to efficiently remove the characteristic pattern, introduced by raster scan machining. The investigated raster scan polishing of silica has been shown to be capable of restoring the optical quality of as-machined surfaces, without additional surface modification. The method offers not only high productivity rates of >16 cm^2/min but also the simplicity and excellent process control. All important parameters, such as melt zone dimensions, polishing time and material viscosity can be controlled solely by the laser beam parameters. Raster scanning mode adds to the simplicity of the method since the beam uniformity is no longer required. The reduction of the melt zone area, in comparison to conventional laser polishing, has reduced the heat load of treated element and laser power requirements.

Polished surfaces were free of cracking and stress-induced birefringence, however more research should be dedicated towards detailed investigation of the impact of heat treatment on the optical and meachanical properties of affected layer of material. It takes one or two polishing passes with characteristics of regime D, 1 mm beam $1/e^2$ diameter at TEM_{00}-like profile, raster pitch 2×10 μm, PRF 5 kHz and pulse duration of 20 μs and fluence 0.42 J/cm^2 to attenuate surface waviness of 10 μm period by more than 60 dB. From the initial surface state, 1.8 μm peak-peak amplitude of machining ripples, this figure can be brought down to <1.8 nm, assuring the removal of worst-case machining pattern. Further improvement of laser polishing can be expected by an application of laser, for which the absorption length

in silica α^{-1} is longer than for CO_2 laser. Just twofold increase of absorption depth would reduce the dwell time necessary for the equivalent ripple attenuation by a factor of 8, according to an idealized flow model. It would increase a productivity of the process. The CO laser, with absorption length longer than for CO_2 radiation, seems to be a good candidate for a more efficient laser polishing tool.

The scattering measurements have shown practically no difference between the laser polished surfaces and unmachined surface of silica sample. They have also confirmed that laser polishing raster does not contribute to the diffraction on the treated surfaces.

Chapter 7

CORRECTION OF LDA BEAM QUALITY

7.1 Introduction

This chapter presents a short overview of basic characteristics of high power, diode laser arrays (HPLDA). These devices become more and more important sources of cheap optical power delivered from efficient and compact packages. There is a number of issues that determines the attractiveness of these lasers, such high wall plug efficiency, high available power levels and low manufacture and ownership costs.

This Chapter demonstrates an original correction technique, which has been developed for the restoration of beam quality of high power diode lasers. It is believed to be the first account of efficient scheme for brightness restoration (M^2 from ~13 down to ~2.4) and reduction of pointing errors (~ten-fold) of commercially available, stacked, high power diode lasers. The novel technique described here involves wavefront characterisation and rapid fabrication of corrective micro-optics using CO_2 laser. The technique has a potential to be incorporated into the manufacturing cycle of HPLDAs to boost their performance and market attractivity.

The work described in this Chapter has been carried out in co-operation with Jesus Fernando Monjardin, who has built the wavefront measurement rig and was responsible for the characterisation of beam properties of laser diode bar stack before and after application of corrective micro-optics. Author was responsible for generation of mentioned micro-optics from available measurement data, for machining and laser polishing procedures and for characterisation of the product.

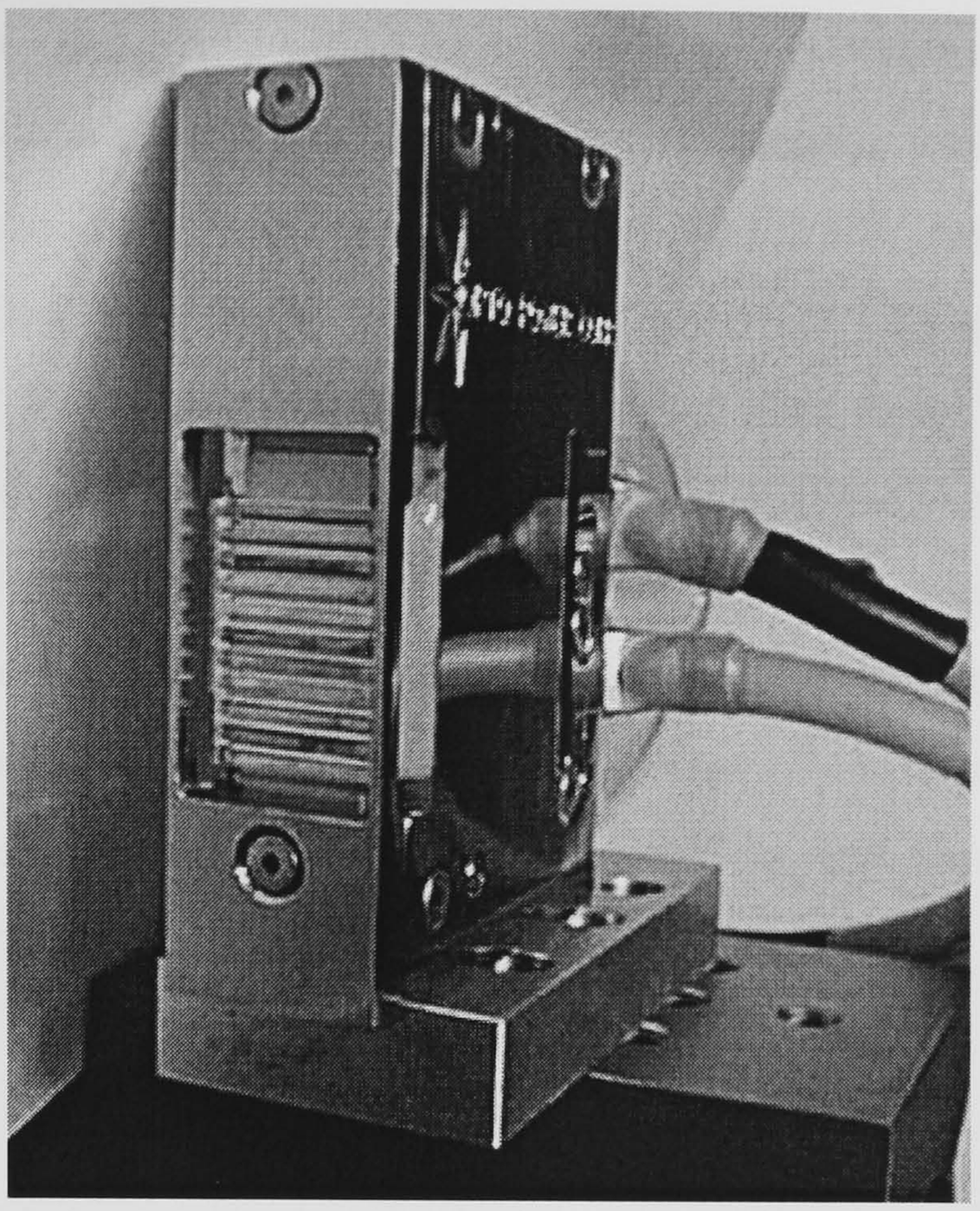

Figure 7.1: Photograph of the LDA under test, natural size. Eleven cylindrical collimating microlenses visible.

7.2 Design and fabrication of corrective optics

The diode bar stack under test was model MBM94011X1CW/L (see Figure 7.1), manufactured in 1998 by OptoPower Corp. (now Spectra Physics). The LDA consisted of 11 monolithic, 1-cm long diode bars (40 W CW per bar at 940 nm), each containing 24 incoherent emitters ($<$ 2 W per emitter, $\sim$200 μm wide), spaced by 390 μm pitch. Each bar was factory fitted with a cylindrical lens for fast-axis collimation, slow-axis patterns of the emitters were allowed to mix in a far field.

The measured beam profiles at some distance from the stack gave evidence of severe beam quality deterioration [17]. Beam pointing and beam profile errors are clearly visible in Figure 7.13 a) on page 183, which shows the LDA beam pattern at a distance from the packaging.

A novel approach has been used to characterise the LDA beams, consisting of wavefront measurement of each single emitter beamlet in a close proximity ($\sim$2 mm) to the surface of collimating optics (see Figure 7.2), where the extent of irreversible free-space transformation of aberrated beamlets was regarded as insignificant. The distance, which should be as little as possible, could be further reduced by removal

of front metal plate (see Figure 7.1), but it was not recommended by the manufacturer. Specially developed, high power wavefront sensor was similar in principle to that of Hartmann. For practical reasons, the wavefront measurement has been organised in an orthogonal mesh depicted in Figure 7.2. As a consequence of the measurement mesh, only fast axes of the emitters have been characterised. The choice was supported by a study carried out by Holdsworth *et al.* [17], who have concluded that fast axis aberrations account for a lion's share of LDA beam quality degradation. The other LDA beam imperfections, such as slow-axis aberrations, relative tilt of slow axes, caused by nonparallelism of emitting bar surfaces and relative shift of the bars, introduced during soldering into the heatsink, have not been addressed in this study.

7.2.1 Corrective plate design

A correction of LDA beam quality is demonstrated on an example of three laser diode bars from the set of eleven in the tested HPLDA. A measured, discreet wavefront slope data can be used to calculate the shape of refractive surface, capable of transforming the fast axis beam profile to fit the desired resultant wavefront. A design of corrective surface consisted of a numbers of stages, shown schematically in Figure 7.3. A knowledge of discreet local wavefront slopes $WS_{i,j}$ and desired corrected wavefront slopes $WR_{i,j}$ (with respect to some reference direction) allows for calculation of local slopes of corrective surface $SS_{i,j}$, according to a simple relation derived from Snell's formula:

$$SS_{i,j} = \frac{n \cdot \sin\Big(\text{atan}(WR_{i,j})\Big) - \sin\Big(\text{atan}(WS_{i,j})\Big)}{n \cdot \cos\Big(\text{atan}(WR_{i,j})\Big) - \cos\Big(\text{atan}(WS_{i,j})\Big)} \tag{7.1}$$

where n is the relative refractive index of silica at the LDA wavelength and i and j denote emitter number and data point index. Polarisation effects have been ignored, since maximum measured slope was much less than $n = \tan(\alpha_B)$, where α_B is the Brewster angle. The above assumption also allows for simplification of Eq. 7.1 into:

$$SS_{i,j} \simeq \frac{n \cdot WR_{i,j} - WS_{i,j}}{n - 1} \tag{7.2}$$

The effect of incompatibility of flat measurement plane and wavefront curvature has also been omitted since the radius of curvature of collimated wavefront is few orders of magnitude grater than its sag on the distance of nonzero fast axis beamlet profile.

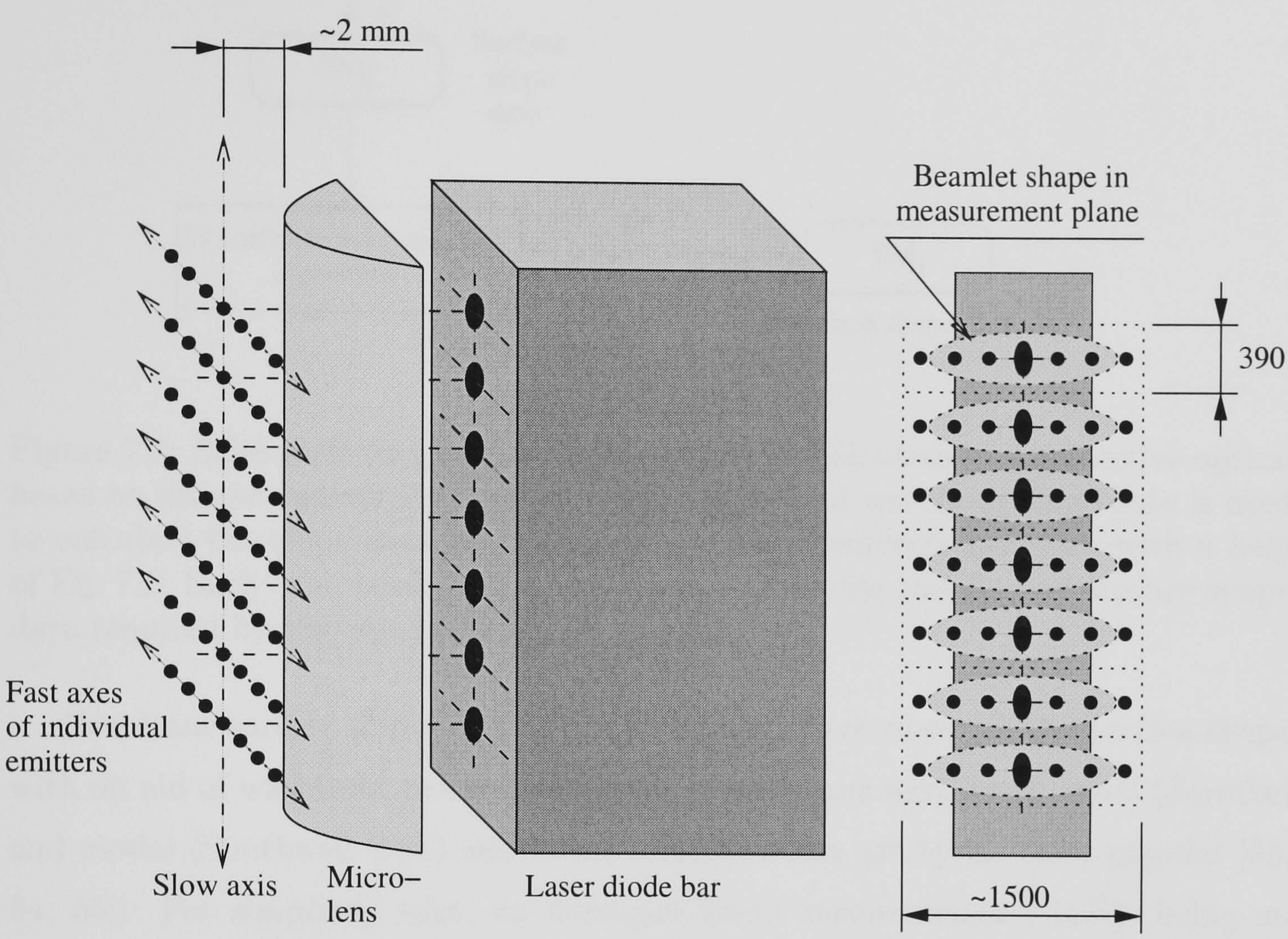

Figure 7.2: Schematic view of collimated diode bar with superimposed measurement mesh. Black dots represent wavefront measurement points, spaced by 20 μm, along the fast axes of individual emitters. The distance between these raster lines was 390 μm, equal to the separation of emitters in the bar. The number of measurement points was determined by the intensity distribution of the collimated beamlet. The distance between diode bar and the measurement mesh was small enough to prevent overlap of beamlets from individual emitters. As a consequence of such arrangement, the correction could be prescribed independently for every individual emitter. The final corrective optics could be constructed by merging such correction zones, or "wobbly arbitrary prisms".

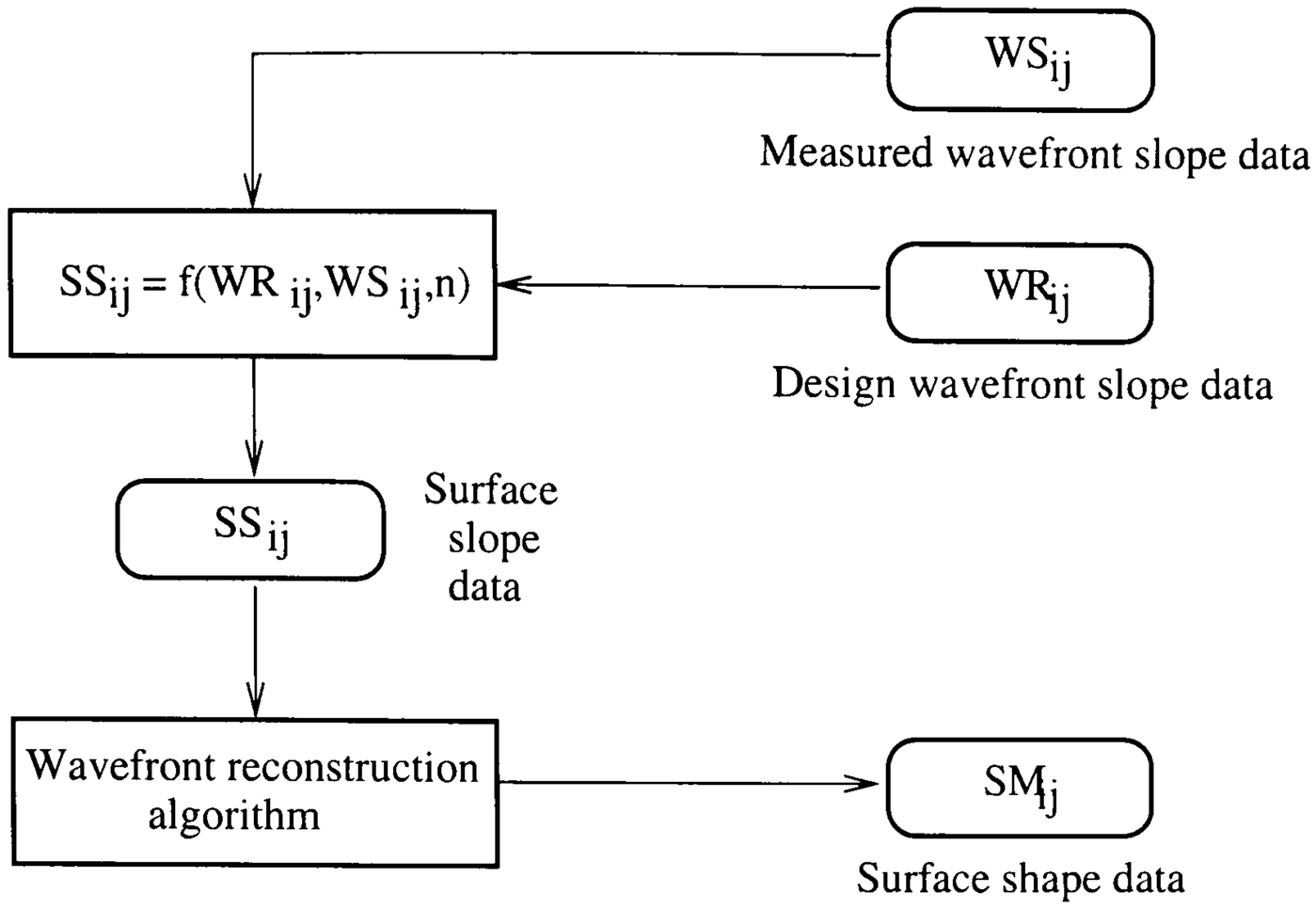

Figure 7.3: Schematic diagram of the algorithm for calculation of corrective optics, based on discreet wavefront slope data. The measured wavefront slope data is used to calculate the slope data describing the profile of corrective surface with a help of Eq. 7.1. Such calculated data is then used to compute the discreet surface shape data required by the rapid-fabrication system.

Resultant surface slope data $SS_{i,j}$ can be used to reconstruct the surface shape with an aid of wavefront reconstruction algorithms, amongst which zonal (Zernike) and modal (Southwell type) and linear reconstructors are by far most popular [83, 84, 85]. For simplicity sake, an averaged linear reconstructor (ALR), being an intermediate between Southwell (SR) and ordinary linear algorithms (LR), has been applied to calculate the surface shape matrix SM. ALR is advantageous to LR and easier to implement than SR, yet producing practically identical results as SR. Formula 7.3 describes the 1-D ALR algorithm:

$$SM_{i,j} = SM_{i,j-1} + \Delta \sum_{k=-1,0,1} \frac{SS_{i,j+k}}{3} \tag{7.3}$$

where Δ is a measurement pitch of the mesh. The ALR algorithm was set up to commence the reconstruction from the data point $SS_{i,j}$ corresponding to the highest intensity of the beam profile, where the wavefront slope measurement was most reliable. The algorithm calculated the surface matrix from that point in both directions of the scan line towards the tails of beamlet intensity distribution, where slope measurement accuracy was worse. This approach minimized the accumulation of reconstruction error in the areas corresponding to the highest beamlet intensity.

Bar Number	Average pointing error of individual bar [mrad]	Pointing error range of individual emitter in a bar [mrad]
1	2.2	1.1 – 3.1
2	-0.3	-1.6 – 0.5
3	-0.3	-2.5 – 0.8
4	-4.7	-5.9 – -3.8
5	3.2	0.7 – 4.2
6	1.3	-1.2 – 5.8
7	-1.8	-2.1 – -0.9
8	1.5	0.7 – 3.0
9	0.4	-1.3 – 1.4
10	1.5	-0.7 – 3.9
11	-3.0	-5.0 – 0.5

Table 7.1: Measured pointing errors of the LDA under test. Average pointing error relates to the pointing of individual bar, while the pointing range shows the pointing spread of individual emitters in each bar. All figures calculated with respect to the average pointing of the whole stack of 11 bars.

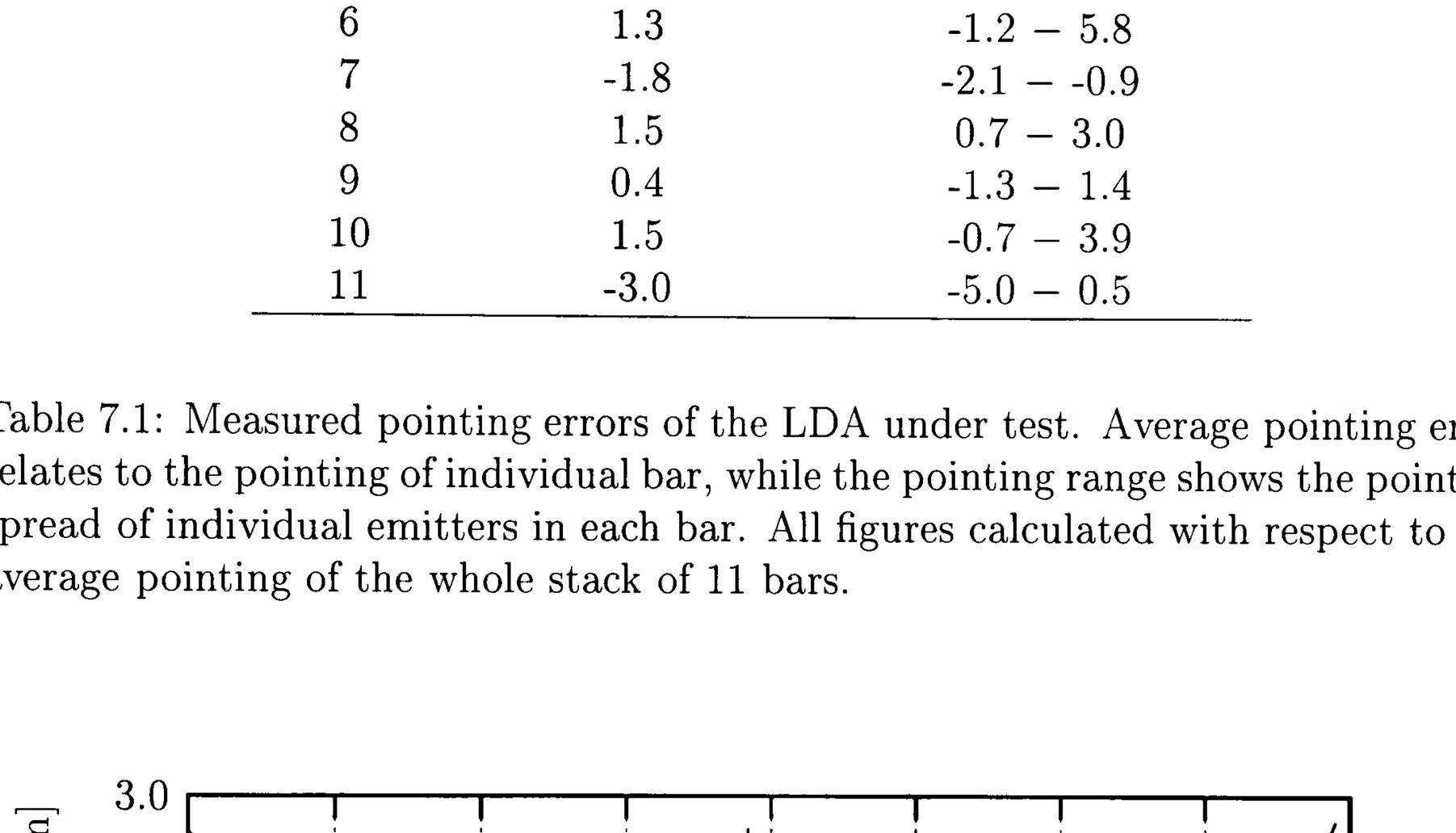

Figure 7.4: Measured wavefront of central emitter in bar 1 a) and calculated silica surface, designed to flatten the wavefront b).

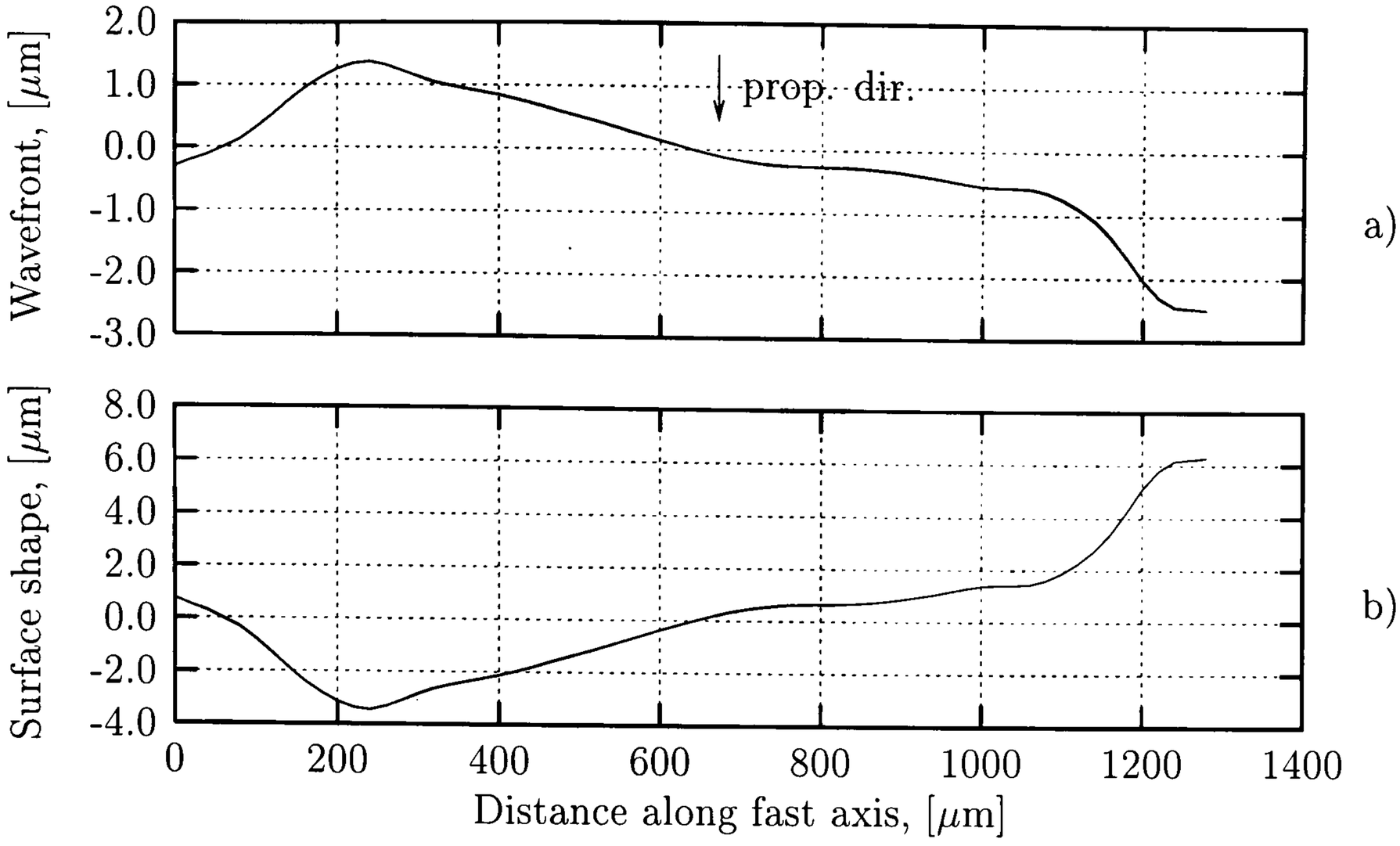

Figure 7.5: Measured wavefront of central emitter in bar 2 a) and calculated silica surface, designed to flatten the wavefront b).

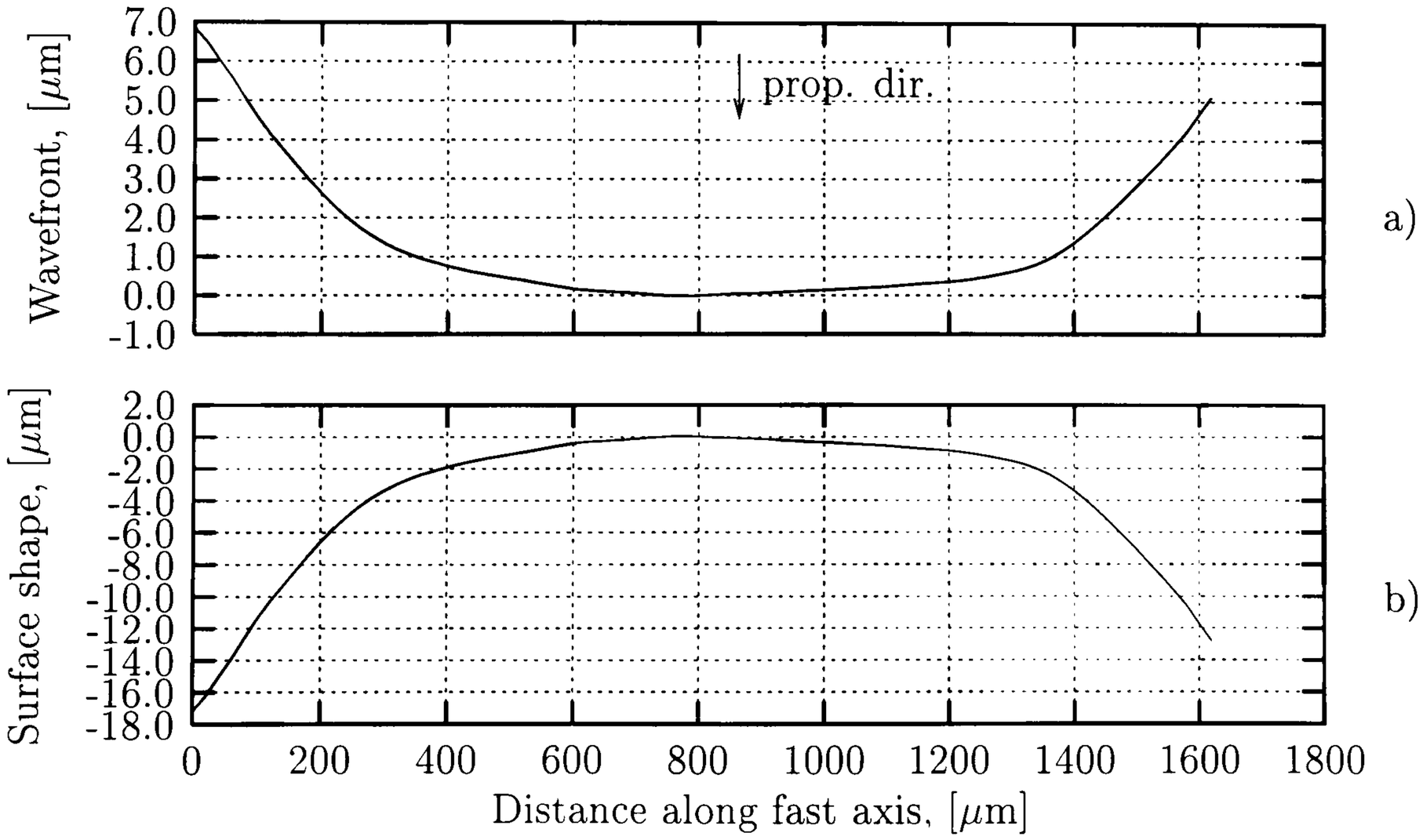

Figure 7.6: Measured wavefront of central emitter in bar 3 a) and calculated silica surface, designed to flatten the wavefront b).

Figures 7.4 a), 7.5 a) and 7.6 a) show measured wavefronts of bar 1, 2 and 3. Each individual emitter exhibited different pointing error (see Table 7.1), most dominant error component, manifesting as a DC level offset of wavefront slope data for different emitters. The pointing errors, presented in Table 7.1, have been calculated with respect to average pointing direction of complete LDA. As much as 7 mrad of emitter-to-emitter pointing variation has been observed, which in practical terms means that crossover between beams from two adjacent bars takes place at distance as little as 0.5 meter. The emitter-to-emitter wavefront shape change is less pronounced, but cannot be ignored.

Figures 7.4 b), 7.5 b) and 7.6 b) display the calculated surface shapes, designed to convert the wavefront of individual beamlet into that of a plane wave ($WR_{i,j} = \text{const} = 0$). The calculated, per-emitter corrective surface profiles were used to construct the final per-bar corrective optics section. Fast axis wavefront profile was with little error assumed to be static throughout the per-emitter section of corrective plate. This assumption lead to a "wobbly arbitrary prism" approach, depicted in Figure 7.7. Figures 7.8, 7.9 and 7.10 illustrate the resultant shape data of corrective optics for three diode laser bars. Surface matrices constructed this way have been processed by the rapid prototyping system and the desired reliefs have been written into the silica substrate.

7.2.2 Fabrication of corrective optics

Designed surface shapes have been converted into corresponding LSD files, according to machining curve of Slow Optimized Speed regime (SOSR), crater class "deep", relative line overlap 0.4 (see Figure 5.17). SOSR regime has been used to assure accurate machining, since the calibration data was most reliable for this particular regime. The time required to machine 15 mm^2 of single bar correction optics, as a consequence, was approximately 30-40 minutes per bar. Although subjectively judged as slow, the overall amount of time needed to machine the complete stack of 11 bars was 5-6 hours, which was still faster than LDA characterisation cycle. Anyway, the measurement-fabrication cycle of correction plates was believed to be the fastest to date scheme for rapid-prototyping of custom beam correction optics for high power diode lasers.

Figure 7.7 shows the arrangement of raster scan writing of the corrective optics. The direction of cutting has been chosen in a way to minimize the number of raster

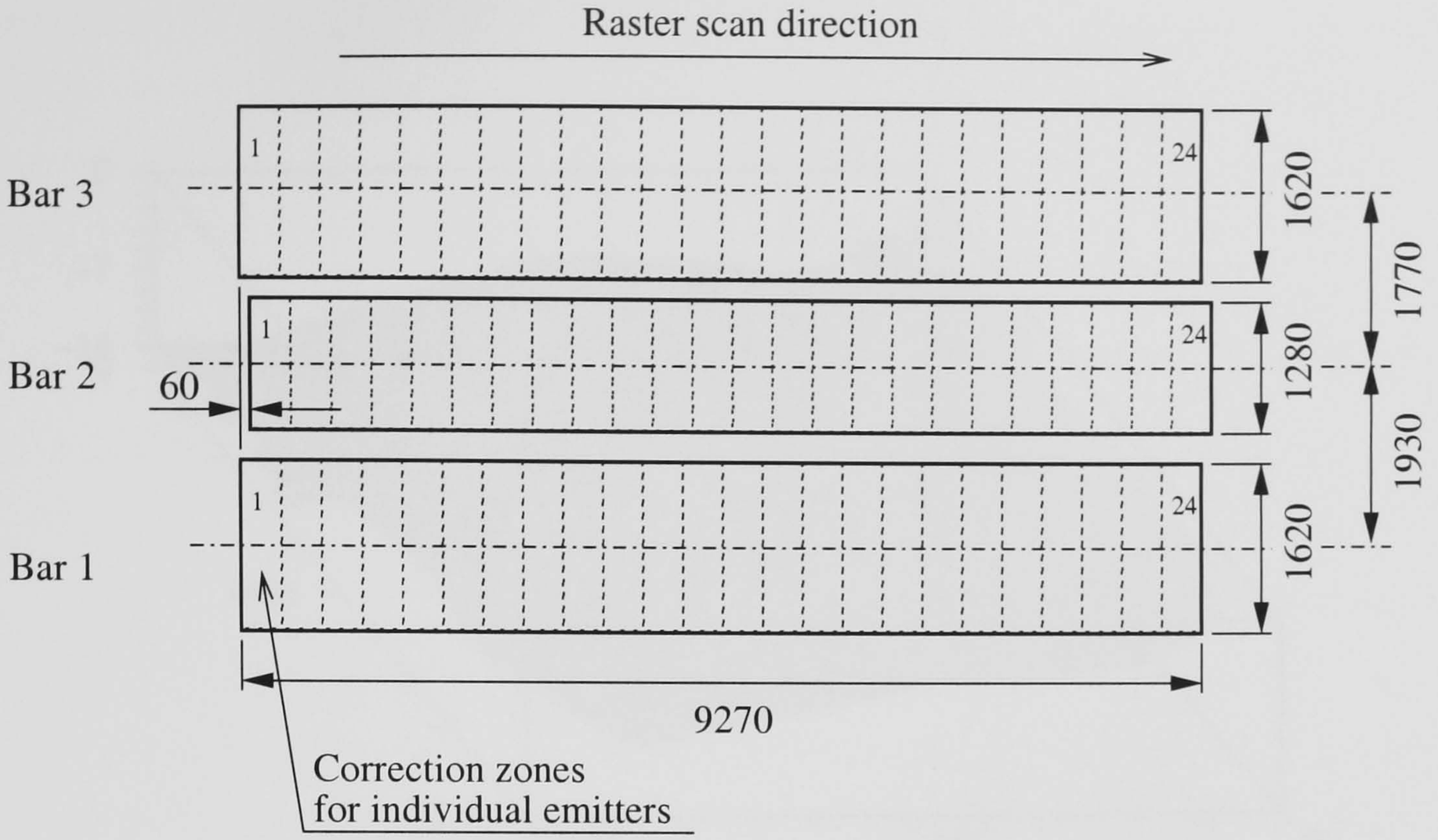

Figure 7.7: The layout of correction surfaces for diode bars 1-3, viewing from the side of machining. The positioning reflects the arrangement of measurement points (illustrated in Figure 7.2 p.172), which in turn shows the extent of assembly errors of three diode bars in the stack. Different height of correction surfaces was the result of different beam widths for individual lensed diode bar. The correction zones, indicated in above figure, have been smoothly merged together, as shown in Figures 7.8-7.10. All dimensions in microns.

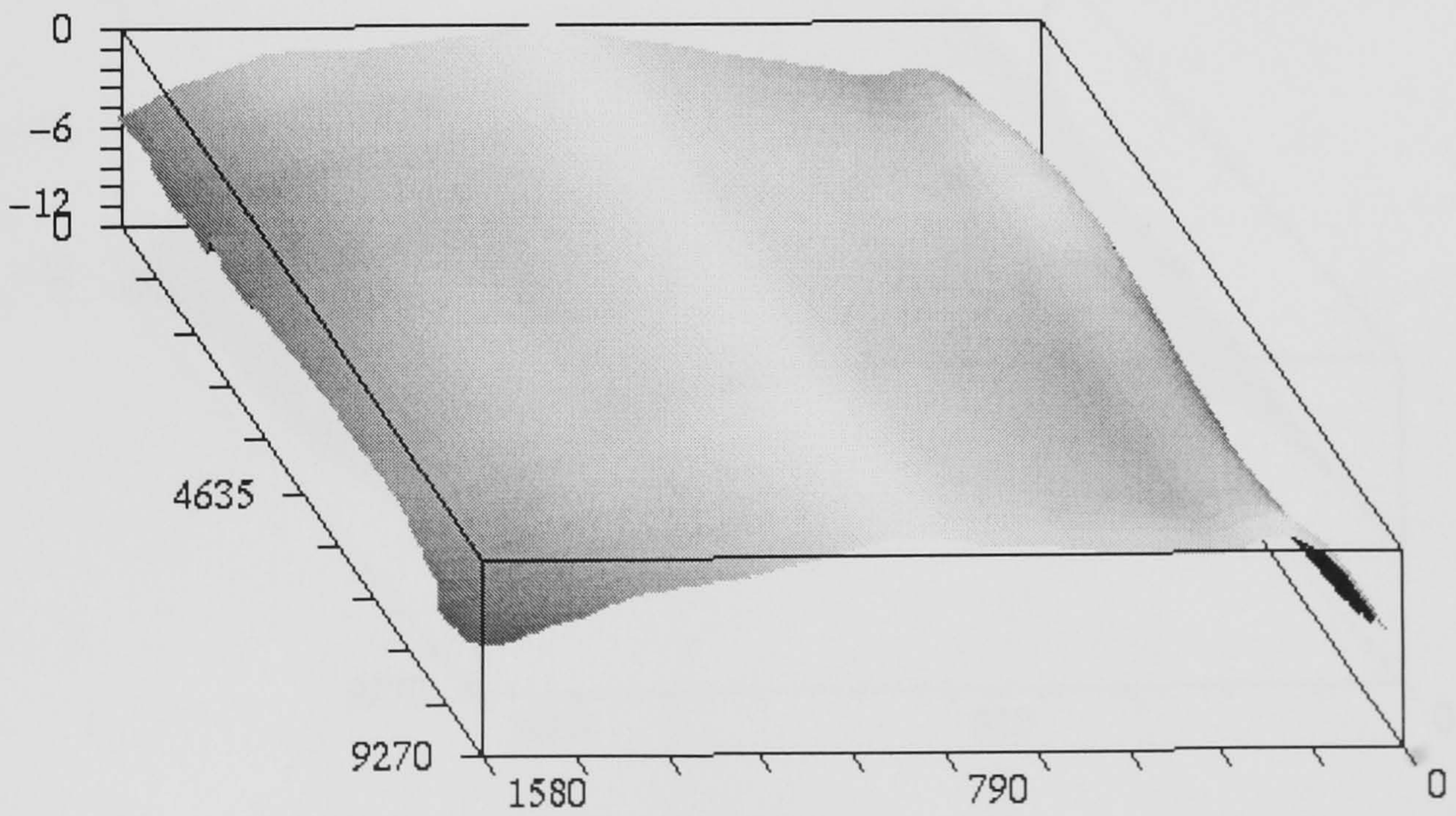

Figure 7.8: Calculated surface profile of corrective optics section designed for bar 1. Aspect ratio not preserved. Dimensions in microns.

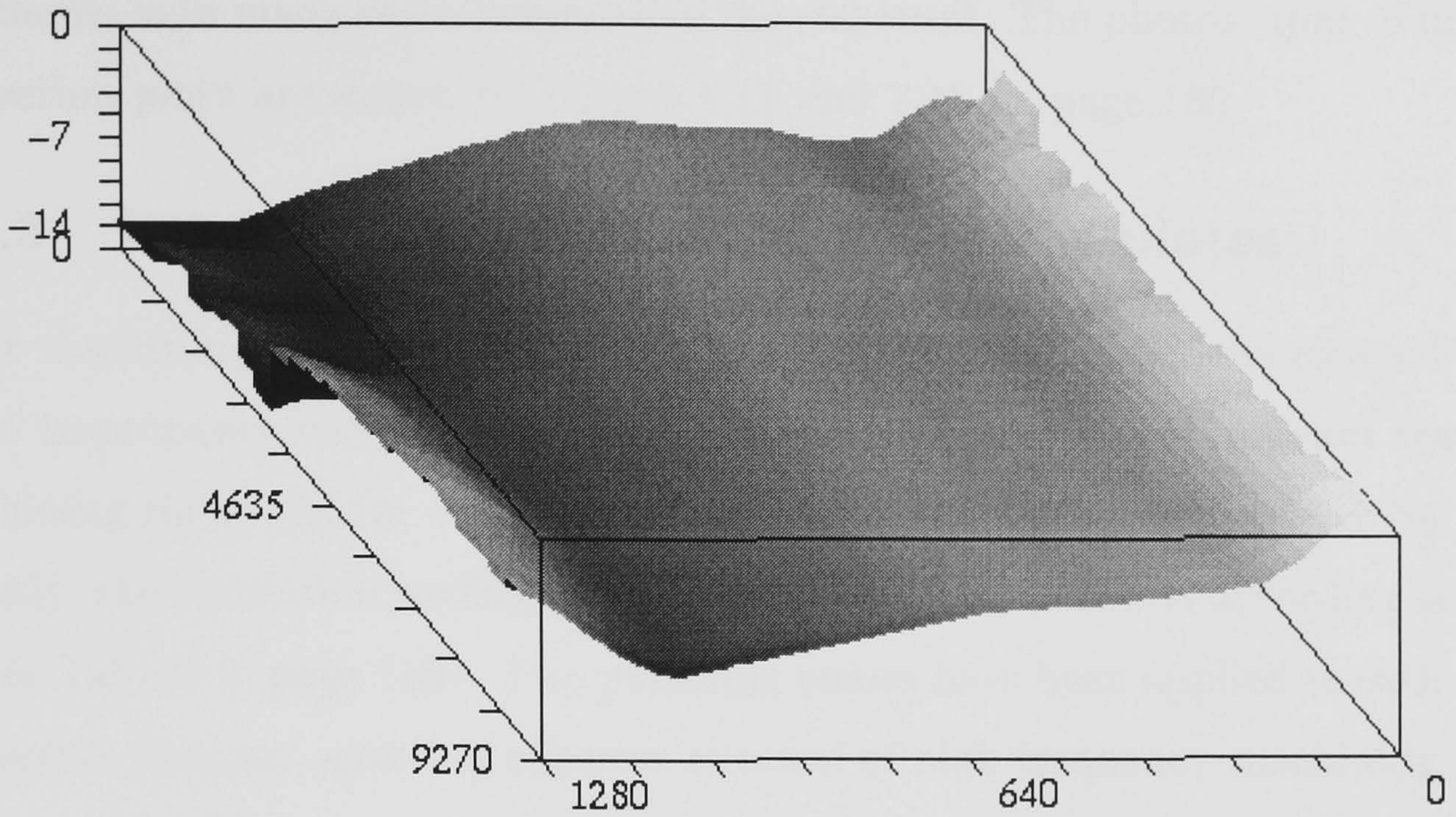

Figure 7.9: Calculated surface profile of corrective optics section designed for bar 2. Aspect ratio not preserved. Dimensions in microns.

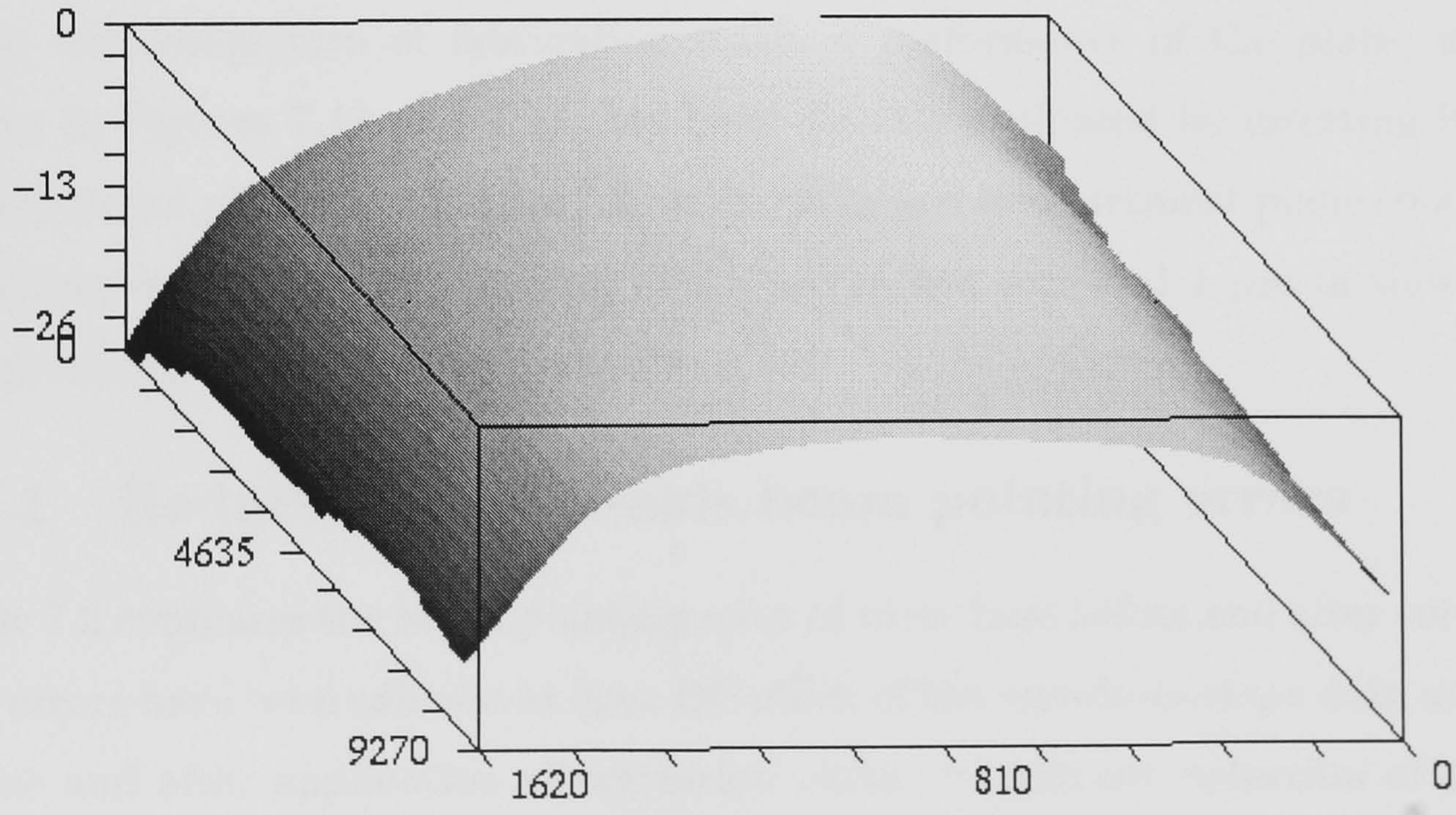

Figure 7.10: Calculated surface profile of corrective optics section designed for bar 3. Aspect ratio not preserved. Dimensions in microns.

lines. The number of raster lines is the main factor determining the fabrication time, since the time it takes to reposition the sample for the next raster line run (1-2 seconds) is in many cases longer than the run itself. The photographs of machined correction plate are shown in Figures 7.11 and 7.12 on page 180.

7.2.3 Laser micro-polishing of corrective plates

After machining stage, the silica substrate has been ultrasonically cleaned in a diluted isopropanol bath for 5 minutes. After the removal of significant fraction of machining micro-debris, the sample was blow-dried with a pressurized N_2. Subsequently, the correction surfaces have been laser micro-polished according to regime D (see Table 6.2, page 159). Two polishing passes have been applied to each of three corrective sections, assuring effective removal of high frequency machining ripples.

Laser polishing was much more time efficient that machining thanks to the fixed raster of laser shots, allowing for production of stable pulse energies at PRF much above dynamic pulse stability limit of 800 Hz. Polishing time of single corrective surface was as short as 4−5 minutes per pass. The correction plate for the whole diode stack has been then double-pass processed in less than 2 hours.

7.3 Evaluation of corrective plate performance

Upon the completion of fabrication stage, a performance of the plate, which is shown in Figures 7.11 and 7.12, has been directly evaluated by inserting it in the measurement plane from Figure 7.2, with optics and measurement plane coordinates matching within positioning error of 0.2 μm in fast axis and 1 μm in slow axis, 5 μm proximity and 2° tilt and rotation errors.

7.3.1 Reduction of fast-axis beam pointing errors

Table 7.2 compares the beam pointing error of three bars before and after correction. The errors have been calculated from DC offset of the wavefront slope data measured before and after application of correction plate. Significant reduction of pointing error of bar 1 has been recorded, from few to a fraction of mrad. The pointing of other bars has also been improved and nearly matched the design pointing of zero mrad (defined as the average pointing of the whole stack of 11 bars before correction).

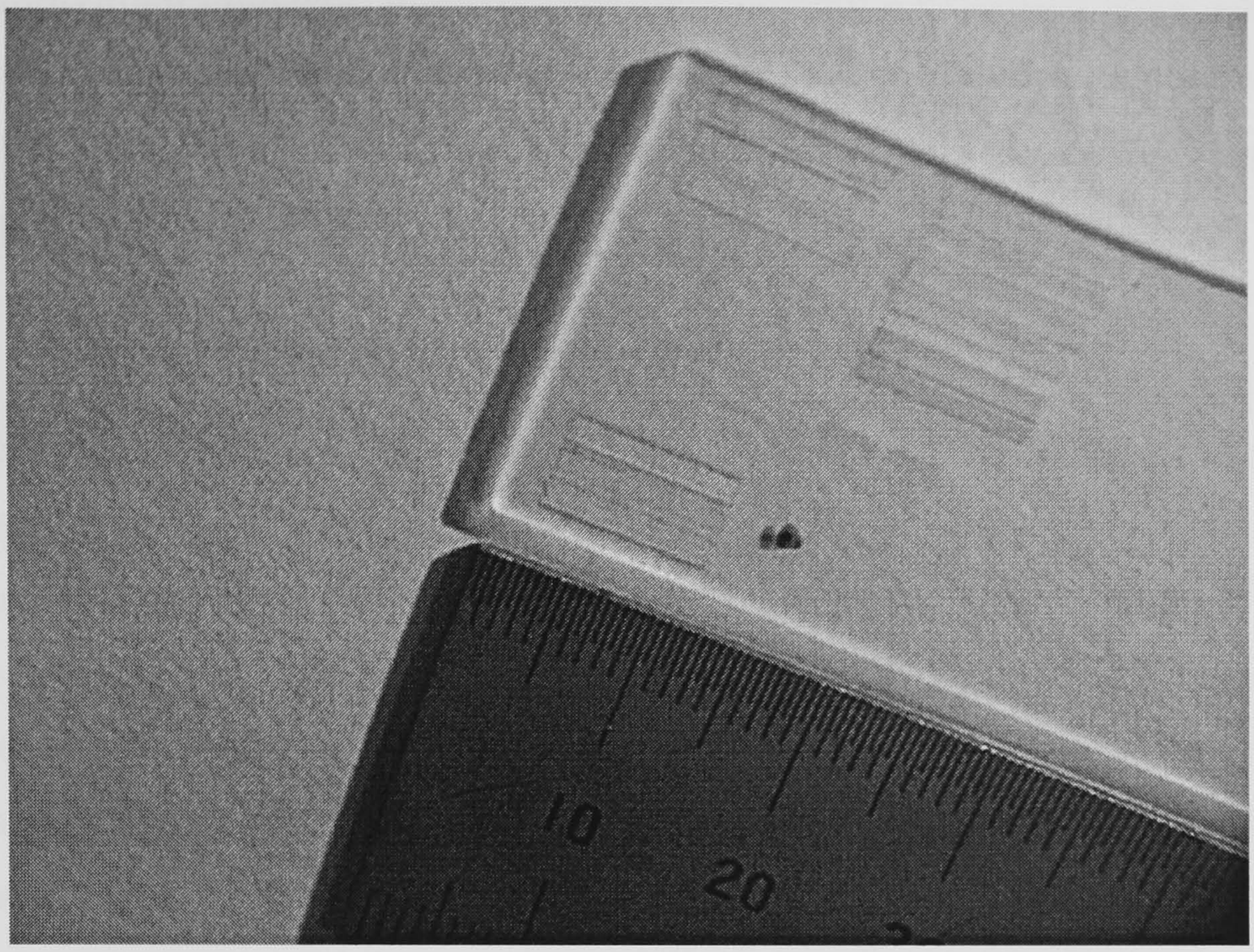

Figure 7.11: Photograph of fabricated corrective optics for bars 1-3 (from bottom up), to left from a dark spot. The layout of corrective surfaces in the Photo corresponds to the layout from Figure 7.7 p.177.

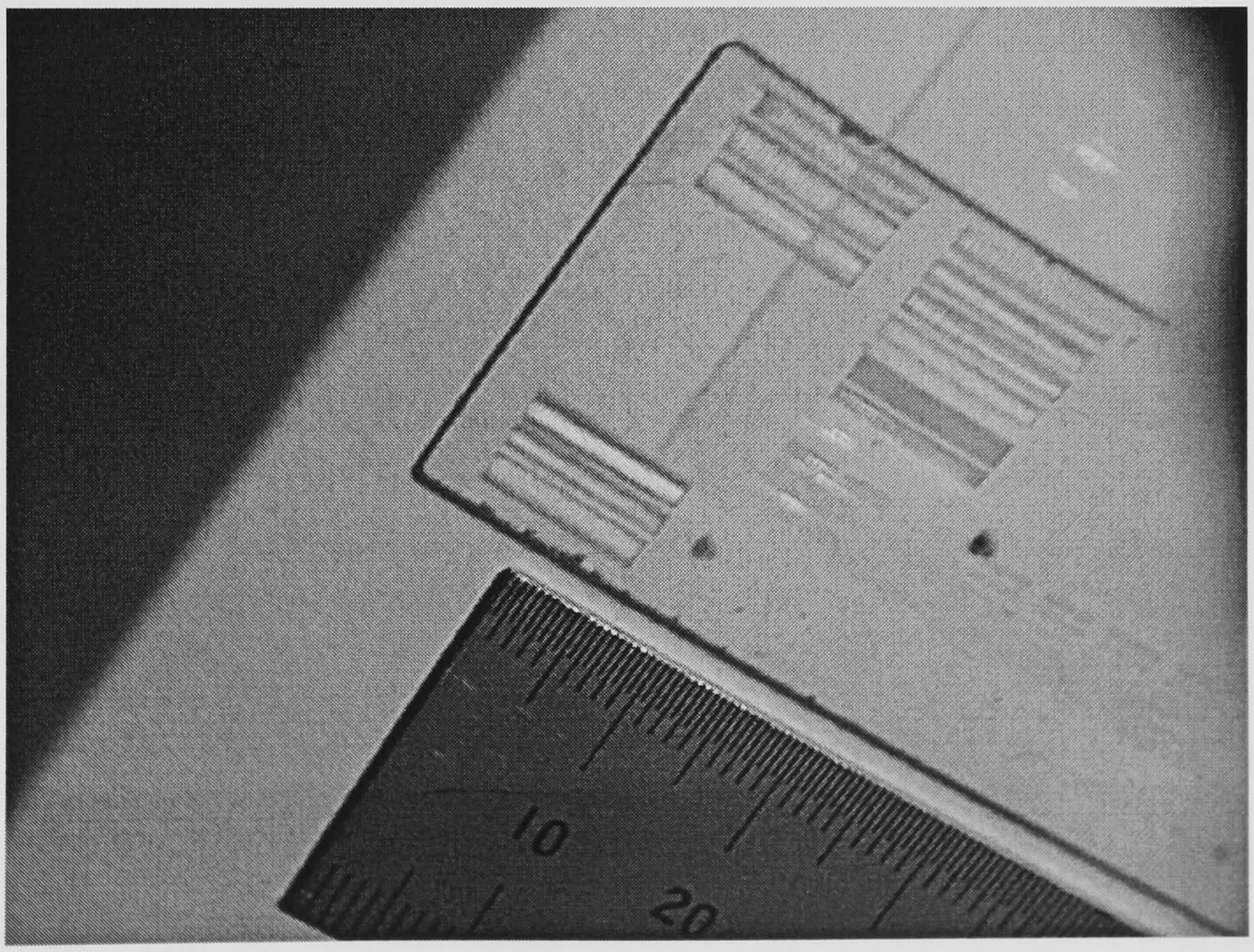

Figure 7.12: Focusing action of corrective sections demonstrated. The plate has been raised to allow the passing light to be focussed on the paper screen underneath.

For individual emitters, however, the measurements exhibited some significant deviation (up to a mrad) from design direction. The observed, corrected beam patterns did not however confirm these figures, which would clearly show up on the screen as the overlap of beams.

7.3.2 Restoration of beam quality

A significant, simultaneous quality restoration of the beams emitted from all three bars has been recorded. Figure 7.13 displays the images of beams before and after correction at a distance 60 cm from the LDA, obtained with Spiricon^{TM} beam imager. The profiles were sensitive to fast axis positioning (>10 μm), moderately sensitive to slow axis positioning (>100 μm) and pretty insensitive to proximity positioning (>1 mm) errors. The set of images, displaying sequentially the beam patterns of bar 1 to 3, has been produced with an aid of a knife edge to visualize the overlap of aberrated beams and spatially ordered structure of corrected ones. The beam quality of all three bars has been dramatically improved. Two distinct far-field lobes in the uncorrected beams 1 and 2 have been combined into single ones with evident increase of brightness (see Figure 7.14). Beam quality improvement has been confirmed by M^2 measurements, shown in Table 7.3. Fast axis pointing errors have been reduced by more than an order of magnitude and M^2 reduction from ~12 down to 2.3–2.5 has been achieved [86]. These numbers agree well with measured fast axis beam quality of high-brightness tapered HPLDAs [87] ($M^2 \simeq$ 1.9–3.5).

The measurement of transmitted power has shown that very little power has been lost to scattering or beam clipping. It has been done by comparing the power transmitted through the aligned corrective plate and the unmachined area of the slide. Only ~2% of transmitted power was lost, thus the technique did not introduce significant losses.

7.3.3 Comparison of aberrated and corrected wavefronts

Figures 7.15, 7.16 and 7.17 compare the uncorrected wavefront of central emitter in bar 1, 2 and 3 and the corresponding corrected one. The corrected and aberrated wavefronts have been measured immediately after the correction plate, with the plate inserted and subsequently removed from the beam path. Significant improvement is clearly visible, however the resultant wavefronts still depart in some cases to

Bar Number	Average pointing error of a whole bar [mrad]	Pointing error range of individual emitter in a bar [mrad]
	Before correction	
1	2.2	1.1 – 3.1
2	-0.3	-1.6 – 0.5
3	-0.3	-2.5 – 0.8
	After correction	
1	-0.1	-0.4 – 0.4
2	0.1	-1.7 – 0.7
3	0.1	-0.6 – 0.9

Table 7.2: Fast-axis pointing errors, before and after correction. Average pointing error relates to the pointing of a whole bar, while the pointing range shows the pointing spread of individual emitters. The figures were calculated with respect to the average pointing of the whole stack of 11 bars, which was used as a reference for the correction procedure.

Bar Number	Beam quality (M^2)	
	Before correction	After correction
1	12.26	2.33
2	8.79	2.39
3	12.07	2.54

Table 7.3: Beam quality improvement of three laser diode bars - a summary, after [86].

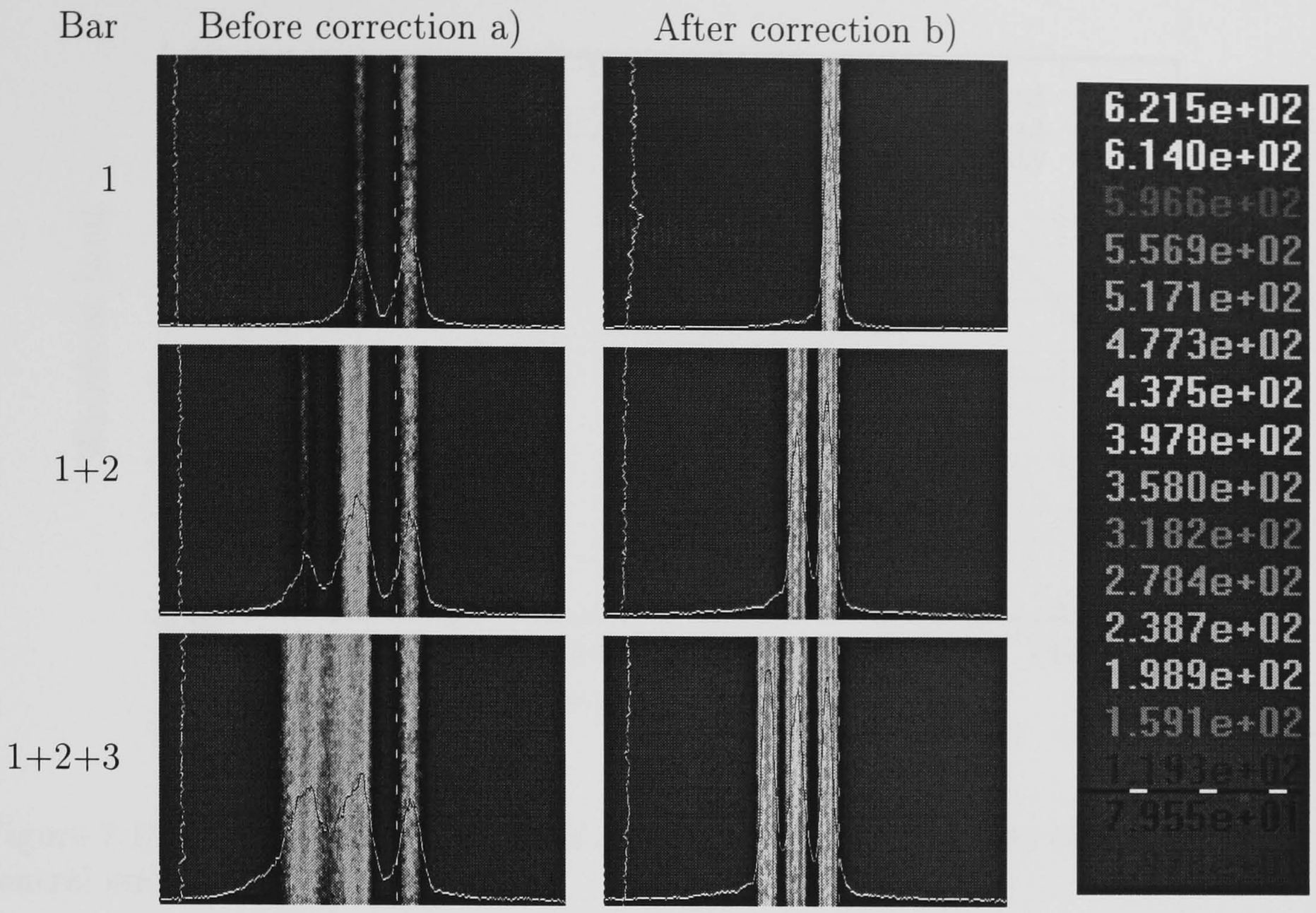

Figure 7.13: Incremental comparison of uncorrected a) and corrected b) beam profiles of bars 1-3, acquired with an aid of traveling knife edge. The beams have been recorded with Spiricon^{TM} beam imager at a distance 60 cm from the diode stack. Beam pointing errors of aberrated beams show up as a visible overlap.

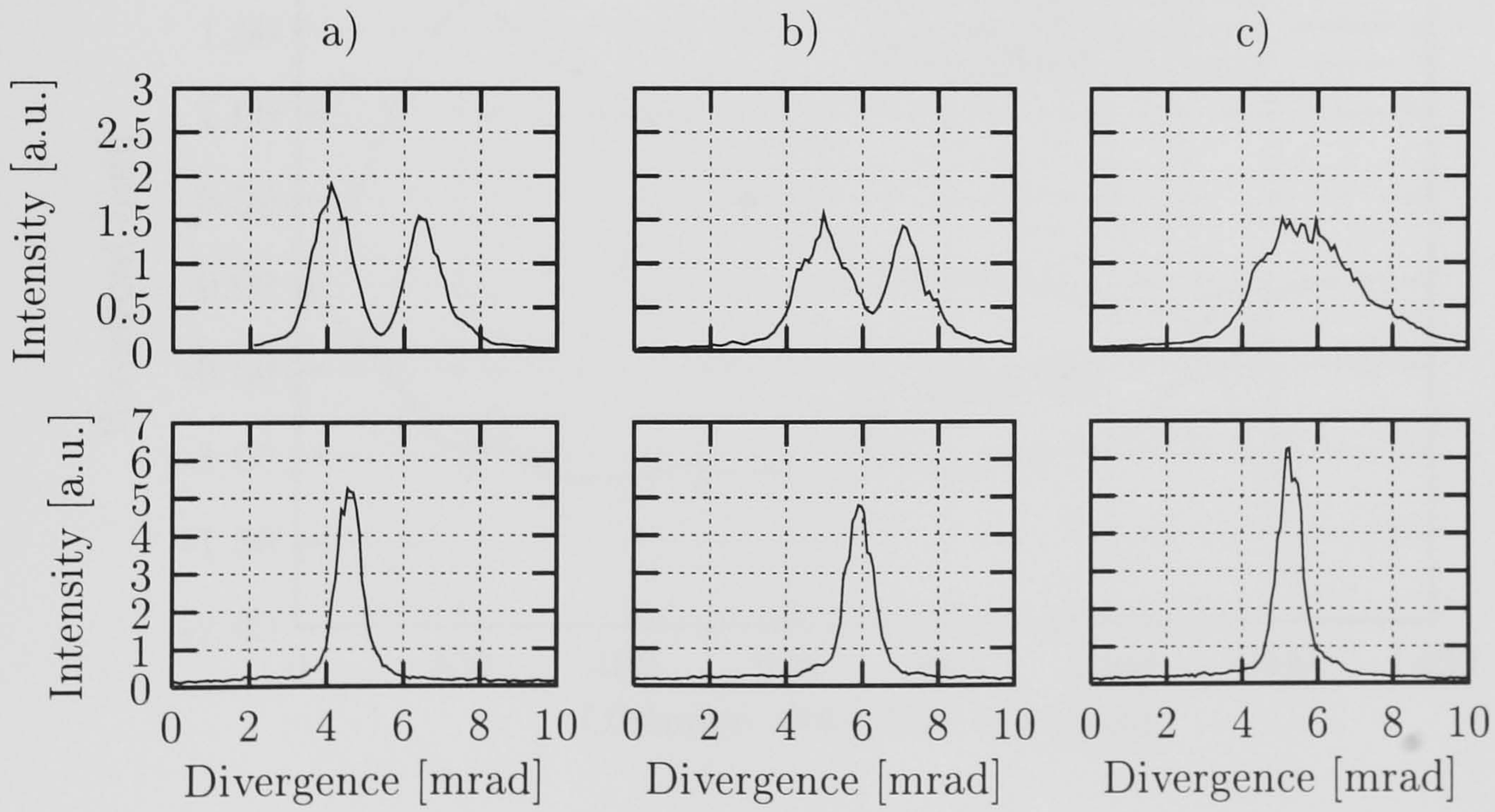

Figure 7.14: Comparison of far-field beam profiles of uncorrected and corrected bars (from Figure 7.13) 1 a), 2 b) and 3 c), after [86]. Substantial improvement of beam quality and brightness.

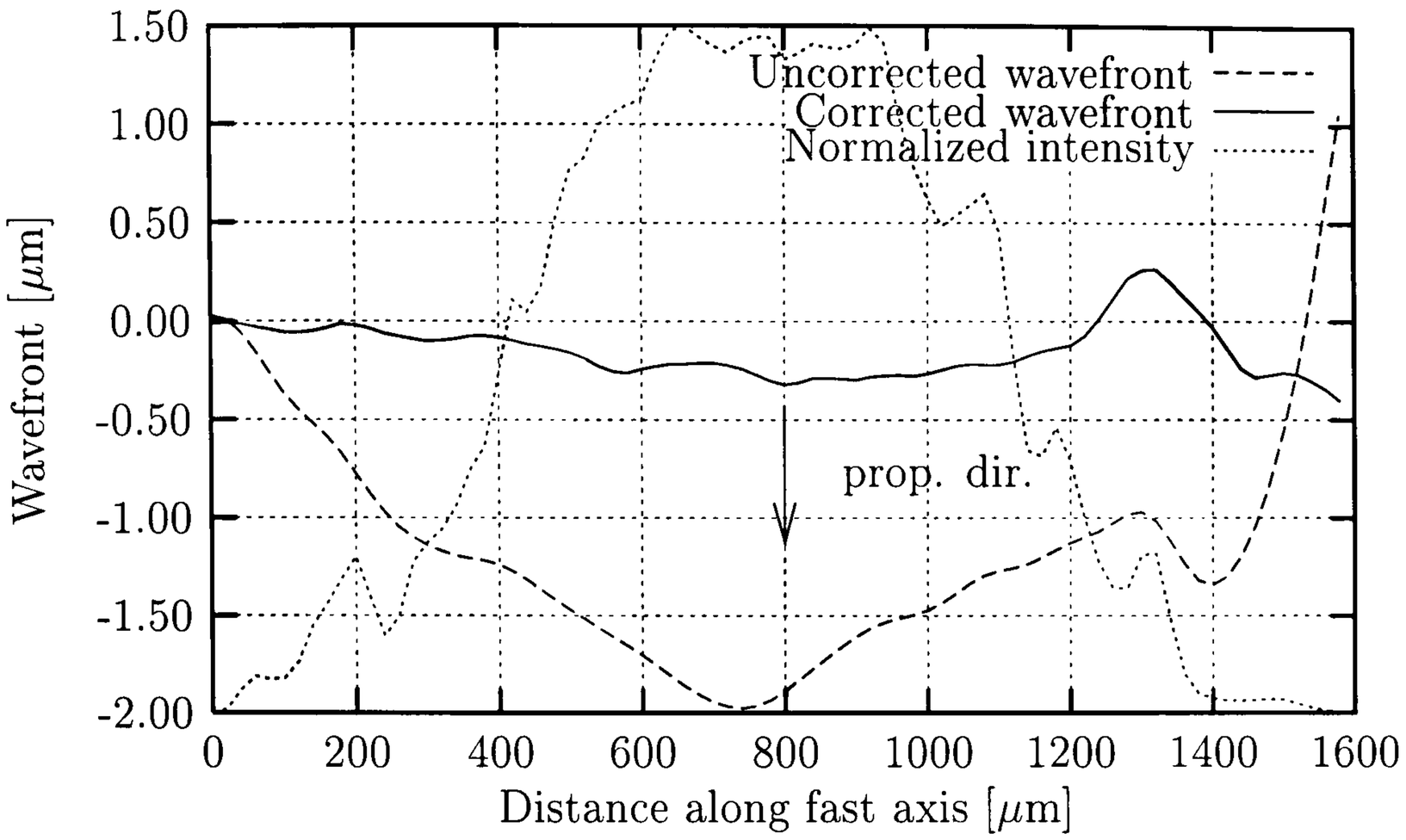

Figure 7.15: Comparison of corrected and uncorrected wavefronts of representative, central emitter in bar 1.

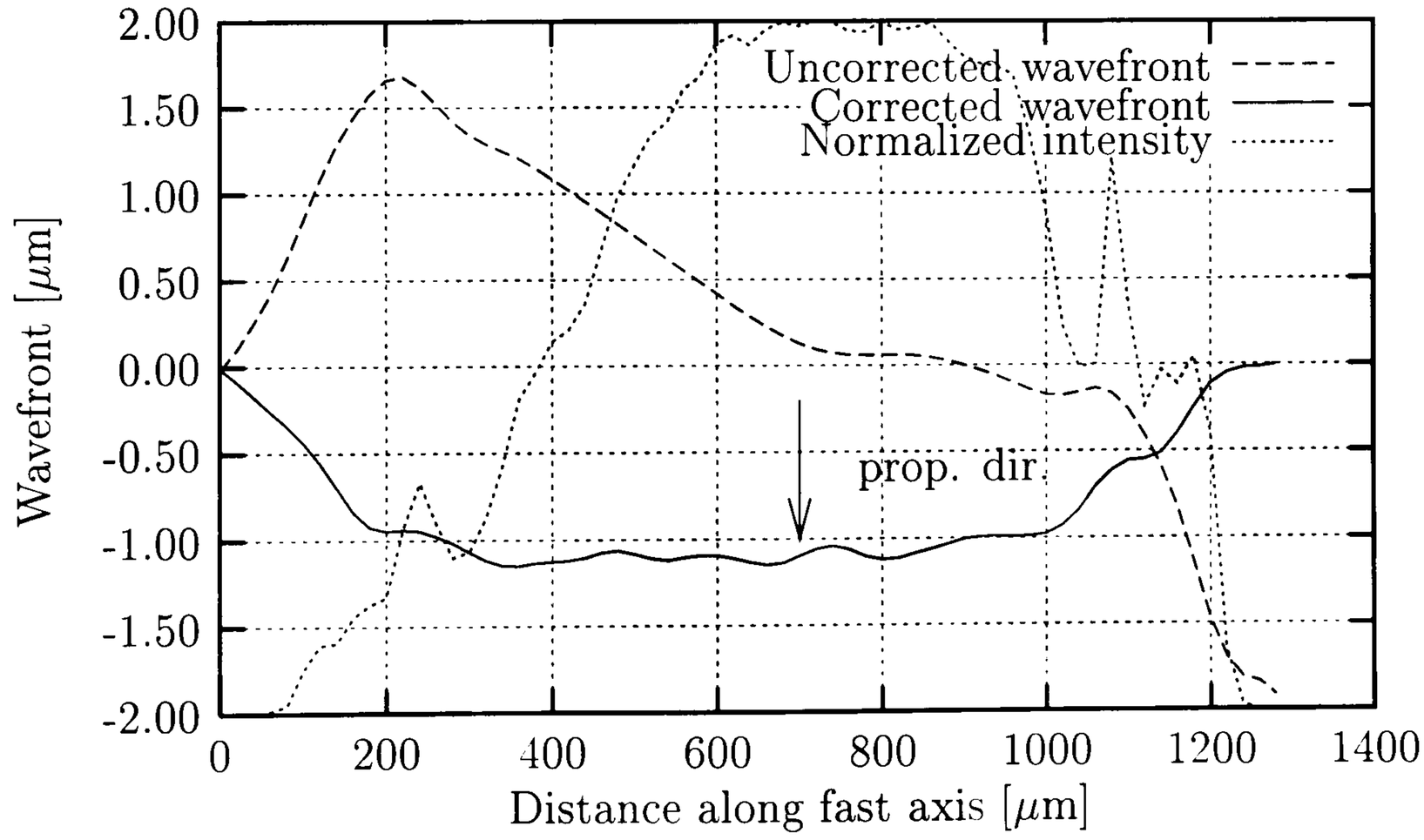

Figure 7.16: Comparison of corrected and uncorrected wavefronts of central emitter in bar 2.

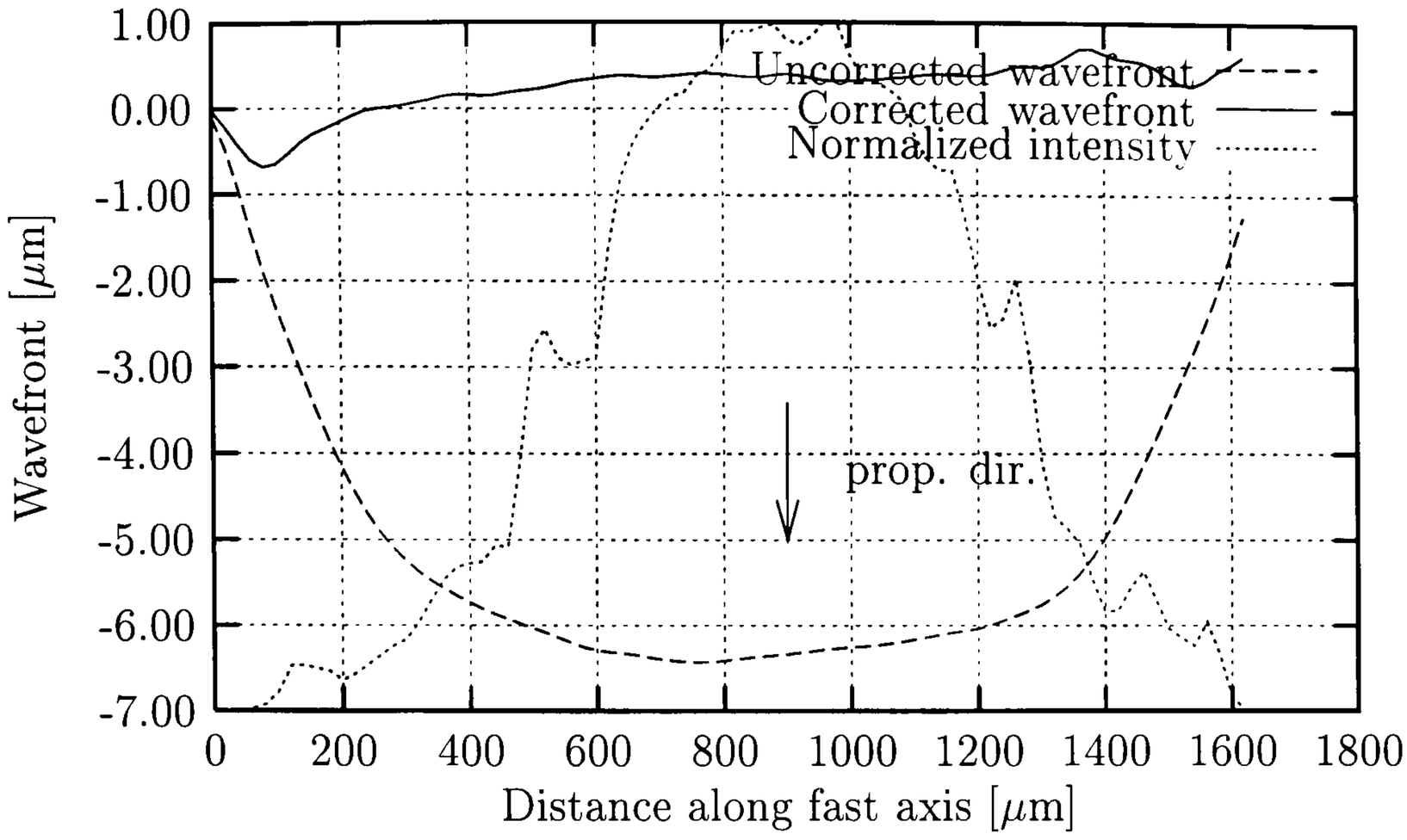

Figure 7.17: Comparison of corrected and uncorrected wavefronts of central emitter in bar 3.

almost λ from the design plane wavefront. There is a number of issues responsible for the departure of the wavefront from desired shape, shown below in an order of importance:

- Pulse-to-pulse ($\pm 2\%$) and long term laser power stability ($\pm 2\%$) affects the high and low spatial frequency content of the surface profiles. The ripples in a figure of resultant wavefront are the consequence of previously observed residual surface waviness, caused by laser pulse energy modulation with 100 Hz rectified line frequency. This unwanted feature is believed to be responsible for setting a limit on lowest achievable value of M^2.

- Wavefront measurement setup and wavefront reconstruction could introduce significant errors. Biggest departure from the design wavefront occurred most frequently in the tails of beam intensity distribution, where the wavefront sensor noise and static image patterns influence the measurement accuracy. Unfortunately, the largest surface slopes also occur in these areas of diminished intensity, thus neither of these two factors can be ruled out with high certainty.

- A calibration of wavefront sensor and machining process could be no longer valid.

- The corrective plate or optics sections could be relatively misaligned.

- Ambient temperature change could have altered the measurement and machining conditions.

- Partial coherence between different emitters in a bar could have been introduced, as a result of reflection from the uncoated surfaces of correction plate, and wavefront shape could have changed upon insertion of uncoated corrective optics.

- Fictive temperature change of processed surfaces has altered the refractive index ($\Delta n_{max} \approx 5 \cdot 10^{-4}$). of thin layer of glass.

- Insufficient substrate flatness, currently ± 15 μm over 2 mm. Optically flat substrates are available, although at a higher price.

- Substrate bending after laser processing. It is minimal, because the slide thickness is much larger than heat affected layer.

The list is rather long, however substantial improvement of correction optics performance is expected to follow the reduction of laser pulse energy variation down to 0.1%. Current $\pm 2\%$ pulse-to-pulse fluence instability contributed to most of the experimentally observed errors of corrected wavefronts, since ± 200 nm surface profile error (see Figure 7.18) corresponds to that variation of pulse energy. The influence of remaining sources of error can become significant after substantial improvement of pulse energy stability.

7.3.4 Surface profile versus wavefront accuracy

The comparison between designed and real shape of correction surface is shown in Figure 7.18 on example of central sections of corrective optics for bar 1. Mean fabrication fidelity (low frequency component of the shape error) is evidently better than 50 nm ($\lambda/20$), which is a substantial achievement. The unwanted surface undulations, however, have increased the shape error to ± 200 nm, which corresponds to $\pm\lambda/5 - \lambda/4$ wavefront accuracy at the LDA wavelength 940 nm. Profile errors, caused by pulse energy fluctuation, is expected to drop below $\sim$50 nm with pulse energy instability reduced down to $<$0.1% (see Section 4.6 p.90).

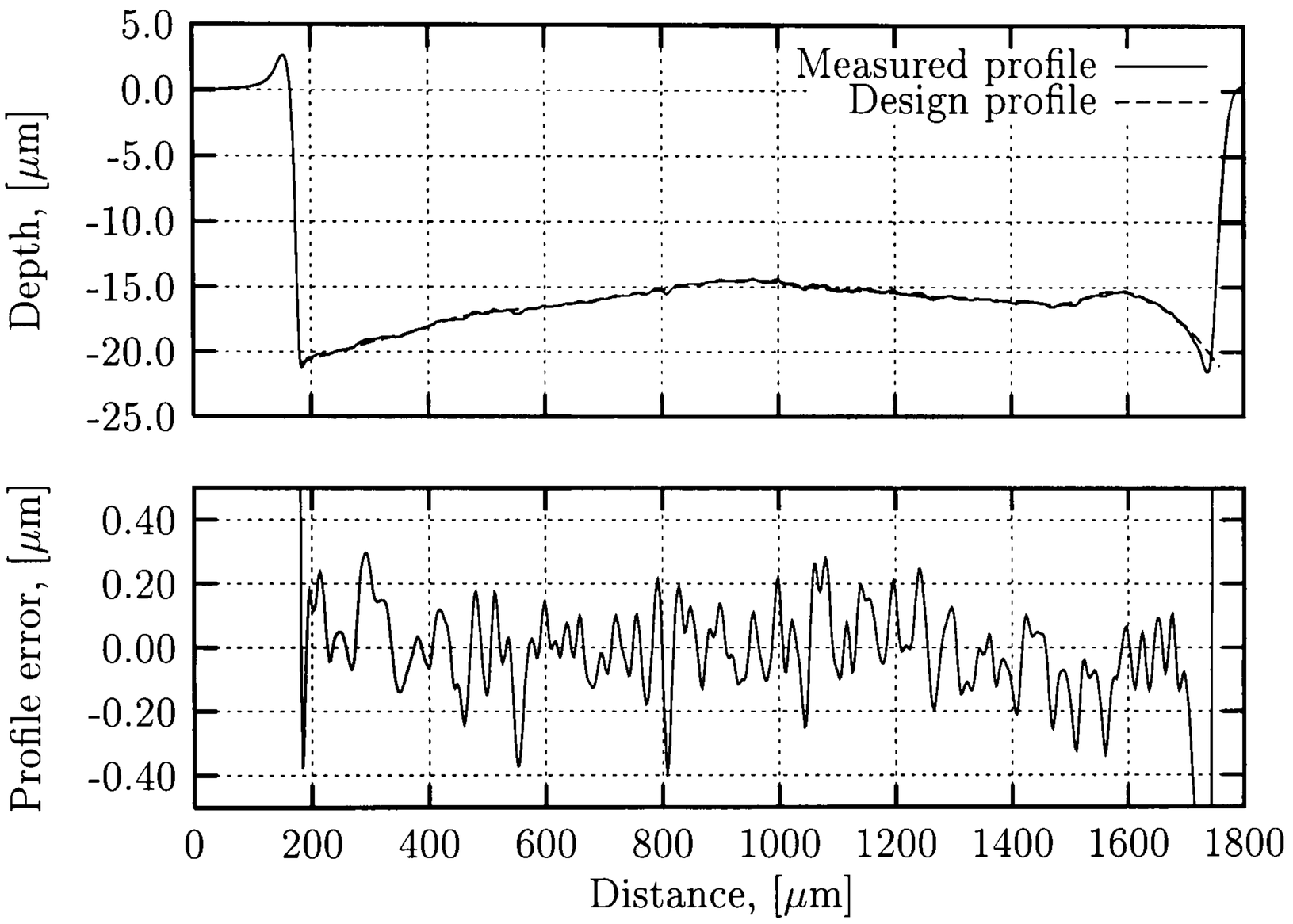

Figure 7.18: DekTak scan of laser polished, corrective optics, central emitter section of bar 1. A correlation between the measured, corrected wavefront from Figure 7.15 and the low-frequency part of the error profile can be observed.

7.4 Conclusions

This chapter has demonstrated a novel method of efficient correction of high power diode lasers, based on wavefront sensing, corrective plate design and subsequent rapid-fabrication. Currently, the time required for the wavefront measurement was 6 hours, corrective plate calculation and machining was approximately 6 hours too. This time can be greatly reduced by further improvement of laser stability and by throughput increase of wavefront sensor rig. Manufacturing time can be reduced down to 2 hours if only laser stability is assured in a wider range of pulsing frequency (see Section 3.3 p.68).

The technique, presented in this chapter, is capable of significant reduction of fast-axis pointing errors (currently an order of magnitude) and substantial restoration of initial fast-axis beam quality (M^2 from $\sim$13 down to $\sim$2.4), resulting in approx. ten-fold increase of brightness. It enables the beam combining, collimating and aperture filling optics to perform their function with greatly improved efficiency. Further reduction of pointing errors is expected to follow the improvement of laser stability and wavefront measurement technique.

Only fast-axis aberrations have been corrected in this study, because of a limited number of measurement points. The limitation has been dictated by the timescale necessary to carry out wavefront measurements in the current rig. The method is not, however, limited to fast-axis correction only, since a fabrication of fully arbitrary shapes is feasible. It is possible to manufacture a corrective plate that would perform a complex correction of beam quality in both fast- and slow-axis ("bow-tie" correction), producing beams of minimal divergence and high brightness, ready for a next stage of beam combining and aperture filling. Additional beam deflection can prescribed per-emitter to compensate for known aberrations of collimating and aperture filling optics, for further optimisation of beam quality. It is also possible to carry out double-sided machining of silica block to construct custom aperture filling optical devices. The correction of off-shelf silica optics can be also carried out. Possible applications of the technique have only started to emerge.

Chapter 8

CONCLUSIONS AND FUTURE WORK

8.1 Introduction

This chapter contains a summary of conclusions following the material presented in the thesis. The summary is divided into paragraphs covering the important aspects of research. It is followed by an outline of future work required for further improvement of the beam correction technique and for exploring new possibilities of precision machining of silica and other glasses with CO_2 lasers.

8.2 Conclusions

Ablation of silica with CO_2 laser. This chapter has provided quantitative answers on CO_2 laser machining of silica. A machining without detrimental cracking has been shown. Material removal rate and machining threshold fluence have been measured and related to irradiance, pulse duration time and spot size. Optimal pulse length and fluence range, which produce smooth near-Gaussian craters, have been found to be 50−80 μs and 25−45 J/cm^2 correspondingly. It has been also shown that source stability, in terms of power (better than %2) and spectrum (single line preferably), was essential to assure a level of accuracy needed for precision machining of optical elements. It has been demonstrated that depth removal accuracy of ∼200 nm, comparable to that of UV and ultrafast ablation, has been achieved in the current machining system. Further improvement of depth accuracy is expected by enhanced stabilisation of pulse fluence to better than 1 J/cm^2 (currently achieved fluence stability). Besides the additional stabilisation of fluence, it

seems that the accuracy can be further improved by ablation in 9.2-9.6 μm wavelength band, which is easily addressable with CO_2 lasers. Substantial reduction of machining rate (~eight- to four-fold) is expected in this wavelength range. Machining resolution of <50 nm can be thus achieved by changing the wavelength alone. The resolution can be as fine as 10 nm when combining the enhanced pulse energy stability of better than 0.2 J/cm^2 and the anticipated ablation characteristics at 9.2−9.6 μm wavelength band. Low power, continuous-wave, CO_2 laser seems to be more suitable for precision machining, because the precise stabilisation of power is less problematic. A selection of laser line is also more flexible with CW than with slab waveguide model.

It has been shown that CO_2 ablation of silica produces surfaces of exceptional smoothness in comparison to ablation with other lasers relevant to precision microfabrication. Excellent surface quality has been associated with a presence of thin, 2−3 μm layer of low viscosity material. However, such melt layer promotes cracking in other silicate glasses that possess high thermal expansion coefficient.

Fabrication of micro-structures in silica with CO_2 laser. The work on precision machining of optical components in a raster scan, one-step, direct writing regime with a slab waveguide CO_2 laser has outlined the outstanding potential of the technique in comparison to other methods discussed in Chapter 5. High productivity rates of >16 minutes per cm^2 can be achieved together with an accuracy better than ±100 nm over tens of microns of machining depth, if only the pulse energy is controlled to better than 1% in a wide range of laser pulse frequencies. Available depth dynamics can also be extended to ~100 μm as a consequence of improved pulse stability. The machining range is scalable with crater diameter and depth, thus further optimisation is possible if more machining depth is needed and less lateral resolution is acceptable. The minimum feature size of the technique, at full machining range dynamics and minimum obtainable spot size of 47 μm, is limited to ~100 μm. The machining scheme can then be applied to fabrication of sub-millimeter size, refractive optical elements.

Laser polishing. The polishing of silica by a raster scan technique has been demonstrated to restore the optical quality of as-machined surfaces, without additional surface modification. The method offers not only high productivity rates

of 16 cm^2/min but also the simplicity and excellent process control. All important parameters, such as melt zone dimensions, polishing time and material viscosity can be controlled solely by the laser beam parameters. Raster scanning mode adds to the simplicity of the method since large scale beam uniformity is no longer required. The reduction of melt zone area, in comparison to conventional laser polishing, has diminished the heat load of treated element and relaxed the power requirements.

Laser-polished surfaces were free of cracking and stress-induced birefringence, however more research should be dedicated towards a detailed investigation of the impact of heat treatment on the optical and mechanical properties of affected layer of material. It takes one or two polishing passes to attenuate surface waviness of 10 μm period by more than 60 dB in following conditions: 1 mm beam ($1/e^2$ diameter at TEM_{00} like profile), raster pitch 2×10 μm, PRF 5 kHz, pulse duration of 20 μs and pulse fluence 0.42 J/cm^2. Initial surface roughness, 1.8 μm peak-peak amplitude of machining ripples, can be brought down to <1.8 nm, assuring the removal of worst-case machining pattern. Further improvement of laser polishing can be expected by an application of a source, for which the absorption length in silica α^{-1} is longer than for CO_2 laser. Just twofold increase of absorption depth would reduce the dwell time by a factor of 8, leading to an increase of the productivity, according to an idealized flow model. The CO laser radiation, with absorption length longer than that of CO_2 radiation, seems to be a good candidate for a more efficient laser polishing tool.

The scattering measurements have shown practically no difference between the laser polished surfaces and unmachined areas of silica samples. They have also confirmed that laser polishing raster does not contribute to the diffraction on the treated surfaces.

Beam quality correction for high power diode lasers. Chapter 7 has demonstrated a novel method of efficient correction of high power diode lasers, based on wavefront sensing, corrective plate design and subsequent rapid-fabrication. Currently, the time required for the wavefront measurement was 6 hours. A time required for a calculation of corrective plate and machining was approximately 6 hours as well. The amount of time can be greatly reduced by further improvement of laser stability and by a throughput increase of the measurement rig. Manufacturing time can be reduced down to 2 hours if only laser stability is improved in a

wide range of pulsing frequency 0-2 kHz.

The technique, presented in this chapter, is capable of significant reduction of fast-axis pointing errors from ~7 mrad down to ~0.4 mrad, an order of magnitude. A restoration of initial fast-axis beam quality (M^2 from ~12 down to ~2.4) has been observed, resulting in approx. ten-fold increase of brightness. It enables the beam combining, collimating or aperture filling optics to perform with greatly improved efficiency. Further reduction of pointing errors is expected to follow the improvement of laser stability and wavefront measurement technique.

Only fast-axis aberrations have been corrected in this study, because of limited number of measurement points. The limitation has been dictated by the time necessary to carry out wavefront measurements using the current rig. The method is not, however, limited to fast-axis correction only, since a fabrication of fully arbitrary shapes is feasible. It is possible to manufacture a corrective plate that would perform a complex correction of beam quality in both fast- and slow-axis ("bow-tie" correction), producing beams of minimal divergence and high brightness, ready for a next stage of beam reshuffling, combining and aperture filling. Additional beam deflection may be prescribed per emitter to compensate for known aberrations of collimating and aperture filling optics, for further optimisation of beam quality. It is also possible to carry out double-sided machining of silica block to construct custom, beam transforming devices. The correction of the off-shelf, silica optics can be also carried out. Possible application of the technique have only started to emerge.

Machining facility. The objective of building the flexible machining center has been achieved. The custom written software interface has enabled flexible, rapid prototyping of arbitrary, continuous-profile structures. The station operated spectrally tunable laser source with 24 hour power stability better than ±1%. The resolution of spot placement was 100×100 nm. Pulse-to-pulse energy stability was currently limited to ±2% due to 100 Hz rectified line frequency, introduced in the laser power supply. At the time of writing, the productivity rate of 800 pixels per second was guaranteed with the above stability. Pixel rate limit was imposed by frequency dependence of pulse energy. Productivity improvement by a factor of three can be expected when the laser pulse energy is controlled better than ±1% at all allowed pulse repetition frequencies. It can be achieved by a development of AOM-based pulse energy stabiliser. This technical difficulty must be overcome

before the station can fully exploit its currently dormant potential of >2000 pixels per second.

The technique presented in this thesis has a potential to revolutionise the area of rapid-prototyping of refractive micro-optics. It may be applied to the correction of diode lasers as well as to any other application requiring custom-made micro-optics.

8.3 Future work

Precise stabilisation of pulse energy (0.1%) is of the highest priority. It can be achieved by development of AOM-based precision energy dispenser. The device would regulate either the pulse duration or peak intensity of each individual pulse according to accurate, real-time measurement of pulse energy. The device would also solve a problem of pulse energy variation with pulsing frequency. An application of low-power, CW, tunable CO_2 laser as a machining tool would solve the frequency related instability of the slab waveguide model. Difficulties associated with beam pointing errors and spectral instability would also be solved with a CW CO_2 laser. However, the available laser power would be limited by the capacity of AOM, which in case of germanium-based devices is around 30 W CW. The experiments have shown however that 10 W is sufficient for laser polishing and too much for the machining.

Improved pulse stability would then enable exploitation of the potential of machining regimes as well. Variable overlap in two dimensions would provide more depth dynamics, reduce the machining time and greatly reduce the amounts of machining debris in the deeper sections of the optics. Additional precision energy control, provided by the dispenser, would allow for combined variable overlap and variable fluence cutting regimes. Depth dynamics of 100 μm would be then achievable, making it possible to fabricate the collimation micro-optics for non-lensed diode lasers. Machining on both sides of silica block could also be used for fabrication of custom aperture filling devices.

Besides the additional stabilisation of pulse fluence, it seems that machining accuracy can be further improved by ablation in 9.2-9.6 μm wavelength band, easily addressable with CO_2 lasers. It is thus very interesting to investigate the ablation characteristics in this wavelength range, where the absorptivity of fused silica peaks. It is also interesting to study the ablation of other glasses, commonly used for optical

applications, such as soda-lime glasses, which are much cheaper than pure silica. Although they badly crack during or after ablation, there is a possibility that the optimal machining conditions (temporal pulse shape, absorption depth, etc.) exist.

Although it has been shown that laser-polished surfaces were free of cracking and stress-induced birefringence, surface condition should be investigated in more detail. Careful measurements of refractive index change in the affected layer and systematic quantisation of residual stresses should be carried out. Further improvement of laser polishing can be expected by using a wavelength that offers longer absorption depth than currently used $\sim$10.6 μm wavelength. Just twofold increase of absorption depth would reduce the dwell time by a factor of 8, increasing the process productivity, according to the experimental findings. It would be very interesting to carry out the polishing experiments with a different wavelength.

Complex correction of diode laser array (elimination of beam pointing errors, restoration of beam quality, collimation of fast- and slow-axis) could be carried out if only the wavefront acquisition speed was improved. To achieve that goal, the throughput of the current system needs to be increased.

References

[1] T. H. Maiman, "Stimulated optical radiation in ruby," *Nature*, vol. 187, pp. 493–494, 1960.

[2] R. V. Steele, "Review and forecast of laser markets: 2003 part ii," *Laser Focus World*, vol. 39, Feb 2003.

[3] K. Kinkade and S. Anderson, "Review and forecast of laser markets part i: nondiode lasers," *Laser Focus World*, vol. 39, Feb 2003.

[4] G. A. J. Markillie, H. J. Baker, F. J. Villarreal, and D. R. Hall, "Effect of vaporisation and melt ejection on laser machining of silica glass micro-optical components," *Appl. Optics*, vol. 41, pp. 5660–5667, Sep 2002.

[5] H. J. Baker, G. A. Markillie, P. Field, Q. Cao, C. Janke, and D. R. Hall, "Precision laser processing of optical microstructures with slab waveguide CO_2 lasers," *Proc. SPIE High Power Lasers in Manufacturing*, vol. 3888, pp. 625–634, 2000.

[6] D. Botez and D. R. Scifres, *Diode Laser Arrays*. Cambridge Studies in Modern Optics, Cambridge University Press, 1994.

[7] R. Diehl, *High-Power Diode Lasers, Fundamentals, Technology, Applications*, vol. 78 of *Topics in Applied Physics*. Springer Verlag, 2000.

[8] H. J. Herfurth, M. Cryderman, and J. A. Clarke, "Automotive sheet metal welding with direct diode lasers."

[9] J. Haake, "Applications and benefits of direct diode lasers," 17-18 June 1999. Laser Processing Consortium, Industrial Laser Processing Workshop.

[10] F. Bachmann, "Present and future prospects of of high power diode and diode-pumped solid-state-laser technology and applications in Germany."

[11] Y. Liu, H. K. Liu, and Y. Braiman, "Injection locking of individual broad-area lasers in an integrated high-power diode array," *Appl. Phys. Lett.*, vol. 81, pp. 978–980, 2002.

[12] L. Goldberg, D. Mehuys, and D. Hall, "3.3 W CW diffraction limited broad area semiconductor amplifier," *Electron. Lett.*, vol. 28, pp. 1082–1084, 1992.

[13] S. Macomber, P. Akkapedi, and A. Montroll *SPIE Proc.*, vol. 723, pp. 36–39, 1986.

[14] W. A. Clarkson and D. C. Hanna, "Two-mirror beam-shaping technique for high-power diode bars," *Opt. Lett.*, vol. 21, pp. 375–377, 1996.

[15] S. Yamaguchi, T. Kobayashi, Y. Saito, and K. Chiba, "Collimation of emissions from a 1-cm aperture tightly arranged, multistripe laser-diode bar with a multiprism array coupling," *Appl. Optics*, vol. 36, pp. 1875–1878, 1997.

[16] V. Daneu, A. Sanchez, T. Y. Fan, H. K. Choi, G. W. Turner, and C. C. Cook, "Spectral beam combining of a broad-stripe diode laser array in an external cavity," *Opt. Lett.*, vol. 25, pp. 405–407, 2000.

[17] H. A. R. and B. H. J., "Assessment of micro-lenses for diode bar collimation," *Laser Diode and LED Applications III, SPIE Proc*, vol. 3000, pp. 209–214, 1997.

[18] L. Holland, *The properties of glass surfaces.* London: Chapman and Hall, 1966.

[19] A. Paul, *Chemistry of glasses.* Chapman and Hall, 1982.

[20] A. Nelson and M. Blander *J. Non-Cryst. Solids*, vol. 16, p. 321, 1974.

[21] D. G. Holloway, *The physical properties of glasses.* Wykeham Publications, 1973.

[22] A. Q. Tool *J. Am. Ceram. Soc.*, vol. 29, pp. 240–, 1946.

[23] U. Haken, O. Humbach, S. Ortner, and H. Fabian, "Refractive index of silica glass: influence of fictive temperature," *J. Non-Cryst. Solids*, vol. 265, pp. 9–18, 2000.

[24] E. D. Palik, *Handbook of optical constants of solids.* Academic Press, 1985.

[25] A. D. McLachlan and F. P. Meyer, "Temperature dependence of the extinction coefficient of fused silica for CO_2 laser wavelengths," *Appl. Optics*, vol. 26, pp. 1728–1731, 1987.

[26] S. Ameer-Beg, W. Perrie, S. Rathbone, J. Wright, W. Weaver, and H. Champoux, "Femtosecond laser microstructuring of materials," *Appl. Surf. Sci.*, vol. 127-129, pp. 875–880, 1998.

[27] M. Lenzner, F. Krausz, J. Kruger, and W. Kautek, "Photoablation with sub-10 fs laser pulses," *Appl. Surf. Sci.*, vol. 154, pp. 11–16, 2000.

[28] P. R. Herman, R. S. Marjoribanks, A. Oettl, K. Chen, I. Konovalov, and S. Ness, "Laser shaping of photonic materials: deep-ultraviolet and ultrafast lasers," *Appl. Surf. Sci.*, vol. 154, pp. 577–586, Feb 2000.

[29] M. von Allmen and A. Blatter, *Laser-beam interactions with materials.* Materials Science, Springer Verlag, 1995.

[30] "http://web.umr.edu/∼ownby/2000 tutorials/silica diagrams.ppt."

[31] "http://www.tosoh.com/englishhomepage/tqg/handling.htm."

[32] Y. M. Xiao and M. Bass, "Thermal-stress limitations to laser fire polishing of glasses," *Appl. Optics*, vol. 22, pp. 2933–2936, 1983.

[33] I. A. Konovalov and P. R. Herman, "Ablation-induced stresses in fused silica by 157-nm F_2-laser radiation," *Mat. Res. Symp.*, vol. 617, pp. J3.3.1–7, 2000.

[34] R. G. Mace, "Annealing of fused quartz," tech. rep., GE Quartz Inc., 1 February 2000.

[35] X. M. Wang, J. R. Leger, and R. H. Rediker, "Rapid fabrication of diffractive optical elements by use of image-based excimer laser ablation," *Appl. Optics*, vol. 36, pp. 4660–4665, 1997.

[36] P. E. Dyer, R. J. Farley, R. Giedl, and D. M. Karnakis, "Excimer laser ablation of polymers and glasses for grating fabrication," *Appl. Surf. Sci.*, vol. 96-8, pp. 537–549, 1996.

[37] G. P. Behrmann and M. T. Duignan, "Excimer laser micromachining for rapid fabrication of diffractive optical elements," *Appl. Optics*, vol. 36, pp. 4666–4674, 1997.

[38] M. Fiebig, M. Kauf, J. Fair, H. Endert, M. Rahe, and D. Basting, "New aspects of micromachining and microlithography using 157-nm excimer laser radiation," *Appl. Phys. A-Mater. Sci. Process.*, vol. 69, pp. S305–S307, 1999.

[39] J. Ihlemann, "Excimer laser ablation of fused-silica," *Appl. Surf. Sci.*, vol. 54, pp. 193–200, 1992.

[40] D. Du, X. Liu, G. Korn, J. Squier, and G. Mourou, "Laser-induced breakdown by impact ionization in SiO_2 with pulse widths from 7 ns to 150 fs," *Appl. Phys. Lett.*, vol. 64, pp. 3071–3073, 1994.

[41] P. P. Pronko, S. K. Dutta, J. Squier, J. V. Rudd, D. Du, and G. Mourou, "Machining of submicron holes using a femtosecond laser at 800nm," *Opt. Commun.*, vol. 114, pp. 106–110, 1995.

[42] B. C. Stuart, M. D. Feit, S. Herman, A. M. Rubenchik, B. W. Shore, and M. D. Perry, "Optical ablation by high-power short-pulse lasers," *J. Opt. Soc. Am. B-Opt. Phys.*, vol. 13, pp. 459–468, 1996.

[43] J. Krüger and W. Kautek, "Femtosecond-pulse visible laser processing of transparent materials," *Appl. Surf. Sci.*, no. 96-98, pp. 430–438, 1995.

[44] D. Ashkenasi, A. Rosenfeld, H. Varel, M. Wahmer, and E. E. B. Campbell, "Laser processing of sapphire with picosecond and sub-picosecond pulses," *Appl. Surf. Sci.*, vol. 120, pp. 65–80, 1997.

[45] R. F. Haglund and D. R. Ermer, "Explosive vaporization of fused silica initiated by a tunable infrared laser," *Appl. Surf. Sci.*, vol. 168, pp. 258–262, 2000.

[46] J. Bartley and W. Goltsos, "Laser ablation of refractive micro-optic lenslet arrays," *Proc. SPIE*, vol. 1544, pp. 140–145, 1991.

[47] V. P. Veiko and Y. B. Yakovlev, "Physical fundamentals of laser forming of micro-optical components," *Opt. Eng.*, vol. 33, pp. 3567–3571, 1994.

[48] H. L. Schick, "A thermodynamic analysis of the high-temperature vaporization properties of silica," *Chem. Rev.*, vol. 60, pp. 331–362, 1960.

[49] P. A. Temple, W. H. Lowdermilk, and D. Milam, "Carbon-dioxide laser polishing of fused-silica surfaces for increased laser-damage resistance at 1064-nm," *Appl. Optics*, vol. 21, pp. 3249–3255, 1982.

[50] F. Laguarta, N. Lupon, and J. Armengol, "Optical-glass polishing by controlled laser surface-heat treatment," *Appl. Optics*, vol. 33, pp. 6508–6513, 1994.

[51] F. Vega, N. Lupon, J. A. Cebrian, and F. Laguarta, "Laser application for optical glass polishing," *Opt. Eng.*, vol. 37, pp. 272–279, 1998.

[52] J. L. Ocana, A. Garcia-Beltran, F. Laguarta, J. Armengol, N. Lupon, and F. Vega, "Laser heat treatments driven by integrated beams: role of irradiation nonuniformities," *Appl. Optics*, vol. 38, pp. 4570–4576, 1999.

[53] M. T. Gale, M. Rossi, J. Pedersen, and H. Schutz, "Fabrication of continuous-relief micro-optical elements by direct laser writing in photoresists," *Opt. Eng.*, vol. 33, pp. 3556–3566, 1994.

[54] T. Jitsuno, K. Tokumura, N. Nakashima, and M. Nakatsuka, "Laser ablative shaping of plastic optical components for phase control," *Appl. Optics*, vol. 38, pp. 3338–3342, 1999.

[55] "http://www.hytek.com/hytekopto-electronicproducts.htm."

[56] "http://www-rocq.inria.fr/scilab/."

[57] P. E. Dyer, "Laser ablation: processes and applications," *Proc. SPIE*, vol. 3092, pp. 412–417, 1996.

[58] J. C. Miller, *Laser ablation.* Springer-Verlag, 1994.

[59] S. M. Metev and V. Veiko, *Laser-assisted micro-technology.* Materials Science, Springer Verlag, 1998.

[60] A. Meftah, M. Djebara, N. Khalfaoui, and M. Toulemonde, "Sputtering of vitreous SiO_2 and $Y_3Fe_5O_{12}$ in the electronic stopping power region. a thermal spike description," *Nucl. Instrum. Methods Phys. Res. Sect. B-Beam Interact. Mater. Atoms*, vol. 146, pp. 431–436, 1998.

[61] E. B. Kley, "Continuous profile writing by electron and optical lithography," *Microelectron. Eng.*, vol. 34, pp. 261–298, 1997.

[62] D. B. Graves and D. Humbird, "Surface chemistry associated with plasma etching processes," *Appl. Surf. Sci.*, vol. 192, pp. 72–87, 2002.

[63] M. R. Taghizadeh, P. Blair, B. Layet, I. M. Barton, A. J. Waddie, and N. Ross, "Design and fabrication of diffractive optical elements," *Microelectron. Eng.*, vol. 34, pp. 219–242, 1997.

[64] M. Ferstl, "Highly selective etching of deep silica components using electron cyclotron resonance plasma," *Microelectron. Eng.*, vol. 61-2, pp. 881–886, 2002.

[65] M. B. Stern, "Pattern transfer for diffractive and refractive microoptics," *Microelectron. Eng.*, vol. 34, pp. 299–319, 1997.

[66] M. T. Gale, "Replication techniques for diffractive optical elements," *Microelectron. Eng.*, vol. 34, pp. 321–339, 1997.

[67] T. Fujita, H. Nishihara, and J. Koyama, "Blazed gratings and Fresnel lenses fabricated by electron-beam lithography," *Opt. Lett.*, vol. 7, pp. 578–580, 1982.

[68] K. Zimmer, D. Hirsch, and F. Bigl, "Excimer laser machining for the fabrication of analogous microstructures," *Appl. Surf. Sci.*, vol. 96-8, pp. 425–429, 1996.

[69] D. von der Linde and K. Sokolowski-Tinten, "The physical mechanisms of short-pulse laser ablation," *Appl. Surf. Sci.*, vol. 154, pp. 1–10, Feb 2000.

[70] V. P. Veiko, *Fabrication of microoptical components, short course notes.* New Munich Trade Fair Centre: St. Petersburg State Inst. for Fine Mech. and Opt., 1999.

[71] H. M. Presby, A. F. Benner, and C. A. Edwards, "Laser micromachining of efficient fiber microlenses," *Appl. Optics*, vol. 29, pp. 2692–2695, 1990.

[72] T. E. Dimmick, G. Kakarantzas, T. A. Birks, and P. S. Russell, "Carbon dioxide laser fabrication of fused-fiber couplers and tapers," *Appl. Optics*, vol. 38, pp. 6845–6848, 1999.

[73] K. M. Nowak, H. J. Baker, and D. R. Hall, "Pulsed-laser machining and polishing of silica micro-optical components using a CO_2 laser and an acousto-optic modulator," *Proc. SPIE*, vol. 4941, pp. 107–112, October 2002.

[74] P. Coley, D. Wallace, and B. Antohe, "Applications of ink-jet printing technology to BioMEMS and microfluidic systems," *Proc. SPIE Conference on Microfluidics and BioMEMS*, October 2001.

[75] W. Royall Cox, T. Chen, and D. Hayes, "Micro-optics fabrication by ink-jet printing," *Opt. Photon. News*, pp. 32–35, June 2001.

[76] R. Danzebrink and M. A. Aegerter, "Deposition of micropatterned coating using an ink-jet technique," *Thin Solid Films*, vol. 351, pp. 115–118, 1999.

[77] E. Hecht, *Optics*. Addison-Wesley, third ed. ed., 1998.

[78] O. W. Fähnle and H. van Brug, "Novel approaches to generate aspherical optical surfaces," *SPIE Conference on Optical Manufacturing and Testing III*, vol. 3782, pp. 170–180, July 1999.

[79] D. Golini, G. Schneider, P. Flug, and M. DeMarco, "Magnetorheological finishing," *Opt. Photon. News*, vol. 12, Oct 2001.

[80] H. Takino, N. Shibata, H. Itoh, T. Kobayashi, K. Yamamura, Y. Sano, and Y. Mori, "Fabrication of optics by use of plasma chemical vaporization machining with a pipe electrode," *Appl. Optics*, vol. 41, pp. 3971–3977, 1 July 2002.

[81] V. P. Veiko, "Laser microshaping: Fundamentals, practical applications, and future prospects," *RIKEN Rev.*, January 2001.

[82] L. K. White, N. A. Miszkowski, W. A. Kurylo, and J. M. Shaw, "Flow properties and contour modeling of fusible borophosphosilicate glasses," *J. Electrochem. Soc.*, vol. 139, pp. 822–826, 1992.

[83] W. H. Southwell, "Wave-front estimation from wave-front slope measurements," *J. Opt. Soc. Am.*, vol. 70, pp. 998–1006, 1980.

[84] S. Groening, B. Sick, K. Donner, J. Pfund, N. Lindlein, and J. Schwider, "Wave-front reconstruction with a Shack-Hartmann sensor with an iterative spline fitting method," *Appl. Optics*, vol. 39, pp. 561–567, 2000.

[85] J. Pfund, N. Lindlein, and J. Schwider, "Misalignment effects of the Shack-Hartmann sensor," *Appl. Optics*, vol. 37, pp. 22–27, 1998.

[86] J. F. Monjardin, K. M. Nowak, A. R. Holdsworth, H. J. Baker, and D. R. Hall, "Brightness improvement for micro-lensed, laser diode bar stacks," *ASSP TOPS Proc.*, pp. 76–78, Technical Digest 2003.

[87] "High-power high-brightness laser diode arrays," tech. rep., Fraunhofer IAF, 1998. Achievements and results.